

10-26-87  
H-26-CR  
12-26-87  
213P.

(NASA-CR-182489) INFLUENCE OF CONVECTION ON  
MICROSTRUCTURE Final Report, 15 Jun. 1984 -  
31 Dec. 1987 (Clarkson Univ.) 213 p

N88-17784

CSCL 11F

Unclas  
G3/26 0124547

INFLUENCE OF CONVECTION ON MICROSTRUCTURE

February 1988

Final Report on Grant NAG8-480  
Reporting Period: 15 June 1984 to 31 December 1987

Prepared for the  
George C. Marshall Space Flight Center  
National Aeronautics and Space Administration

Prepared by  
William R. Wilcox, Gaber Faheem Eisa, S. Chandrasekhar,  
Mark Larrousse and Mohsen Banan

Department of Chemical Engineering  
and  
Center for Advanced Materials Processing  
Clarkson University  
Potsdam, New York 13676

## ABSTRACT

The objective of this research was to determine the influence of convection during directional solidification on the resulting microstructure of eutectics, specifically lead - tin and manganese - bismuth. During the grant period 3 Ph.D. theses were completed, 5 papers were published, and 10 presentations were made. An additional paper has been accepted, another is under review, and 4 others are being prepared.

Convection was generated by alternately rotating and not rotating the vertical Bridgman - Stockbarger ampoule during solidification. (The hydrodynamicists call this spin-up / spin-down, while the crystal growers call it the accelerated crucible rotation technique, or ACRT.) As the rotation rate was increased, the MnBi phase in the MnBi-Bi eutectic became more coarse. At low freezing rates the volume fraction of MnBi depended on ampoule rotation rate and radial position, with the radial dependence sensitive to the shape of the solid - liquid interface during solidification.

Spin-up / spin-down did not change the lamellar spacing of lead - tin eutectic frozen at 1.58 and 4.8 cm/hr. It did, however, lead to an increase in the rotation rate of the lamellae and reduced the length of the material solidifying cooperatively.

Theory was developed for the influence of convection on the microstructure of lamellar and fibrous eutectics, through the effect of convection on the concentration field in the melt in front of the growing eutectic. While the theory agrees with our experimental spin-up / spin-down results, it predicts that the weak convection expected due to buoyancy will not produce a measurable change in eutectic microstructure. Thus this theory does not explain the two-fold decrease in MnBi fiber size and spacing observed when MnBi-Bi is solidified in space or on earth with a magnetic field applied (courtesy of Larson and Pirich at Grumman). Attention was turned to the morphology of the MnBi-Bi

interface and to the generation of freezing rate fluctuations by convection.

Decanting the melt during solidification of MnBi-Bi eutectic showed that the MnBi phase projects into the melt ahead of the Bi matrix. Pulling apart directionally solidified rods at elevated temperatures showed that the MnBi fibers are smooth and straight over long distances. There is a wide range of fiber sizes, shapes and orientations, but little evidence of fiber branching or termination. The tensile strength increased as the MnBi fiber size and spacing decreased.

Temperature measurements in a bismuth melt in the vertical Bridgman - Stockbarger configuration showed temperature fluctuations of up to 25 C, with the amplitude decreasing near the solid - liquid interface and the frequency decreasing with decreasing height of the melt.

Electrochemical limiting current density measurements showed that the mass transfer rate varies significantly both radially and with time during the spin-up / spin-down cycle in the vertical Bridgman - Stockbarger configuration. These variations are minimized by maximizing the rotation rate and minimizing the period of stopping and starting the rotation. Thus spin-up / spin-down during directional solidification produces a periodic variation in freezing rate and segregation, which may produce compositional variations and alterations in microstructure. Theoretical calculations show the conditions under which compositional variations will diffuse away in the crystal while it is cooling to room temperature. This diffusional decay is favored by a slow freezing rate, low temperature gradient, rapid compositional fluctuations, and high diffusion coefficient in the solid.

Interpretation of the influence of spin-up / spin-down on MnBi-Bi eutectic microstructure is complicated by the facts that the MnBi fibers project out into the melt in front of the Bi, and that spin-up / spin-down both increases convection and causes the freezing rate to fluctuate rapidly. Additional research is needed to:

Determine the influence of fibers projecting out into the melt on convective effects on MnBi-Bi microstructure with a constant freezing rate.

Determine the influence on MnBi-Bi microstructure of a fluctuating freezing rate without convection.

Expand the knowledge of the effects of convection on the lead - tin eutectic.

## CONTENTS

Abstract	i
Contents	
1. Introduction	1
2. MnBi-Bi eutectic solidification	3
3. Pb-Sn eutectic solidification	4
4. Theory for influence of convection	5
5. Microstructure and mechanical properties of fibrous MnBi-Bi	6
6. Temperature fluctuations due to natural convection	7
7. Mass transfer variations with spin-up / spin-down	8
References	12
Appendices: Publications and excerpts from Ph.D. theses	
A. Effect of convection on the microstructure of the MnBi/Bi eutectic	
B. Influence of convection on spiral structure in lead-tin eutectic	
C. Influence of convection on lamellar spacing of eutectics	
D. Diffusional decay of striations	
E. Influence of convection on the rod spacing of eutectics	
F. MnBi-Bi experimental results	
G. Spin-up / spin-down experimental results	

## 1. INTRODUCTION

Directional solidification of eutectic and off-eutectic alloys in space has been observed to make the microstructure finer (1-4), coarser (5) and to have no effect (5,6). Vigorous stirring significantly coarsens Pb-Sn and Cd-Zn eutectics (7) and Fe-Fe<sub>2</sub>B and Ti-Ti<sub>5</sub>Si<sub>3</sub> eutectics (8). Application of a magnetic field to damp the convection gave the same effect on MnBi-Bi microstructure as solidification in space (9).

The primary long term goal of the Clarkson research program over the last 10 years has been to elucidate the mechanism underlying the extreme sensitivity of the MnBi-Bi microstructure to convection during solidification. Especially relevant are our prior experimental results that showed that the microstructure is independent of the temperature gradient during solidification (10), that it responds relatively quickly to a change in freezing rate (11), and that it coarsens significantly when convection is induced by alternately rotating the ampoule and not rotating it (spin-up / spin-down) (12). Theoretical results showed that convection can coarsen a lamellar microstructure by altering the compositional field in the adjacent melt, but that the effect of natural convection is likely to be negligible (12).

The specific objectives of the research performed under the latest grant were to:

1. Obtain comprehensive data for the influence of spin-up / spin-down on the MnBi-Bi microstructure, correlate these data, and compare the results with theory.
2. Determine theoretically the effect of convection on the microstructure of fibrous eutectics.
3. Determine the fluctuations in mass transfer and heat transfer caused by spin-up / spin-down to see if freezing rate fluctuations are likely to be significant.
4. Determine the influence of convection on the microstructure of a lamellar eutectic and compare with theoretical predictions.
5. Obtain information on the longitudinal microstructure of MnBi-Bi, especially branching and

termination of MnBi fibers and the planarity of the freezing interface.

6. Determine the mechanical properties of MnBi-Bi vs. microstructure.

These objectives were achieved. During the period of this grant 3 Ph.D. theses were completed, 5 papers were published, and 10 talks were given at meetings or other institutions. An additional paper has been accepted for publication, one has been revised after a review and 4 others are being written. Completed works are listed below and the papers are reproduced in the appendices.

Completed Ph.D. Theses:

G.F. Eisa, "Effect of Convection on the Microstructure of MnBi/Bi Eutectic Solidified from the Melt," 1985

S. Chandrasekhar, "Effect of Convection on the Microstructure of MnBi-Bi Eutectic," 1987

Mark F. Larrousse, "Transport Phenomena during Spin-up / Spin-down in the Bridgman - Stockbarger Technique," 1987

Papers:

V. Baskaran, I. Ghias and W.R. Wilcox, "Modeling the Influence of Convection on Eutectic Microstructures," p. 115 in Modeling of Casting and Welding Processes II, Metallurgical Society AIME, Warrendale (1984).

V. Baskaran and W.R. Wilcox, "Influence of Convection on Lameller Spacing of Eutectics," J. Crystal Growth 67 (1984) 343-352.

S. Chandrasekar, G.F. Eisa and W.R. Wilcox, "Influence of Convection on Lameller Spacing of Eutectics," J. Crystal Growth 76 (1986) 485-488.

G.F. Eisa, W.R. Wilcox and G. Busch, "Effect of Convection on the Microstructure of the MnBi/Bi Eutectic," J. Crystal Growth 78 (1986) 159-174.

D. Popov and W.R. Wilcox, "Influence of Convection on Spiral Structure in Lead - Tin Eutectic," J. Crystal Growth 78 (1986) 175-176.

R.T. Gray, M.F. Larrousse and W.R. Wilcox, "Diffusional Decay of Striations," J. Crystal Growth (in press).

S. Chandrasekhar and W.R. Wilcox, "Influence of Convection on Rod Spacing of Eutectics," J. Crystal Growth (in review).

M.F. Larrousse and W.R. Wilcox, "Interfacial Mass Transfer to a Cylinder Endwall during Spin-up / Spin-down," (in preparation).

Presentations:

W.R. Wilcox, "The Influence of Convection on the Microstructure of the MnBi-Bi Eutectic,"



University of Southampton (July 1984); Mullard Co. (July 1984).

G.F. Eisa and W.R. Wilcox, "Influence of Gravity on MnBi-Bi Eutectic Microstructure," 5th International Conference on Surface and Colloid Science and 59th Colloid and Surface Science Symposium, Potsdam, NY (June 1985).

S. Chandrasekhar and W.R. Wilcox, "Theory of the Influence of Convection on the Microstructure of Rod Eutectics," American Conference on Crystal Growth / East-1, Atlantic City (October 1986).

S. Chandrasekhar and W.R. Wilcox, "Influence of Convection on the Microstructure of the MnBi/Bi Eutectic," *ibid.*

M. Larrousse and W.R. Wilcox, "Accelerated Crucible Rotation in the Bridgman - Stockbarger Technique," American Conference on Crystal Growth-7 / II-VI - 87, Monterey (July 1987).

W.R. Wilcox, S. Chandrasekhar and G.F. Eisa, "Influence of Convection on the Microstructure of the Mn-Bi Eutectic," *ibid.*

R. Gray, M. Larrousse and W.R. Wilcox, "Decay of Compositional Striations," *ibid.*

M. Larrousse, R. Gray and W.R. Wilcox "Fluctuations in Mass Transfer due to Spin-up / Spin-down in the Bridgman - Stockbarger Technique and Striation Decay during Cooldown," AIChE meeting, NY (November 1987).

M. Larrousse, R. Gray and W.R. Wilcox "Use of Spin-up / Spin-down in Growth of Compound Semiconductor Crystals," AIME meeting, Phoenix (January 1988).

## 2. MnBi-Bi EUTECTIC SOLIDIFICATION

MnBi-Bi eutectic was directionally solidified in a vertical Bridgman - Stockbarger apparatus with the ampoule alternately rotated and stopped. Details of the experimental methods are in the theses mentioned above (13, 14). The detailed results are given in Appendices A and F, and are only summarized here.

An extensive series of experiments was performed over a wide range of freezing rates and ampoule rotation rates. At freezing rates of 9 mm/hr and above the MnBi formed quasi-regular fibers with a spacing  $L$  that obeyed the equation:

$$LV^{0.5} = 6.26 + 0.000112(RN^{1.5}/V)^{1.1} \quad (1)$$

where  $L$  is in microns,  $V$  is the freezing rate in cm/hr,  $R$  is the radial position in mm, and  $N$  is the rotation rate in RPM.

At freezing rates of 4.8 mm/hr and below the MnBi formed irregular blades (broken lamellae). With a concave interface there was a core of MnBi at the center surrounded by a ring devoid of MnBi. At the periphery there were large broken lamellae of MnBi. With a convex interface all of the MnBi was concentrated near the periphery with no MnBi at the center.

### 3. Pb-Sn EUTECTIC SOLIDIFICATION

A limited set of experiments was performed on the lead-tin eutectic, with the conditions and apparatus identical to those used for MnBi-Bi. The freezing rate was 1.58 or 4.8 cm/hr with rotation rates up to 128 RPM. As shown in Appendix B, under these conditions spin-up / spin-down did not detectably influence the lamellar spacing of Pb-Sn. Spin-up / spin-down did, however, have two other effects that we are not able to explain.

As reported by Mourer and Verhoeven (16), the lamellar structure in directionally solidified Pb-Sn slowly rotates as one moves down the ingot, presumably via faults. We found that the lamellae rotation rate increases as the ampoule rotation rate of spin-up / spin-down increases, presumably due to an increase in faulting frequency of the lamellae.

With spin-up / spin-down not all of the ingot exhibited cooperative growth. The top of the ingot was almost entirely tin while the bottom was lead. The fraction of the ingot containing lamellar lead-tin eutectic decreased as the rotation rate of spin-up / spin-down was increased.

#### 4. THEORY FOR THE INFLUENCE OF CONVECTION

By assuming a planar interface and a linear velocity profile in the adjacent melt, one can calculate numerically the concentration field in front of a growing eutectic. From the concentration field one determines the deviation of the average interfacial concentration from the value obtained without convection. This concentration change manifests itself as a deviation in lamellar spacing caused by the convection. We performed these computations for lamellar eutectics of three different compositions (17), but later found the results were valid only for a 50% eutectic and had to issue a correction (Appendix C). In the later paper we also developed a correlation for the influence of convection on the interfacial temperature.

The experimental results cited above (Eq. 1) for fibrous MnBi with spin-up / spin-down agree well with the theory. No effect on the lamellar spacing of Pb-Sn is predicted, as observed. The effect of spin-up / spin-down on broken lamellar MnBi was somewhat larger than predicted by theory.

Dr. Sheu at Clarkson used his computer code to estimate the amount of convection expected due to buoyancy in the apparatus used by Grumman in their flight and ground - based experiments. Our theory predicts that this convection would cause an unobservable change in MnBi fiber spacing, whereas Grumman's experiments showed a two-fold decrease in the flight samples. Thus our theory for a lamellar eutectic with a planar interface cannot explain Grumman's experimental results.

We suspected that the microstructure of a fibrous eutectic might be more sensitive to convection than a lamellar eutectic. So a computer code was developed for a regular array of square fibers, as described in Appendix E. However the results predict that the spacing of a fibrous eutectic would be affected less by convection than a lamellar eutectic. We next turned our attention to the possibility that the MnBi fibers project ahead of the Bi matrix during solidification, so that convection would have a much larger influence on the concentration field at the tips of the fibers,

and thereby alter the fiber spacing much more.

## 5. MICROSTRUCTURE AND MECHANICAL PROPERTIES OF FIBROUS MnBi-Bi

The solid-liquid interfacial morphology was revealed by pouring off the melt, as described in Chandrasekhar's Ph.D. thesis (14). As shown in the scanning electron micrographs in Appendix F, the MnBi fibers did project out into the melt. The amount of this projection varied widely for adjacent fibers, from approximately 1 diameter to 10 diameters.

We suspected that both spin-up / spin-down and Grumman's ground-based experiments produced a fluctuating freezing rate. Since the fiber spacing is known to decrease as freezing rate increases, a lack of symmetry in fiber termination and creation kinetics would increase the fiber spacing in the presence of a rapidly fluctuating freezing rate. The idea is as follows. Fibers would be expected to terminate easily. Thus a sudden decrease in freezing rate would quickly terminate many fibers. On the other, fiber nucleation would be unlikely. Furthermore since MnBi tends to facet, one would expect the other mechanism of fiber creation, splitting or branching, to be difficult. Thus a sudden increase in freezing rate would increase the number of fibers only slowly.

One key component in the above mechanism is the ease of fiber branching. One might expect to obtain a feeling for this from the longitudinal microstructure of the MnBi-Bi, but this has not been successful. Cutting the samples longitudinally reveals only short lengths of fibers because the fibers are thin and the cut cannot be precisely aligned with them. A variety of etchants were tried in an attempt to preferentially etch away the bismuth, but they either preferentially attacked the MnBi or dissolved both MnBi and Bi at the same rate. Another approach proved somewhat successful.

As described in his thesis (14), Chandrasekhar pulled apart directionally solidified MnBi-Bi samples while they were heated to elevated temperatures. We had hoped that the Bi would soften and allow the MnBi fibers to pull out. As shown in the scanning electron micrographs in Appendix F, this hope was realized. The fibers were found to have very straight sides with evidence of branching seldom seen. The fibers had a wide variety of sizes and orientations relative to one another and to the solidification direction. Thus these results tend to confirm our notion that fiber branching does not readily occur, although our techniques did not allow a quantitative determination of branching kinetics for a known increase in freezing rate.

While performing the above pull-out experiments, it was decided to measure the mechanical properties of directionally solidified MnBi-Bi eutectic. As shown in Appendix F, the tensile strength increased as the fiber size and spacing decreased, i.e. as the freezing rate increased.

## 6. TEMPERATURE FLUCTUATIONS DUE TO NATURAL CONVECTION

A thermocouple was inserted into the top of an ampoule identical to that used for the MnBi-Bi eutectic experiments. When immersed in a melt of bismuth, periodic temperature fluctuations of up to 25 C in amplitude were observed, as shown in Appendix F. As the ampoule was moved slowly down into the cooler, the amplitude of the temperature fluctuations decreased while the frequency increased.

Periodic temperature fluctuations have been observed many times in horizontal boats and in Czochralski crucibles, but this is believed to be the first time they have been observed in the Bridgman - Stockbarger arrangement. Such fluctuations would cause a fluctuating freezing rate and may thereby alter the microstructure of a resulting eutectic. It is conceivable that the Grumman

results may have been due to such a fluctuating freezing rate on earth that was not present in space.

To test this it will be necessary to perform experiments in the absence of convection with known fluctuating freezing rates. While these would best be performed in space, it should be possible to approximate convection - free conditions on earth by a proper choice of ampoules and vertical temperature gradient. We would like to do such experiments.

## 7. MASS TRANSFER VARIATIONS WITH SPIN-UP / SPIN-DOWN

Mass transfer and heat transfer at the melt-solid interface in the Bridgman - Stockbarger technique were modeled experimentally using limiting current density measurements. The melt, the melt-solid interface, and the crucible walls were replaced by an electrolyte, a cathode, and an anode, respectively. Ferrocyanide was converted to ferricyanide at the cathode surface, with the reverse reaction at the anode. Increasing the potential at such a cathode accelerates the reaction, which lowers the ferrocyanide concentration in the solution at the surface of the cathode. Eventually the surface concentration reaches zero, and further increases in potential do not change the reaction rate. The current density under such mass transfer controlled conditions is known as the limiting current density. Measuring this limiting current density gives a direct measurement of the mass transfer rate to the cathode in the presence of a known concentration difference -- the bulk ferrocyanide concentration.

The fluid flow caused by increasing the cylinder rotation rate is known as spin-up. Similarly the flow caused by decreasing the cylinder rotation is known as spin-down. Most of the theoretical and experimental work on the hydrodynamics was done for cylinders with an aspect ratio of unity or less. (The aspect ratio is defined as the ratio of height to diameter.) During spin-up, a layer of

fluid, known as the Ekman layer, is pumped radially outward along the cylinder endwall. When the fluid in the Ekman layer meets the cylinder sidewall, it turns and climbs up the wall. By continuity, fluid is sucked towards the endwall along the central axis and fluid is pulled radially inward in the regions away from the endwall. Spin-up produces stable flow. During spin-down, the flow is reversed. However spin-down is inherently unstable and vortices are shed along the cylinder wall and endwalls in a chaotic manner (see Appendix G).

Many analytic models have been published describing the flow produced in spin-up. Spin-down, being complicated by the inherent instability, requires numerical models to predict the flow pattern. Two dimensionless groups are used to characterize the fluid motion resulting from spin-up and spin-down. The first is the Ekman number, the ratio of the viscous to inertial forces, which is given by:

$$Ek = \nu / (wR^2) \quad (2)$$

where Ek is the Ekman number,  $\nu$  is the kinematic viscosity,  $w$  is the rotation rate, and  $R$  is the cylinder radius. The second dimensionless group is the Rossby number, the ratio of the Coriolis force to the inertial force, which is given by:

$$Ro = (w_{large} - w_{small}) / w_{large} \quad (3)$$

where Ro is the Rossby number and the subscripts refer to the larger and smaller of the two rotation rates after an impulsive change.

The experimental apparatus and procedures are described in detail elsewhere (15). To measure local rates of mass transfer, 1 mm diameter electrodes were embedded in the large nickel cathode covering the bottom of the cylinder. These small cathodes were insulated from the main cathode by a thin non-conducting region. The kinetics of mass transfer is traditionally represented by the

Sherwood number, which is the dimensionless interfacial concentration gradient at the cathode surface. The Sherwood number  $Sh$  is obtained from the limiting current density  $i$  by:

$$Sh = ir/nFDC \quad (4)$$

where  $C$  is the concentration of the reactant species in the bulk solution (the surface concentration is zero at the limiting current density),  $r$  is either the radial position of the electrode or the cylinder radius (for an electrode at the center),  $n$  is the moles of electrons transferred per mole of reactant,  $F$  is Faraday's constant, and  $D$  is the reactant diffusivity in the electrolyte.

The experiments were performed in two major series. The first series of experiments was conducted at various Ekman numbers with the Rossby number equal to unity (spin up from rest). Long and short period experiments were conducted. The long period experiments consisted of rotating the cylinder for ten minutes (spin-up) and not rotating for the next ten minutes (spin-down). The short period experiments consisted of alternately rotating and not rotating, with a period of one minute or less. In the short period work, the spin-up time equalled the spin-down time.

The second series of experiments was conducted at a single Ekman number with the Rossby number held at 0.08 and using short rotation periods. The two groups of experiments demonstrated the effect the Stewartson layer had during spin-up / spin-down.

The experimental results are given in detail in Appendix G. Large variations in Sherwood number occurred both radially and with time during the spin-up / spin-down cycle. The spatial and temporal variations were shown to be minimized by maximizing the rotation rate and minimizing the period.

Strong variations in heat transfer are expected as well due to spin-up / spin-down, since both heat transfer and mass transfer are influenced by convection. Thus one would expect spin-up / spin-down to strongly influence the compositional homogeneity and microstructure of materials frozen



under such conditions. Appendix D shows that compositional striations will diffuse away in the crystal if they are close together, the freezing rate is low, the temperature gradient in the solid is low, and the diffusion coefficient is high.

The effect of freezing rate oscillations on eutectic microstructure are uncertain, as noted in the preceding section. However, it may be that much of the change in microstructure of MnBi-Bi and Pb-Sn caused by spin-up / spin-down may have resulted from a fluctuating freezing rate and not solely from enhanced convection. Further experiments are needed.

## APPENDIX F

### MnBi-Bi EXPERIMENTAL RESULTS

Excerpts from a 1987 Ph.D. thesis by S. Chandrasekhar at Clarkson University.

Complete copies of this thesis may be obtained from University Microfilms or from W.R. Wilcox for the costs of reproduction.

## 4 EXPERIMENTAL RESULTS

### 4.1 Three-dimensional microstructure of the MnBi-Bi eutectic

The primary objective of this work was to determine the three-dimensional microstructure of MnBi fibers formed by the directional solidification of the MnBi-Bi eutectic. The purpose of investigating the nature of the fibers was to check the hypothesis that the MnBi fibers, being faceted, terminate with ease but branch with difficulty in response to a perturbation in the growth rate. During solidification on earth irregular convection is expected in the melt and should result in a fluctuating growth rate. It is speculated that every time there is an increase in the growth rate, the MnBi fibers have difficulty branching and do not adjust their spacing corresponding to the higher growth rate. On the other hand a decrease in the growth rate should result in termination of some of the fibers to increase the spacing between them. Thus the average spacing between the fibers will be greater than the spacing corresponding to the minimum undercooling as predicted by Jackson and Hunt [24].

The MnBi/Bi eutectic solidifies with essentially four different microstructures based on the growth rate  $V$  [68]. The ranges of these growth rates are:

1. Very low growth rates,  $V < 0.5$  cm/hr
2. Low growth rates,  $0.5 < V < 0.9$  cm/hr
3. Medium growth rates,  $0.9 < V < 12$  cm/hr
4. High growth rates,  $V > 12$  cm/hr.

At very low and low freezing rates, the MnBi phase is in the form of broken lamellae or blades. They are not oriented in any particular direction and are distributed randomly across the cross-section of the ingot. At medium and high growth rates the MnBi phase forms fibers oriented along the direction of solidification. In the transition region between the low and medium translation rates the MnBi fibers are faceted and are not circular in cross-section.

To obtain a three-dimensional view of the MnBi fibers, directionally solidified ingots of the eutectic were heated to a temperature close to its melting point ( $265^{\circ}\text{C}$ ) and fractured. The eutectic directionally solidified at different growth rates was fractured either on the Gleeble or the Vacuum Strain Gauge apparatus. Details of the experiment are given in Chapter 3. The samples fractured on the Vacuum Strain Gauge were heated to  $204^{\circ}\text{C}$  and strained at a rate of  $0.873\text{ hr}^{-1}$ . On the Gleeble it was not possible to measure the strain rate but it was on the order of 10 inches per second. The specimen was heated to  $225^{\circ}\text{C}$  before fracture.

For the temperatures and times used in the present experiments (2 hours on the VSG and 10 minutes on the Gleeble), heating should have had no effect on the microstructure of the eutectic. The effect of annealing the MnBi-Bi eutectic at a temperature close to its melting point was investigated by Pirich and Larson [69] at Grumman Aerospace Corporation. The eutectic was heated to a temperature of  $250^{\circ}$ . After more than 24 hours the MnBi fibers were more circular in cross-section with no change in spacing.

After each experiment, scanning electron micrographs were taken of the two fracture surfaces of the specimen. Typical scanning electron micrographs are shown in the following pages. The growth conditions and the magnification are indicated at the bottom of each. Possible cases of branching are indicated within circles.

Substantial fiber pull-out was obtained in all cases. Figures 4.1 to 4.12 show samples fractured on the Gleeble at a high strain rate. Figures 4.12 to 4.30 are of samples fractured on the Vacuum Strain Gauge. Figures 4.1 to 4.23 are of the eutectic directionally solidified without spin-up/spin-down at medium and high translation rates.

Certain features in these photographs need explanation. In figure 4.1, the growth direction was upwards and the two fibers were moving towards each other probably resulting in a termination. In figure 4.5 different shapes of fibers are seen. The sample was solidified at 1.05 cm/hr, which corresponds to the transition region between low and medium translation rate morphologies. In figures 4.6, 4.7, 4.8 and 4.9 tiny globules are also present along with the fibers on the fractured surface. An EDEX (Energy Dispersive X-Ray) analysis was performed to identify the elements present in these globules. While they contained manganese and bismuth, their exact proportion is not known. Part of the fibers probably melted during straining in the Gleeble because the electric power was concentrated in a small region of the ingot during fracture.

Figure 4.24 shows a fracture surface typical of eutectics solidified at very low and low growth rates. No MnBi pull-out was observed on either of the fracture surfaces of the specimen.

Figures 4.25 to 4.30 are of samples solidified at different growth rates with spin-up/spin-down. The fibers appear to be the same as without spin-up/spin-down.

No clear evidence of branching, that is, one fiber branching into two, was observed in any of the fractured samples. However in a number of instances two fibers growing adjacent to each other were observed.

ORIGINAL PAGE IS  
OF POOR QUALITY



Figure 4.1: Fracture surface. Growth rate: 2.2 cm/hr, Growth direction: left to right. Magnification: 4.5 kX



Figure 4.2: Fracture surface. Growth rate: 2.2 cm/hr, Growth direction: left to right. Magnification: 9.0 kX

ORIGINAL PAGE IS  
OF POOR QUALITY

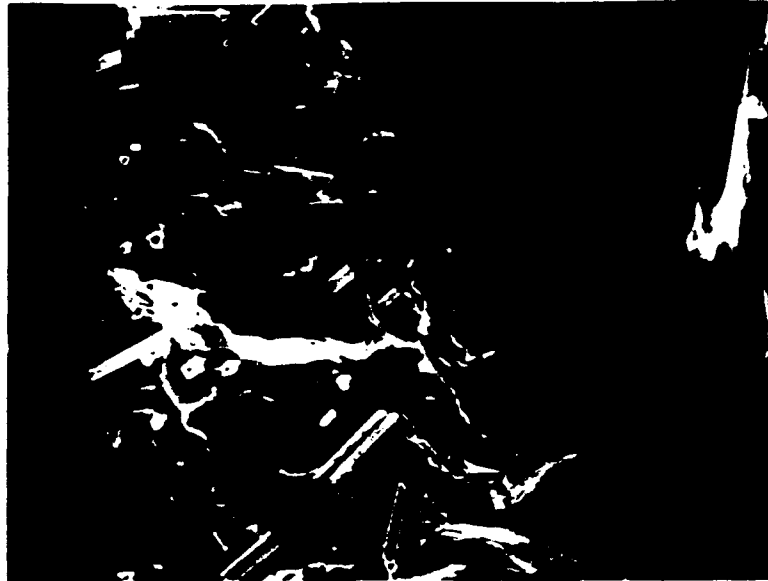


Figure 4.3: Fracture surface. Growth rate: 2.2 cm/hr, Growth direction: left to right. Magnification: 1.37 kX



Figure 4.4: Fracture surface. Growth rate: 1.05 cm.hr, Growth direction: down. Magnification: 1.47 kX

ORIGINAL PAGE IS  
OF POOR QUALITY



Figure 4.5: Fracture surface. Growth rate: 1.05 cm/hr, Growth direction: up.  
Magnification: 3.01 kX

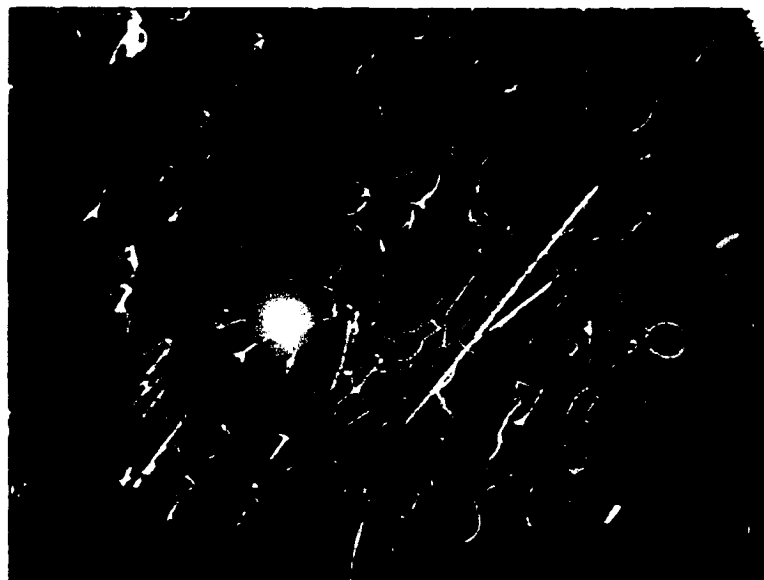
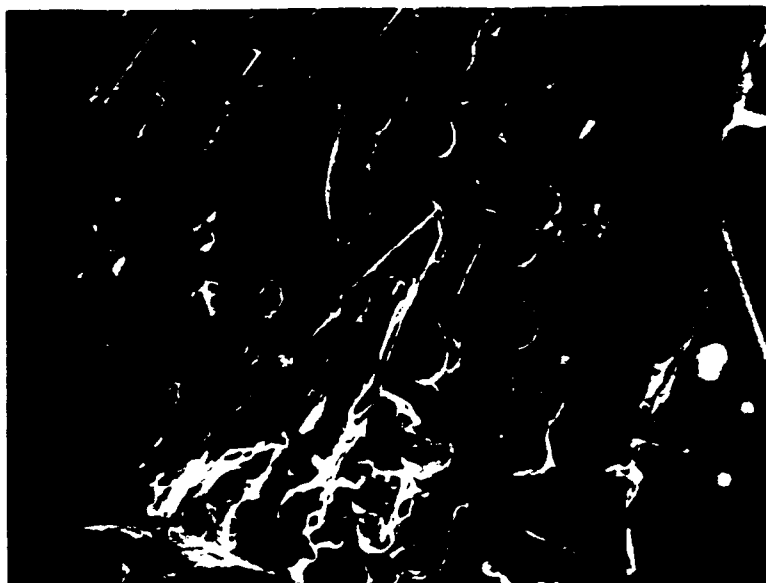


Figure 4.6: Fracture surface. Growth rate: 1.05 cm/hr, Growth direction: left to  
right. Magnification: 1.01 kX



ORIGINAL PAGE IS  
OF POOR QUALITY



**Figure 4.7:** Fracture surface. Growth rate: 1.05 cm/hr, Growth direction: left to right. Magnification: 1.02 kX



**Figure 4.8:** Fracture surface. Growth rate: 1.05 cm/hr, Growth direction: left to right. Magnification: 1.12 kX

ORIGINAL PAGE IS  
OF POOR QUALITY

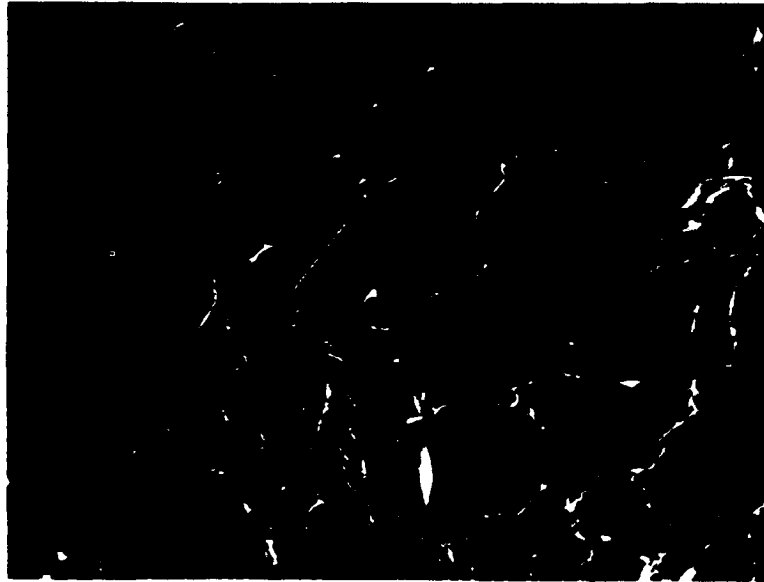


Figure 4.9: Fracture surface. Growth rate: 1.05 cm/hr, Growth direction: right to left. Magnification: 1.01 kX



Figure 4.10: Fracture surface. Growth rate: 1.05 cm/hr, Growth direction: left to right. Magnification: 5.1 kX

ORIGINAL PAGE IS  
OF POOR QUALITY



Figure 4.11: Fracture surface. Growth rate: 1.05 cm/hr, Growth direction: up.  
Magnification: 2.01 kX

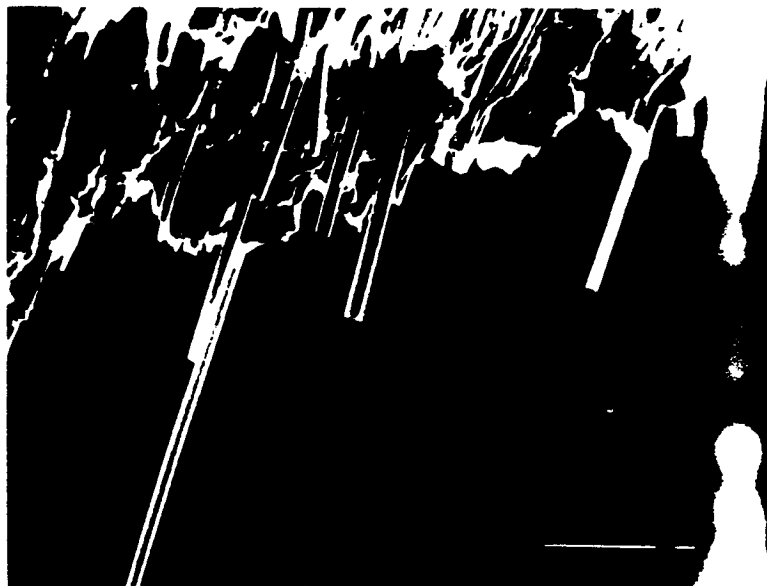


Figure 4.12: Fracture surface. Growth rate: 4.69 cm/hr, Growth direction: down.  
Magnification: 1.5kX

ORIGINAL PAGE IS  
OF POOR QUALITY.

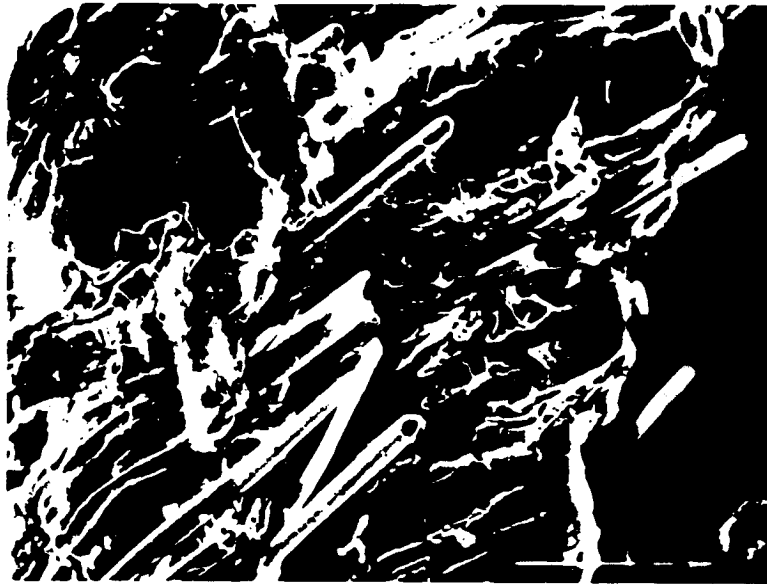


Figure 4.13: Fracture surface. Growth rate: 2.98 cm/hr, Growth direction: left to right. Magnification: 1.6 kX



Figure 4.14: Fracture surface. Growth rate: 2.31 cm/hr, Growth direction: up. Magnification: 1.17 kX

ORIGINAL PAGE IS  
OF POOR QUALITY

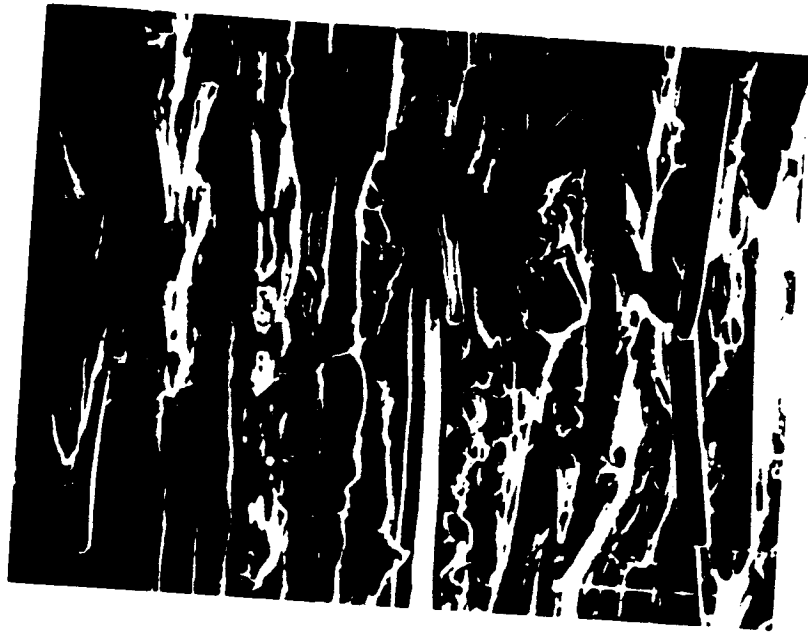


Figure 4.15: Fracture surface. Growth rate: 2.31 cm/hr, Growth direction: up.  
Magnification: 1.16 kX

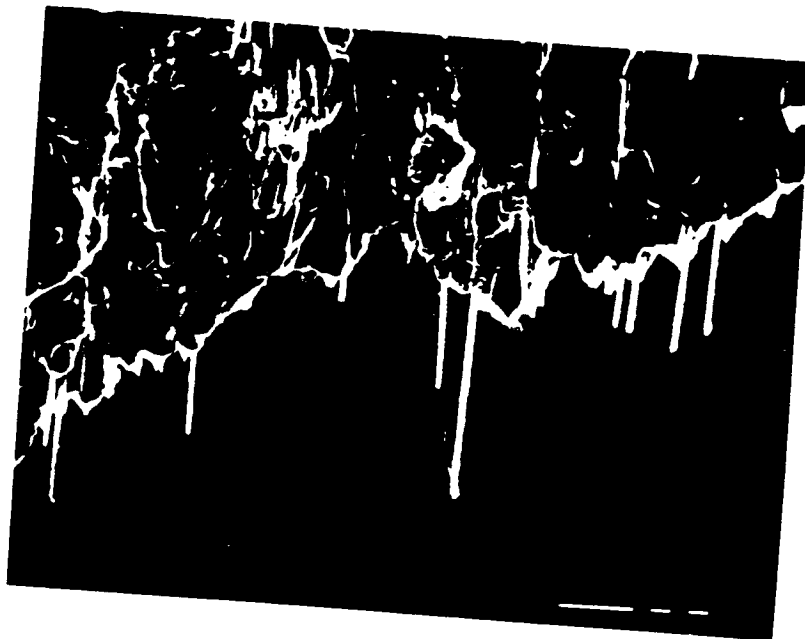


Figure 4.16: Fracture surface. Growth rate: 8.94 cm/hr, Growth direction: down.  
Magnification: 1.02 kX

ORIGINAL PAGE IS  
OF POOR QUALITY

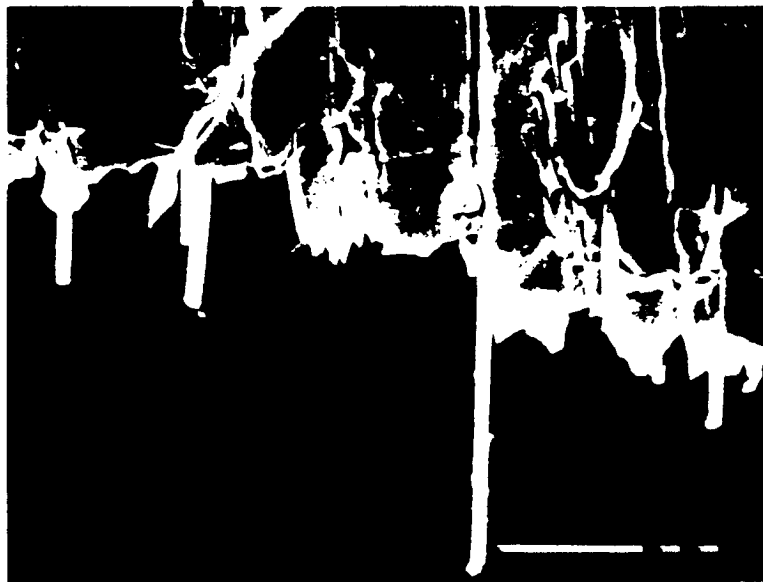


Figure 4.17: Fracture surface. Growth rate: 8.94 cm/hr, Growth direction: down.  
Magnification: 2.0 kX

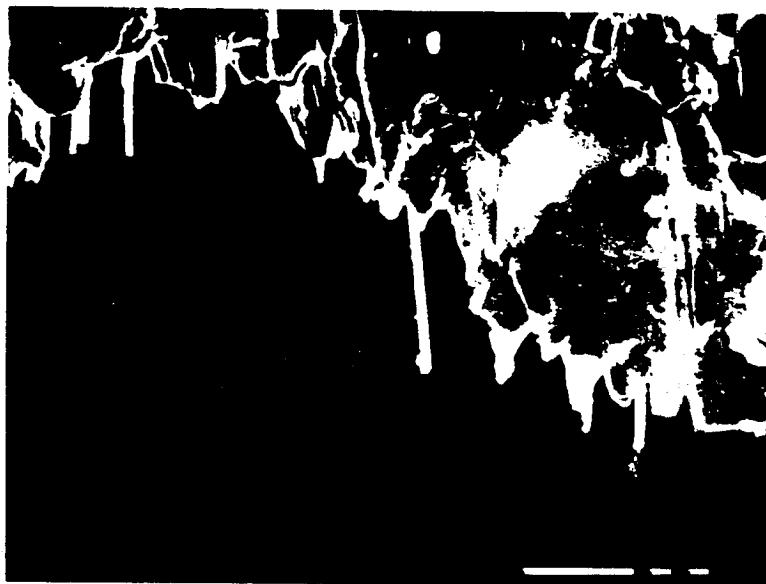


Figure 4.18: Fracture surface. Growth rate: 8.94 cm/hr, Growth direction: down.  
Magnification: 1.53 kX

ORIGINAL PAGE IS  
OF POOR QUALITY

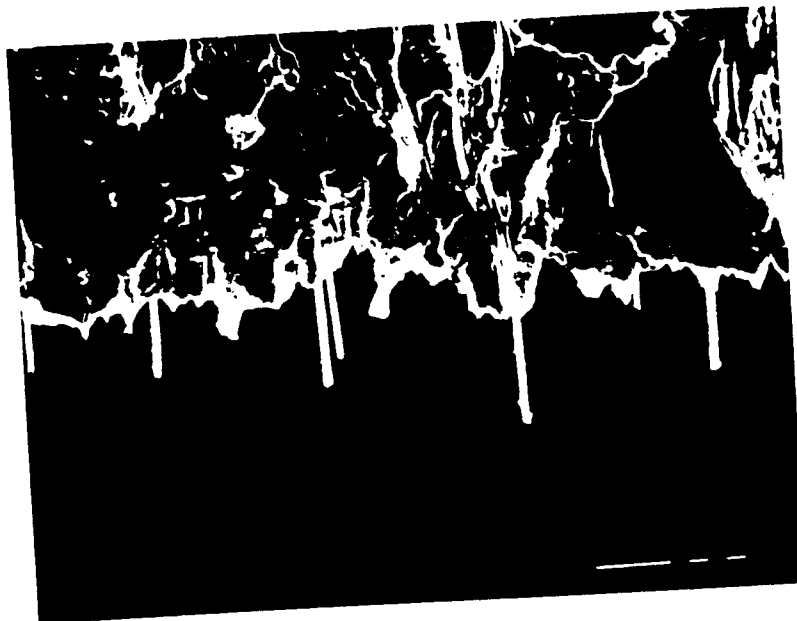


Figure 4.19: Fracture surface. Growth rate: 8.94 cm/hr, Growth direction: Up, Magnification: 1.02 kX.

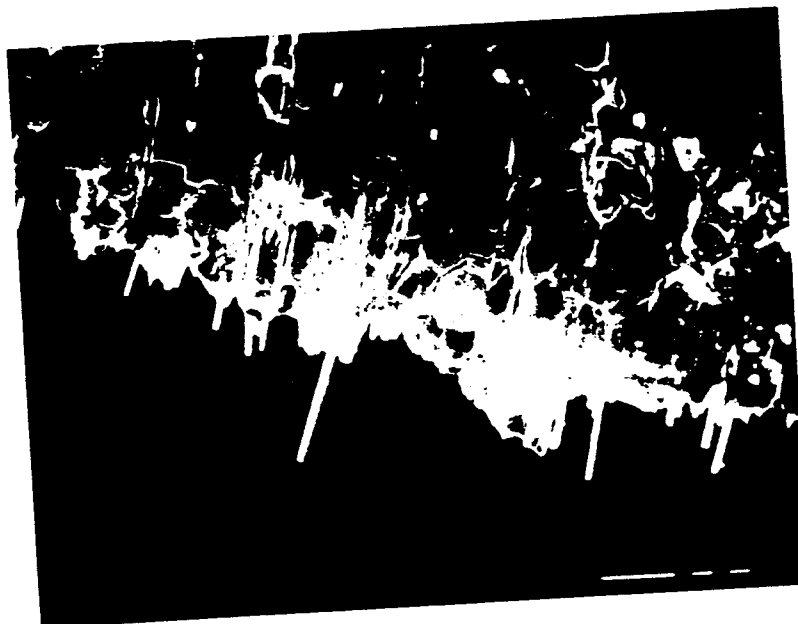


Figure 4.20: Fracture surface. Growth rate: 8.94 cm/hr, Growth direction: Up, Magnification: 1.0 kX.

ORIGINAL PAGE IS  
OF POOR QUALITY

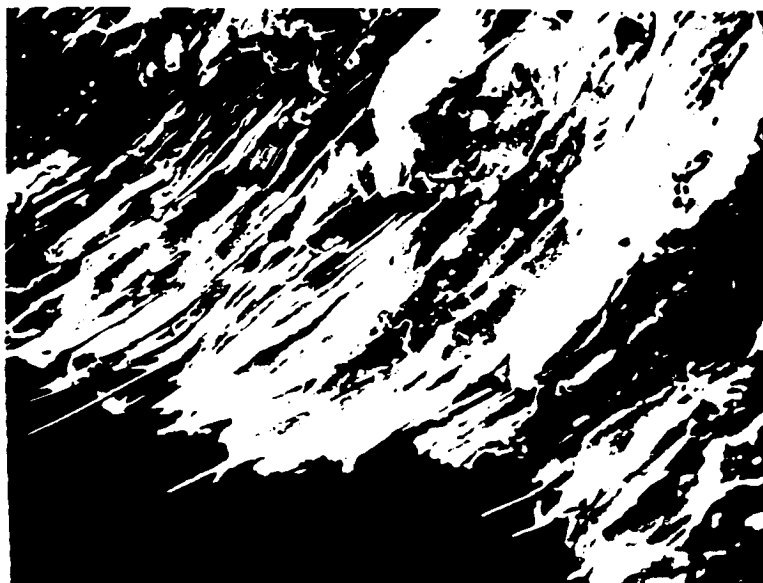


Figure 4.21: Fracture surface. Growth rate: 4.69 cm/hr, Growth direction: Right to left, Magnification: 0.74 kX.

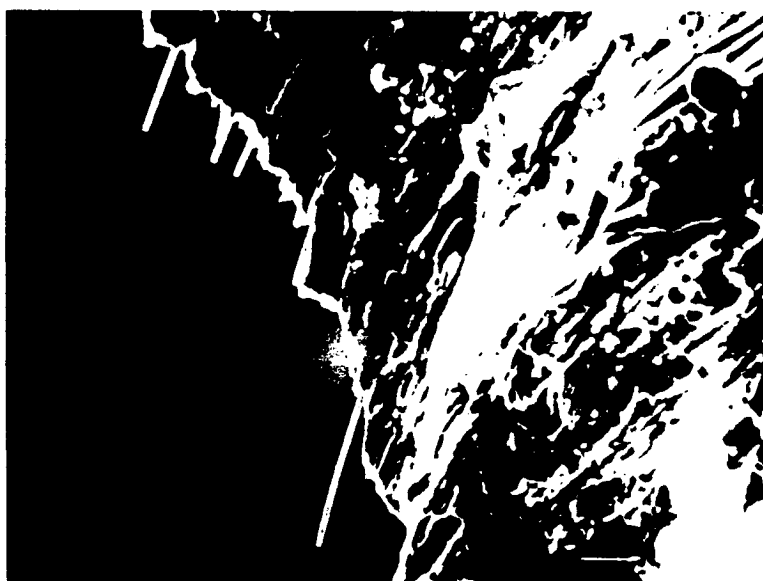


Figure 4.22: Fracture surface. Growth rate: 6.23 cm/hr, Growth direction: Up, Magnification: 0.54 kX.



ORIGINAL PAGE IS  
OF POOR QUALITY

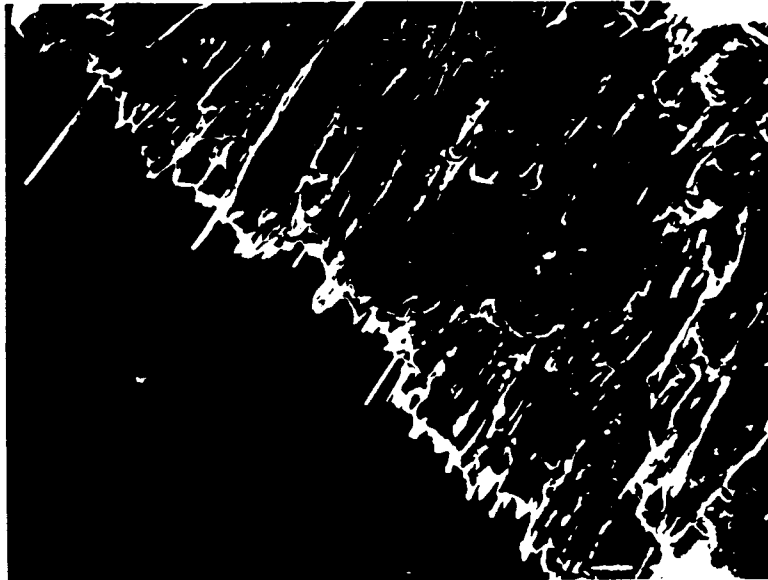


Figure 4.23: Fracture surface. Growth rate: 4.69 cm/hr, Growth direction: Left to right, Magnification: 0.74 kX.

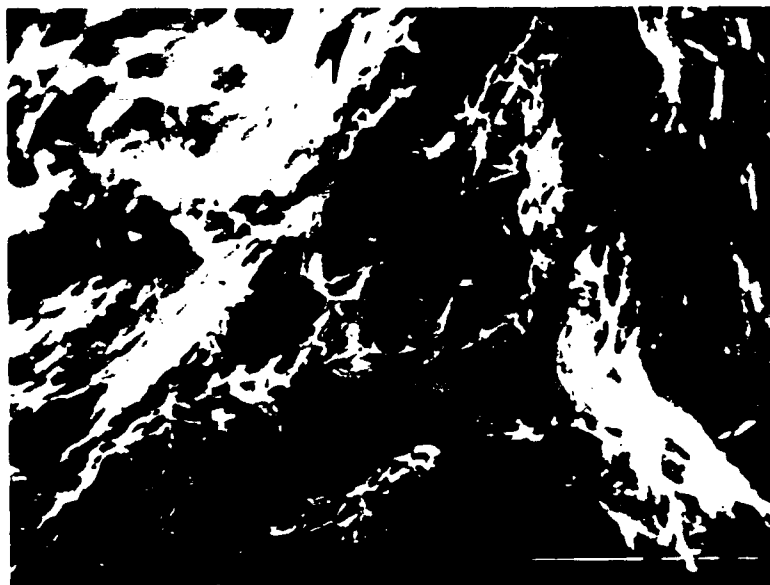


Figure 4.24: Fracture surface. Growth rate: 0.8 cm/hr, Growth direction: Up, Magnification: 0.74 kX.

ORIGINAL PAGE IS  
OF POOR QUALITY



Figure 4.25: Fracture surface. Growth rate: 2.98 cm/hr with 100 rpm spin-up/  
spin-down, Growth direction: Right to left, Magnification: 3.2 kX.



Figure 4.26: Fracture surface. Growth rate: 2.98 cm/hr with 100 rpm spin-up/  
spin-down, Growth direction: Left to right, Magnification: 1.99 kX.

ORIGINAL PAGE IS  
OF POOR QUALITY



Figure 4.27: Fracture surface. Growth rate: 2.98 cm/hr with 100 rpm spin-up/  
spin-down, Growth direction: Down, Magnification: 3.2 kX.

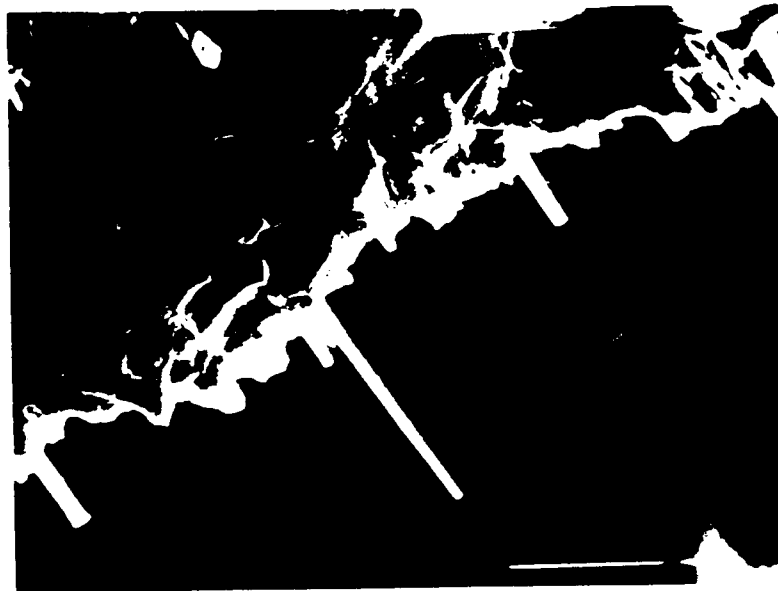


Figure 4.28: Fracture surface. Growth rate: 2.98 cm/hr with 100 rpm spin-up/  
spin-down, Growth direction: Down, Magnification: 2.13 kX.

ORIGINAL PAGE IS  
OF POOR QUALITY

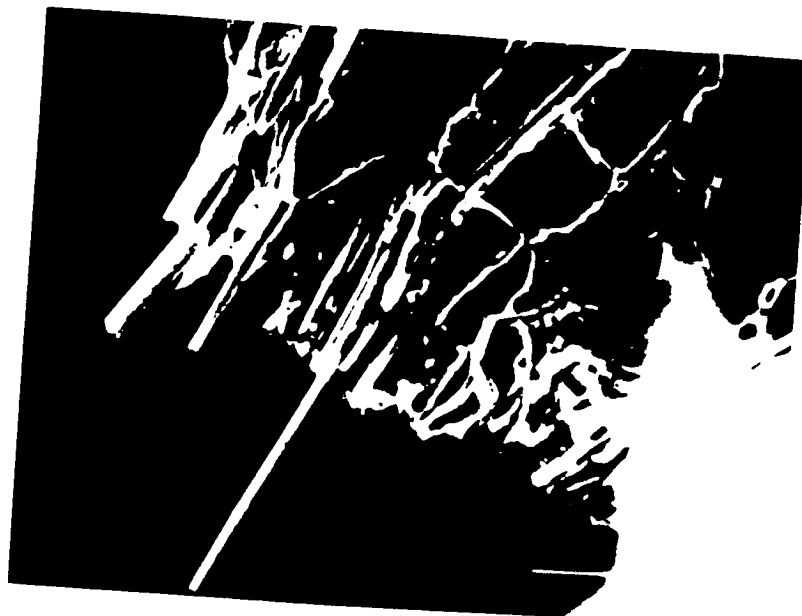


Figure 4.29: Fracture surface. Growth rate: 6.23 cm/hr with 100 rpm spin-up/spin-down, Growth direction: Up, Magnification: 6.9 kX.



Figure 4.30: Fracture surface. Growth rate: 4.69 cm/hr with 100 rpm spin-up/spin-down, Growth direction: Right to left, Magnification: 1.51 kX.

## 4.2 Decantation experiments

The details of this experiment are given in the chapter 3. Briefly, solidification of the melt was stopped half way through and the whole furnace assembly was tilted to decant the remaining melt off the freezing interface. These decanted surfaces were examined in a SEM. An energy dispersive X-ray analysis of the surface identified the presence of Mn and Bi of constant concentration across the entire decanted surface. This indicates that a thin film of melt remained on the interface and solidified after decanting.

Figure 4.31 shows a side and a top view of a typical decanted surface. The surfaces were all more or less flat. A lip formed on the side the melt was poured off. Figures 4.32 to 4.60 show scanning electron micrographs of the decanted surfaces of the eutectic solidified at different growth rates. Possible instances of branching are indicated within circles. The extent of projection of the MnBi phase and the length/diameter ratio for the different growth rates are tabulated in Tables 2, 3, 4 and 5. The extent of projection was directly measured from the scanning electron micrographs using a vernier calipers to an accuracy  $5 \times 10^{-3}$  cm.

Figures 4.32 and 4.33 show the interface of the eutectic solidified at a very low growth rate of 0.4 cm/hr without spin-up/spin-down. Figures 4.31 and 4.32 show broken lamellae projecting out. Figures 4.34 to 4.38 show the interface of the eutectic solidified at the same growth rate as the sample above (0.4 cm/hr) but with 200 rpm spin-up/spin-down. Each of the photographs shows a different shape of the MnBi phase. Figures 4.33 and 4.38 show larger areas of the eutectic solidified at 0.4 cm/hr with 200 rpm spin-up/spin-down.

Table 2: Extent of projection and diameter of MnBi phase under different growth conditions.

Growth Conditions	Figure No.	Length $\times 10^4$ cm	Diameter $\times 10^4$ cm	l/d
0.4 cm/hr	4.32	13.7		
0.4 cm/hr	4.33	18.3		
0.4 cm/hr	4.34	13.7	10.4	1.32
with 100 rpm	4.35	22.6	9.67	2.34
SU/SD		16.9	2.58	6.55
				30 with l/d $\approx$ 1
	4.36	26.4	13.2	2
	4.37	36.8	6.01	6.12
		25.7	6.01	4.28
	4.38	25.9	17.5	1.48
2.98 cm/hr	4.39			2 with l/d $\approx$ 1
	4.40	7.87	3.27	2.41
		7.67	2.67	2.87
				7 with l/d $\approx$ 1
	4.41	7.62	2.5	3.05
		7.62	2.5	3.05
	4.42	34.3	4.02	8.53
	4.43	16.0	3.14	5.1
				25 with l/d $\approx$ 1
	4.44	6.84	3.56	1.92
		5.3	2.75	1.93

Table 3: Extent of projection and diameter of MnBi phase under different growth conditions.

Growth Conditions	Figure No.	Length $\times 10^4$ cm	Diameter $\times 10^4$ cm	l/d
2.98 cm/hr	4.45	10.9	2.5	4.36
		10.5	2.29	4.59
		2.7	2.29	1.18
				15 with l/d $\approx 1$
3.68 cm/hr	4.46			47 with l/d $\approx 1$
	4.47	4.52	1.49	3.03
		6.67	1.13	5.9
	4.48			5 with l/d $\approx 1$
		3.89	0.91	4.27
				40 with l/d $\approx 1$
	4.49			60 with l/d $\approx 1$
	4.50			50 with l/d $\approx 1$
	4.51			15 with l/d $\approx 1$
	4.52			9 with l/d $\approx 1$
3.68 cm/hr with 100 rpm SU/SD	4.53	9.04	1.9	4.76
		4.76	1.43	3.33
		11.9	1.67	7.12
		4.76	0.95	5
		20.4	1.19	17.1
		16.7	1.43	11.68
		13.8	0.95	14.5

Figures 4.39 to 4.45 show the decanted interface of the eutectic solidified at 2.98 cm/hr. Two decantation experiments were performed and are indicated by I and II.

Figures 4.46 to 4.52 show the decanted interface of the eutectic solidified at a high growth rate of 3.68 cm/hr. Four different decantation experiments were performed at this growth rate. The interfaces corresponding to each of these experiments are indicated by A, B, C and D. Figures 4.53 and 4.56 show the interface of the eutectic solidified at the same rate of 3.68 cm/hr with 200 rpm spin-up/spin-down. No difference in the extent of projection of the fibers is observed for the two different growth conditions. Figure 4.54 shows fibers sticking out like a flag post from a tent. The tent is probably formed by melt trapped around the projecting fibers during decantation.

Figure 4.57 shows the decanted interface of eutectic solidified at 6.1 cm/hr.

The MnBi fiber projection for the different growth conditions averaged approximately one to two fiber diameters as tabulated in table 4. There were a few fibers with a length to diameter ratio greater than 10.



Table 4: Extent of projection and diameter of MnBi phase under different growth conditions.

Growth Conditions	Figure No.	Length $\times 10^4$ cm	Diameter $\times 10^4$ cm	l/d
3.68 cm/hr with 100 rpm SU/SD	4.53	9.52	0.95	10.0
		10.7	0.95	11.24
		20.5	1.43	14.34
		10.7	0.95	11.24
	4.54			100 with l/d $\approx$ 1
		3.72	1.2	3.1
		2.03	1.26	1.6
	4.55			4 with l/d $\approx$ 1
		1.6	1.17	1.37
		5.15	0.78	6.63
		1.94	0.49	4
		7.09	0.58	12.2
		3.79	0.78	4.88
	4.56			10 with l/d $\approx$ 1
		10.3	1.45	7.1
		6.45	1.45	4.45
		9.03	1.29	7.0
		5.16	0.97	5.33
		5.16	0.97	5.33
				60 with l/d $\approx$ 1
6.1 cm/hr	4.57			25 with l/d $\approx$ 1

ORIGINAL PAGE IS  
OF POOR QUALITY

Table 5: Average  $l/d$ , standard deviation and 95% confidence limit of projection of MnBi phase for different growth conditions

Growth Conditions	Average $l/d$	Standard Deviation	95% Confidence Limit
0.4 cm/hr with 100 rpm SU/SD	1.46	1.32	$\pm 0.45$
2.98 cm/hr	1.47	1.30	$\pm 0.34$
3.68 cm/hr	1.04	0.41	$\pm 0.053$
3.68 cm/hr with 100 rpm SU/SD	1.87	2.59	$\pm 0.36$
6.1 cm/hr	1.0	0	0



Figure 4.31: Side and top view of a decanted ingot

ORIGINAL PAGE IS  
OF POOR QUALITY



Figure 4.32: Decanted interface. Growth rate: 0.25 cm/hr. Magnification: 2.41 kX.

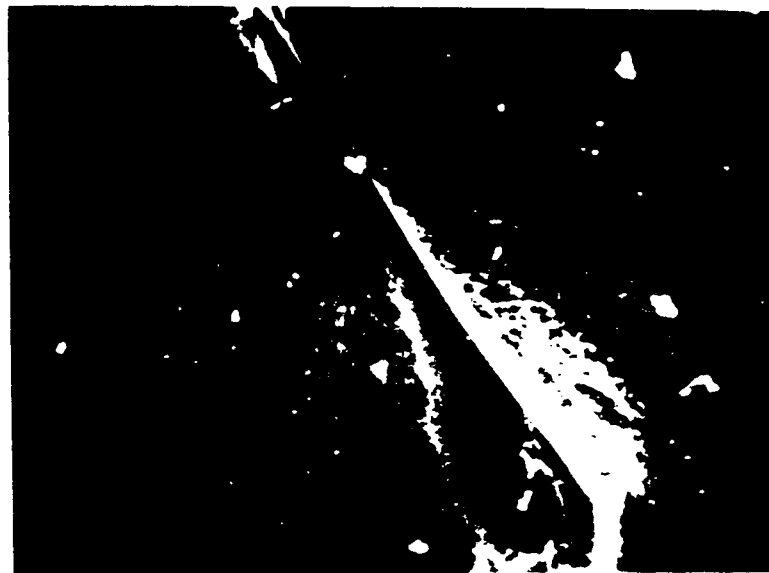


Figure 4.33: Decanted interface. Growth rate: 0.25 cm/hr. Magnification: 0.60 kX.

ORIGINAL PAGE IS  
OF POOR QUALITY



Figure 4.34: Decanted interface. Growth rate: 0.4 cm/hr with 100 rpm spin-up/spin-down. Magnification: 2.12 kX.

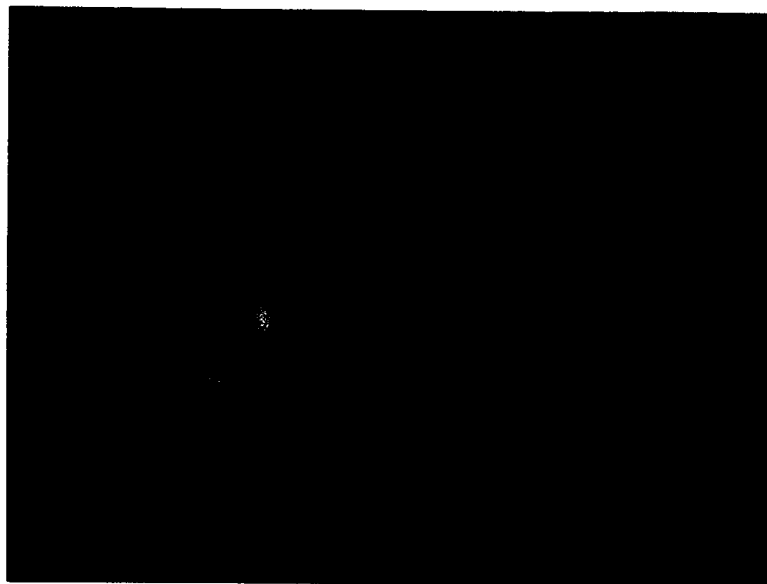


Figure 4.35: Decanted interface. Growth rate: 0.4 cm/hr with 100 rpm spin-up/spin-down. Magnification: 0.31 kX.

ORIGINAL PAGE IS  
OF POOR QUALITY

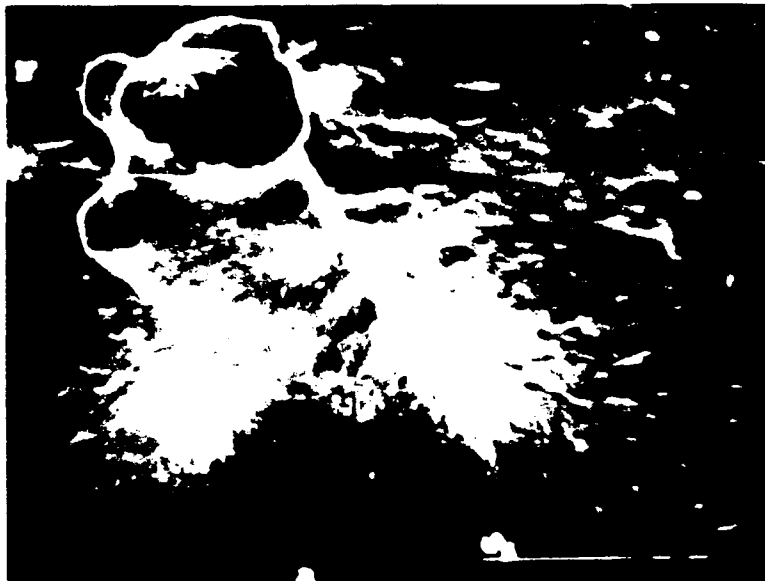


Figure 4.36: Decanted interface. Growth rate: 0.4 cm/hr with 100 rpm spin-up/spin-down. Magnification: 2.12 kX.



Figure 4.37: Decanted interface. Growth rate: 0.4 cm/hr with 100 rpm spin-up/spin-down. Magnification: 1.83 kX.

ORIGINAL PAGE IS  
OF POOR QUALITY



Figure 4.38: Decanted interface. Growth rate: 0.4 cm/hr with 100 rpm spin-up/spin-down. Magnification: 1.83 kX.

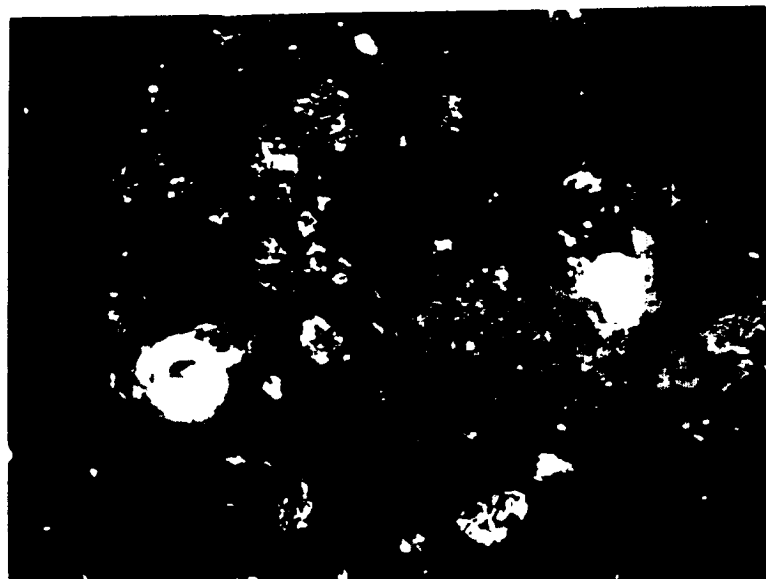


Figure 4.39: Decanted interface. Growth rate: 2.98 cm/hr. Sample I. Magnification: 1.2 kX.

ORIGINAL PAGE IS  
OF POOR QUALITY.

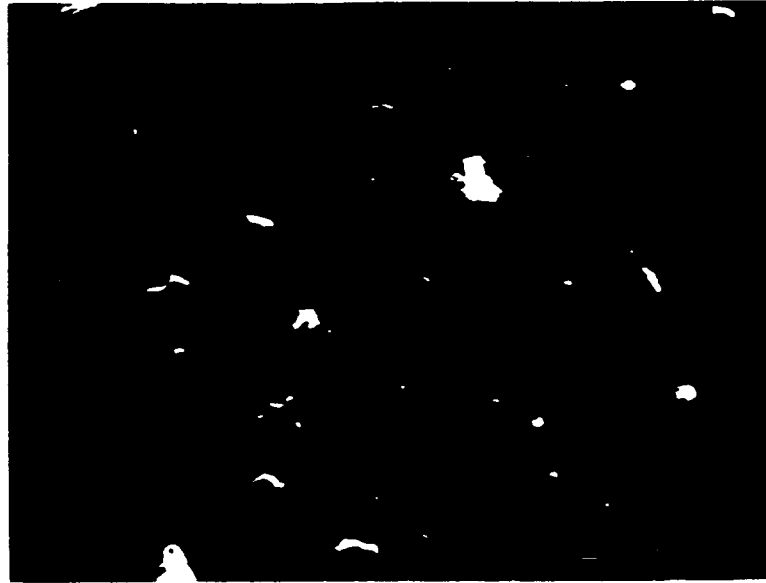


Figure 4.40: Decanted interface. Growth rate: 2.98 cm/hr. Sample II. Magnification: 0.75 kX.

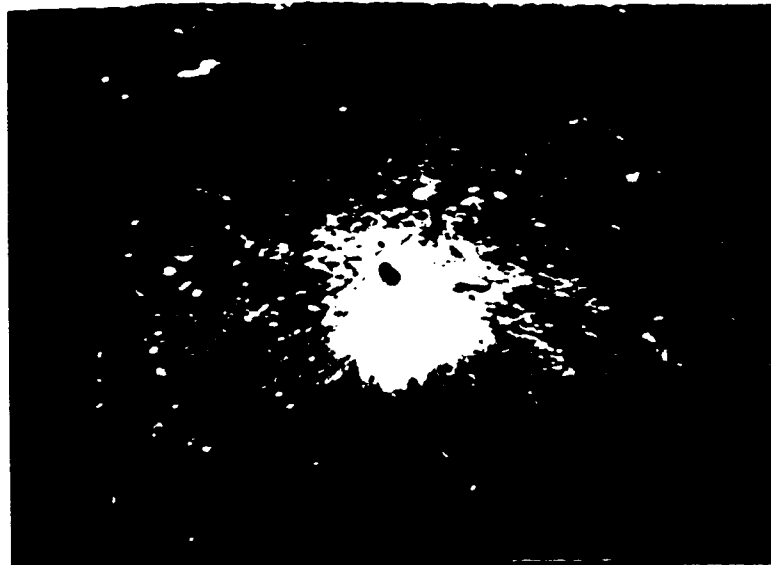


Figure 4.41: Decanted interface. Growth rate: 2.98 cm/hr. Sample II. Magnification: 2.12 kX.

ORIGINAL PAGE IS  
OF POOR QUALITY

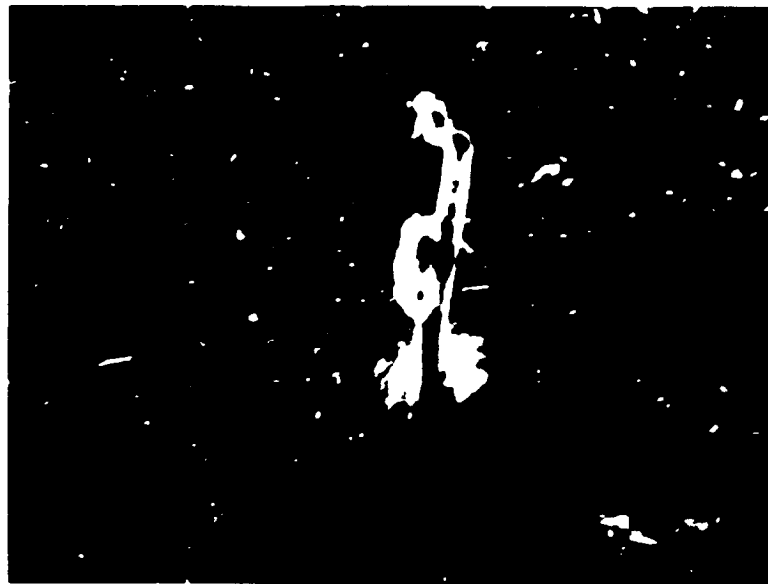


Figure 4.42: Decanted interface. Growth rate: 2.98 cm/hr. Sample II. Magnification: 1.07 kX.

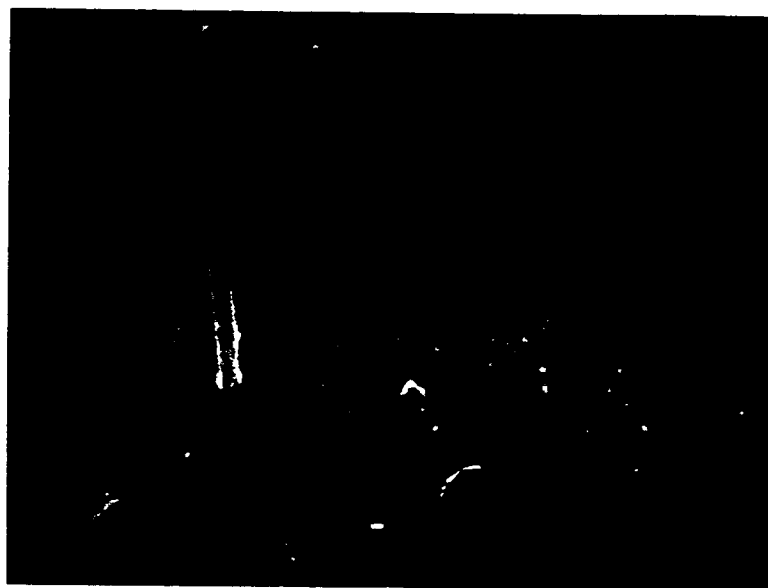


Figure 4.43: Decanted interface. Growth rate: 2.98 cm/hr. Sample II. Magnification: 1.05 kX.



ORIGINAL PAGE IS  
OF POOR QUALITY

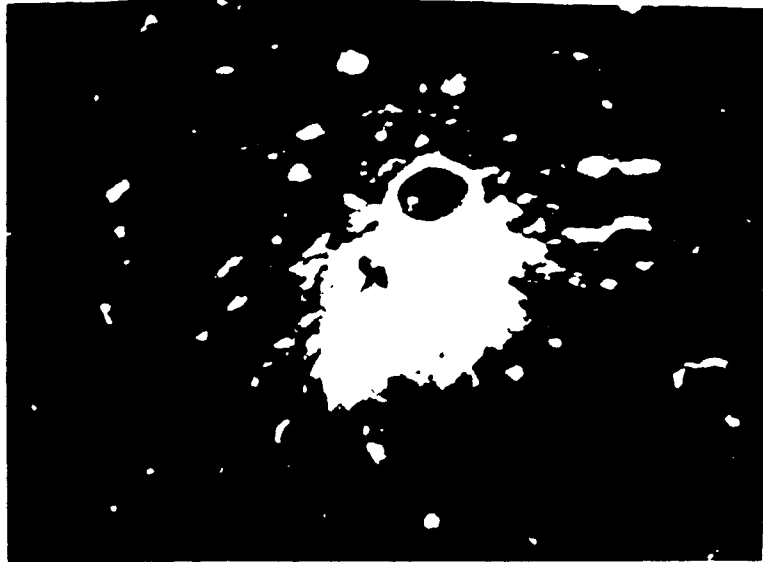


Figure 4.44: Decanted interface. Growth rate: 2.98 cm/hr. Sample II. Magnification: 3.2 kX.

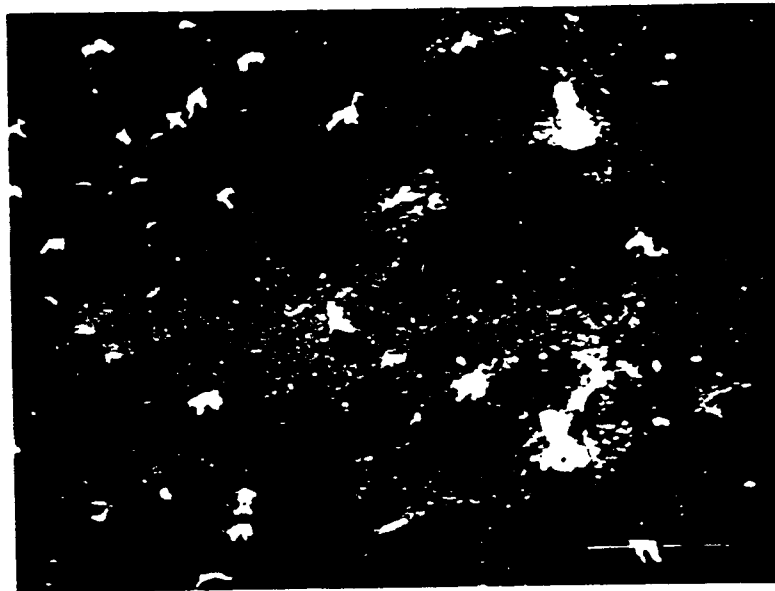


Figure 4.45: Decanted interface. Growth rate: 2.98 cm/hr. Sample II. Magnification: 0.74 kX.

ORIGINAL PAGE IS  
OF POOR QUALITY

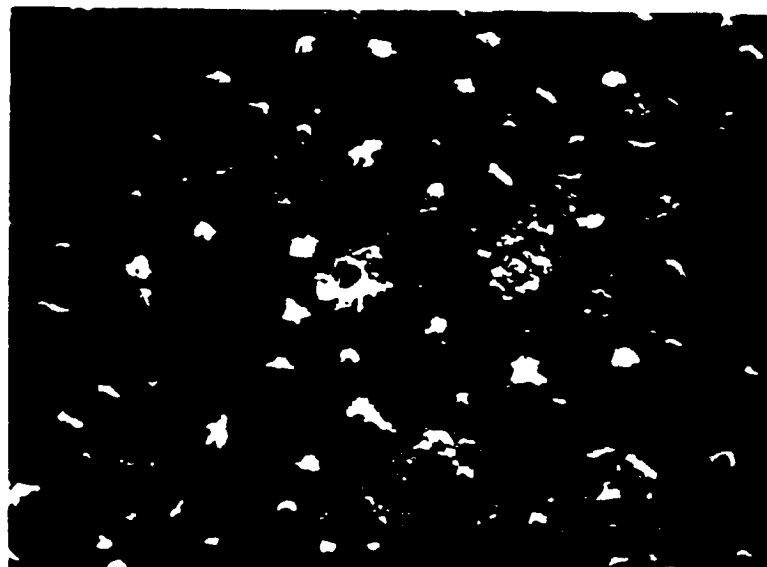


Figure 4.46: Decanted interface. Growth rate: 3.68 cm/hr. Sample A. Magnification: 0.73 kX.



Figure 4.47: Decanted interface. Growth rate: 3.68 cm/hr. Sample A. Magnification: 1.68 kX.

ORIGINAL PAGE IS  
OF POOR QUALITY

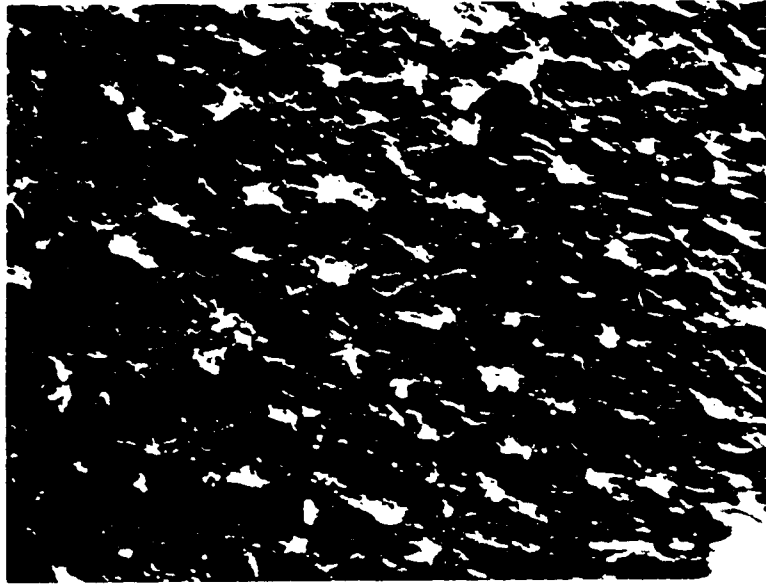


Figure 4.48: Decanted interface. Growth rate: 3.68 cm/hr. Sample B. Magnification: 0.77 kX.

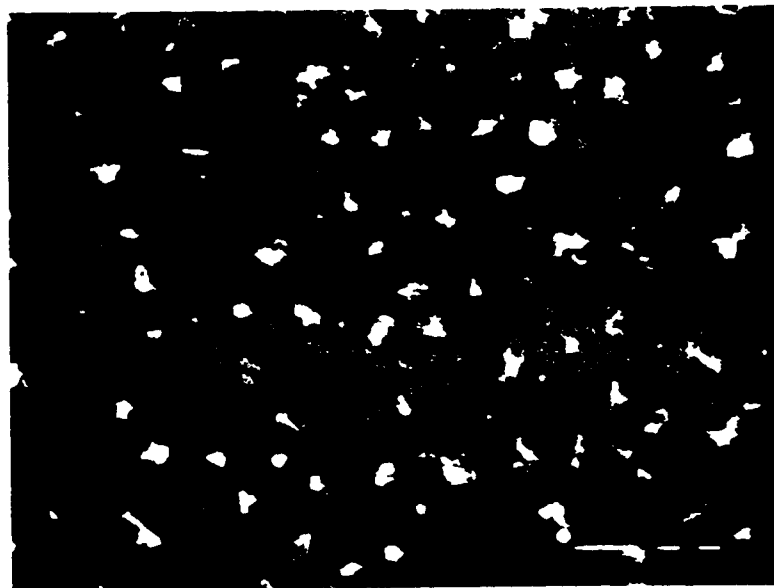


Figure 4.49: Decanted interface. Growth rate: 3.68 cm/hr. Sample C. Magnification: 0.80 kX.

ORIGINAL PAGE IS  
OF POOR QUALITY

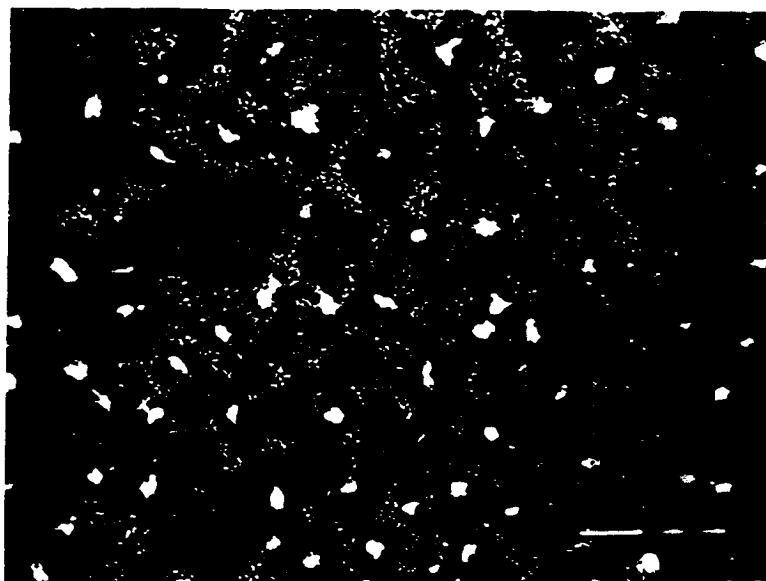


Figure 4.50: Decanted interface. Growth rate: 3.68 cm/hr. Sample C. Magnification: 0.78 kX.



Figure 4.51: Decanted interface. Growth rate: 3.68 cm/hr. Sample D. Magnification: 1.03 kX.

ORIGINAL PAGE IS  
OF POOR QUALITY



Figure 4.52: Decanted interface. Growth rate: 3.68 cm/hr. Sample D. Magnification: 1.03 kX.

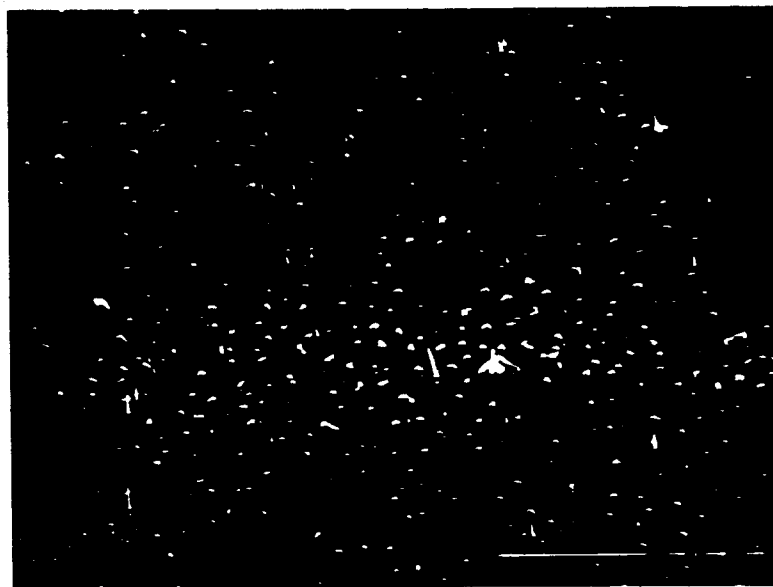


Figure 4.53: Decanted interface. Growth rate: 3.68 cm/hr with 200 rpm spin-up/spin-down. Magnification: 0.21 kX.

ORIGINAL PAGE IS  
OF POOR QUALITY



Figure 4.54: Decanted interface. Growth rate: 3.68 cm/hr with 200 rpm spin-up/spin-down. Magnification: 2.07 kX.



Figure 4.55: Decanted interface. Growth rate: 3.68 cm/hr with 200 rpm spin-up/spin-down. Magnification: 1.03 kX.

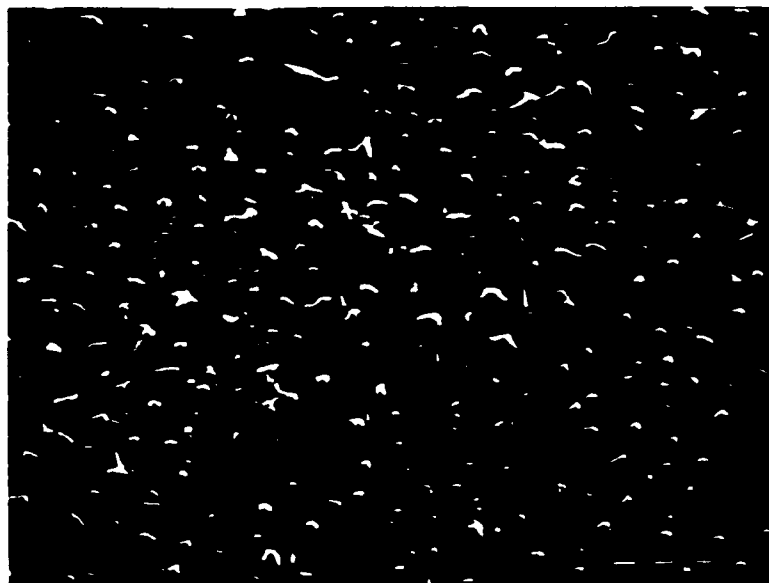


Figure 4.56: Decanted interface. Growth rate: 3.68 cm/hr with 200 rpm spin-up/spin-down. Magnification: 0.31 kX.

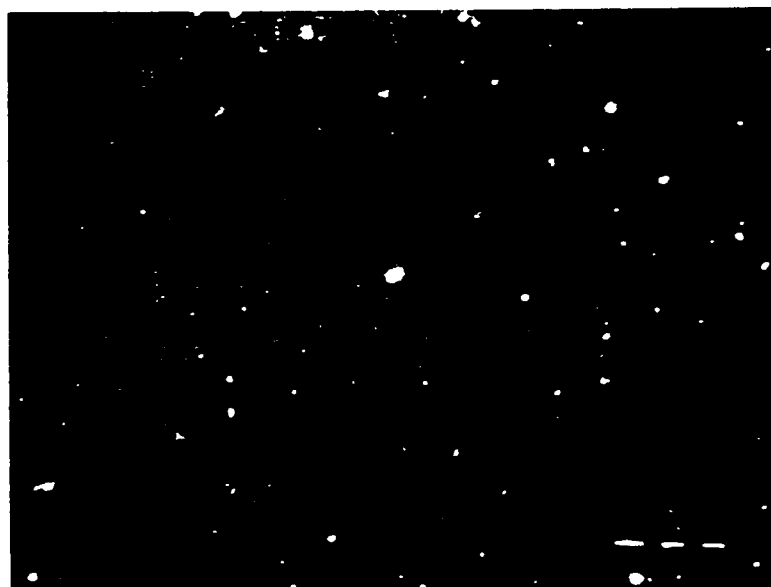


Figure 4.57: Decanted interface. Growth rate: 6.1 cm/hr. Magnification: 0.31 kX.

### 4.3 Effect of spin-up/spin-down and interface curvature on the microstructure.

The MnBi-Bi eutectic solidifies with a quasi-regular rod-type eutectic microstructure at medium and high growth rates [68]. At low growth rates the microstructure consists of randomly oriented broken lamellae or blades of MnBi. The effect of spin-up/spin-down on the microstructure of the MnBi/Bi eutectic was studied by Eisa [13]. Spin-up/spin-down (SU/SD) resulted in a small change in spacing between the MnBi fibers for the eutectic solidified at medium and high growth rates. At low growth rates SU/SD caused the MnBi blades to be concentrated along the periphery of the ingot and to be totally absent from the center. This is an interesting observation and it cannot be explained on the basis of centrifugal force throwing Mn to the outside because Mn is less dense than Bi.

Further experiments were performed in the low growth rate range to try and understand the effect of spin-up/spin-down on the microstructure of the eutectic. The effect of SU/SD on the microstructure of the eutectic solidified at 0.25 cm/hr was investigated. The microstructure of the eutectic without SU/SD and with 100 rpm SU/SD is shown in figures 4.58 and 4.59. For the eutectic directionally solidified without SU/SD, broken blades of MnBi are uniformly distributed across the entire cross-section of the ingot. With SU/SD the microstructure was different from that observed by Eisa [13]. There was a central core of the MnBi phase surrounded by a ring with no MnBi present (figure 4.59). At the periphery large broken blades of MnBi formed.

The difference in microstructure of the eutectic between that observed by Eisa and the above experiment was suspected to be a result of a difference in interface curvature. To check this hypothesis, three different experiments were performed





ORIGINAL PAGE IS  
OF POOR QUALITY

Figure 4.58: Microstructure of MnBi-Bi eutectic solidified at 0.25 cm/hr. Magnification: 37.5 X.

ORIGINAL PAGE IS  
OF POOR QUALITY



Figure 4.59: Microstructure at the a) center and b) edge of MnBi-Bi eutectic solidified at 0.25 cm/hr with 100 rpm spin-up/spin-down. Magnification 37.5 X

with different heater and cooler temperatures and at the same growth rate. Increasing the heater or the cooler temperature moves the interface into the cooler and makes it more concave [34]. Decreasing the heater or the cooler temperature moves the interface into the heater making it more convex. Four experiments with different heater and cooler temperatures were performed. The conditions of these experiments are tabulated in Table 6.

Figures 4.60 to 4.62 show schematics of the different microstructures obtained with different heater and cooler temperatures and 100 rpm spin-up/spin-down.

With a heater temperature of 615°F and cooler temperature of 50°F the microstructure consisted of a central core of MnBi phase surrounded by a ring with no MnBi present. Along the periphery large broken blades of MnBi formed. Decreasing the heater temperature to 550°F and the cooler temperature to 8°F decreased the diameter of the central core of MnBi and more MnBi was formed along the periphery. Lowering the heater temperature to 515°F resulted in no MnBi at the center at all and all the MnBi being segregated along the periphery.

Figures 4.63 to 4.66 show a higher magnification of the microstructure obtained in each of the four experiments.

The microstructure changes was strongly influenced by different interface shapes when spin-up/spin-down was used. There was no effect of interface shape and in the absence of spin-up/spin-down.

Table 6: Different heater and cooler temperatures and diameter of central core of MnBi.

Run No.	Heater Temp.	Cooler Temp.	Diameter of central core
1	597°K	323°K	2.7 mm
2	597°K	281°K	2.4 mm
3	561°K	281°K	1.7 mm
4	541°K	281°K	No central core

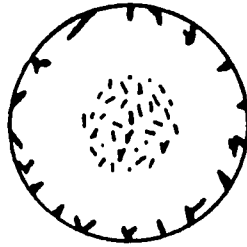


Figure 4.60: Microstructure of MnBi-Bi eutectic solidified at 0.25 cm/hr with 100 rpm spin-up/spin-down and run 1.

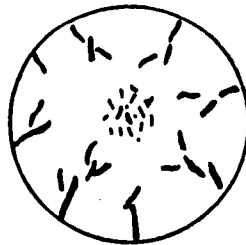


Figure 4.61: Microstructure of MnBi-Bi eutectic solidified at 0.25 cm/hr with 100 rpm spin-up/spin-down and run 2.



Figure 4.62: Microstructure of MnBi-Bi eutectic solidified at 0.25 cm/hr with 100 rpm spin-up/spin-down and run 3.

ORIGINAL PAGE IS  
OF POOR QUALITY

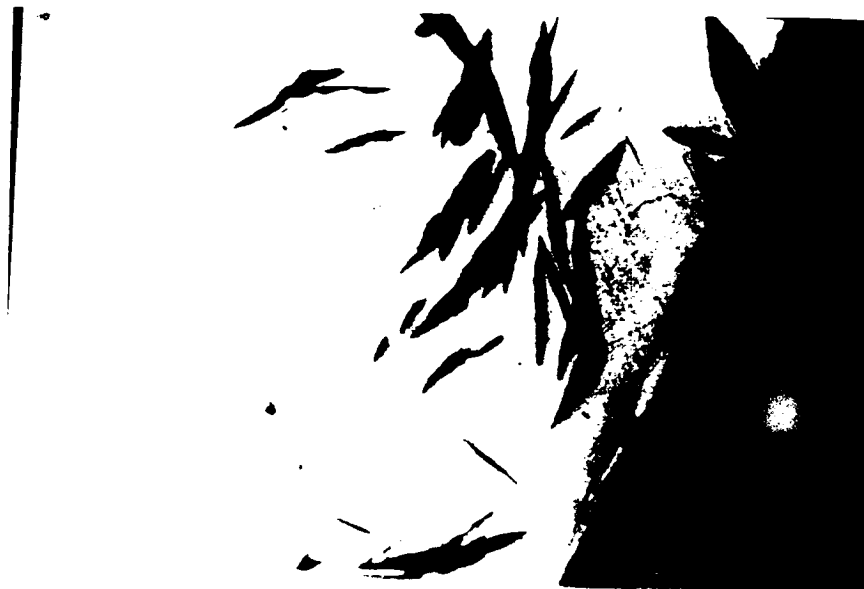


Figure 4.63: Microstructure at the a) center and b) edge of MnBi-Bi eutectic solidified under conditions of run 1. Magnification 37.5 X.

ORIGINAL PAGE IS  
OF POOR QUALITY



Figure 4.64: Microstructure at the a) center and b) edge of MnBi-Bi eutectic solidified under conditions of run 2. Magnification 37.5 X.

ORIGINAL PAGE IS  
OF POOR QUALITY



Figure 4.65: Microstructure at the a) center and b) edge of MnBi-Bi eutectic solidified under conditions of run 3. Magnification 37.5 X.



ORIGINAL PAGE IS  
OF POOR QUALITY



Figure 4.66: Microstructure at the a) center and b) edge of MnBi-Bi eutectic solidified under conditions of run 4. Magnification 37.5 X.

#### 4.4 Mechanical properties of the MnBi-Bi eutectic.

Mechanical properties of the MnBi-Bi eutectic, directionally solidified at different growth rates, were determined in the vacuum strain gauge apparatus. Tensile specimens with a gauge diameter of 0.325 cm and a gauge length of 1.366 cm were machined from the ingots in the direction parallel to that of solidification. A typical machined ingot of eutectic is shown in figure 4.67. The tensile tests were conducted at  $204^{\circ}\text{C}$  (melting point of eutectic =  $265^{\circ}\text{C}$ ) and a strain rate of  $0.873\text{ hr}^{-1}$ . The furnace of the vacuum strain gauge is designed to heat the sample by radiation. For the temperature used in the experiments,  $204^{\circ}\text{C}$ , it was impossible to obtain a uniform temperature along the length of the specimen. The variation in temperature along the length of the specimen was  $\pm 4^{\circ}\text{C}$ . Based on the temperature measured at different points along the length of the specimen a new set of specimen holders was machined to ensure that the hottest region was at the center of the sample.

Stress-strain plots of the eutectic solidified at different growth rates are shown in figures 4.68 to 4.79. The stress-strain plots of eutectics solidified at low growth rates are shown in figures 4.68 to 4.72. (Recall that at low growth rates the microstructure of the MnBi-Bi eutectic consists of randomly oriented broken blades of MnBi distributed uniformly across the cross section of the ingot.) The stress-strain plots of the eutectic solidified at medium and high growth rates are shown in figures 4.73 to 4.79. (The MnBi-Bi eutectic solidifies with a quasi-regular rod-type structure at medium and high growth rates.)

The fracture was always ductile and the fractured surfaces were wedge shaped. The fractured surfaces of the eutectic solidified at low growth rates had gaping holes and no pull-out of the MnBi phase. There was substantial MnBi fiber pull-out on fracture of the eutectic solidified with a rod-type structure.



**Figure 4.67: Machined ingot of MnBi-Bi eutectic for tensile test on the vacuum strain gauge**

ORIGINAL PAGE IS  
OF POOR QUALITY

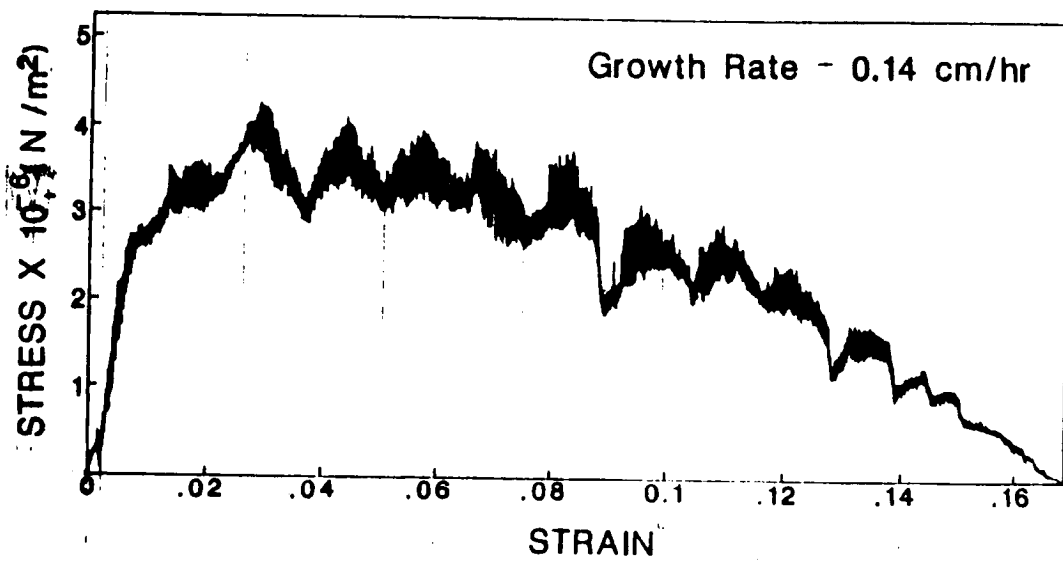


Figure 4.68: Stress-strain plot of MnBi-Bi eutectic directionally solidified at 0.14 cm/hr.

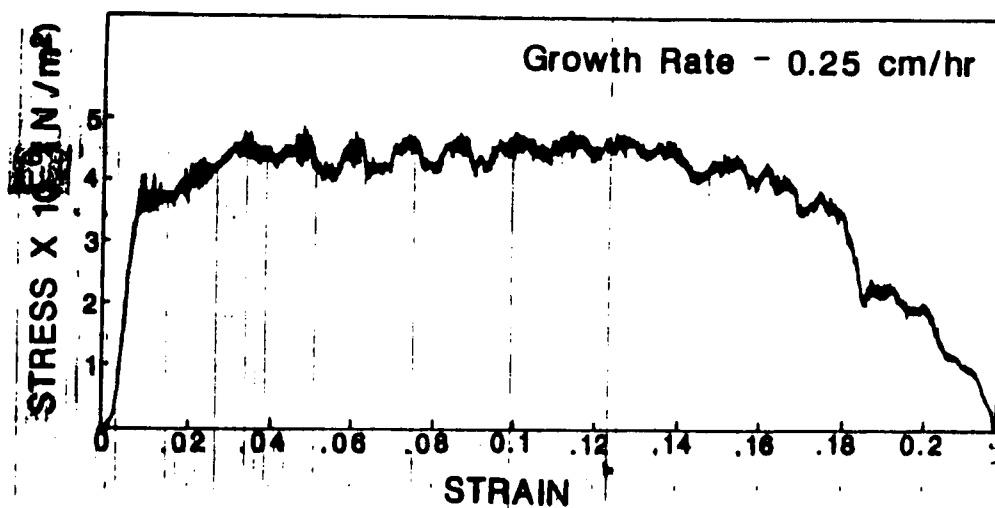


Figure 4.69: Stress-strain plot of MnBi-Bi eutectic directionally solidified at 0.25 cm/hr.

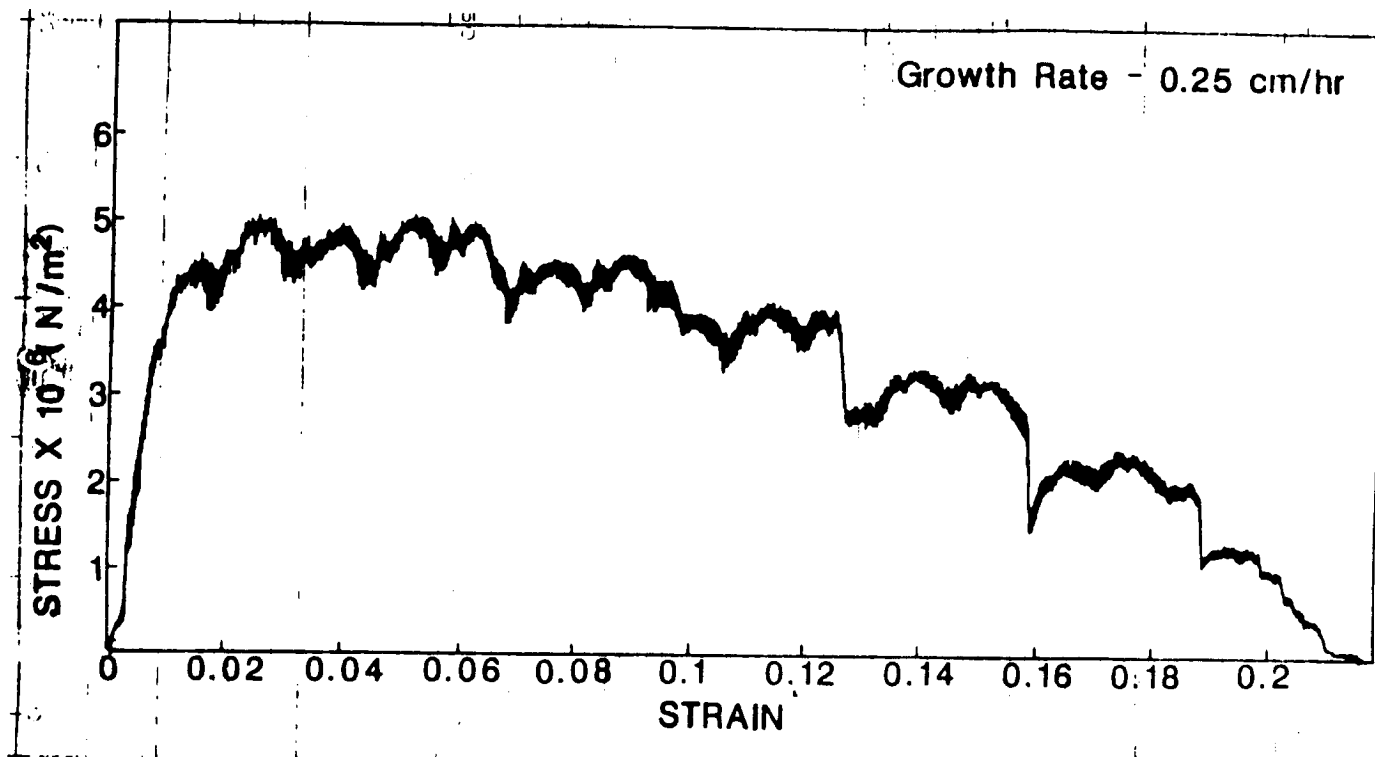


Figure 4.70: Stress-strain plot of MnBi-Bi eutectic directionally solidified at 0.25 cm/hr.

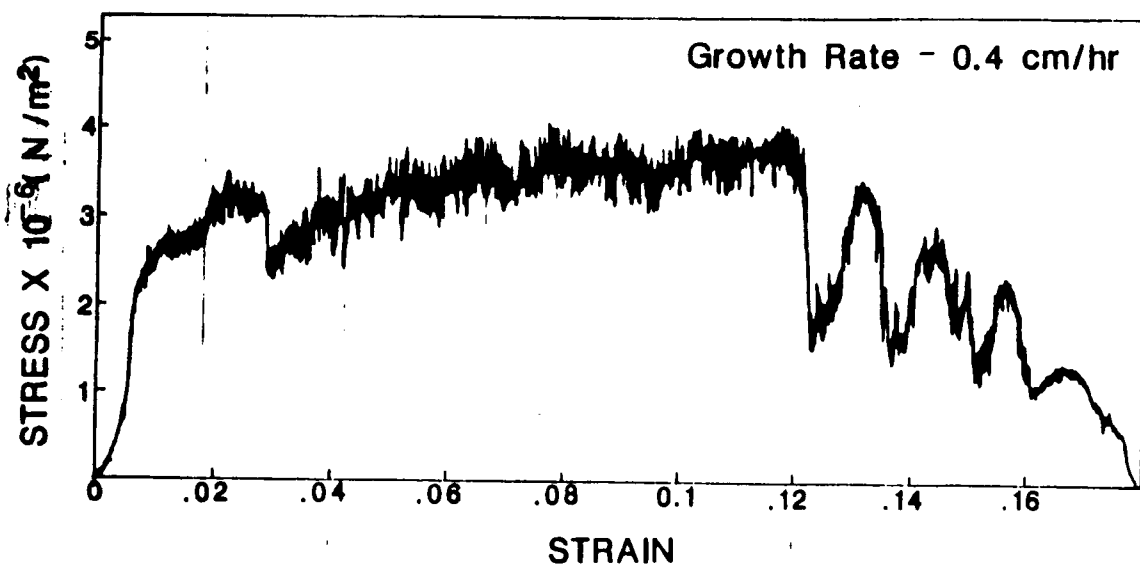


Figure 4.71: Stress-strain plot of MnBi-Bi eutectic directionally solidified at 0.4 cm/hr.

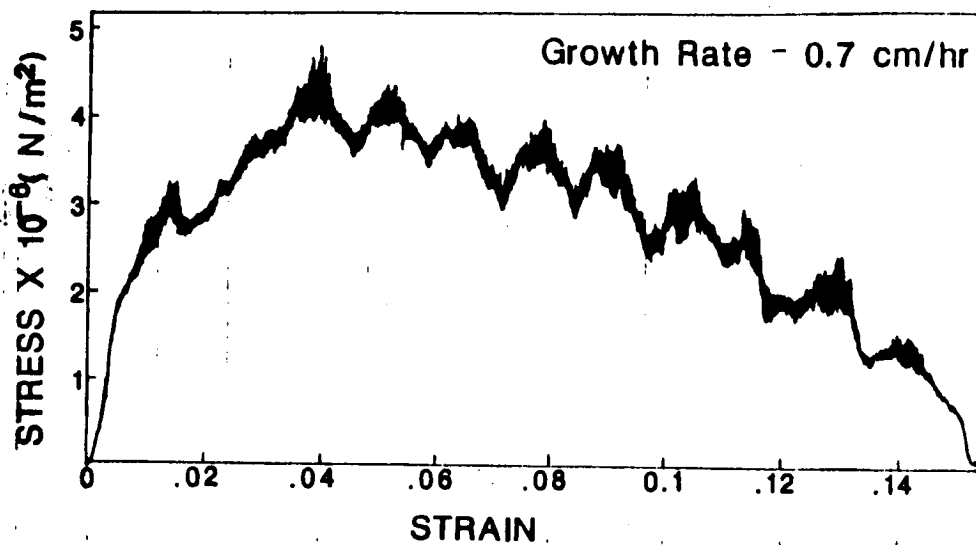


Figure 4.72: Stress-strain plot of MnBi-Bi eutectic directionally solidified at 0.7 cm/hr.



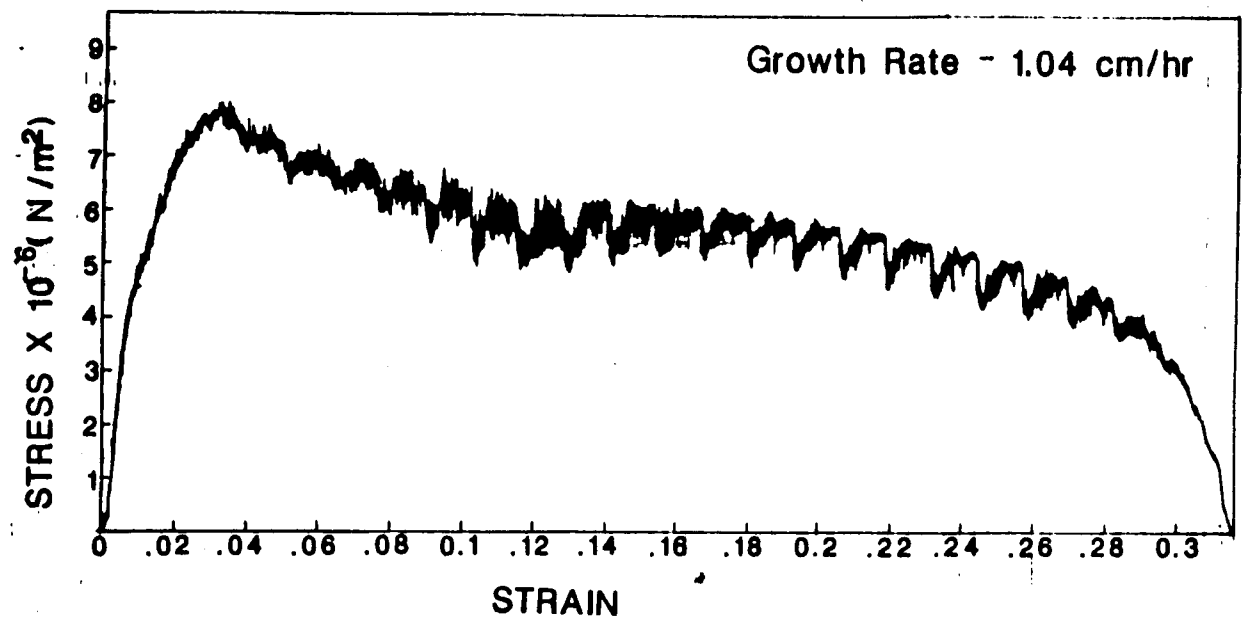


Figure 4.73: Stress-strain plot of MnBi-Bi eutectic directionally solidified at 1.04 cm/hr.

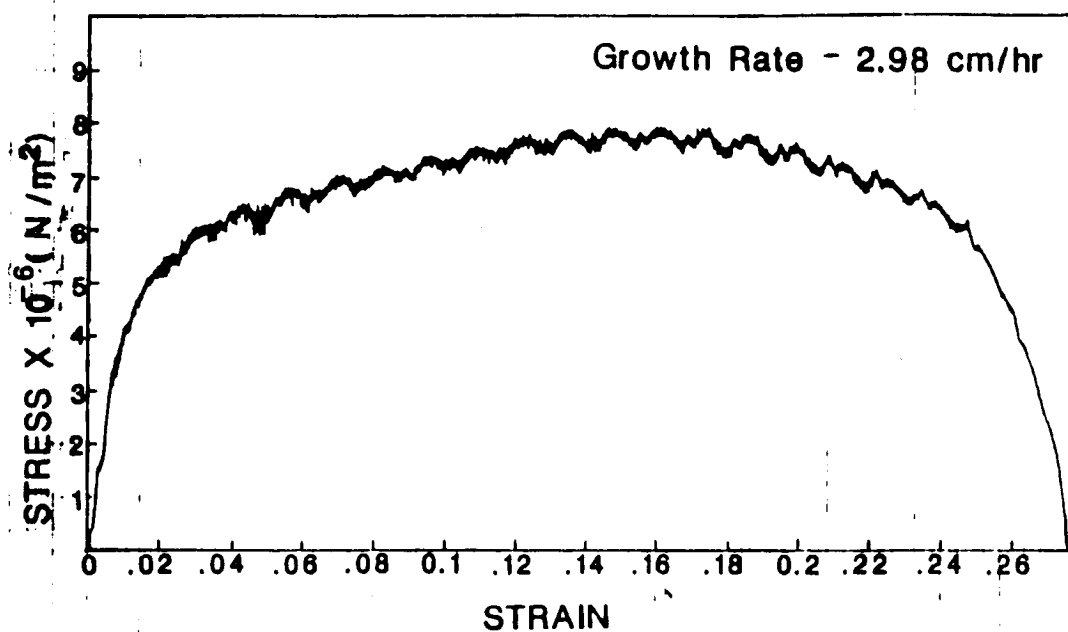


Figure 4.74: Stress-strain plot of MnBi-Bi eutectic directionally solidified at 2.98 cm/hr.

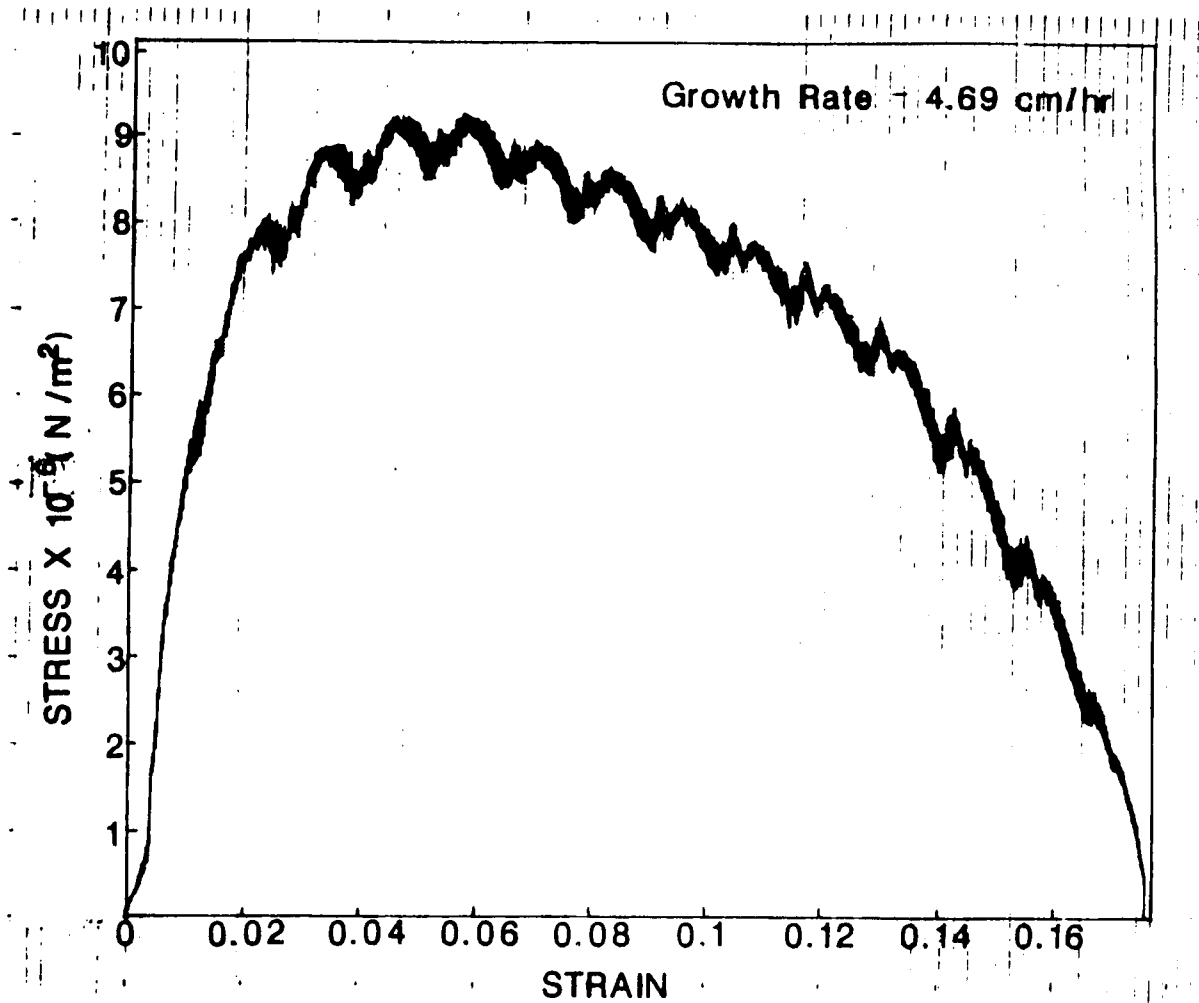


Figure 4.75: Stress-strain plot of MnBi-Bi eutectic directionally solidified at 4.69 cm/hr.

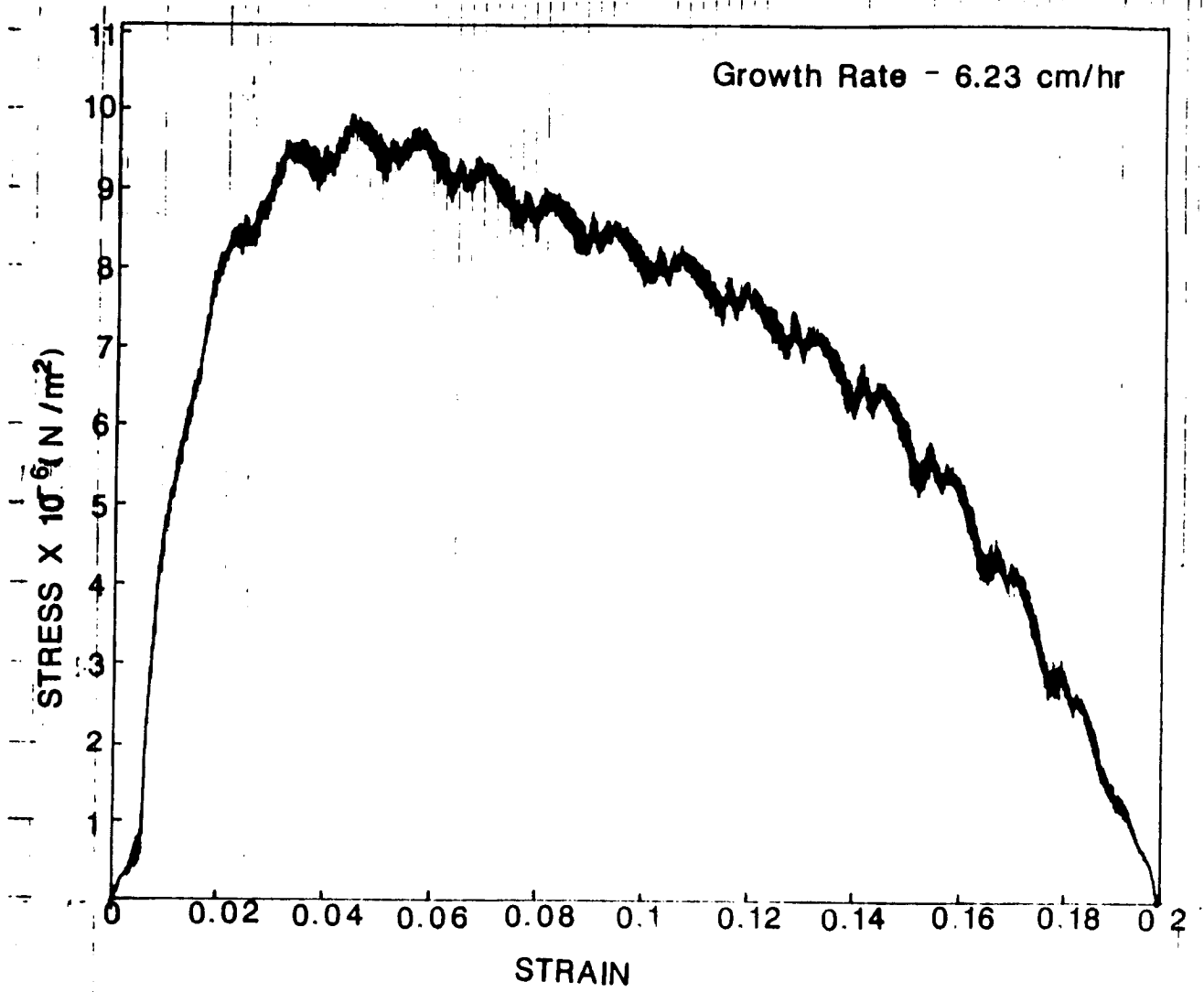


Figure 4.76: Stress-strain plot of MnBi-Bi eutectic directionally solidified at 6.23 cm/hr.

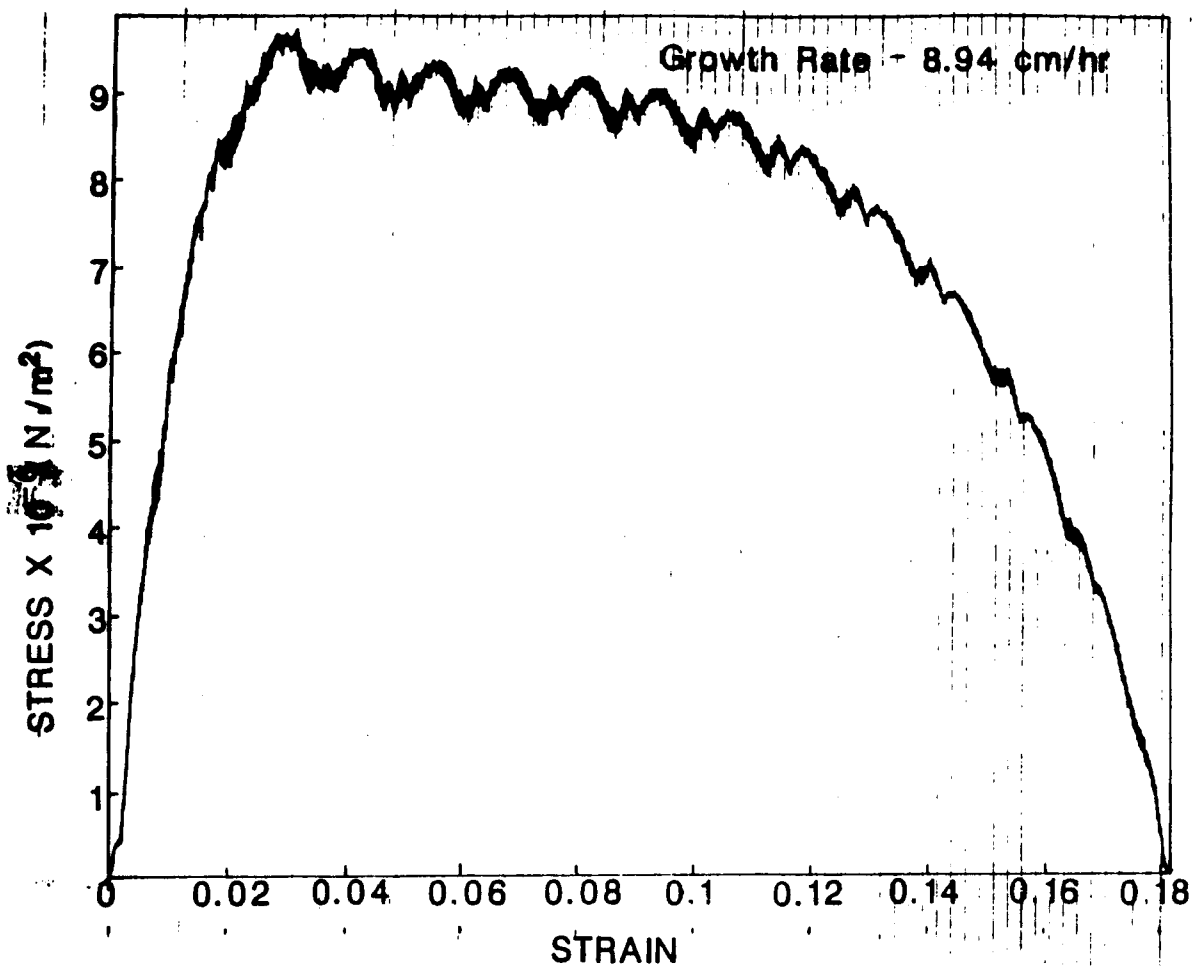


Figure 4.77: Stress-strain plot of MnBi-Bi eutectic directionally solidified at 8.94 cm/hr.

ORIGINAL PAGE IS  
OF POOR QUALITY

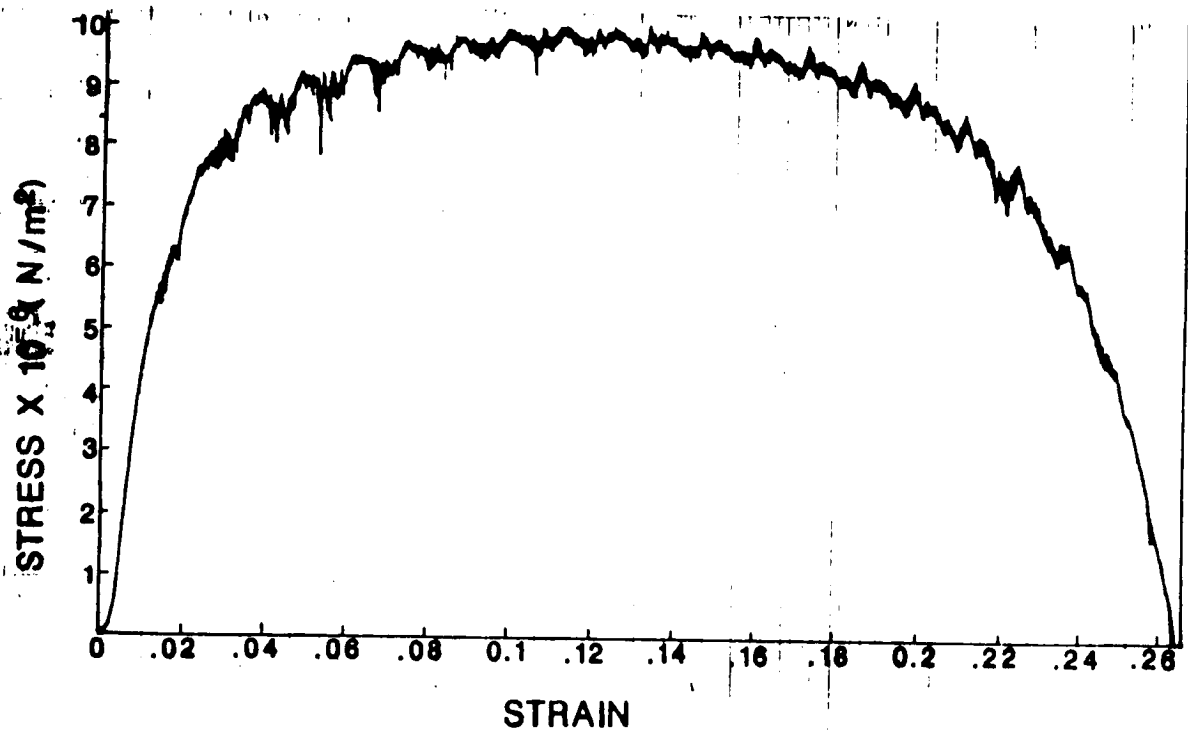


Figure 4.78: Stress-strain plot of MnBi-Bi eutectic directionally solidified at 8.94 cm/hr.

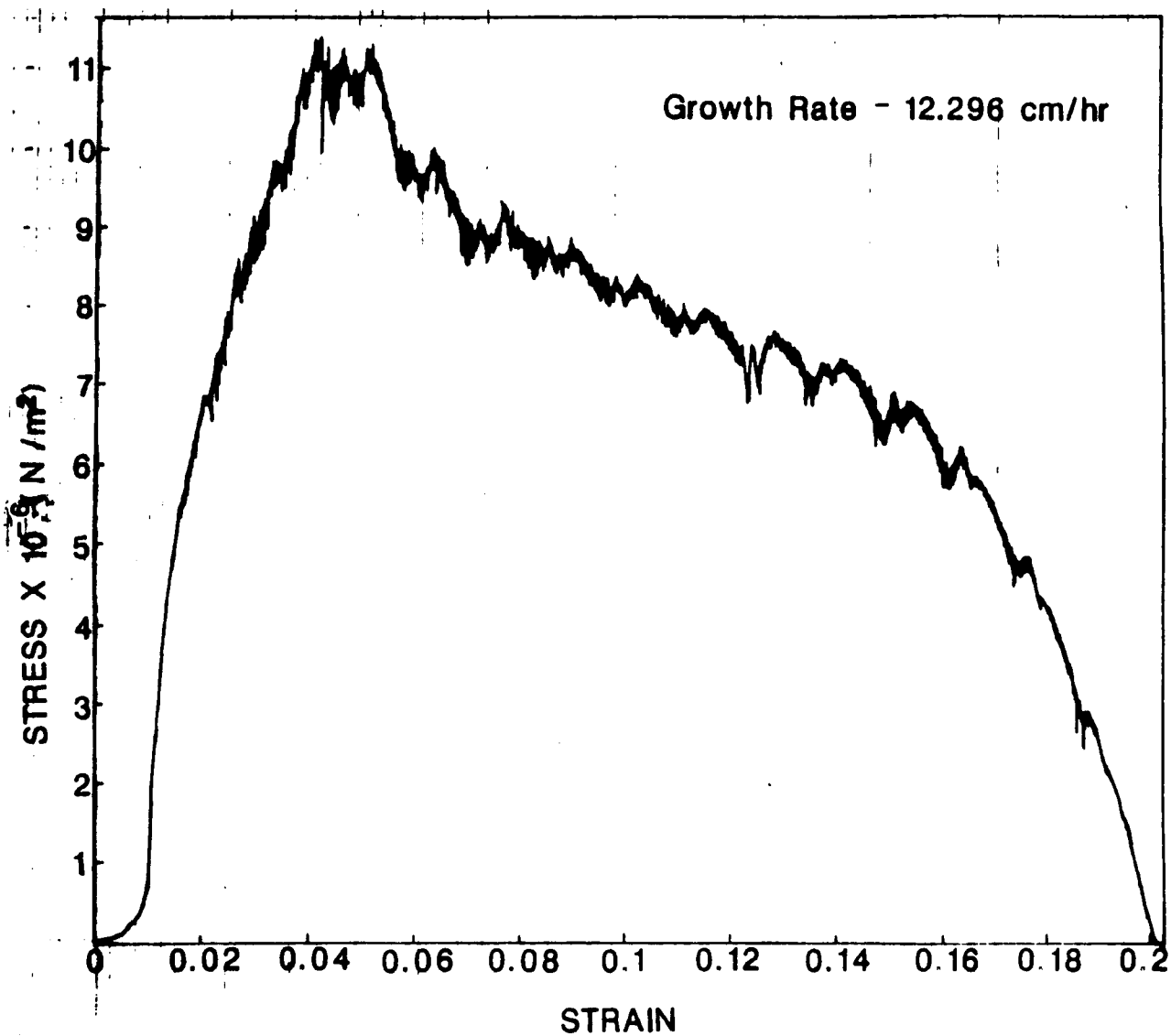


Figure 4.79: Stress-strain plot of MnBi-Bi eutectic directionally solidified at 12.296 cm/hr.

Three of the specimens tested fractured near the center of the gauge length (figures 4.73, 4.74 and 4.78) and the other specimens fractured close to the lower jaw that held the specimen. Two fractured specimens of the eutectic are shown in figure 4.80. The specimens that fractured near the center had higher strains at fracture than the specimens that fractured close to the lower jaw. Also there was a difference in the stress-strain behaviour for these two cases. The specimens that fractured closer to the center had a bell shaped stress-strain plot with the maximum in the engineering stress at about 50% of the total strain of the specimen. The stress-strain plots for the other specimens exhibited a maximum in the engineering stress at lower strains, usually soon after the end of elastic deformation. The stress decreased with further increase in strain. Figures 4.77 and 4.78 show the stress-strain plots of two samples solidified under identical conditions but fractured by the two different modes discussed above. The maximum engineering stress was not very different for the two types of fracture.

The fluctuations in the stress were originally attributed to the rods breaking off. However, a tensile test of an ingot of bismuth resulted in similar fluctuations as shown in figure 4.81. The periodicity of the fluctuations was  $\approx 0.01$  (unit same as the strain) and more or less the same for all the experiments. This is attributed to a varying strain rate during the experiment resulting from a periodic variation in the rotation of the motor which drives the yoke and pull rod assembly. The stress at different values of the strain was read off from the original stress-strain plots and a SAS (SAS Institute Inc., NC) graphics routine GPLOT with the option to smoothen noisy data was used to replot the data. A smooth line is fit to the noisy data using a spline routine. The data points do not necessarily fall on the line. The cubic spline that is fitted minimizes a linear combination of the sum of squares of the residuals of fit and the integral of the square of the second derivative. The



ORIGINAL PAGE IS  
OF POOR QUALITY

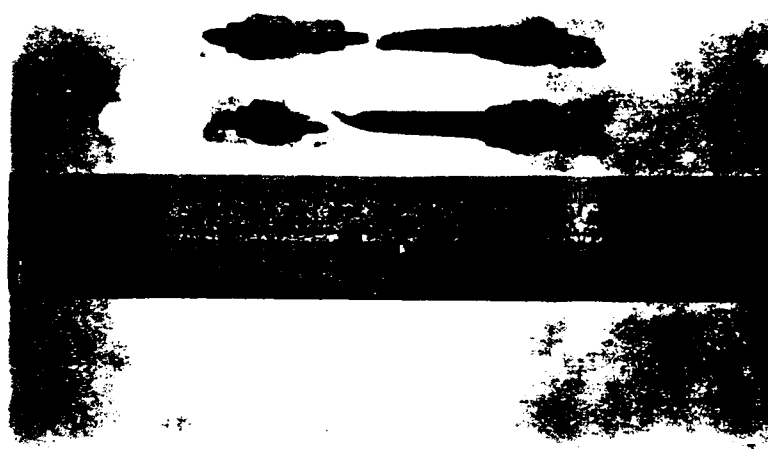


Figure 4.80: MnBi-Bi specimens fractured on the vacuum strain gauge

stress-strain plots obtained thereby are shown in figures 4.82 to 4.94.

The elastic modulus, the total strain, the engineering stress at 50% and 85% of the total strain, and the maximum engineering stress as a function of growth rate are tabulated in Table 7. The normal procedure used to determine the elastic modulus involves mounting a strain measuring device on the body of the sample and noting the stress which produces a small amount of deformation, generally equal to a strain of 0.002. The slope of the linear portion of the stress-strain plot before any permanent deformation occurs gives the elastic modulus. In the tensile tests conducted on the MnBi-Bi eutectic, no strain measuring device was mounted on the sample and the exact location of the yield point could not be identified. The slope of the stress-strain plot was taken in the region where the elastic portion was most linear. The elastic modulus is relatively independent of the growth rate.

There seems to be a controversy over the dependence of the strength of a eutectic on rod spacing (discussed in the literature review). The maximum engineering strength of the MnBi-Bi eutectic solidifying with a rod-type microstructure is plotted as a function of  $\lambda$  and  $\lambda^{-1/2}$  in figures 4.95 and 4.96. A relationship found between  $\lambda$  and the growth rate  $V$  for a rod-type microstructure of MnBi-Bi eutectic by Eisa [68] is:

$$\lambda^{2.06}V = 2.87 \times 10^{-7} \quad r^2 = 0.978 \quad (4.1)$$

A least squares fit yields for maximum engineering stress versus  $\lambda$ :

$$\sigma_{maz} = 1.381 \times 10^7 - 1.679 \times 10^{10}\lambda \quad r^2 = 0.992 \quad (4.2)$$

and for the maximum engineering stress versus  $\lambda^{-1/2}$ :

$$\sigma_{mazm} = 1.566 \times 10^5 \lambda^{-1/2} - 453100 \quad r^2 = 0.967 \quad (4.3)$$

ORIGINAL PAGE IS  
OF POOR QUALITY

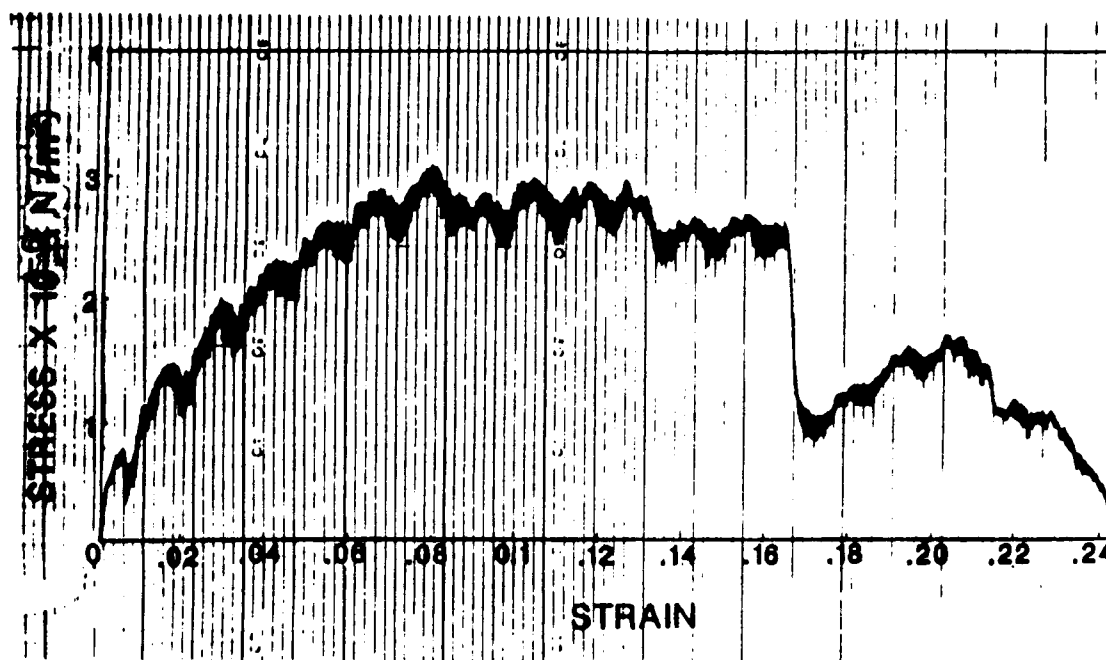


Figure 4.81: Stress-strain plot of directionally solidified Bi.

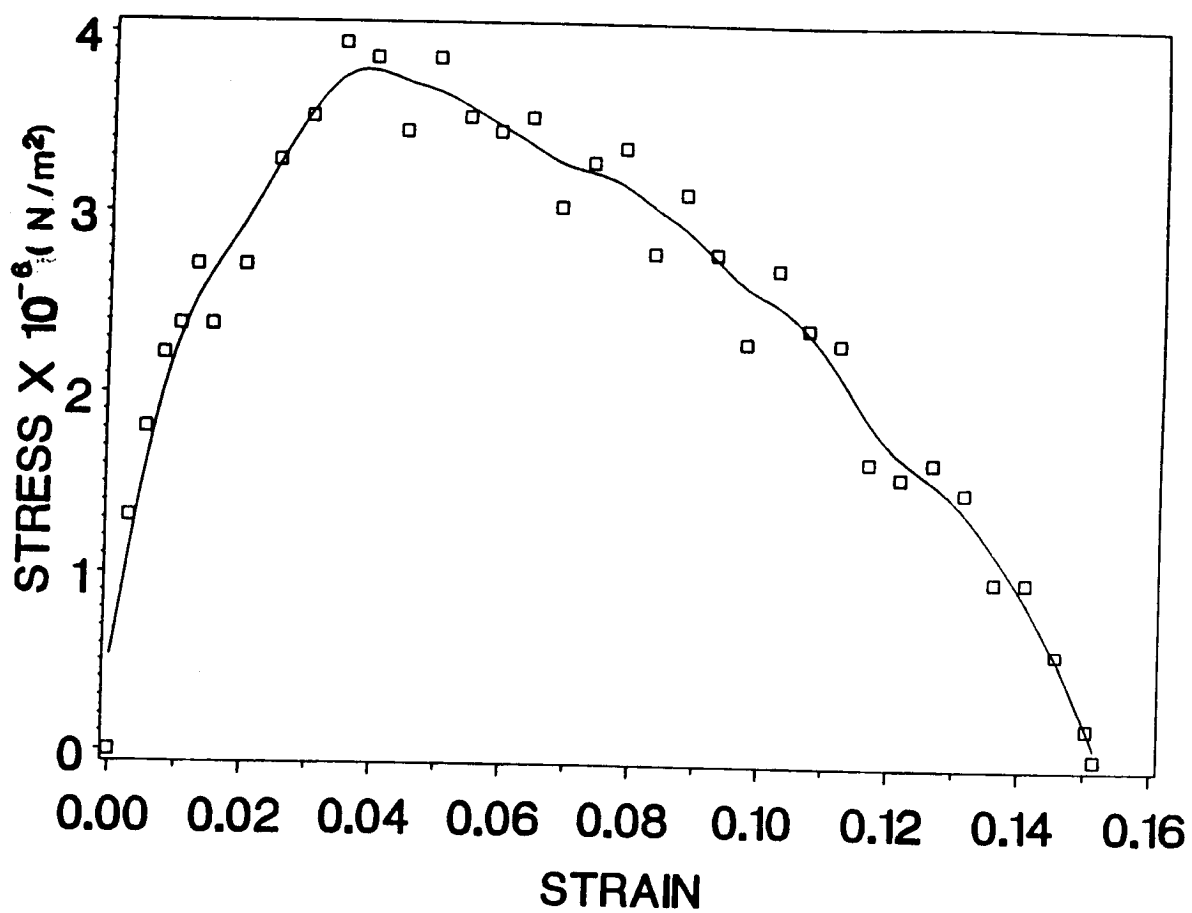


Figure 4.82: Smoothed stress-strain plot of MnBi-Bi eutectic directionally solidified at 0.14 cm/hr.

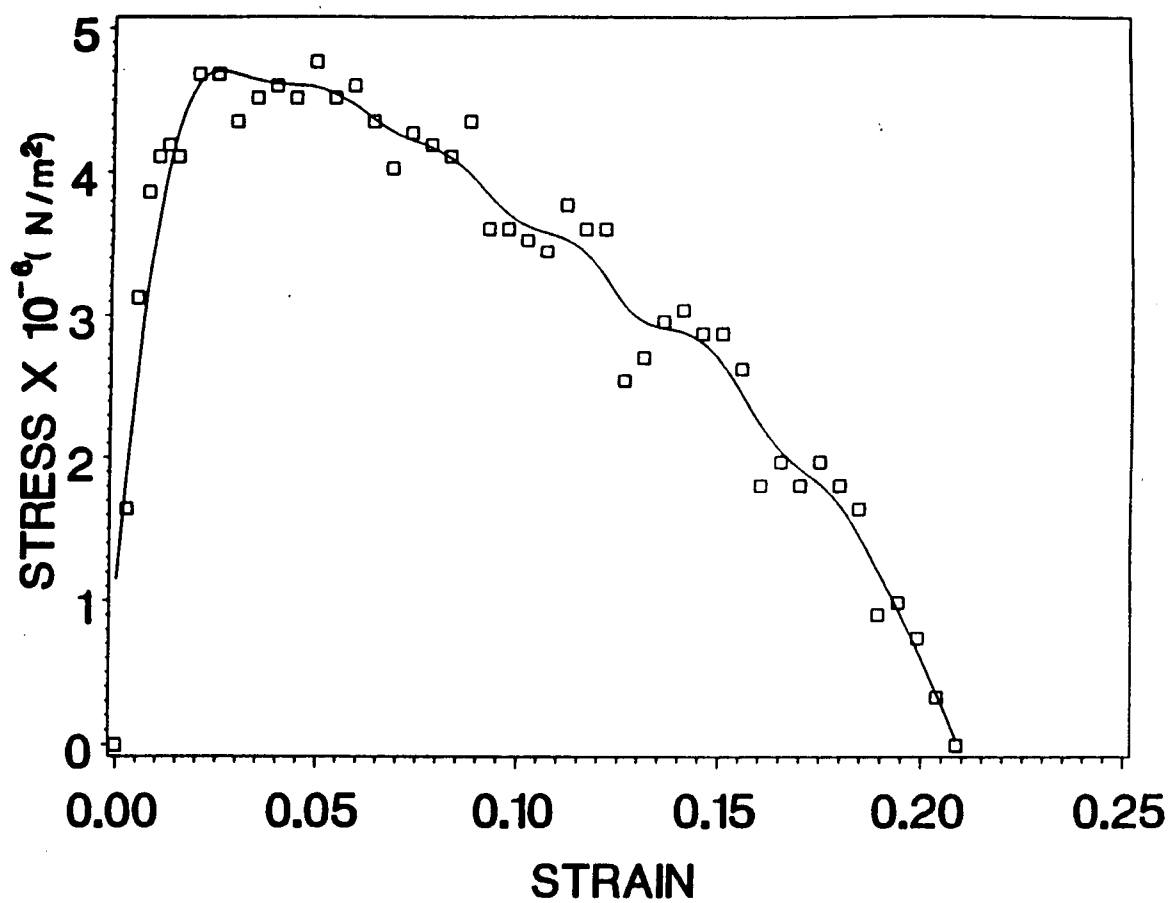


Figure 4.83: Smoothed stress-strain plot of MnBi-Bi eutectic directionally solidified at 0.25 cm/hr.

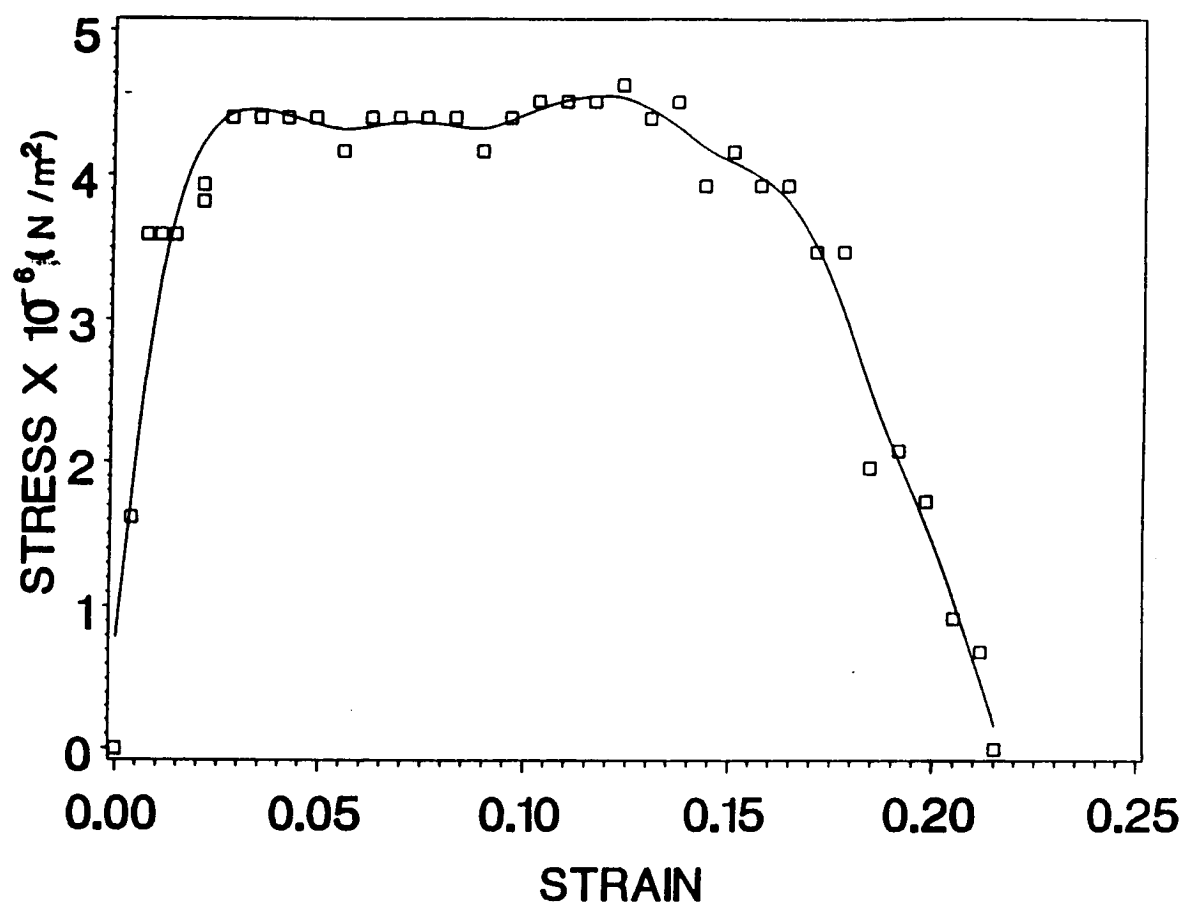


Figure 4.84: Smoothed stress-strain plot of MnBi-Bi eutectic directionally solidified at 0.25 cm/hr.

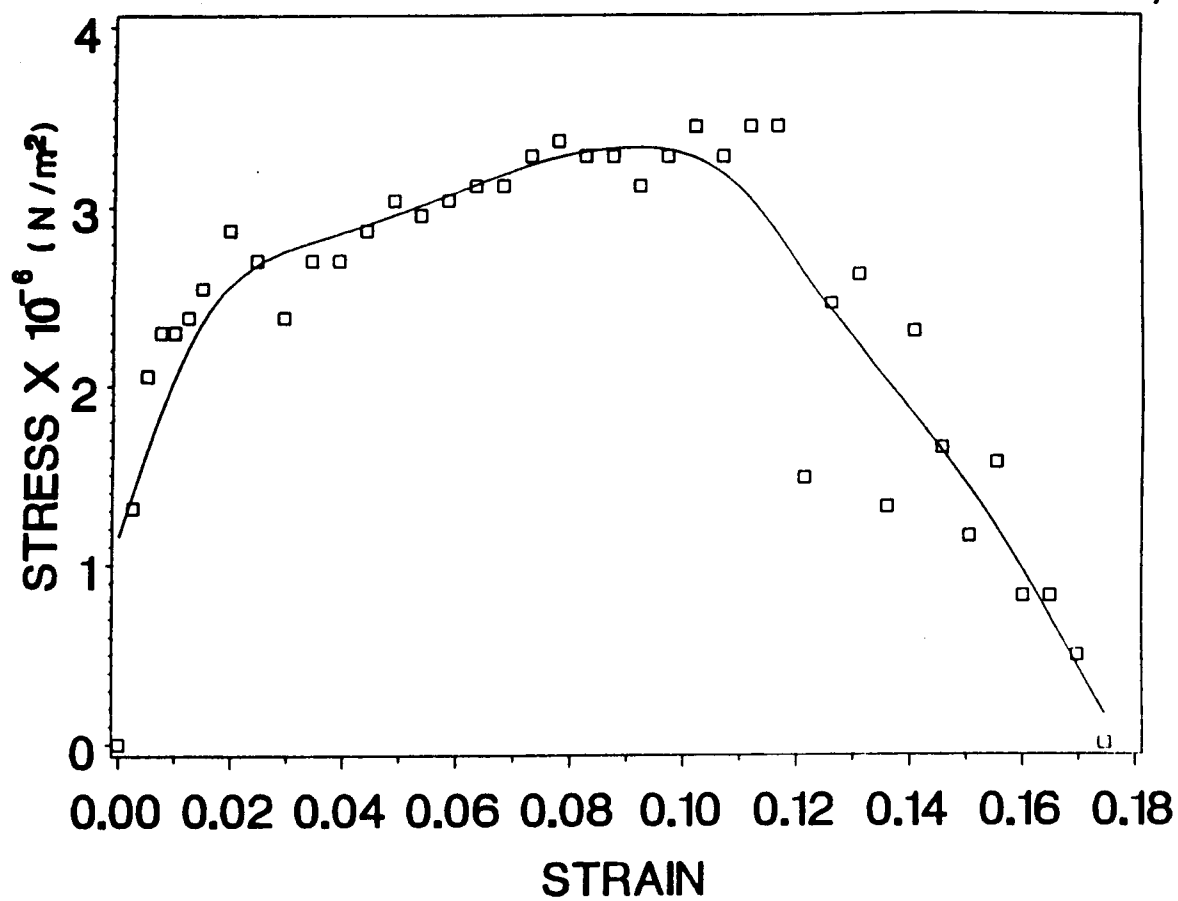


Figure 4.85: Smoothed stress-strain plot of MnBi-Bi eutectic directionally solidified at 0.4 cm/hr.

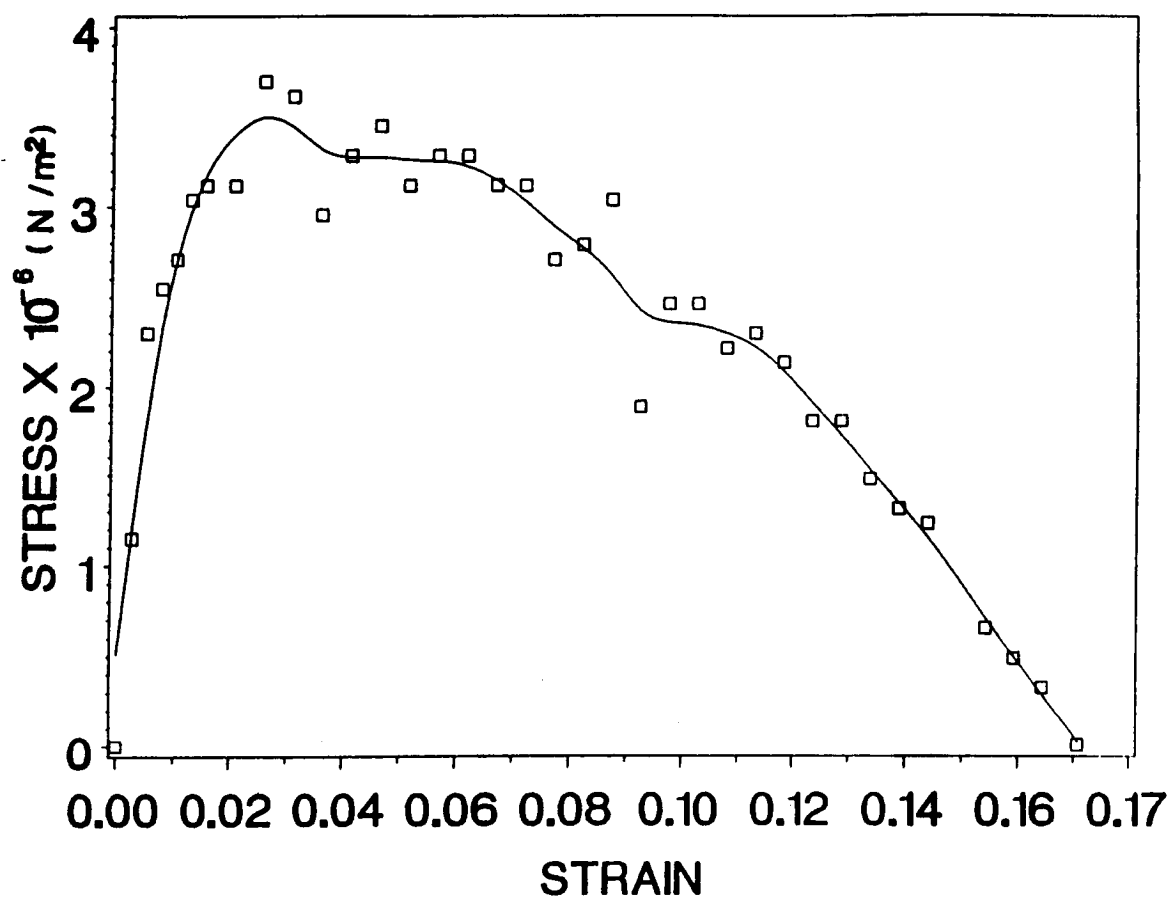


Figure 4.86: Smoothed stress-strain plot of MnBi-Bi eutectic directionally solidified at 0.7 cm/hr.



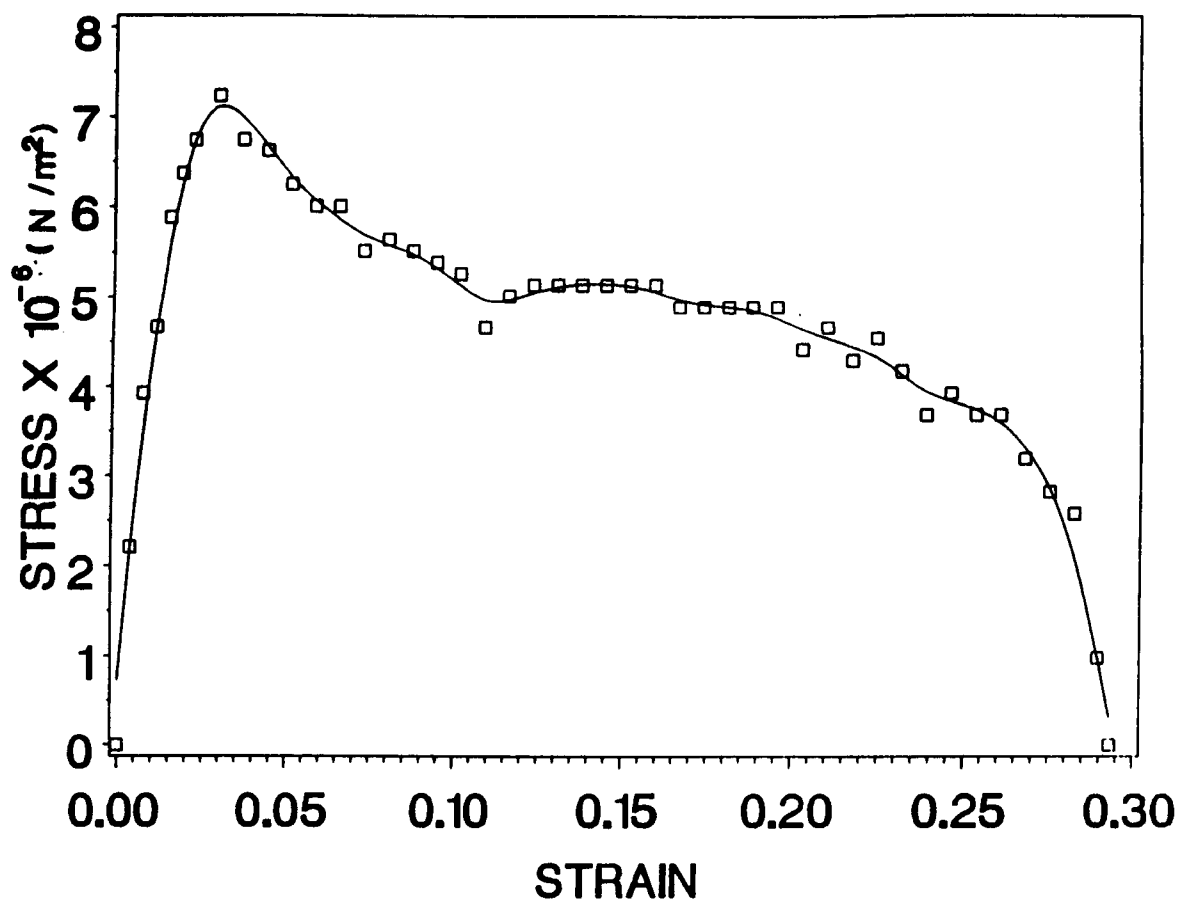


Figure 4.87: Smoothed stress-strain plot of MnBi-Bi eutectic directionally solidified at 1.04 cm/hr.

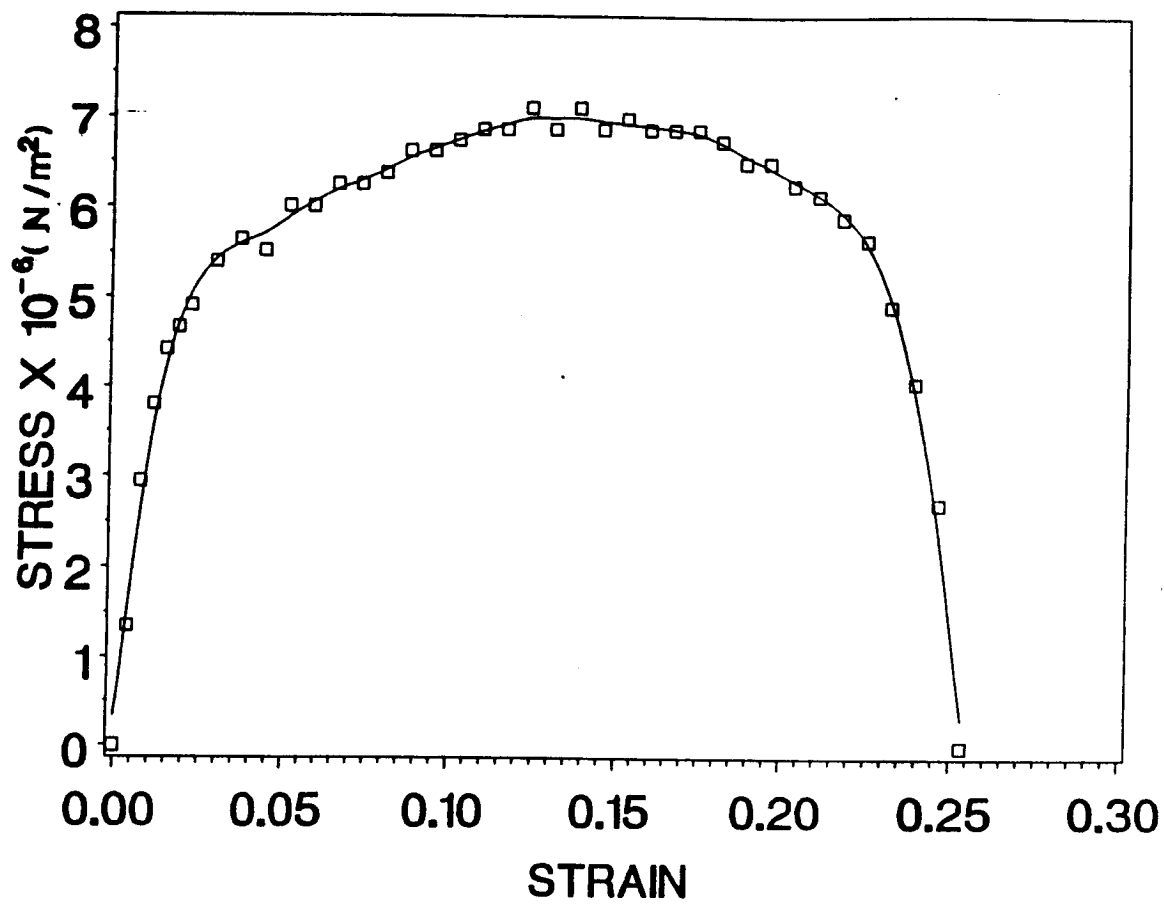


Figure 4.88: Smoothed stress-strain plot of MnBi-Bi eutectic directionally solidified at 2.98 cm/hr.

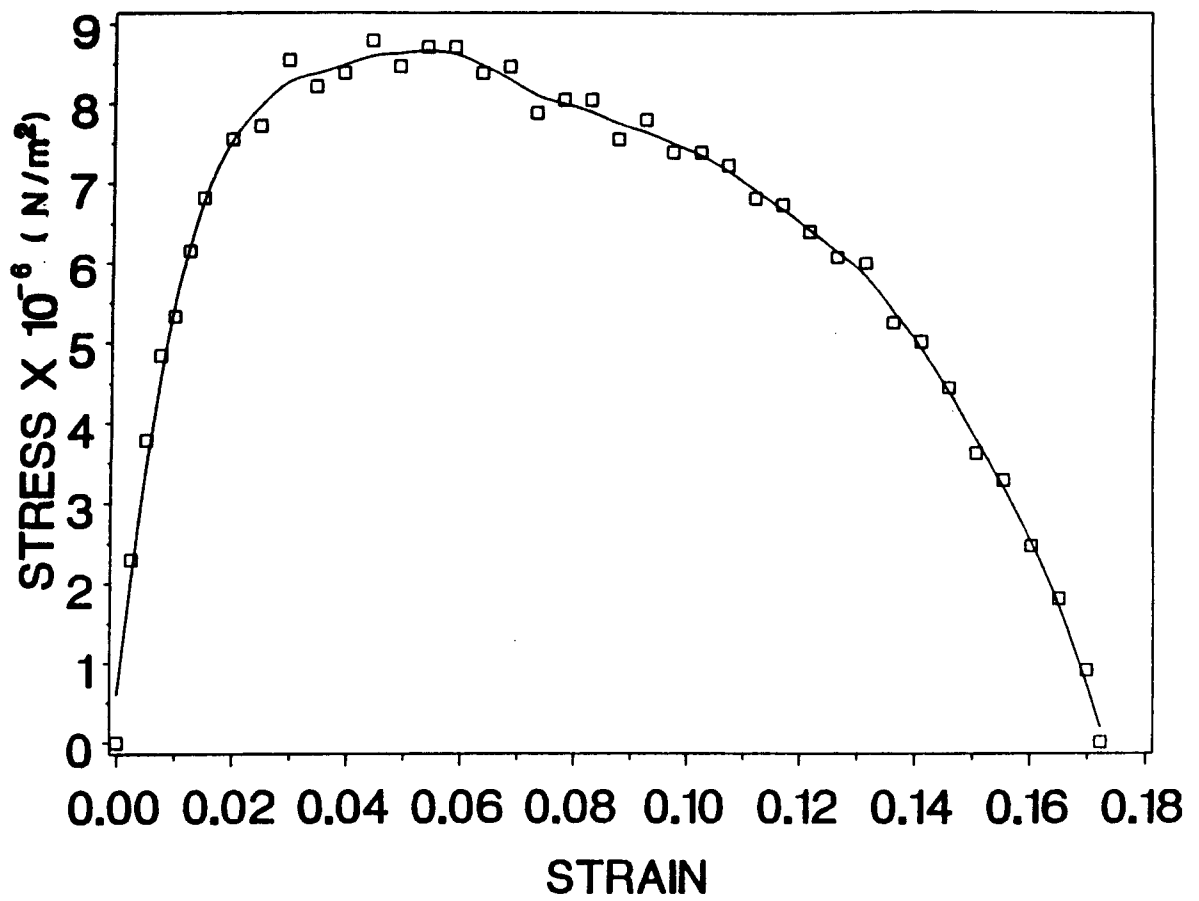


Figure 4.89: Smoothed stress-strain plot of MnBi-Bi eutectic directionally solidified at 4.69 cm/hr.

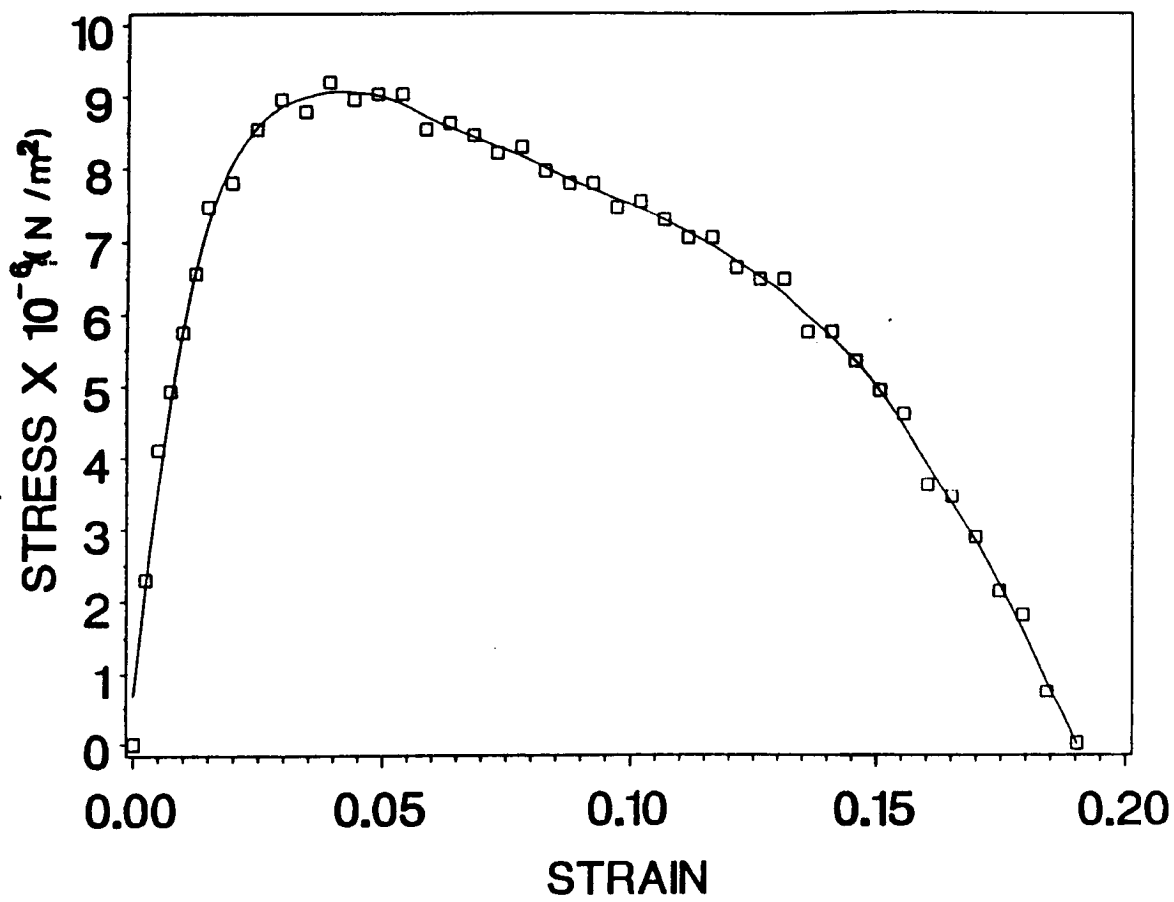


Figure 4.90: Smoothed stress-strain plot of MnBi-Bi eutectic directionally solidified at 6.23 cm/hr.

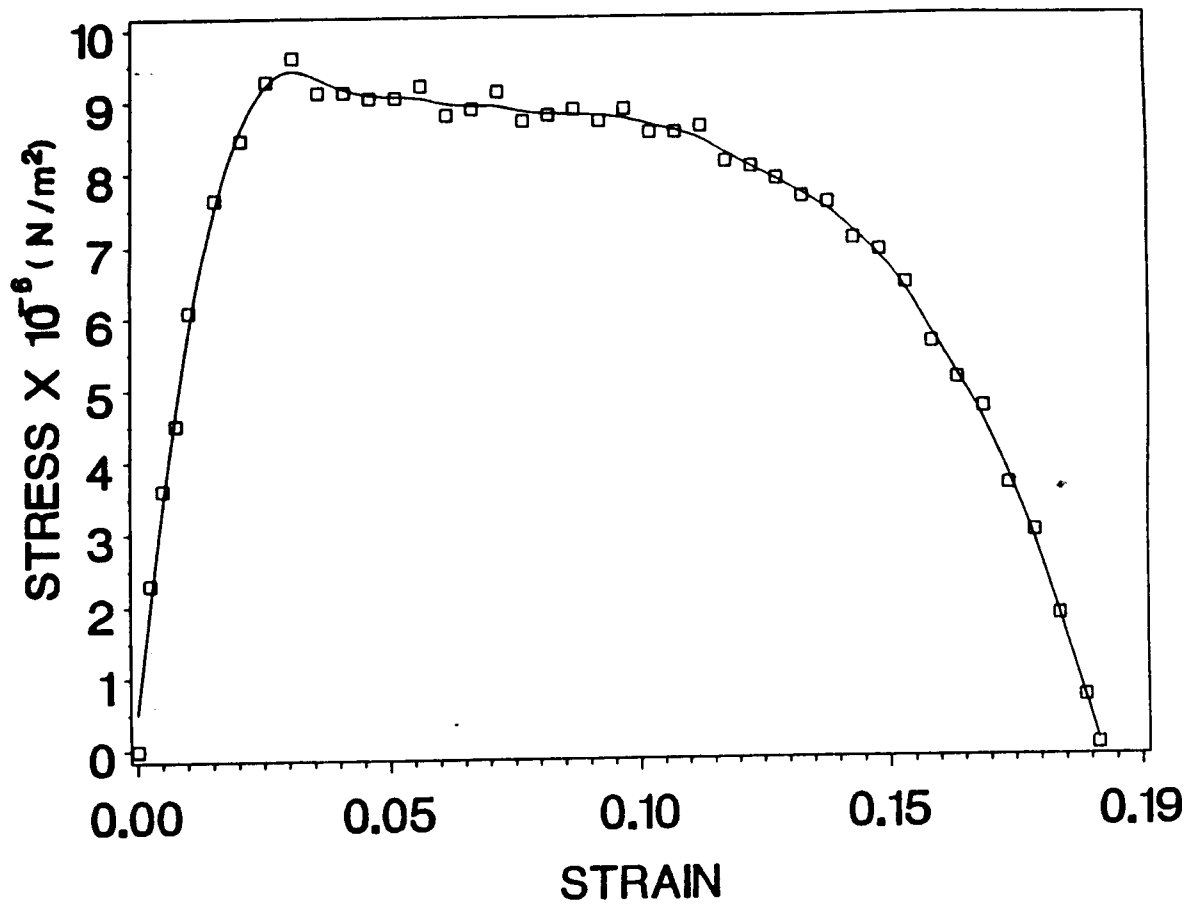


Figure 4.91: Smoothed stress-strain plot of MnBi-Bi eutectic directionally solidified at 8.94 cm/hr.

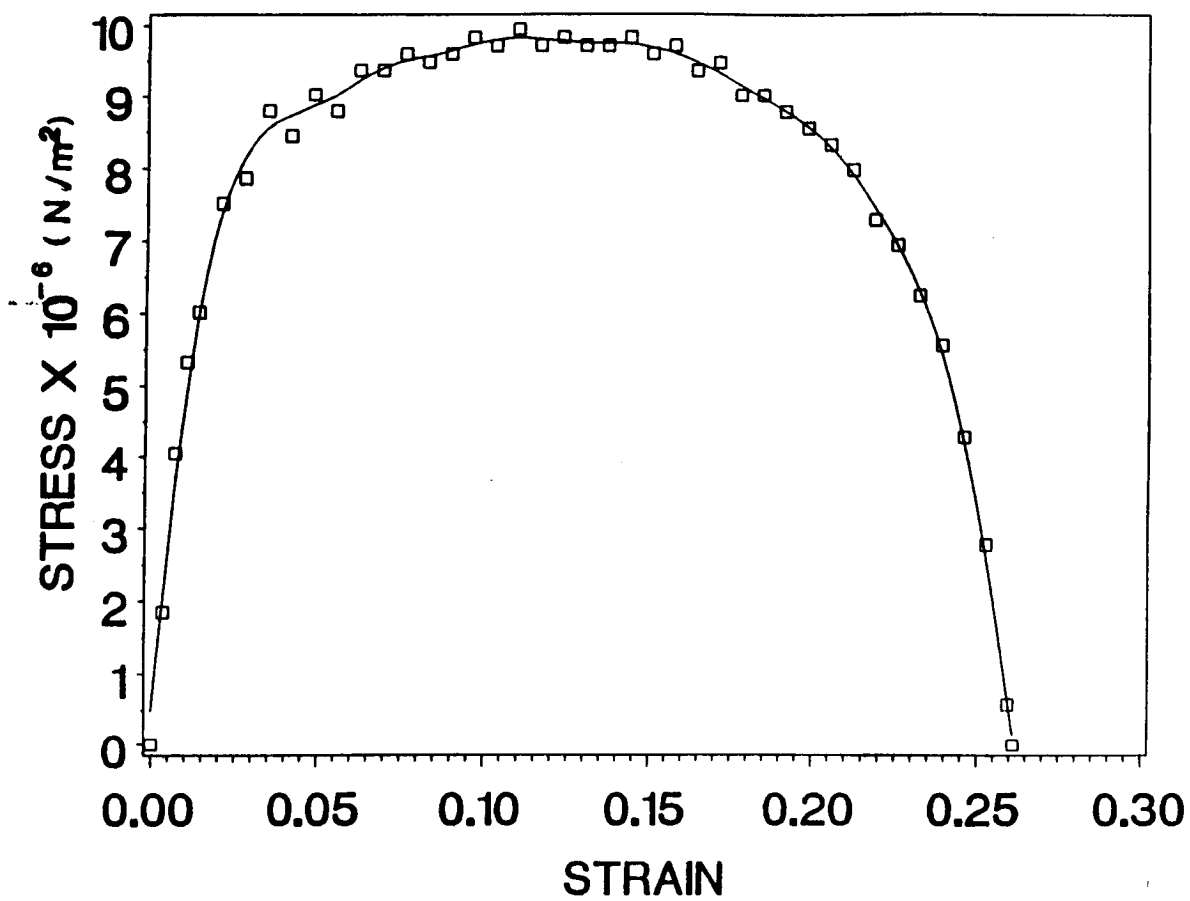


Figure 4.92: Smoothed stress-strain plot of MnBi-Bi eutectic directionally solidified at 8.94 cm/hr.

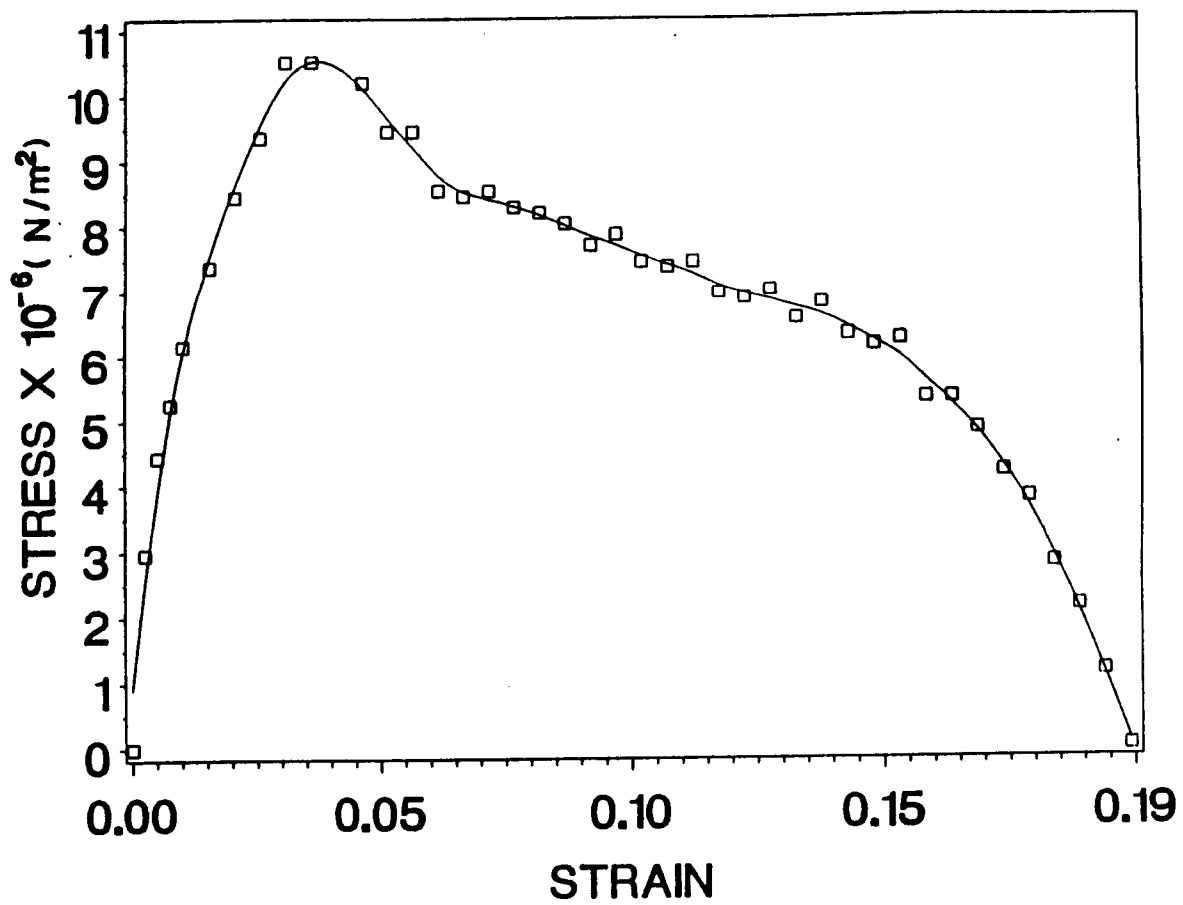


Figure 4.93: Smoothed stress-strain plot of MnBi-Bi eutectic directionally solidified at 12.296 cm/hr.

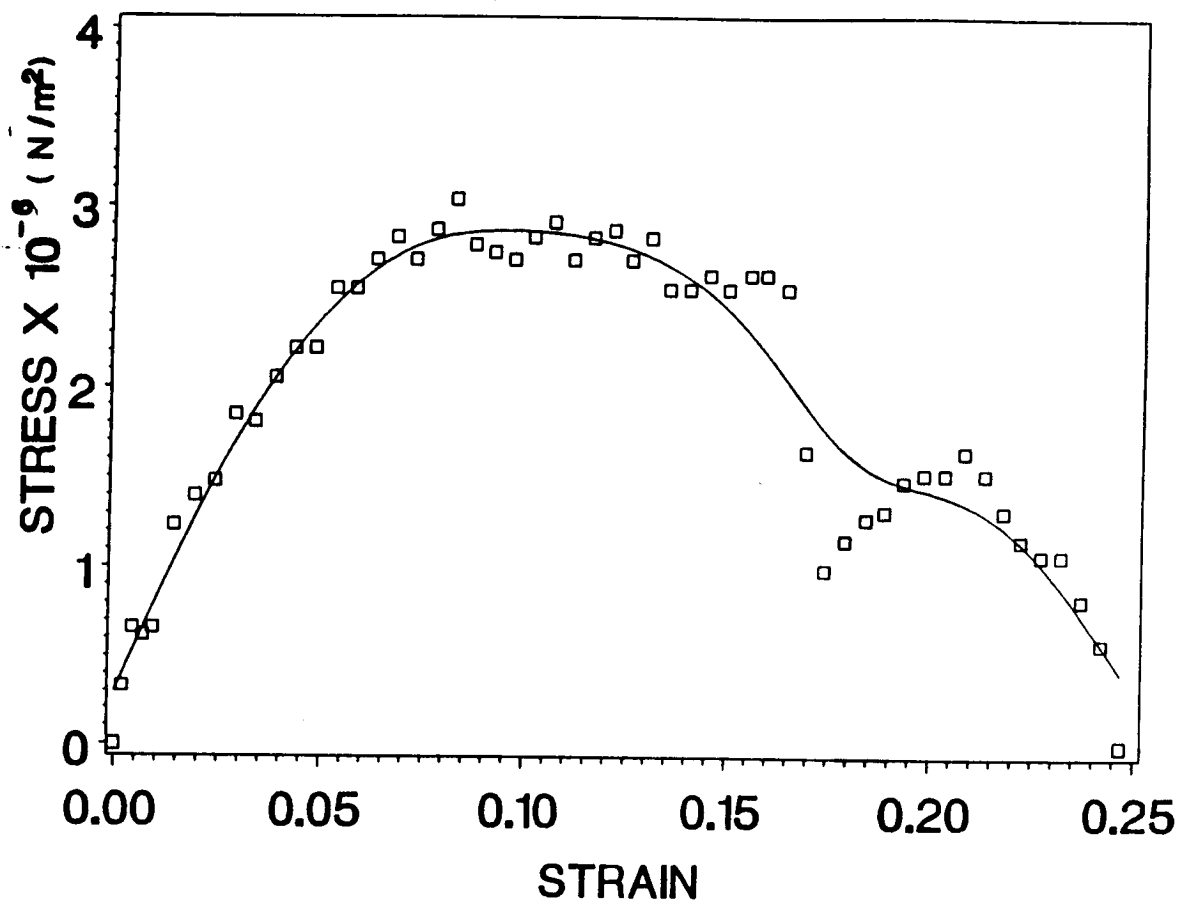


Figure 4.94: Smoothed stress-strain plot of Bi.



Table 7: Mechanical properties of the eutectic as a function of growth rate.

Growth Rate (cm/hr)	Elastic Modulus (N/m <sup>2</sup> )	Maxm. Eng. Stress (N/m <sup>2</sup> )	Total Strain
0.14	$1.01 \times 10^9$	$3.5 \times 10^6$	0.17
0.25	$1.47 \times 10^9$	$4.7 \times 10^6$	0.21
0.25	$1.07 \times 10^9$	$4.57 \times 10^6$	0.22
0.40	$1.42 \times 10^9$	$3.37 \times 10^6$	0.18
0.70	$0.73 \times 10^9$	$3.81 \times 10^6$	0.16
1.04	$0.84 \times 10^9$	$7.13 \times 10^6$	0.30
2.98	$1.04 \times 10^9$	$7.16 \times 10^6$	0.28
4.69	$1.13 \times 10^9$	$8.69 \times 10^6$	0.18
6.23	$2.53 \times 10^9$	$9.1 \times 10^6$	0.20
8.94	$0.97 \times 10^9$	$9.39 \times 10^6$	0.18
8.94	$1.23 \times 10^9$	$9.89 \times 10^6$	0.26
12.29	$1.87 \times 10^9$	$10.54 \times 10^6$	0.20

where growth rate  $V$  is in cm/hr, maximum engineering stress  $\sigma_{max}$  is in N/m<sup>2</sup>, spacing  $\lambda$  is in  $m$  and  $r$  is the correlation coefficient.

For the eutectic solidified with a broken blade microstructure the maximum strength is plotted as a function of spacing in figure 4.97. The relationship between the growth rate and spacing for the broken blade microstructure of the MnBi-Bi eutectic as determined by Eisa [68] is:

$$\lambda^{1.14}V = 2.41 \times 10^{-4} \quad r^2 = 0.961 \quad (4.4)$$

There seems to be no consistent behaviour of the strength of the broken-blade eutectic as a function of the growth rate. The average maximum strength of the MnBi-Bi eutectic with a broken blade microstructure is about half that of the maximum strength of the eutectic solidified with a rod type microstructure.

The elastic modulus and the maximum engineering stress for the bismuth ingot are  $3.1 \times 10^8$  N/m<sup>2</sup> and  $2.94 \times 10^6$  N/m<sup>2</sup> respectively. The average value of the elastic modulus (calculated using SAS) for the MnBi-Bi eutectic is  $1.276 \times 10^9$  N/m<sup>2</sup> (standard deviation =  $5.0 \times 10^8$  N/m<sup>2</sup>, and 95% confidence limit is  $\pm 3.18 \times 10^7$ ). The maximum engineering strength of the eutectic solidified with a broken blade structure is only slightly higher than that for bismuth. However for the rod type microstructure the maximum engineering strength of the eutectic solidified at 2.98 cm/hr is more than twice the strength of bismuth, with the difference increasing with decreasing spacing between the fibers.

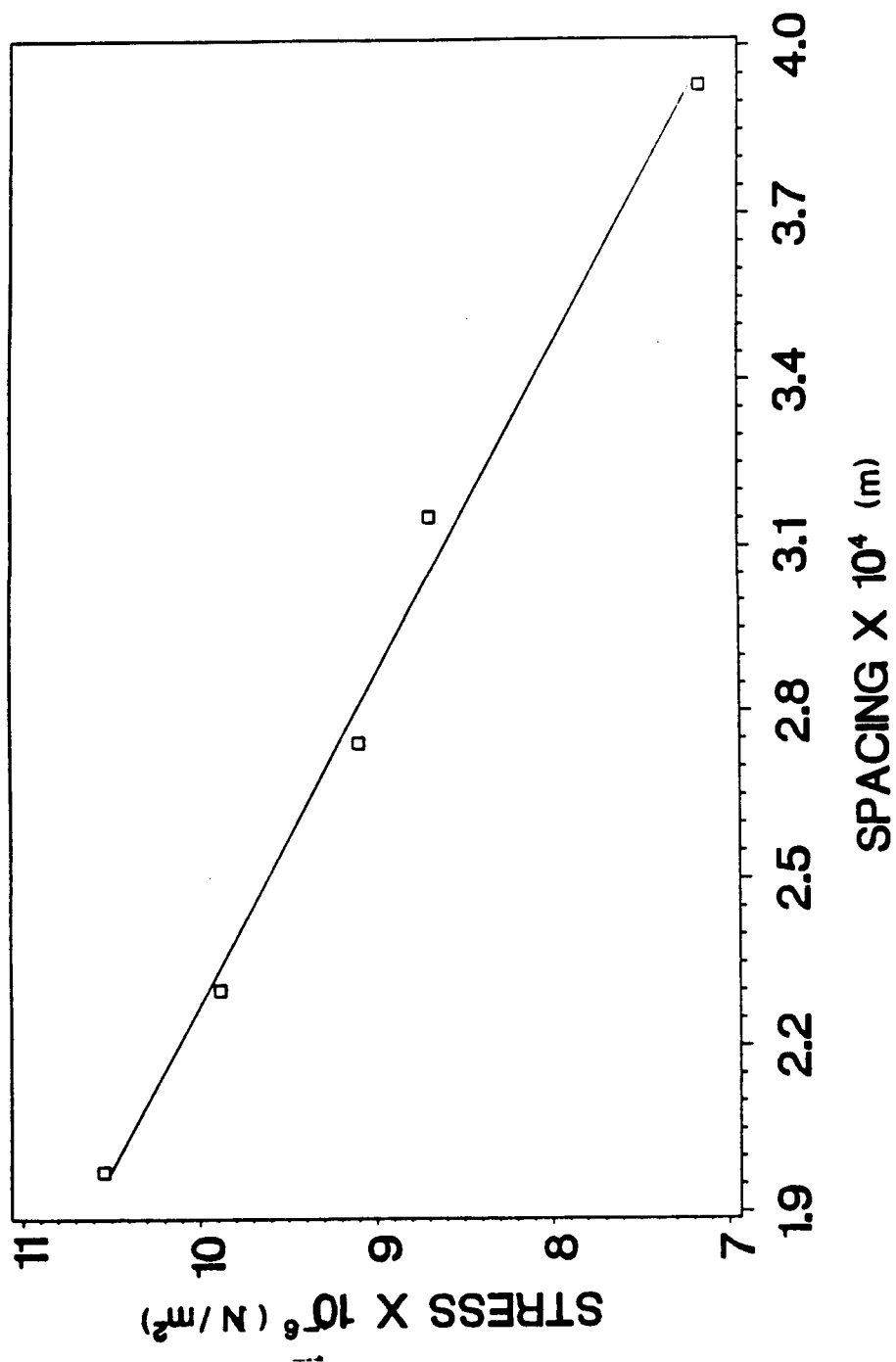


Figure 4.95: Maximum engineering stress of MnBi-Bi eutectic versus average rod spacing for rod type microstructure  $\sigma_{max} = 1.381 \times 10^7 - 1.679 \times 10^{10} \lambda$ .

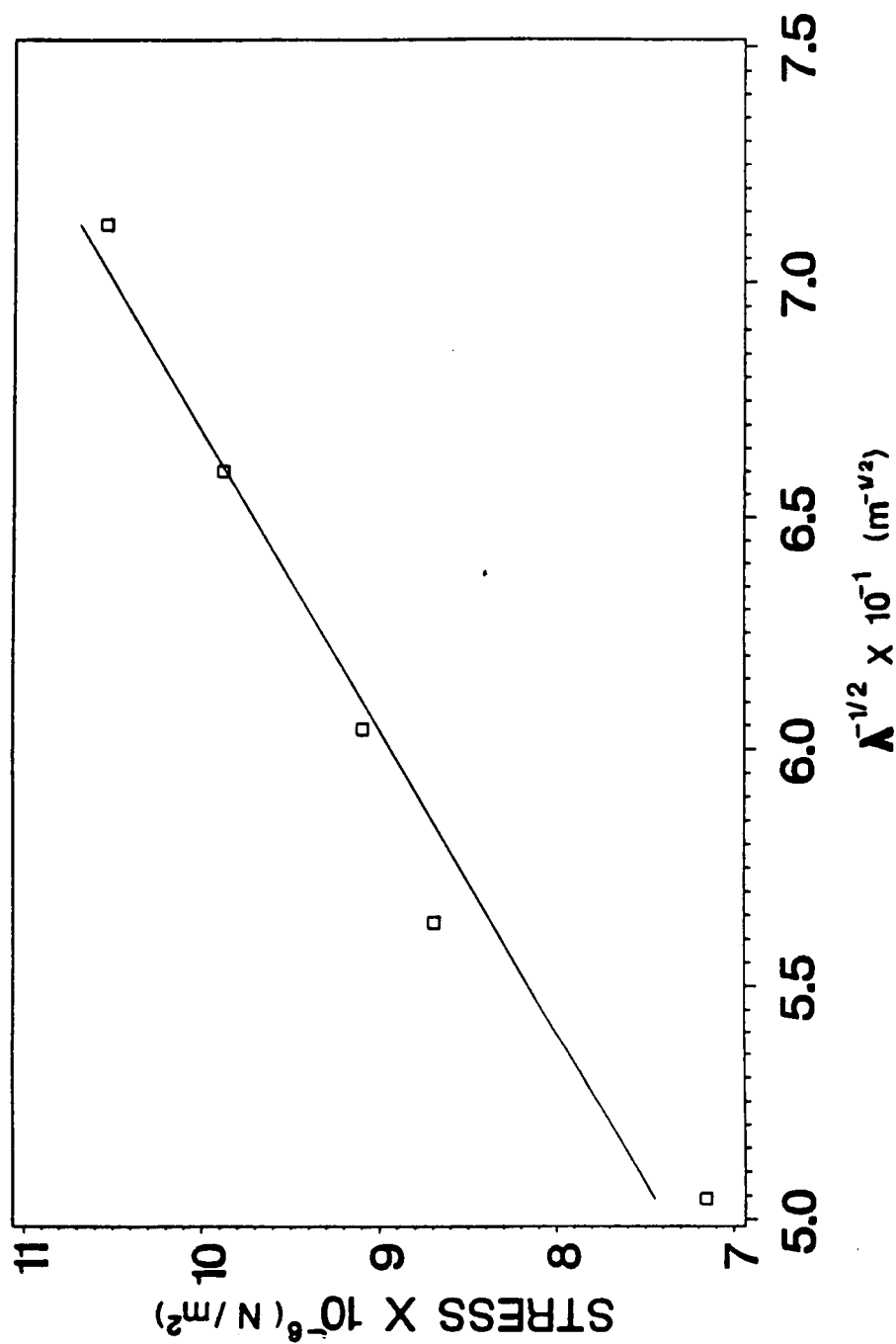


Figure 4.96: Maximum engineering stress of MnBi-Bi eutectic versus  $\lambda^{-1/2}$ , where  $\lambda$  is the average rod spacing for rod type microstructure  $\sigma_{max} = 1.566 \times 10^5 \lambda^{-1/2} - 453100$ .

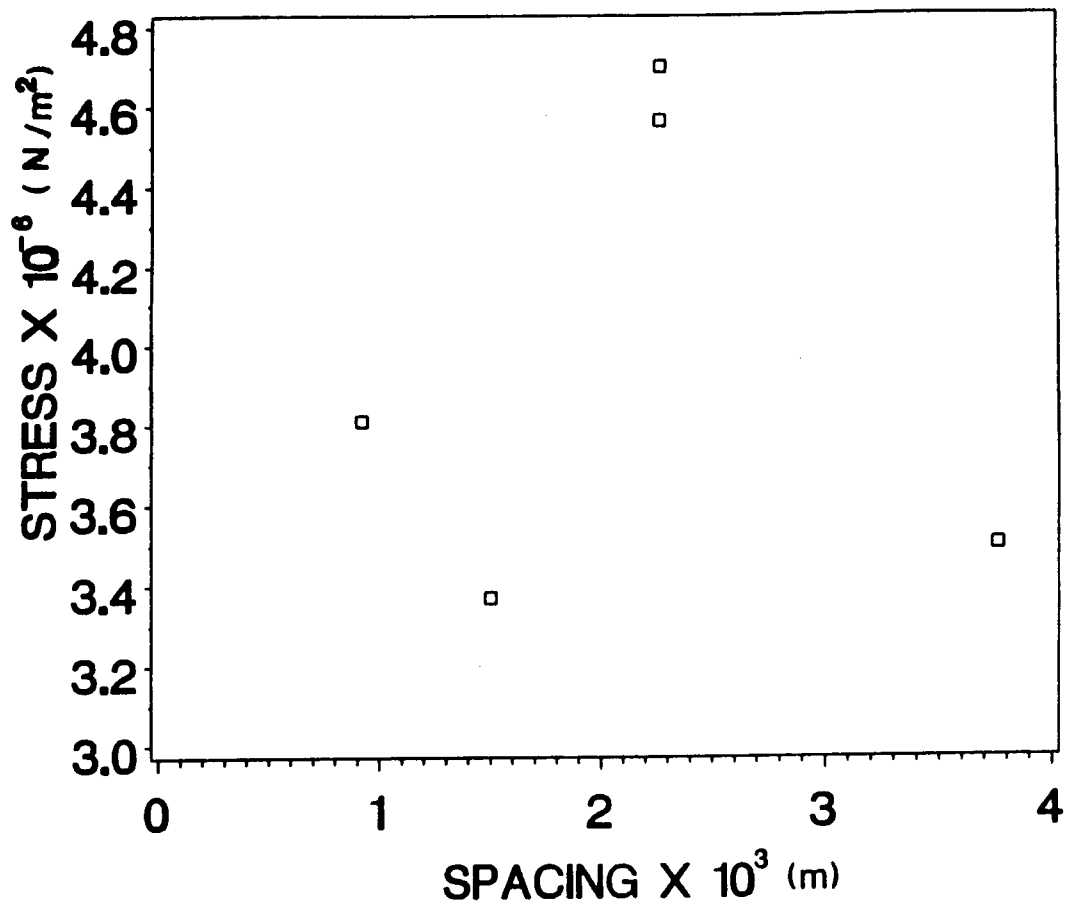


Figure 4.97: Maximum engineering stress of MnBi-Bi eutectic versus spacing for broken blade microstructure.

## 4.5 Temperature measurements

Temperature measurements were conducted in bismuth both with and without spin-up/spin-down. The details of the measurement technique are discussed in the experimental section.

In a typical experiment the ampoule was translated at 12.27 cm/hr. Temperature fluctuations were recorded on a strip chart recorder. The position of the thermocouple was fixed relative to the ampoule and the temperature fluctuations recorded correspond to different positions of the thermocouple in the furnace. The height of the melt above the thermocouple junction and the distance of the solid/melt interface below the thermocouple junction varied during the experiment. The temperature fluctuations corresponding to different positions of the solid/melt interface with respect to the thermocouple junction and different heights of the melt are tabulated in Table 8 and shown in figures 4.98 to 4.104. The amplitude and frequency of the temperature fluctuations are plotted versus height of the melt and distance of the solid/melt interface below the thermocouple junction in figures 4.105 to 4.108.

To verify the above temperature measurements another experiment was performed with another thermocouple assembly. The results of this experiment are shown in figures 4.109 to 4.111.

The amplitude of the temperature fluctuations decreased as the solid/melt interface approached the thermocouple. Temperature fluctuations were as high as 25°C when the solid/melt interface was 5 cm below the thermocouple junction and the height of the melt was 12.6 cm. About 0.8 cm above the solid/melt interface and a melt height of 8.0 cm, the temperature fluctuations decreased to about 2°C. The

**Table 8: Amplitude and frequency of temperature fluctuations as a function of melt height and thermocouple position from the solid/melt interface.**

<b>Height of melt cm</b>	<b>Height of thermocouple from interface cm</b>	<b>Amplitude of fluctuations °C</b>	<b>Frequency of fluctuations °C/sec</b>
12.6	5.1	25	2
11.3	3.8	19	3
10.5	3.0	14	7
10.0	2.5	9	8
8.8	1.3	3	10
8.0	0.8	2	
7.5	0	0	0

ORIGINAL PAGE IS  
OF POOR QUALITY

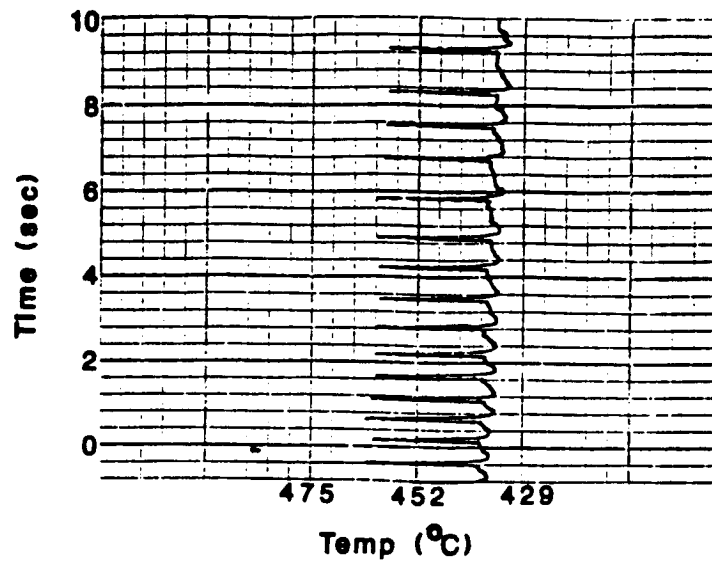


Figure 4.98: Temperature fluctuations with a melt height of 12.6 cm and the thermocouple junction 5.1 cm above the solid/melt interface.

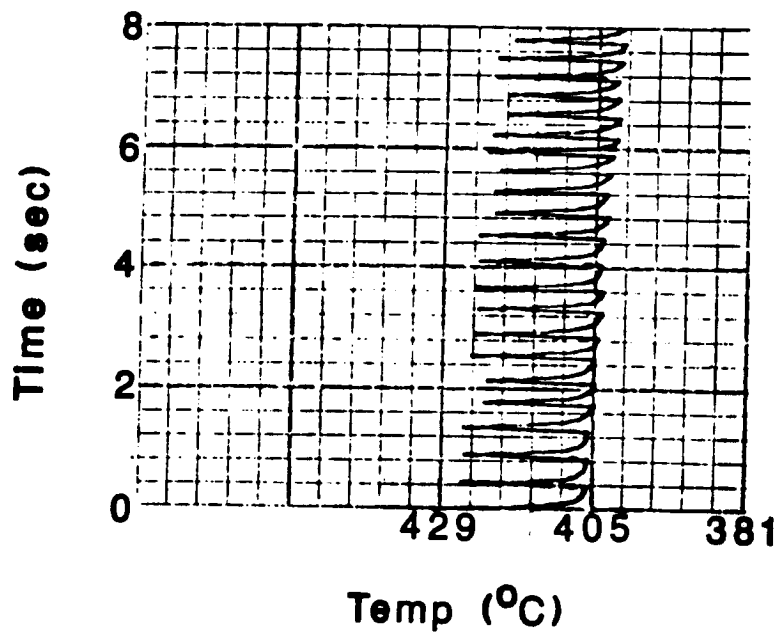


Figure 4.99: Temperature fluctuations with a melt height of 11.3 cm and the thermocouple junction 3.8 cm above the solid/melt interface.



ORIGINAL PAGE IS  
OF POOR QUALITY

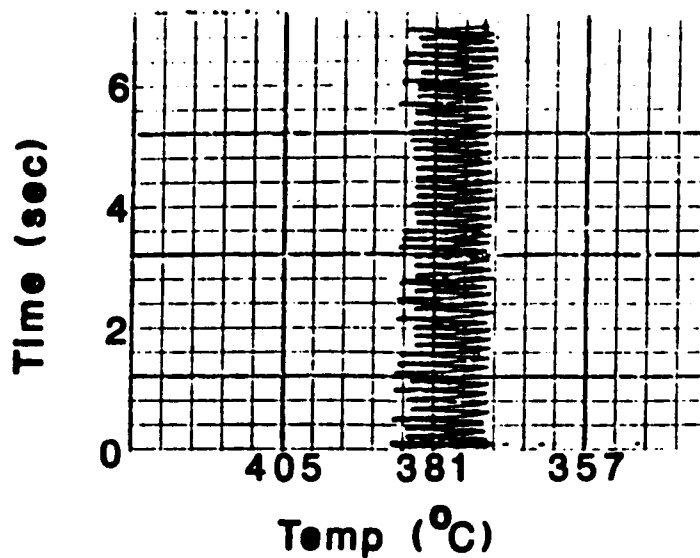


Figure 4.100: Temperature fluctuations with a melt height of 10.5 cm and the thermocouple 3.0 cm above the solid/melt interface.

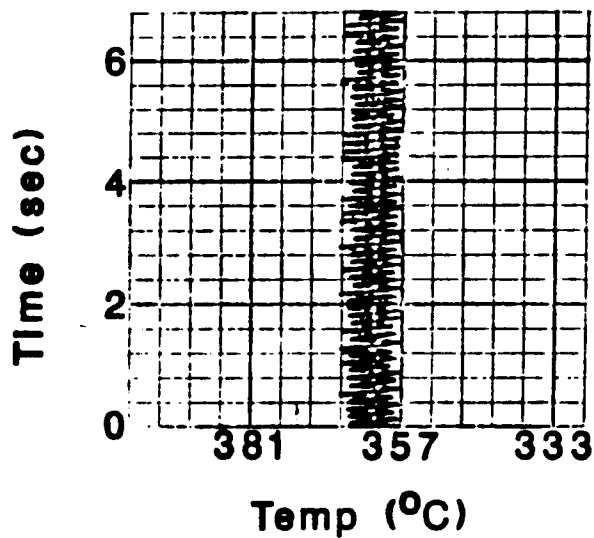


Figure 4.101: Temperature fluctuations with a melt height of 10.0 cm and the thermocouple 2.5 cm above the solid/melt interface.

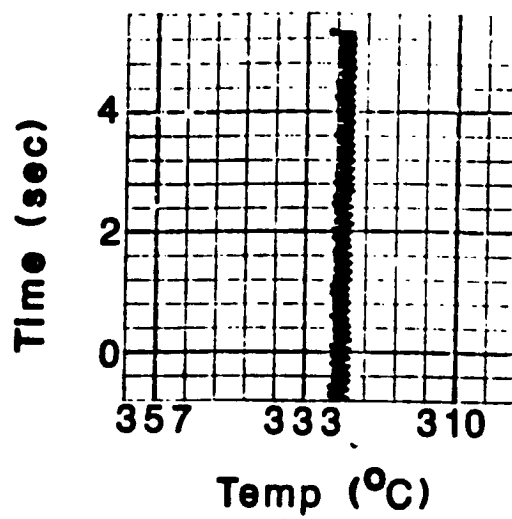


Figure 4.102: Temperature fluctuations with a melt height of 8.8 cm and the thermocouple junction 1.3 cm above the solid/melt interface.

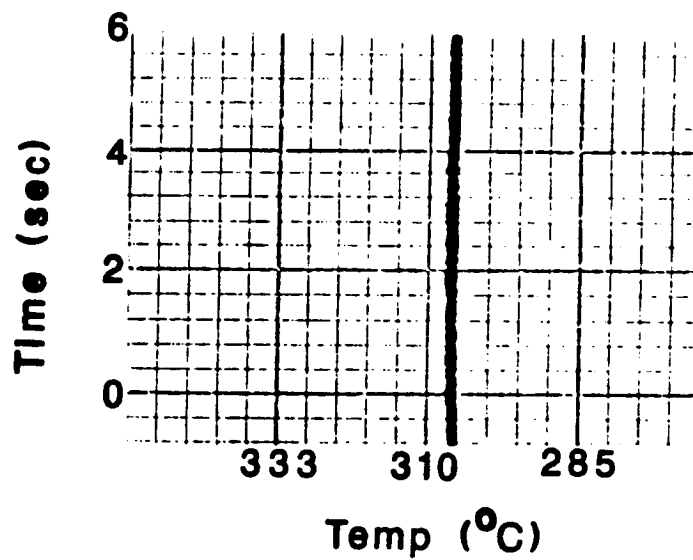


Figure 4.103: Temperature fluctuations with a melt height of 8.0 cm and the thermocouple junction 0.8 cm above the solid/melt interface.

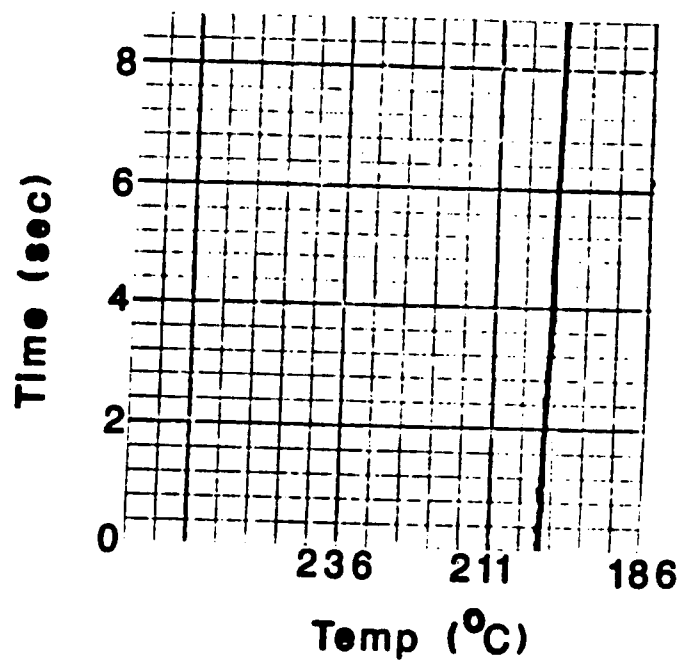


Figure 4.104: Temperature with the thermocouple embedded in the solid.

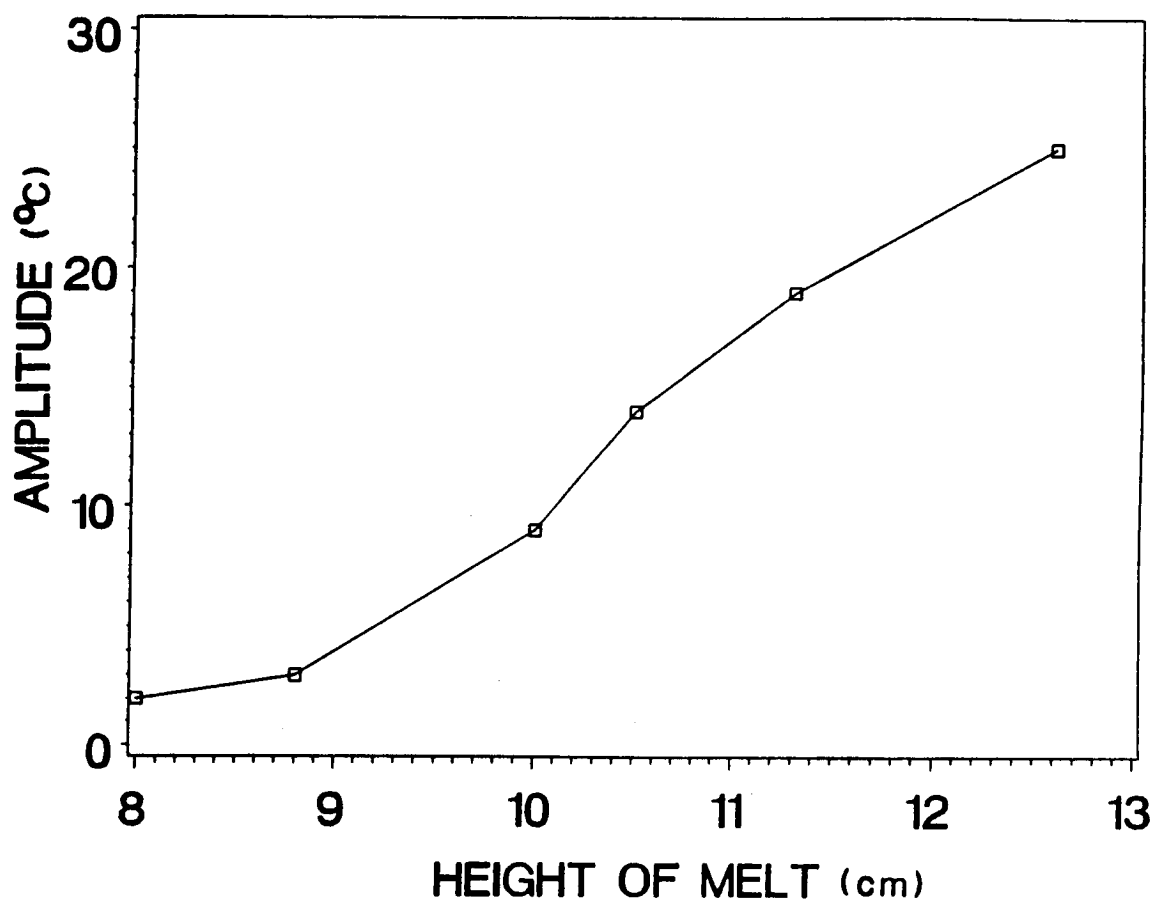


Figure 4.105: Amplitude of temperature fluctuations versus height of melt.

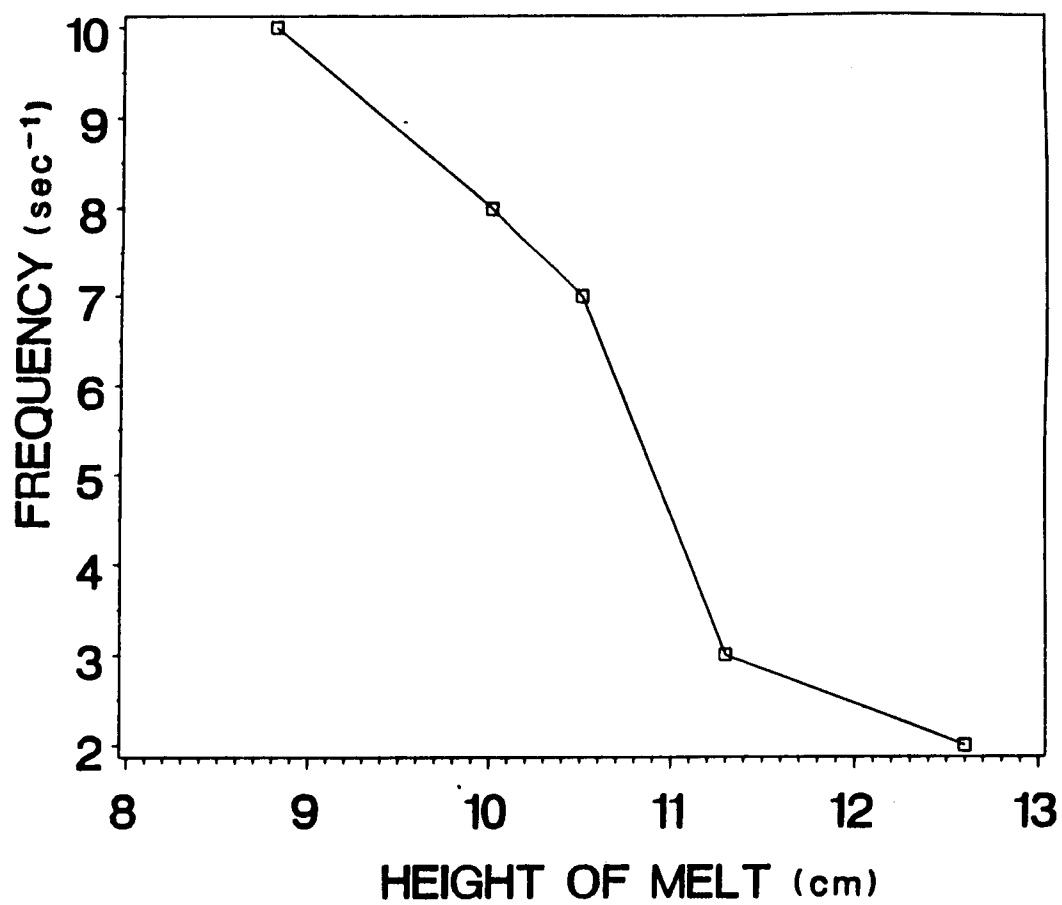


Figure 4.106: Frequency of temperature fluctuations versus height of melt.

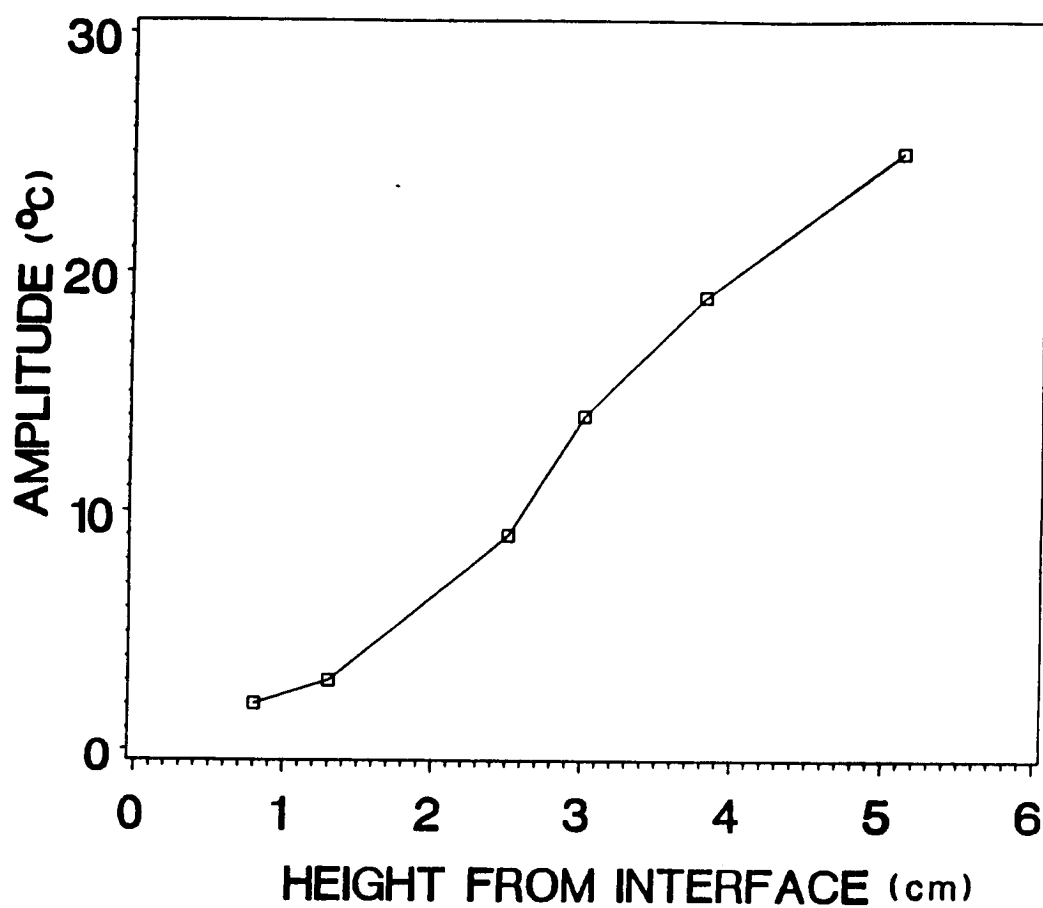


Figure 4.107: Amplitude of temperature fluctuations versus distance of thermocouple junction from the solid/melt interface.

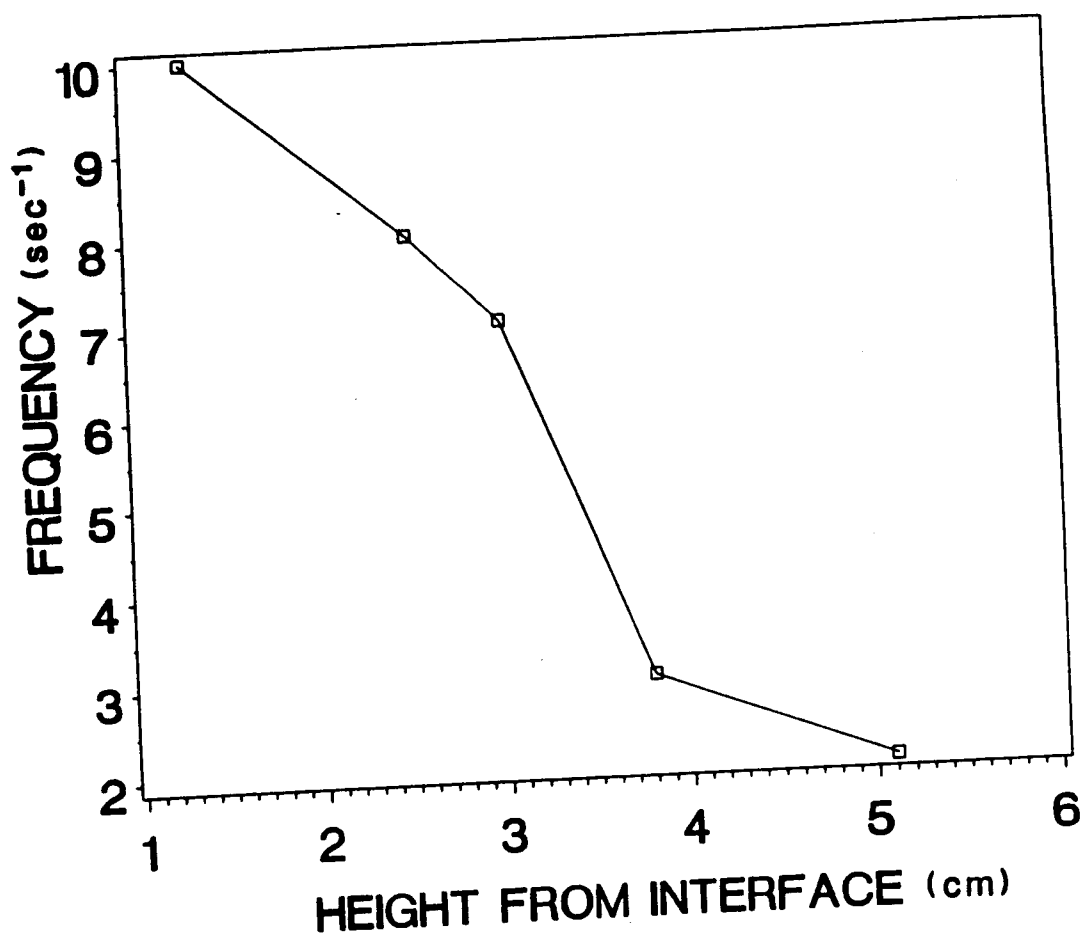


Figure 4.108: Frequency of temperature fluctuations versus distance of thermocouple junction from the solid/melt interface.

ORIGINAL PAGE IS  
OF POOR QUALITY

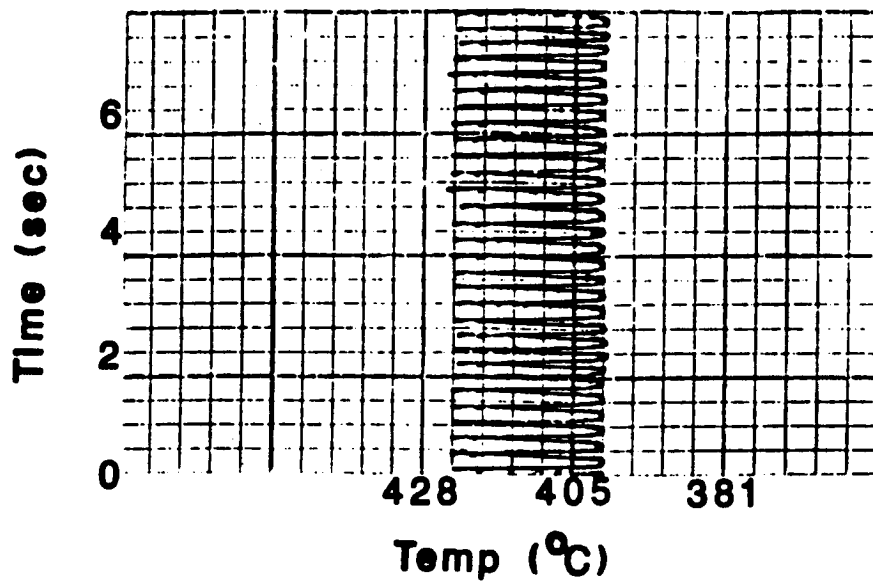


Figure 4.109: Temperature fluctuations with a melt height of 11.0 cm and the thermocouple junction 4.0 cm above the solid/melt interface.

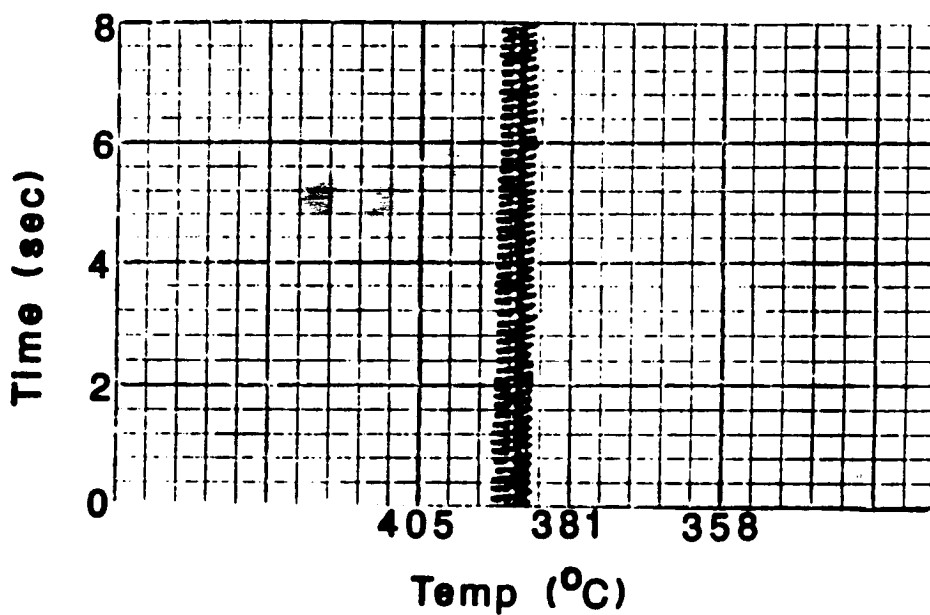


Figure 4.110: Temperature fluctuations with a melt height of 10.2 cm and the thermocouple 3.2 cm above the solid/melt interface.



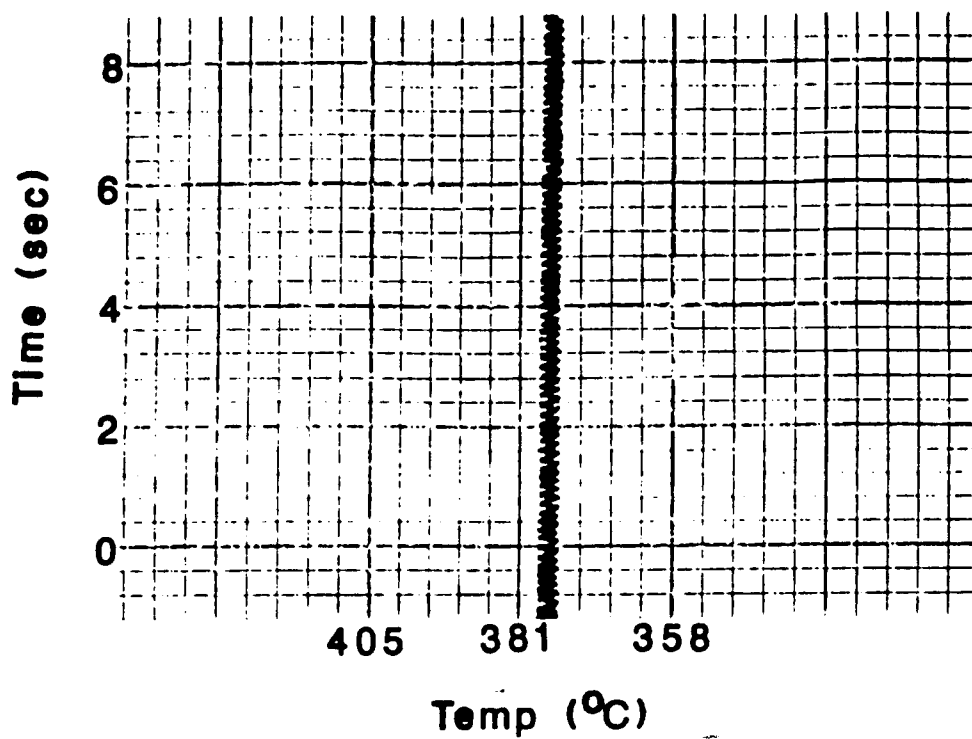


Figure 4.111: Temperature fluctuations with a melt height of 9.7 cm and the thermocouple junction 2.7 cm above the solid/melt interface.

thermocouple did not record any fluctuations thereafter. Temperature fluctuations close to the interface were probably small to be picked up by the thermocouple. The sensitivity of the temperature measuring system was  $0.1^{\circ}\text{C}$ . However the accuracy of the temperature measured was limited by the range selected on the strip chart recorder. A range of 20 mv was used for the temperature measurements on the strip chart recorder which resulted in an accuracy of  $2^{\circ}\text{C}$  for the temperature fluctuations.

When the melt around the thermocouple had solidified, i.e. at temperatures below the melting point of Bi, there were no fluctuations in the temperature at all. This confirms that the fluctuations in temperature were caused by convection.

Both the height of the melt above the solid/melt interface and the distance of the solid/melt interface below the thermocouple junction varied during the experiment. Thus it is difficult to attribute the change in amplitude and frequency to any one factor, i.e. either a decrease in melt height or decreasing distance between the thermocouple junction and the solid/melt interface.

Only one temperature measurement experiment with 50 rpm spin-up/spin-down was successfully conducted. Also temperature measurements were only made close to the interface. This was primarily for two reasons (i) the technique used to measure the temperature with spin-up/spin-down was cumbersome and (ii) the magnitude of temperature fluctuations without spin-up/spin-down higher up in the melt was large.

The temperature fluctuations at two different positions in the melt with 50 rpm spin-up/spin-down (7.91 s spin-up and 7.08 s spin-down) and a growth rate of 12.27 cm/hr are shown in figures 4.112 and 4.113. The twisting of the thermocouple during the experiment generated noise in the temperature measurements as shown in figure 4.114. The noise was  $7^{\circ}\text{C}$  just when spin-up was started and then decreased to  $3^{\circ}\text{C}$ .

There was no noise during spin-down as there was no twisting of the thermocouple wire.

Immediately following spin-up the temperature fluctuated about 40°C at a melt height of 9.5 cm with the thermocouple junction 2.5 cm above the solid/melt interface. The fluctuations decrease to 15°C after the initial impulse. During spin-down the temperature fluctuated as much as 30°C.

With the thermocouple junction 0.8 cm above the solid/melt interface the temperature fluctuated by 7°C immediately following spin-up and decreased to 3°C. During spin-down the temperature fluctuated 3°C.

ORIGINAL PAGE IS  
OF POOR QUALITY

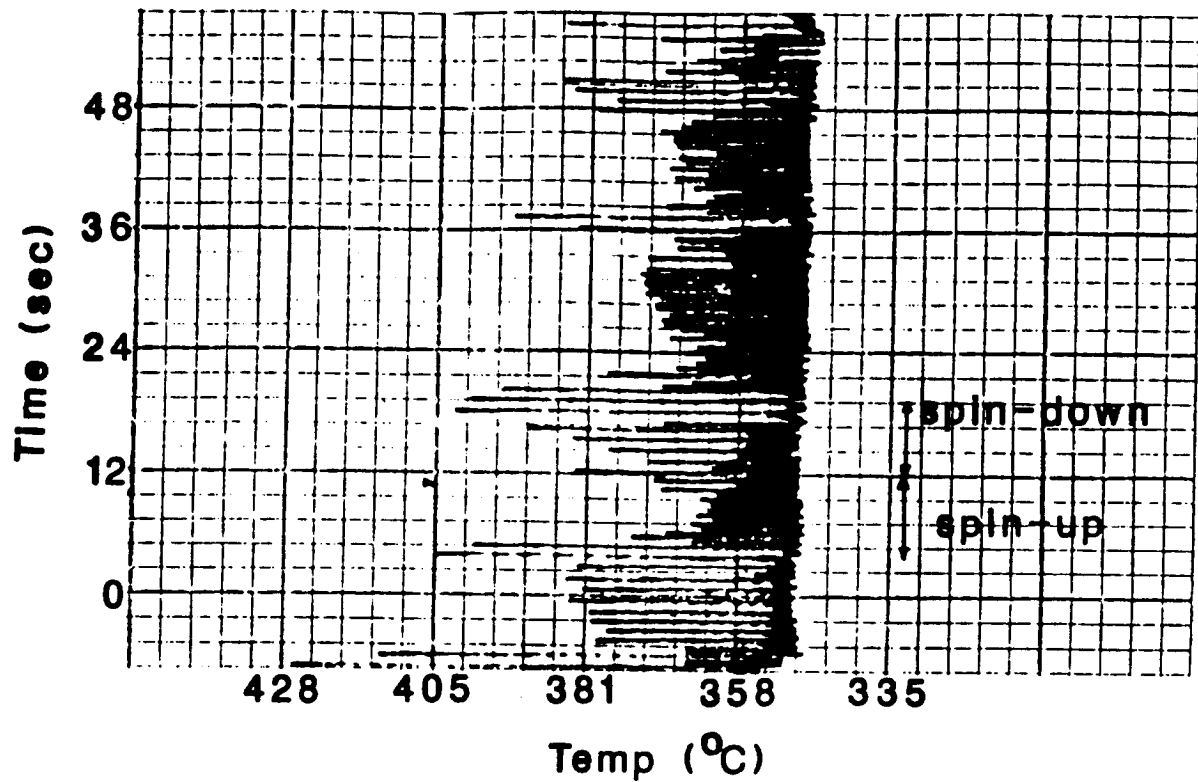


Figure 4.112: Temperature fluctuations with 50 rpm spin-up/spin-down. The height of the melt above the melt was 9.5 cm and the thermocouple junction was 2.5 cm above the solid/melt interface.

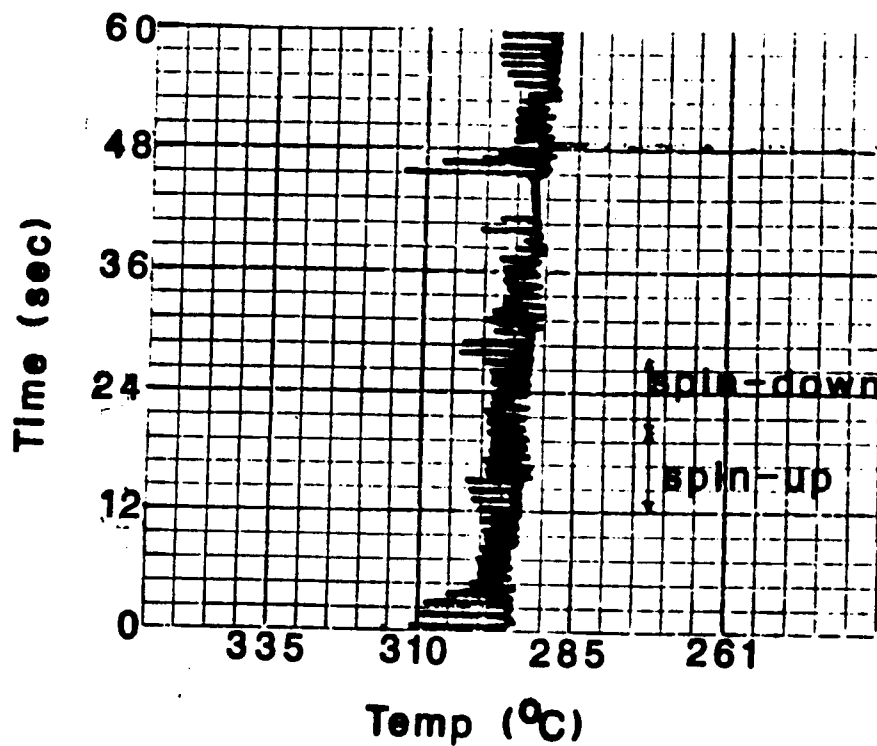


Figure 4.113: Temperature fluctuations with 50 rpm spin-up/spin-down. The height of the melt was 7.8 cm and the thermocouple junction was 0.8 cm above the solid/melt interface.

ORIGINAL PAGE IS  
OF POOR QUALITY

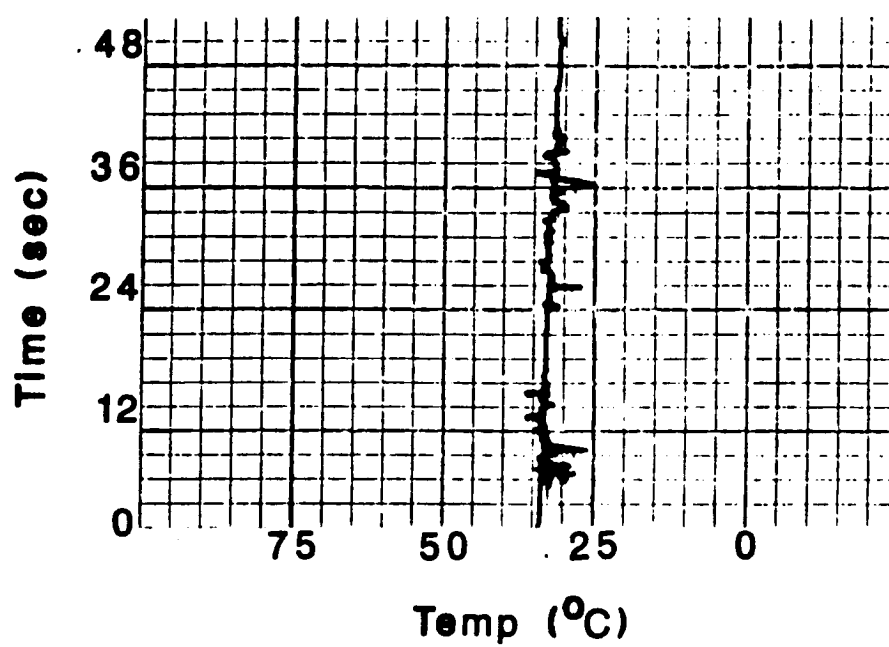


Figure 4.114: Noise due to twisting of the thermocouples in temperature measurements with spin-up/spin-down.

## APPENDIX G

### SPIN-UP / SPIN-DOWN EXPERIMENTAL RESULTS

Excerpts from a 1987 Ph.D. thesis by Mark Larrousse at Clarkson University.

Complete copies of this thesis may be obtained from University Microfilms or from W.R. Wilcox for the costs of reproduction.

## 4 RESULTS

This chapter is broken into three parts. The first discusses the flow visualization experiments. These were undertaken to understand the results obtained in the electrochemical experiments. The results of the two electrochemical sections are related back to the fluid flow observations whenever possible. The second part covers the electrochemical results when a fluid is impulsively spin-up from rest and impulsively spun-down to rest for long time periods. The last section discusses the electrochemical results when the container was spun-up and spun-down for short periods.

### 4.1 Flow Visualization

The first series of spin-up and spin-down tests were conducted with 50 micrometer (large axis) sublimed sulfur powder flakes in tap water at  $21^{\circ}\text{C}$  and a HeNe laser beam slit. The solution was agitated before an experimental run to suspend the particles. The agitation was stopped for at least three minutes or until particle motion was no longer witnessed. Then 65 RPM rotation was impulsively started. Four second exposures with 400 ASA film were made with the f-stop at 5.6.

In the initial stages of spin-up, many particles were in the field of view, as shown in figure 4.1. (The zig-zag pattern was caused by wobble during the cylinder rotation.) A strong downward flow was seen. Particles closest to the cylinder wall had curved trajectories caused by the Stewartson layer pushing non-spun-up fluid inward and the Ekman layer suction pulling them downward. These curved trajectories were predicted and observed by Wedemeyer [53].

Figure 4.2 shows that the width of the downward flow had decreased by 8



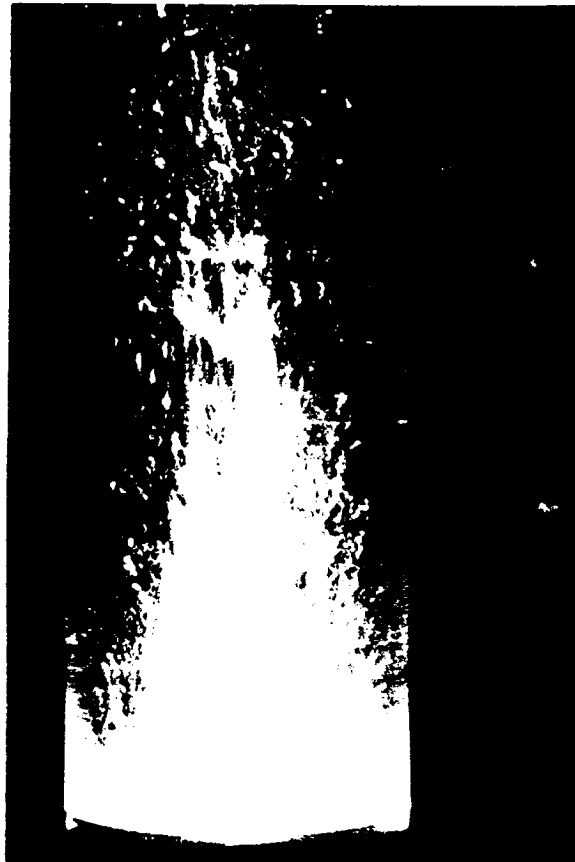
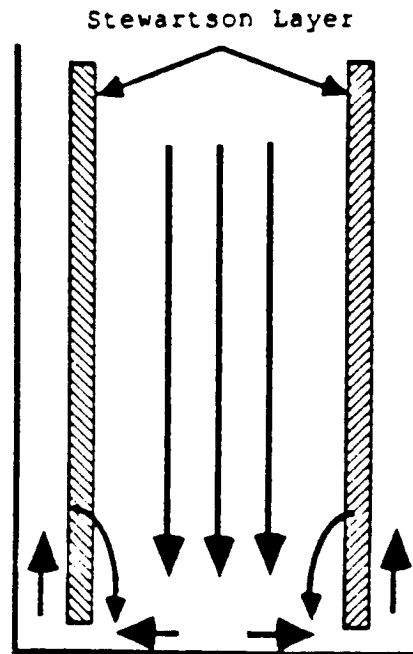


Figure 4.1: Flow patterns in the first 4 seconds of spin-up. Laser lit sublimed sulfur powder

seconds. Ekman pumping decreased as the Stewartson layer moved inward. Thus, the streaks near the top of the photograph are not as long as those near the bottom. The Ekman suction was not as strong as in the previous photograph, in which the Stewartson layer had not moved in very far (the streaks appear to be of equal length at the top and the bottom). The curved particle trajectories seen in Figure 4.1 are no longer evident because the velocity of the Stewartson layer had decreased. Around the central column of fluid moving downward is a mottled region. Here the fluid was nearly spun-up; the particles were not in the light beam long enough to leave a streak on the photograph. This effect is even more evident in figure 4.3, where the tube had been rotating about 5 minutes. Most of the photograph is mottled, except where very large particles were settling. Since sulfur has a higher density than water, any curvature in the streaks was probably caused by centrifugal force throwing the particles outward.

Figure 4.4 shows spin-down immediately after rotation ceased. The important features of this photograph are near the endwall. The region near the cylinder wall is mottled because the angular velocity had not significantly decayed. At the endwall an in-rush of fluid and its rise at the center are revealed. A circular "cloud" of powder is at the central axis. This is a stagnation region, caused by fluid turning away from the endwall. It persisted throughout most of the spin-down process. Figure 4.5 shows that after about 8 seconds, the central vortex had risen higher into the cylinder. In figure 4.6, about 12 seconds into spin-down, the central vortex was still rising. The central vortex continued rising after about 16 seconds (figure 4.7). Strong non-axisymmetric vortices appeared above the endwall in the rising central vortex after 20 seconds (in figure 4.8). These persisted for as long as three to four minutes before dying out.

In the photographs lit by the laser beam, the central region was brightest

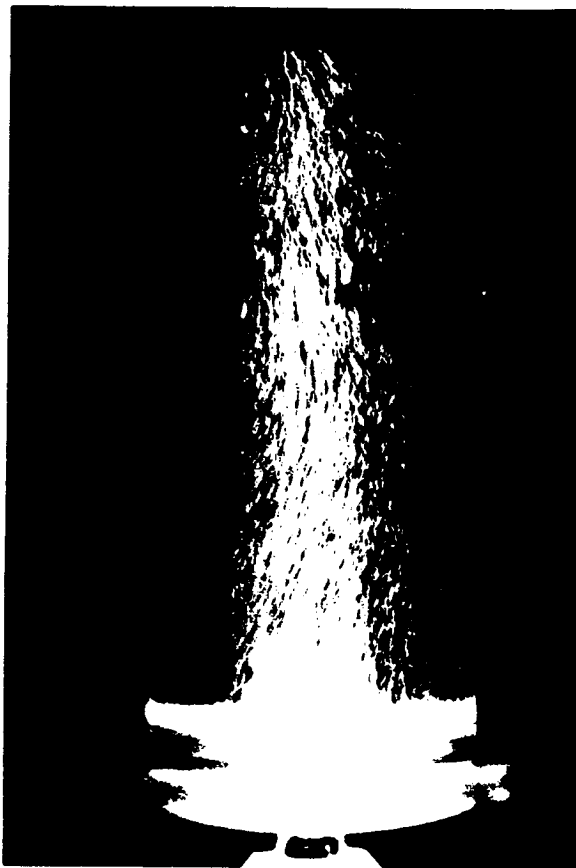
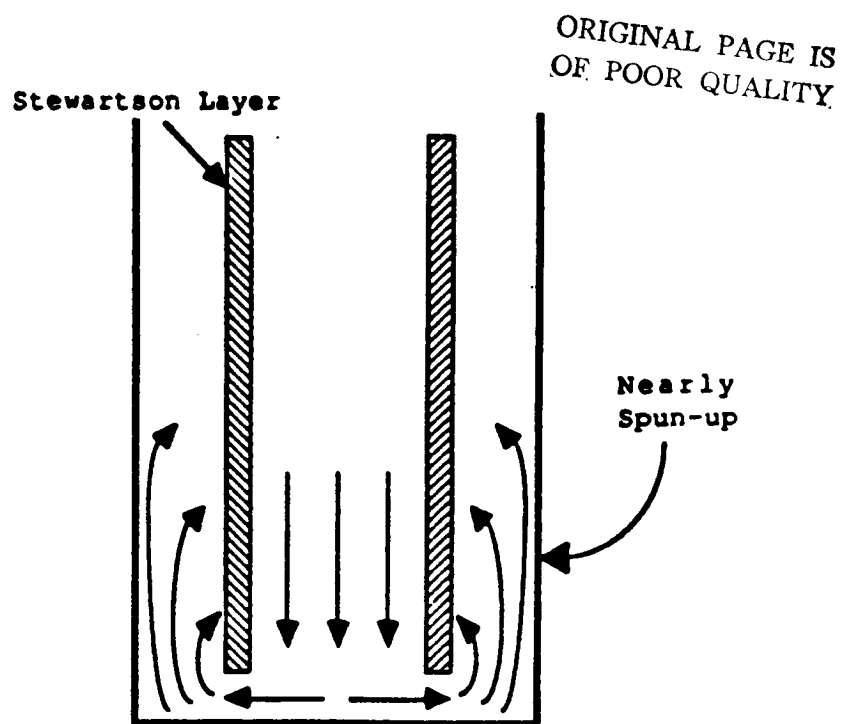
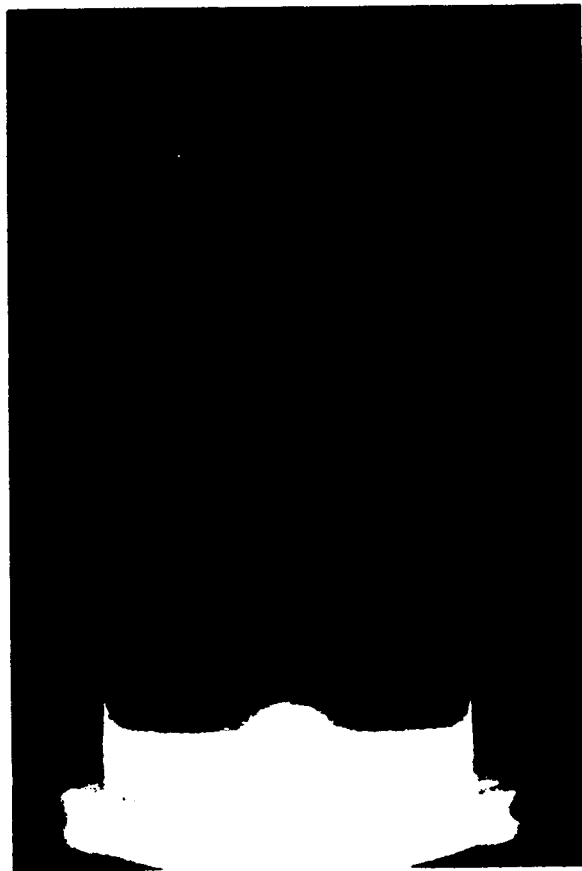


Figure 4.2: Flow patterns 8 seconds after the initiation of spin-up. Laser lit sulfur powder.

ORIGINAL PAGE IS  
OF POOR QUALITY



**Figure 4.3: Flow patterns 5 minutes after the initiation of spin-up. Laser lit sulfur powder.**

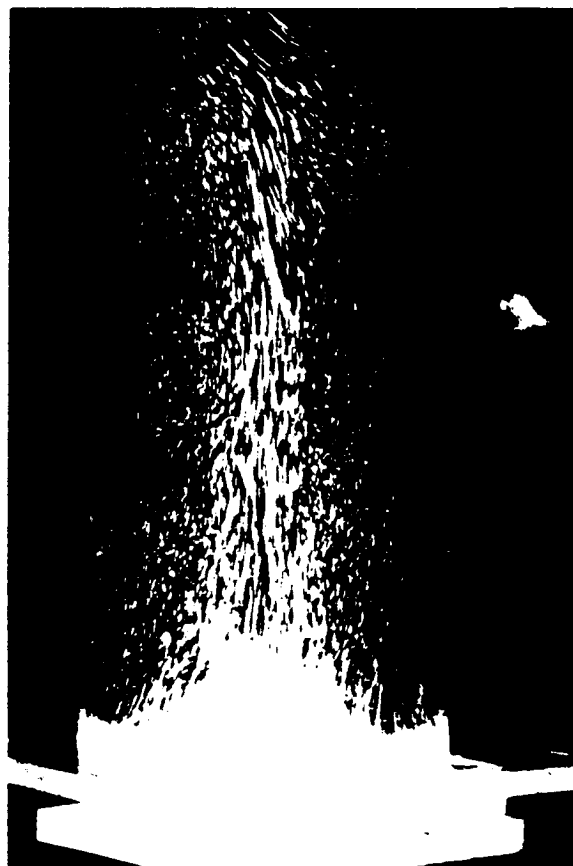
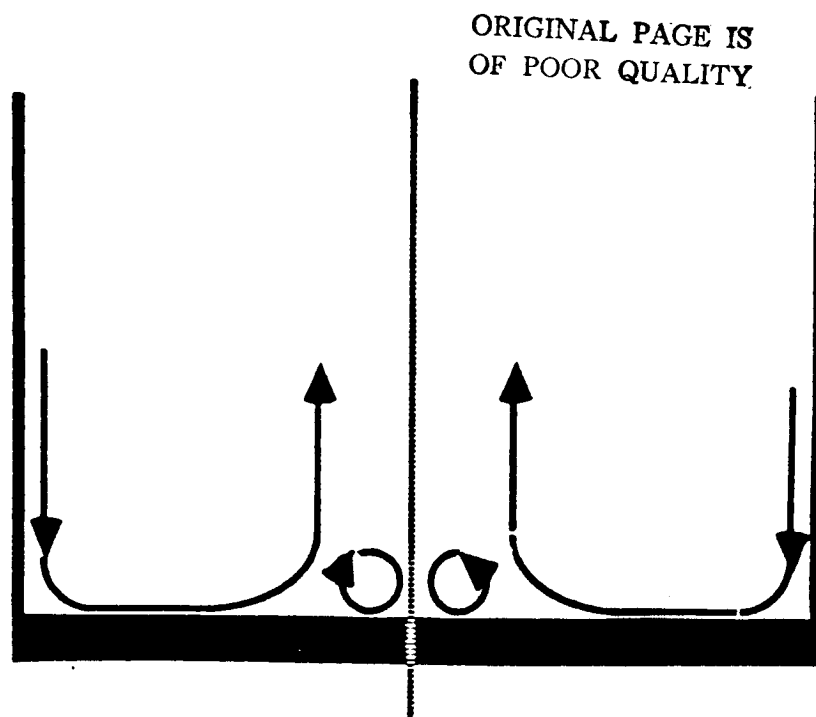


Figure 4.4: Flow patterns in the first four seconds after the initiation of spin-down.  
Laser lit sulfur powder.

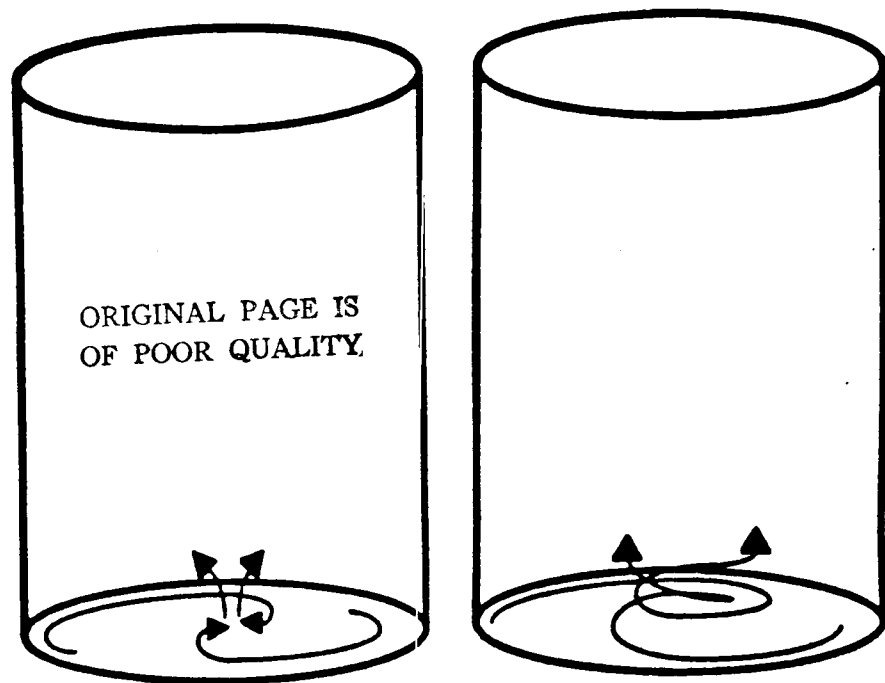


Figure 4.5: Flow patterns 8 seconds after the initiation of spin-down. Laser lit sulfur powder.

ORIGINAL PAGE IS  
OF POOR QUALITY.

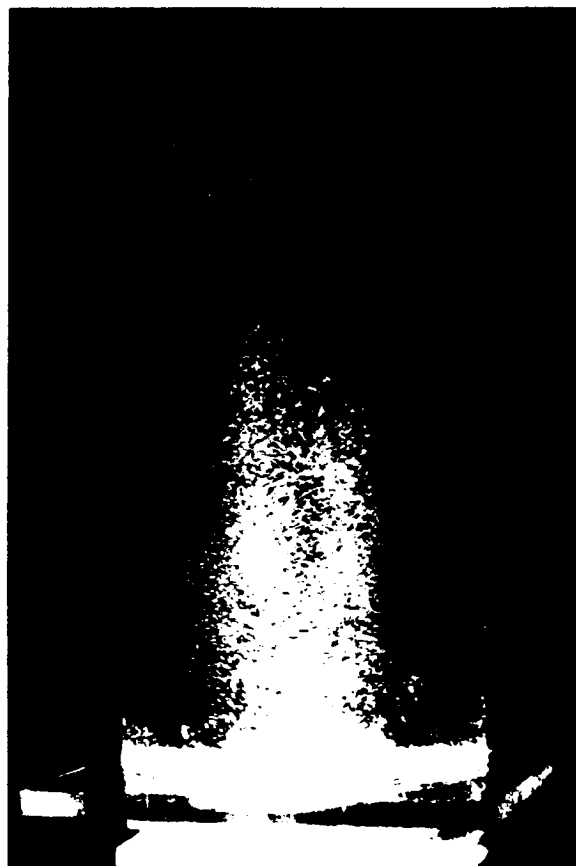
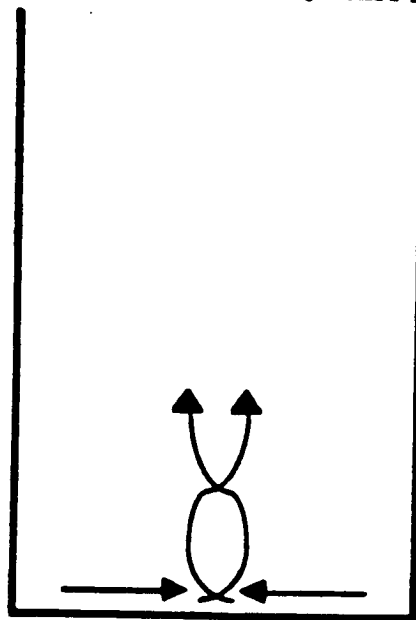


Figure 4.6: Flow patterns 12 seconds after the initiation of spin-down. Laser lit sulfur powder.

ORIGINAL PAGE IS  
OF POOR QUALITY

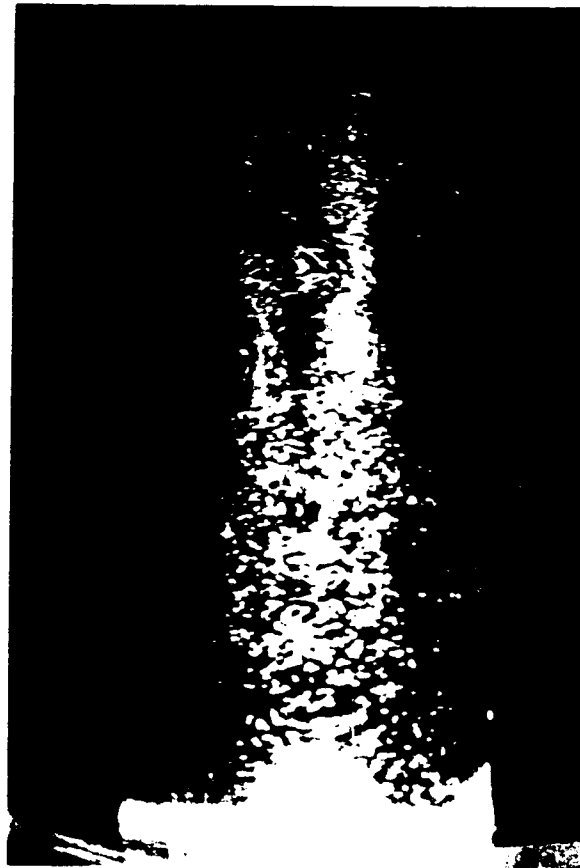
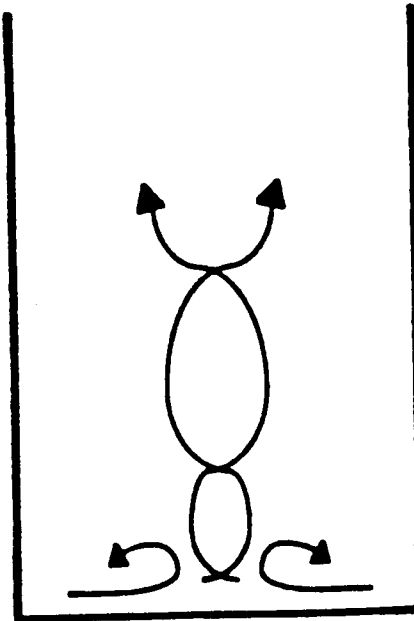


Figure 4.7: Flow patterns 16 seconds after the initiation of spin-down. Laser lit sulfur powder.



ORIGINAL PAGE IS  
OF POOR QUALITY

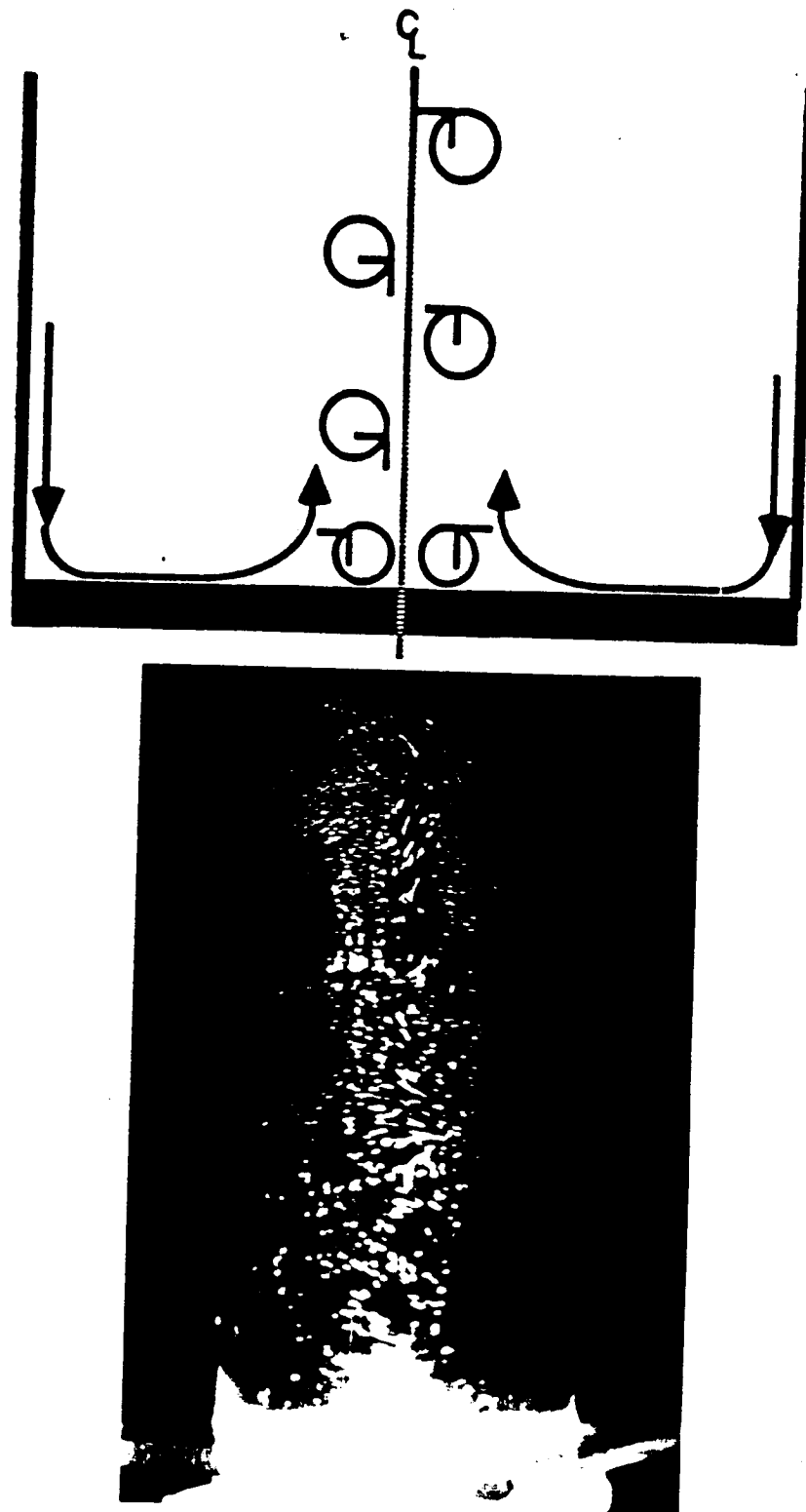


Figure 4.8: Flow patterns 20 seconds after the initiation of spin-down. Laser lit sulfur powder.

because the particles in this region remained in the light slit. Spin-up was a subtle process which require streak photographs to see any fluid motion. Spin-down, however, was more dramatic and simple snapshots revealed much of what occurred.

An incandescent light slit was used to take snapshots of spin-down. A 400 ASA film and  $\frac{1}{64}$  second exposure were used. The container was filled to an aspect ratio of seven with lycopodium powder in tap water at  $22^{\circ}\text{C}$ . The cylinder was rotated for 10 minutes at 65 RPM to ensure rigid body rotation. Then the rotation was stopped and a series of snapshots was taken at intervals of approximately 2 seconds.

In figure 4.9, taken immediately after the start of spin-down, small pronounced vortex rings surround the periphery of the cylinder. Since lycopodium particles are smaller (30 micrometers in diameter) than the sulfur particles, small eddies can affect their motion and reveal flows on a smaller size scale than with sulfur particles. These rings rotated about the central axis and quickly dissipated. Then inward Ekman pumping caused the powder to rise in the center, spreading outward like a tornado, increasing in height and width (figure 4.10). This vortex could not sustain itself and began to break down (figure 4.11). It continued to break down and rise higher into the cylinder (figures 4.12 and 4.13). Then, the flow broke down into the non-axisymmetric modes shown in the sulfur powder experiment.

ORIGINAL PAGE IS  
OF POOR QUALITY

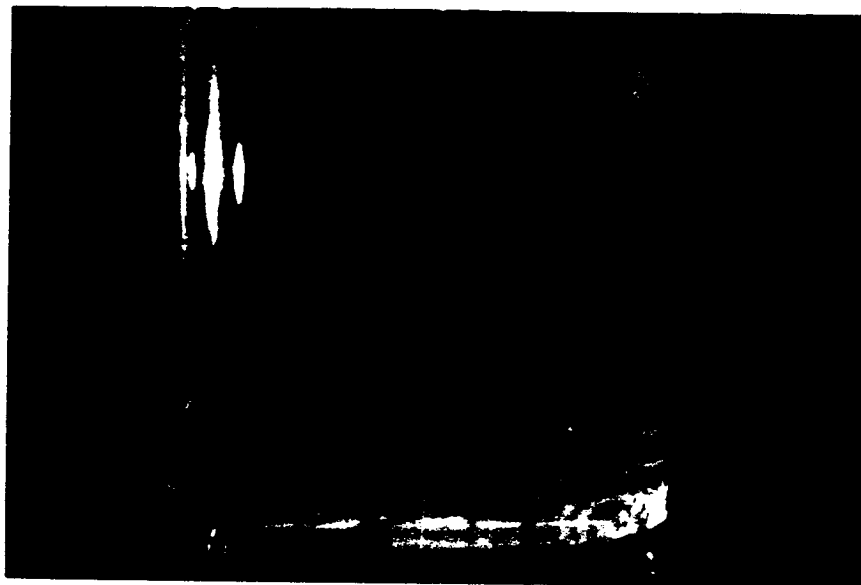


Figure 4.9: Flow patterns at the start of spin-down. Lycopodium powder incandescently lit.

ORIGINAL PAGE IS  
OF POOR QUALITY.

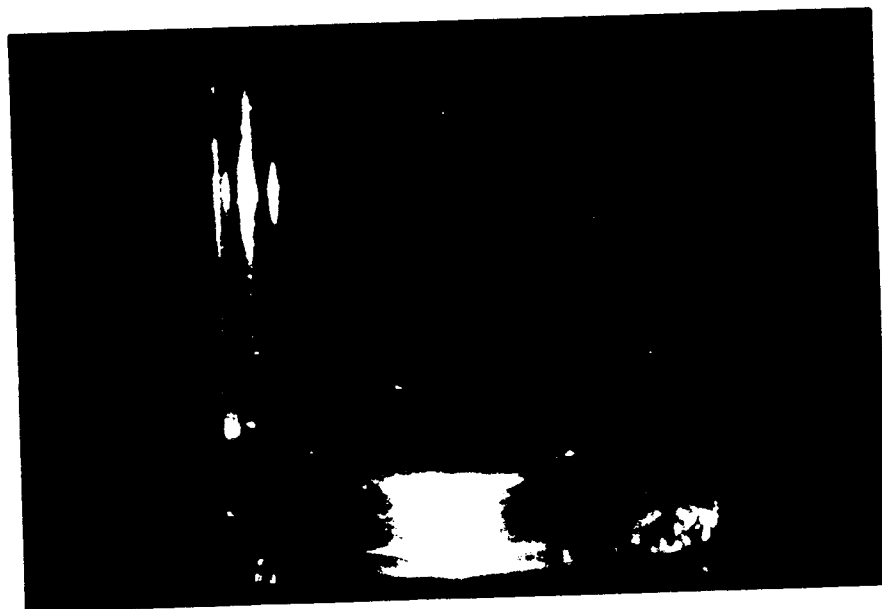
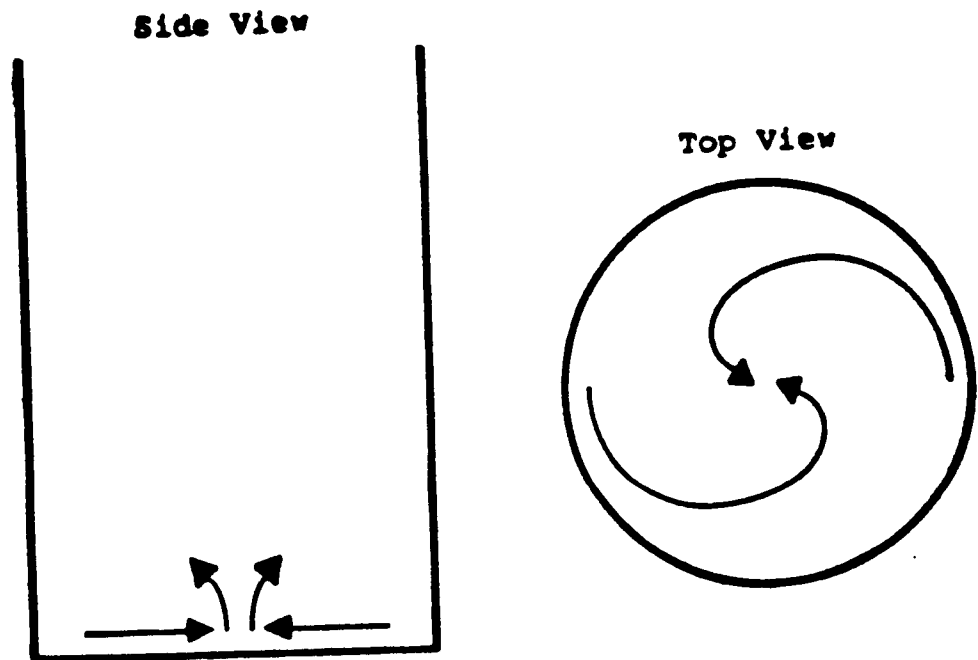


Figure 4.10: Flow patterns 2 seconds after the initiation of spin-down. Lycopodium powder incandescently lit.

ORIGINAL PAGE IS  
OF POOR QUALITY

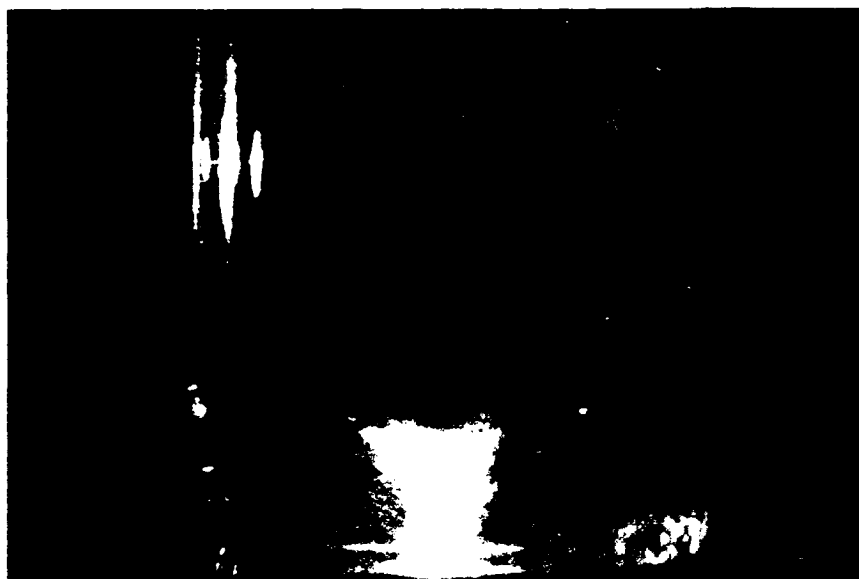


Figure 4.11: Flow patterns 4 seconds after the initiation of spin-down. Lycopodium powder incandescently lit.

ORIGINAL PAGE IS  
OF POOR QUALITY



Figure 4.12: Flow patterns 6 seconds after the initiation of spin-down. Lycopodium powder incandescently lit.

ORIGINAL PAGE IS  
OF POOR QUALITY



Figure 4.13: Flow patterns 8 seconds after the initiation of spin-down. Lycopodium powder incandescently lit.

## 4.2 Electrochemical Results

### 4.2.1 Conventions Used in Reporting the Results

The mass transfer data are reported as the local Sherwood number. The definition of the Sherwood number is:

$$Sh = \frac{K_m L}{D} \quad (4.38)$$

where  $Sh$  is the Sherwood number,  $K_m$  is the mass transfer coefficient,  $L$  is a characteristic length and  $D$  is the mass diffusivity. Here the characteristic length  $L$  was the radial position of the point electrode, measured from the central axis. The only exception to this convention is the Sherwood number at the center of the cylinder, where the characteristic length is taken to be the cylinder radius.

The current measured in the experiment was first converted to a current density by dividing by the area of the electrode. At the limiting current plateau the surface concentration of the reactant is zero. Upon rearrangement equation 2.35 becomes:

$$K_m = \frac{-i}{nFC_{A,b}} \quad (4.39)$$

where  $K_m$  is the mass transfer coefficient,  $i$  is the current density,  $n$  is the number of moles of electrons transferred per mole of reactant, and  $C_{A,b}$  is the bulk concentration of reactant. The Sherwood number is estimated from the current density by combining equations 4.38 and 4.39, giving:

$$Sh = \frac{-iL}{nFD_A BC_{A,b}} \quad (4.40)$$

where  $Sh$  is the Sherwood number,  $L$  is the characteristic length given by the convention mentioned above,  $D_A B$  is the diffusivity of the reactant in the electrolyte,



and the rest of the symbols are given after equation 4.39. The diffusivity was measured using a rotating disk electrode, the details are given later in this chapter.

#### 4.2.2 Long Time Period Spin-Up/Spin-Down

In rotational hydrodynamics, three time scales are important [52]. The first, designated  $t_w$ , is given by  $\frac{2}{\omega}$  [52], where  $\omega$  is the angular velocity. It is the time necessary to establish the Ekman layer at a rotating endwall after an impulsive change in the angular velocity of the endwall. At the lowest rotation rates used here (10 RPM), it is about 1 second. Higher rotation rates provide better interfacial transfer of reactant and  $t_w$  is less. Next is the Ekman time scale, designated  $t_{Ek}$ . It is given in the literature review as equation 2.5. It is on the order of the lifetime of the Ekman layer. Between  $t_w$  and  $t_{Ek}$ , the Ekman layer is at steady state. After  $t_{Ek}$  the pumping in the Ekman layer begins to decay. Last is the viscous time scale, designated  $t_\nu$ . It is given by  $\frac{R^2}{\nu}$ , where  $R$  is the cylinder radius and  $\nu$  is the kinematic viscosity. It is on the order of the time it takes any residual motion in the fluid to die away.

Figure 4.14 compares values of Sherwood number vs. time experimentally measured for three rotation rates at a radial position of 0.76 cm. The figure reveals that the two highest rotation rates produced two peaks in the Sherwood number while the lowest rotation rate produced only one peak. It must be determined what mechanisms caused these peaks and why a change in rotation rate caused a transition from single to double peaks.

The 10 RPM data are the easiest to analyze. The data shown in figure 4.15 follow a pattern one expects from the theories for spin-up from rest in short cylinders [5,6,7,8,52,53]. After 10 seconds the Sherwood number remained constant in time, although the data end at 10.4 seconds. In the early stages of spin-up the Sherwood

number increases rapidly. At these times the available theories suggest that the suction into and the radial pumping outward in the Ekman layer are strong. These theories state that the Ekman layer decays for times larger than  $t_{Ek}$ , and the data show Sherwood number falling off to a steady value at this time. Figure 4.16 illustrates this point. The data from figure 4.15 are replotted on log-log coordinates in figure 4.16, but with the time scaled by the Ekman time. This shows that all of the enhancement in the interfacial mass transfer occurs during the same time period the theories for short cylinders say there is bulk mixing in the cylinder [5,6,7,8,52,53]. Brice et al. [10] used the Ekman time scale to predict an optimum time for mixing in continuous spin-up/spin-down for all types of rotation, that is for any Rossby and Ekman number combination. Their prediction will be shown to be incorrect.

Since the 10 RPM data discussed in the last paragraph do not include the Sherwood number at the center electrode, a 12 RPM experiment will be used to discuss the behavior of the Sherwood number at the center electrode. Figures 4.17 and 4.18 give plots of Sherwood number vs. time for 4.64 and 22.9 cm tall cylinders, respectively. The maximum in the Sherwood number at the center always occurred after the Ekman time while the maximum in the edge Sherwood number occurred during the Ekman time (figures 4.19 and 4.20). This was true regardless of the cylinder's aspect ratio (the ratio of cylinder's height to radius).

Consider figures 4.21 and 4.22 for 40 and 65 RPM, respectively. The center electrode values of Sherwood number had a single maximum in time. The 0.71 cm electrode Sherwood number values had one minimum between two maxima. Upon plotting on log-log coordinates with time scaled by the Ekman time, it is seen that the first peak in the edge data occurs in the Ekman time for the 0.71 cm data (figure 4.23 and 4.24). The minimum between the peaks occurs on the order the Ekman

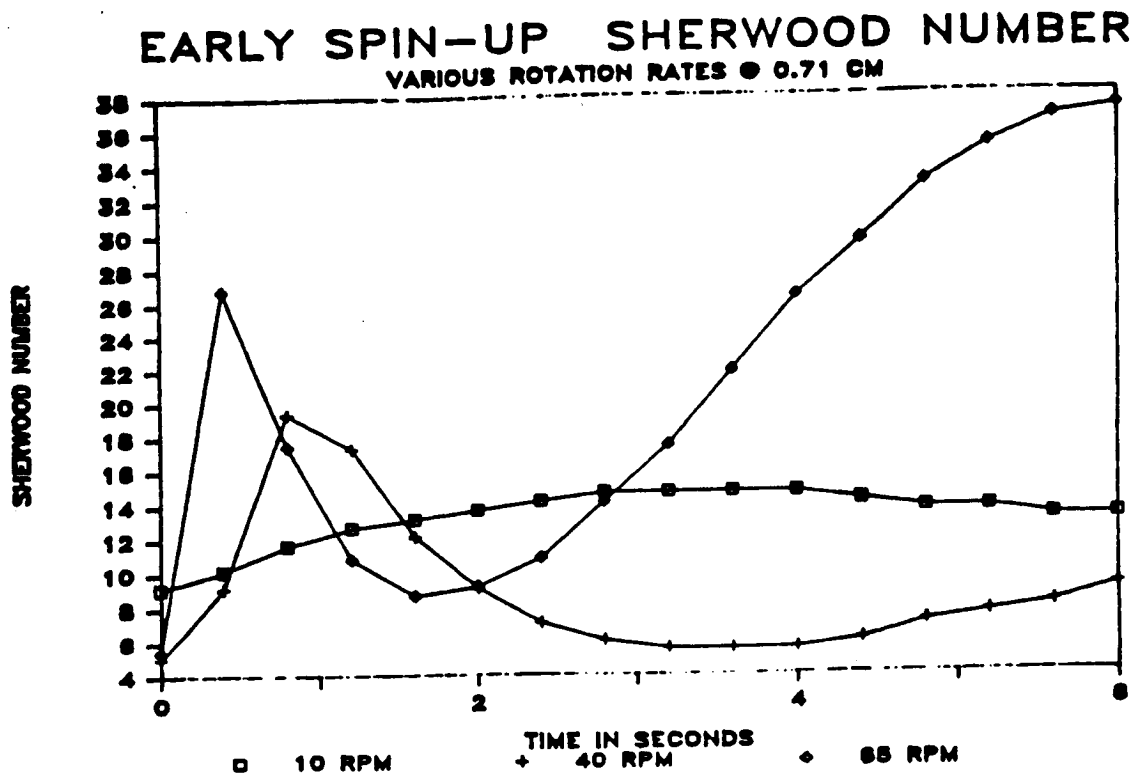


Figure 4.14: The Sherwood number vs. time for 10, 40, and 65 RPM during the early stages of spin-up.

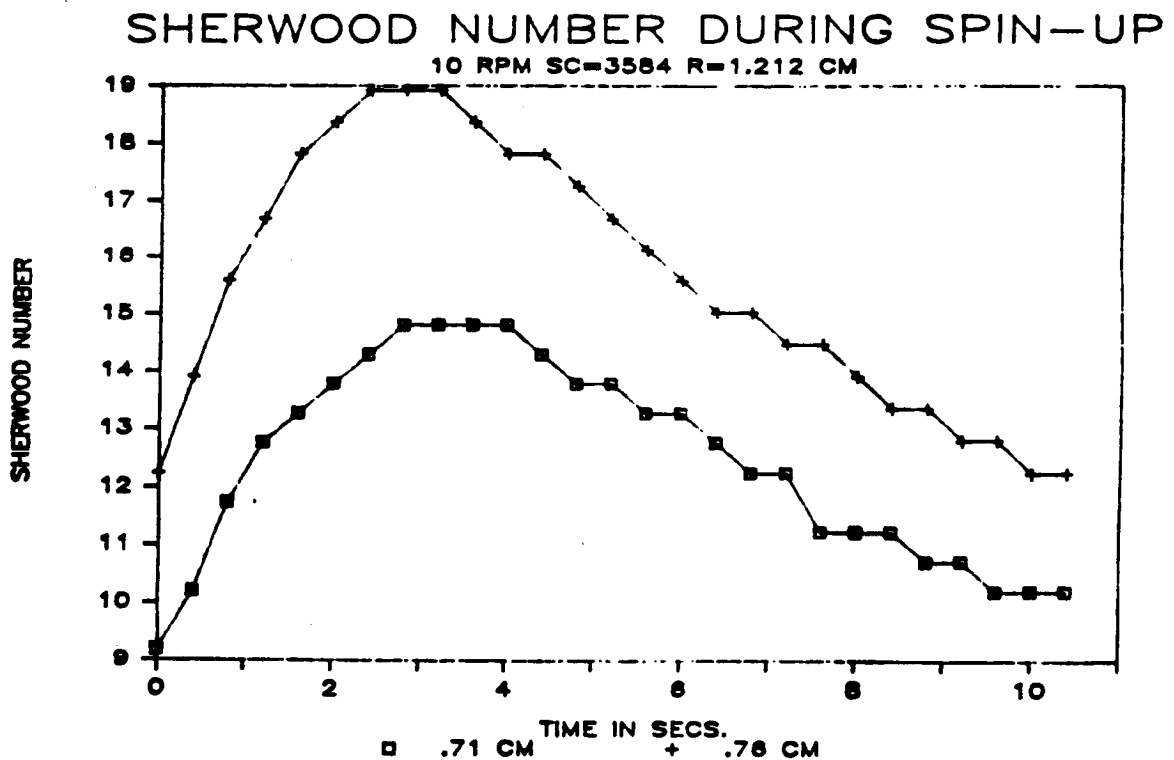


Figure 4.15: Sherwood number vs. time during spin-up at 10 RPM.

ORIGINAL PAGE IS  
OF POOR QUALITY

# SHERWOOD NUMBER DURING SPIN-UP 12 RPM TALL CYLINDER R=1.212 CM

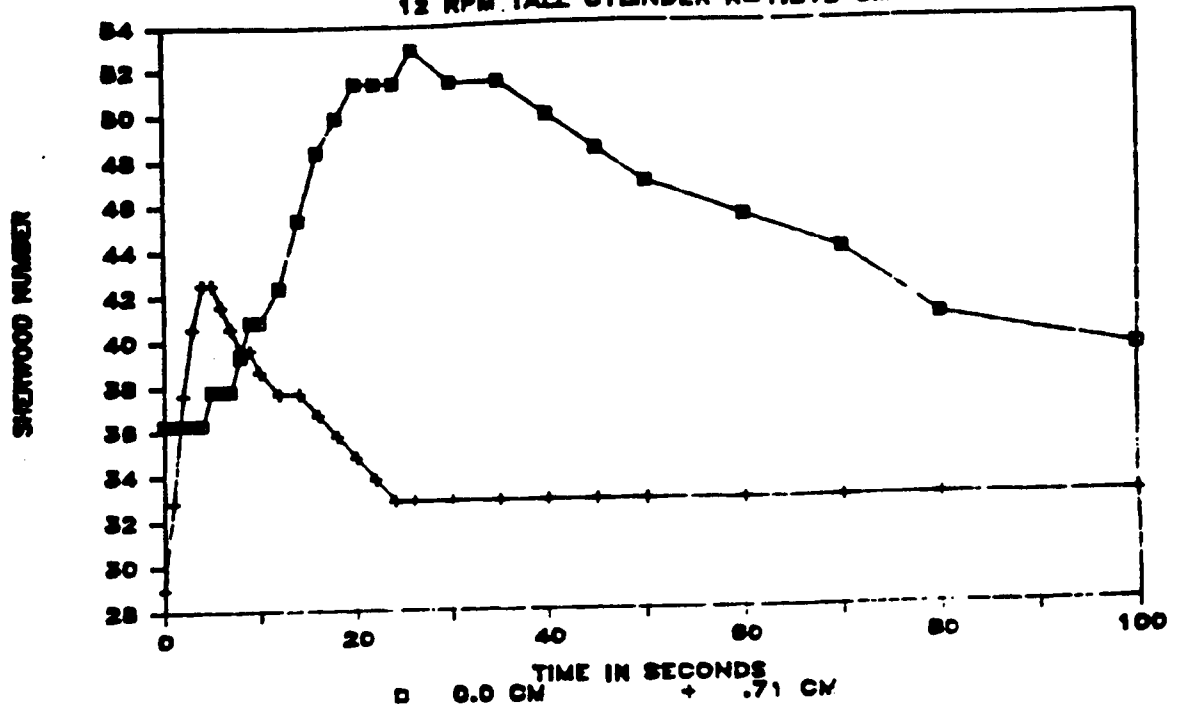


Figure 4.18: The Sherwood number vs. time in spin-up at 12 RPM for a tall aspect ratio cylinder.

# SHERWOOD NUMBER DURING SPIN-UP 12 RPM TALL CYLINDER R=1.212 CM

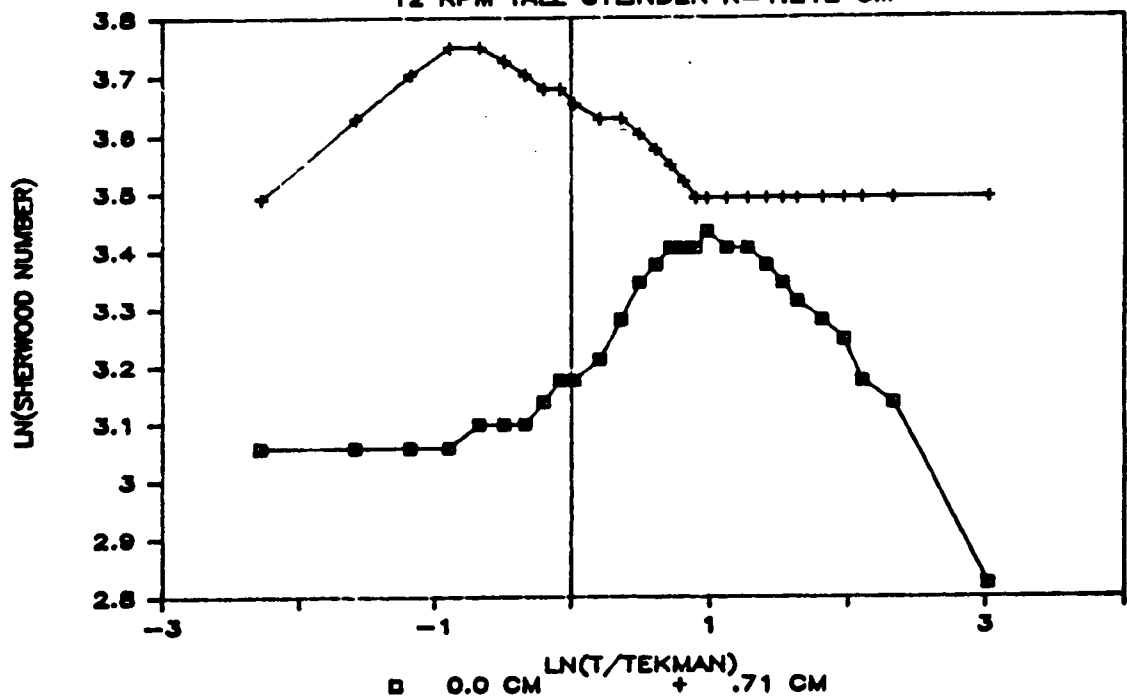


Figure 4.19: The log of the Sherwood number vs. the log of time scaled with the Ekman time during spin-up, 12 RPM.

time. The second peak is higher and broader than the first peak and persists for much longer times than the Ekman time.

The area under a Sherwood number versus time graph divided by the time gives the average Sherwood number. Thus, the area under such a plot qualitatively indicates the amount of interfacial mass transfer. From these arguments, the mechanism producing the second peak provided greater interfacial mass transfer than that produced in Ekman time. The hydrodynamic theories for spin-up in a short cylinder state that after the Ekman time the fluid motion decays rapidly [5,6,7,8,52,53]. This suggests that the second peak is caused by a disturbance not accounted for in the theories [5,6,7,8,52,53].

Figures 4.25 and 4.26 are log-log plots of the Sherwood number vs. time scaled with the viscous time for 40 and 65 RPM, respectively. The diagrams show that the second peaks are caused by a disturbance which damps on the order of the viscous time scale. The exact origin of these disturbances is not known. Speculation centers on three possible mechanisms. First, the large aspect ratio may be a cause. The flow visualization experiments did not reveal any difference in the results for spin-up near the endwall in a tall cylinder compared to that predicted in short cylinders, allowing the aspect ratio to be ruled out. Figures 4.27, 4.28 and 4.29 show early spin-up data for 10, 40 and 65 RPM in three different aspect ratio cylinders. The aspect ratio ranges from 4 to 24. Figures 4.27, 4.28 and 4.29 all show the same qualitative trends. The lowest rotation rate has a single maximum and the larger rotation rates have two maxima.

The second possibility is wobble. The cylinder runs out about 0.08 cm. At large rotation rates, the accelerations produced by the wobble may produce disturbances which damped out on the viscous time scale. Any real Bridgman-Stockbarger

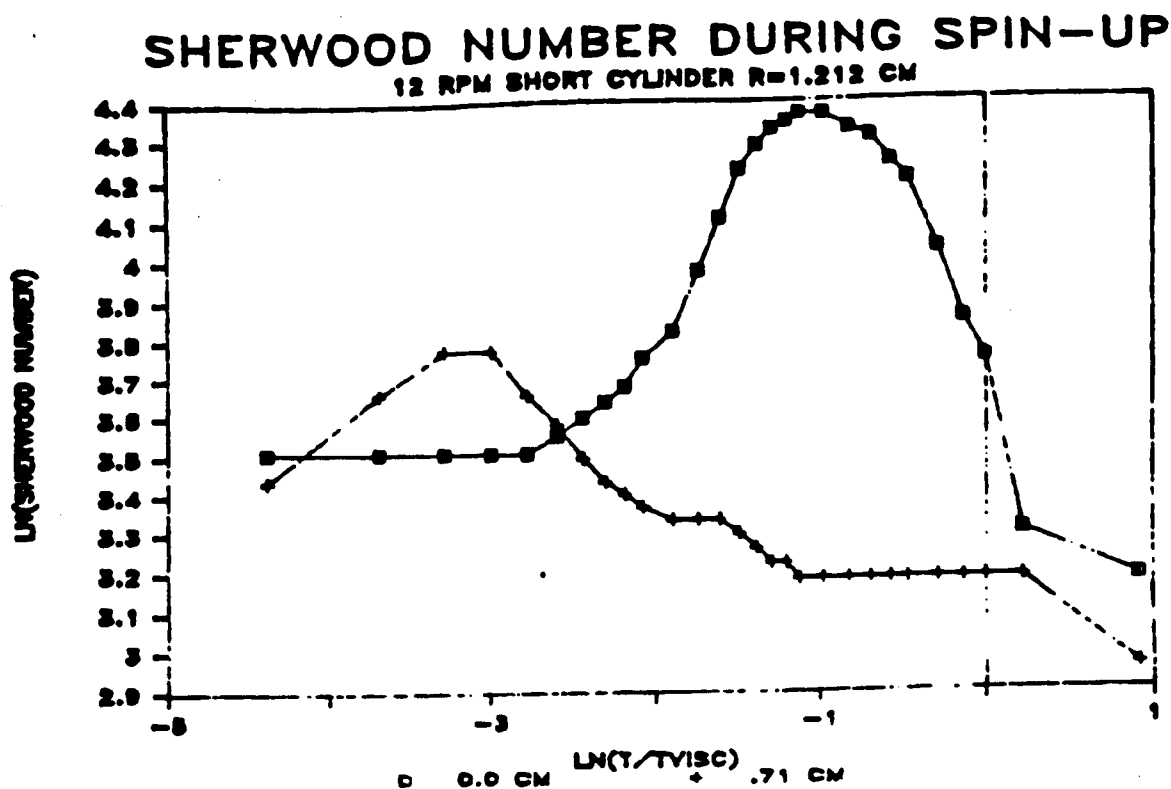


Figure 4.20: The log of the Sherwood number vs. the log of time scaled with the viscous time scale during spin-up, 12 RPM.

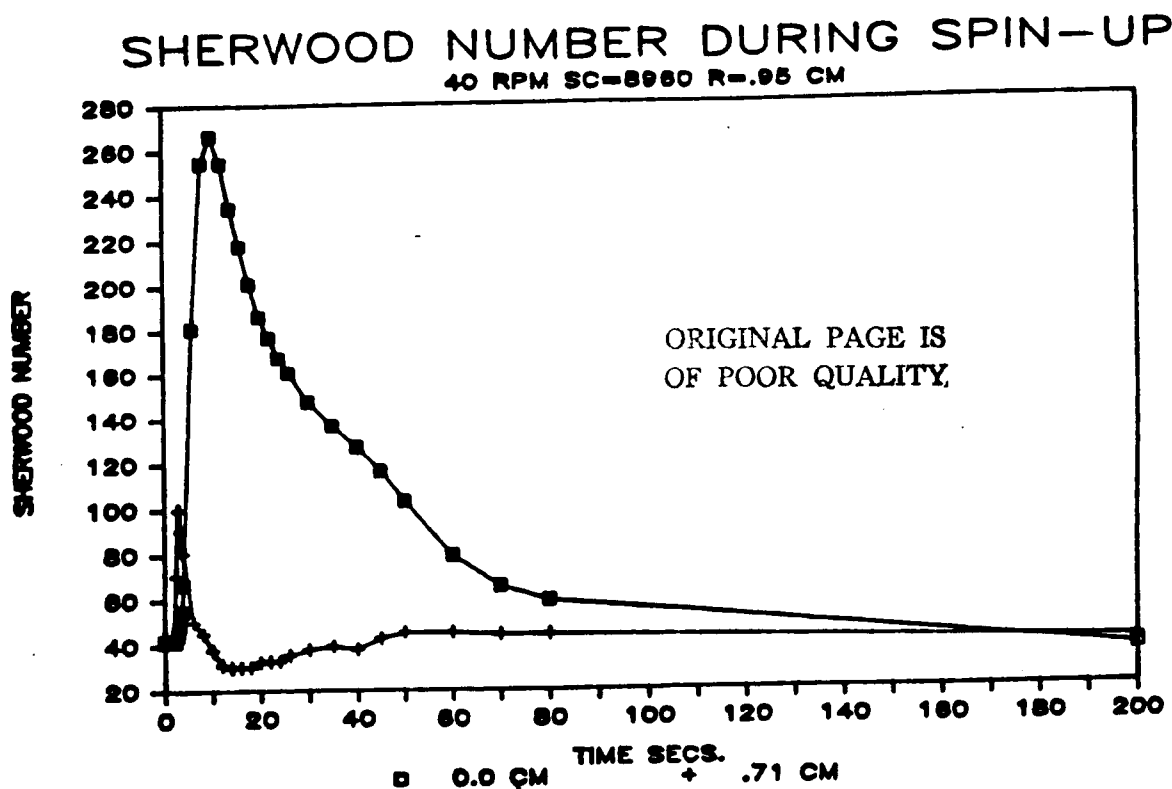


Figure 4.21: The Sherwood number vs. time in spin-up at 40 RPM

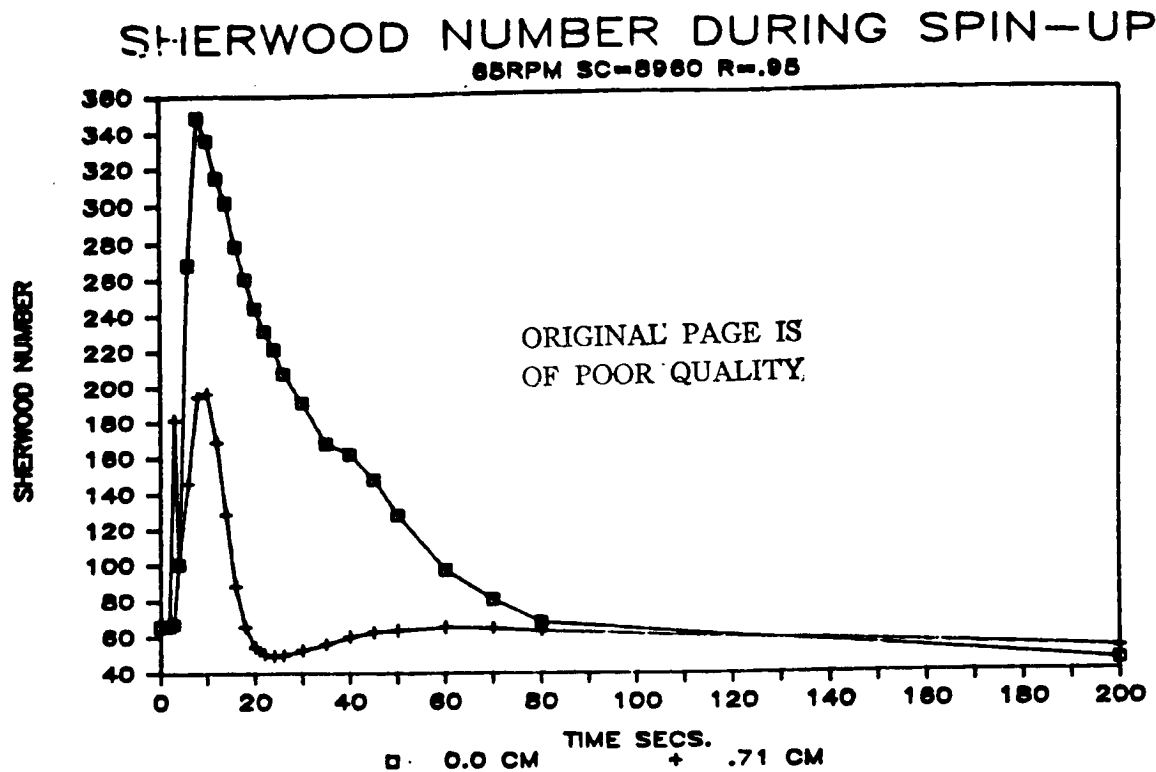


Figure 4.22: The Sherwood number vs. time in spin-up at 65 RPM.

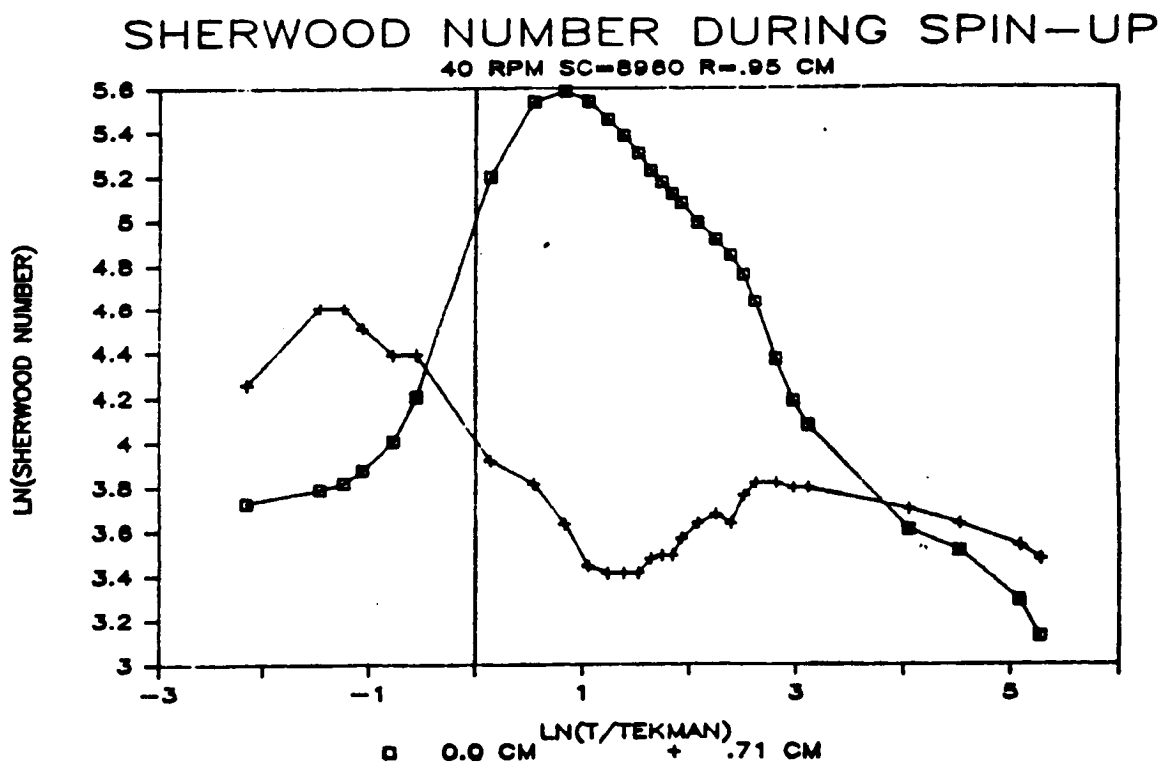


Figure 4.23: The log of the Sherwood number vs. the log of time scaled with the Ekman time during spin-up at 40 RPM.

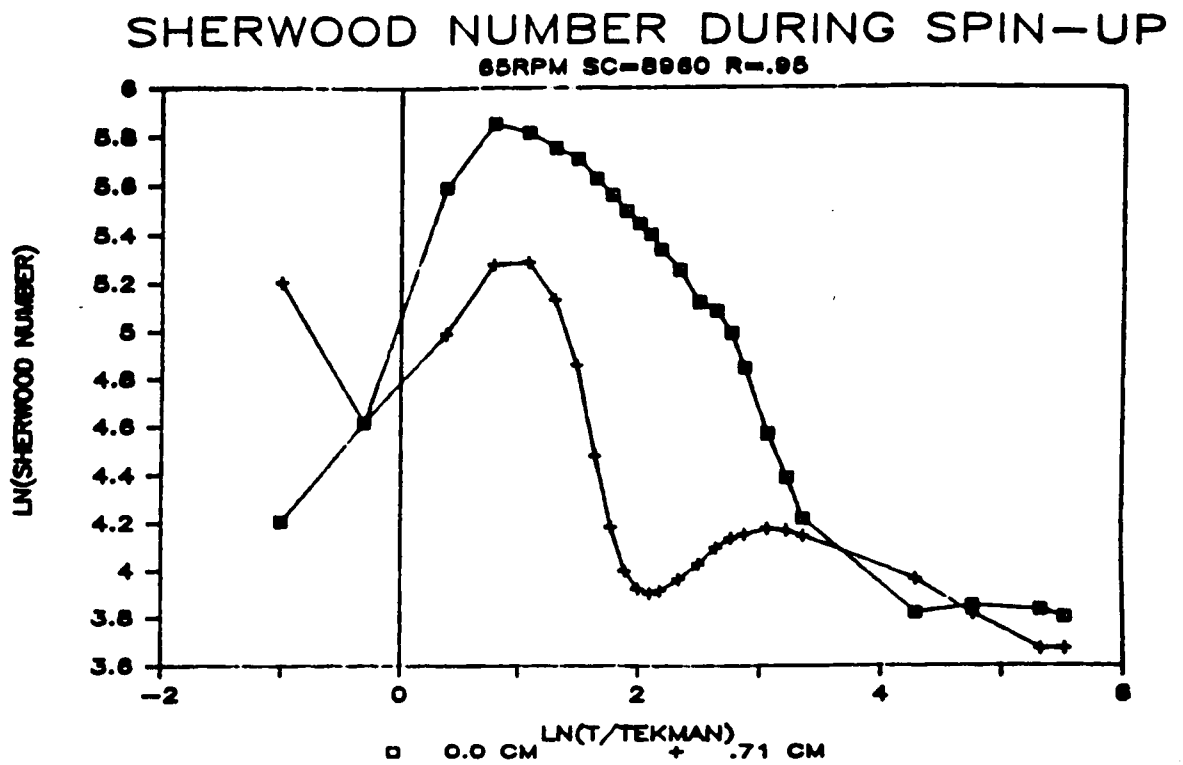


Figure 4.24: The log of the Sherwood number vs. the log of time scaled with the Ekman time during spin-up at 65 RPM.

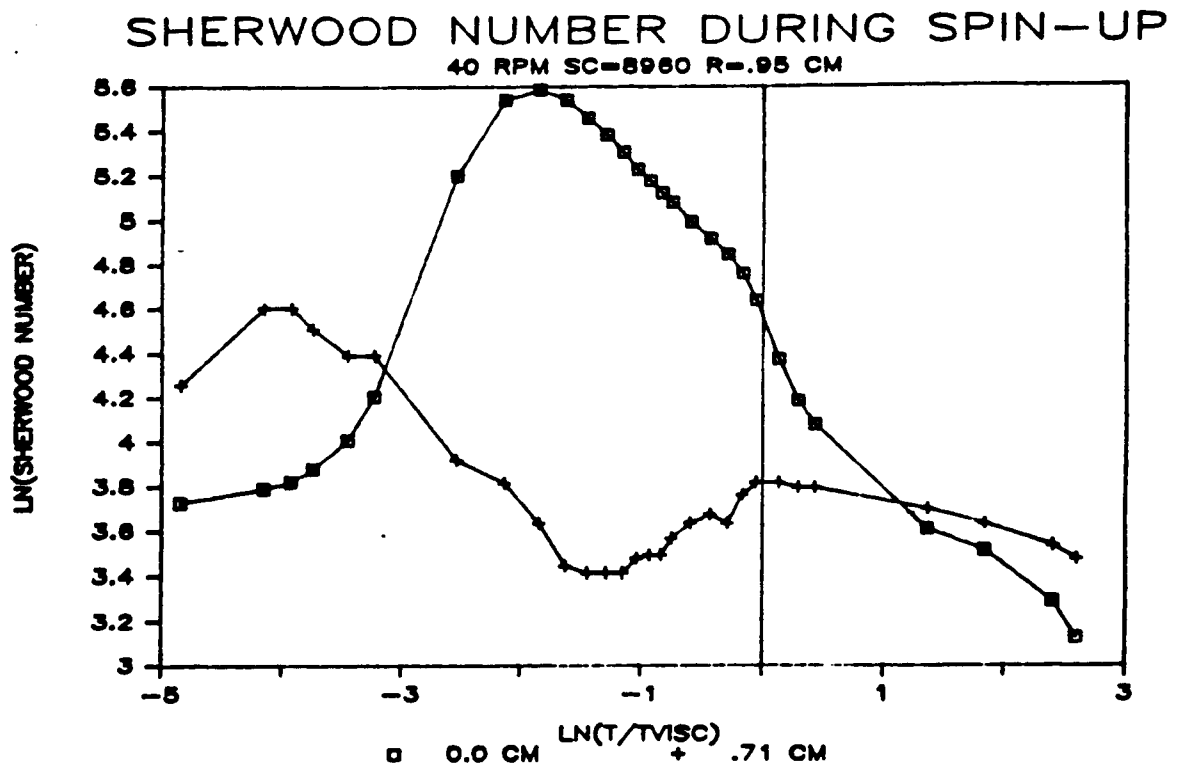


Figure 4.25: The log of the Sherwood number vs. the log of time scaled with the viscous time during spin-up at 40 RPM.



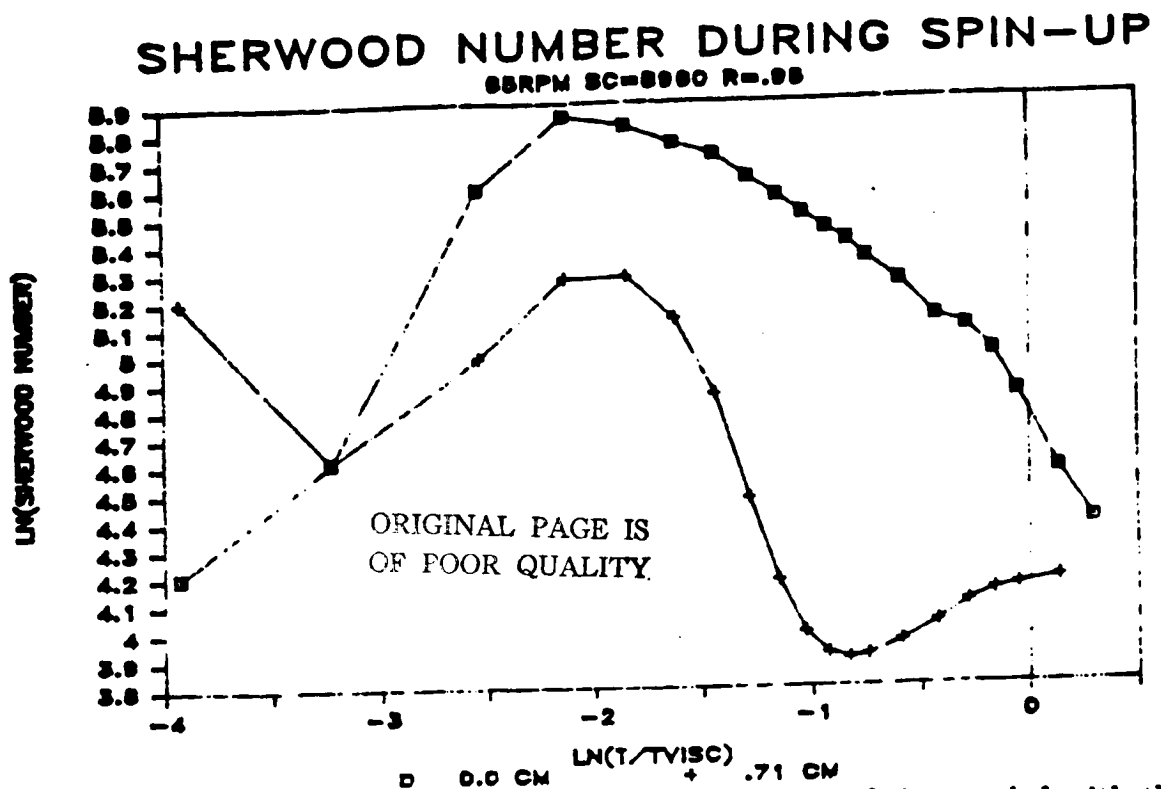


Figure 4.26: The log of the Sherwood number vs. the log of time scaled with the viscous time during spin-up at 65 RPM.

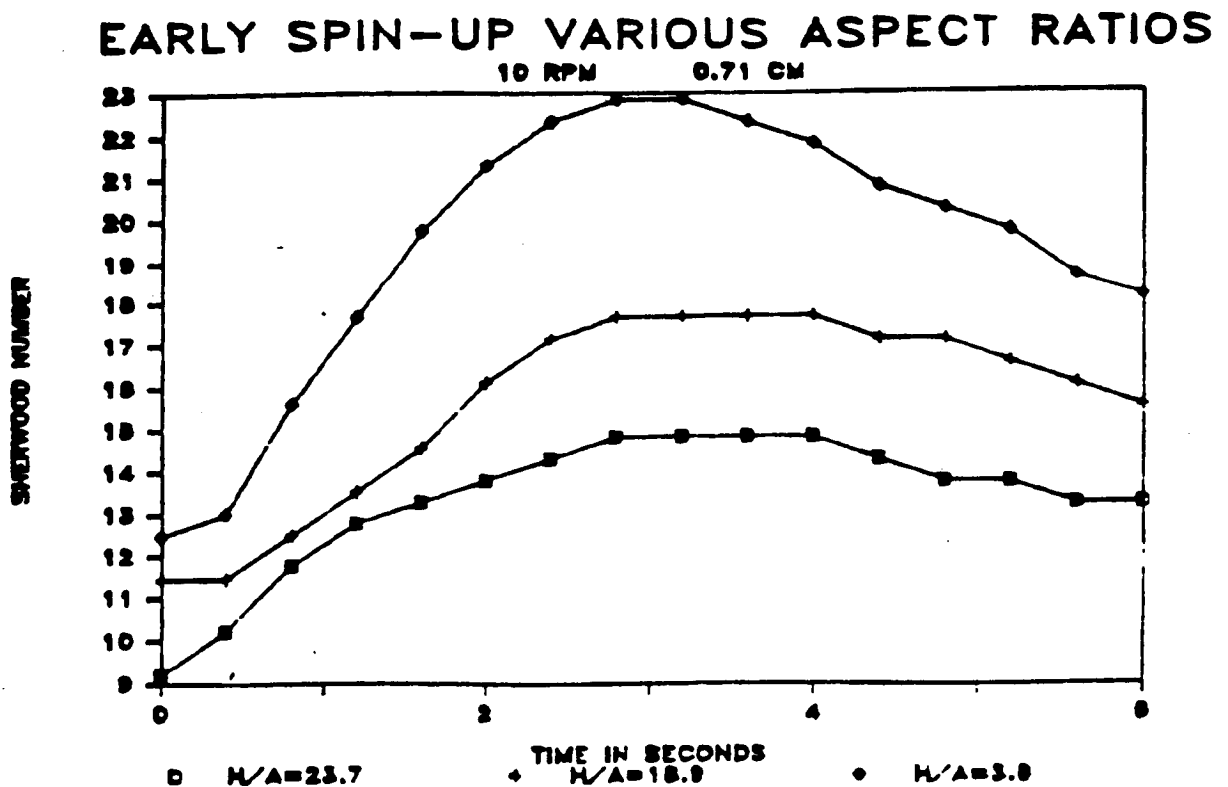


Figure 4.27: The Sherwood number vs. time during spin-up in various aspect ratio cylinders, 10 RPM.

## EARLY SPIN-UP VARIOUS ASPECT RATIOS

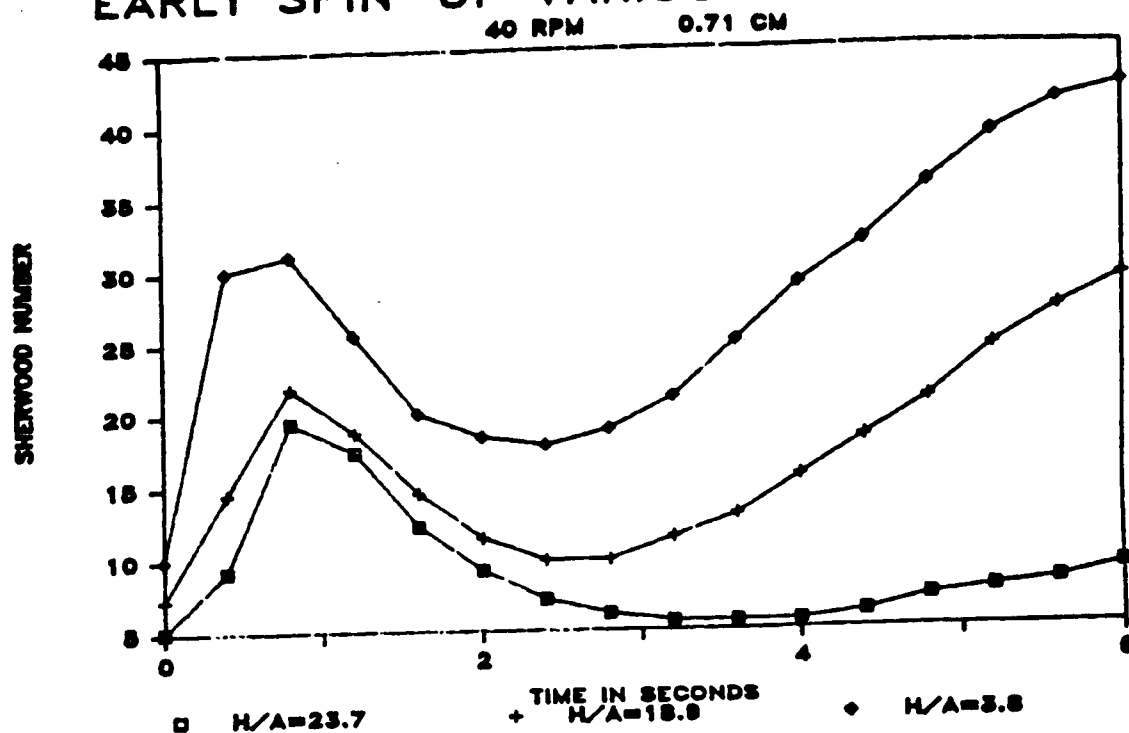


Figure 4.28: The Sherwood number vs. time during spin-up in various aspect ratio cylinders, 40 RPM.

## EARLY SPIN-UP VARIOUS ASPECT RATIOS

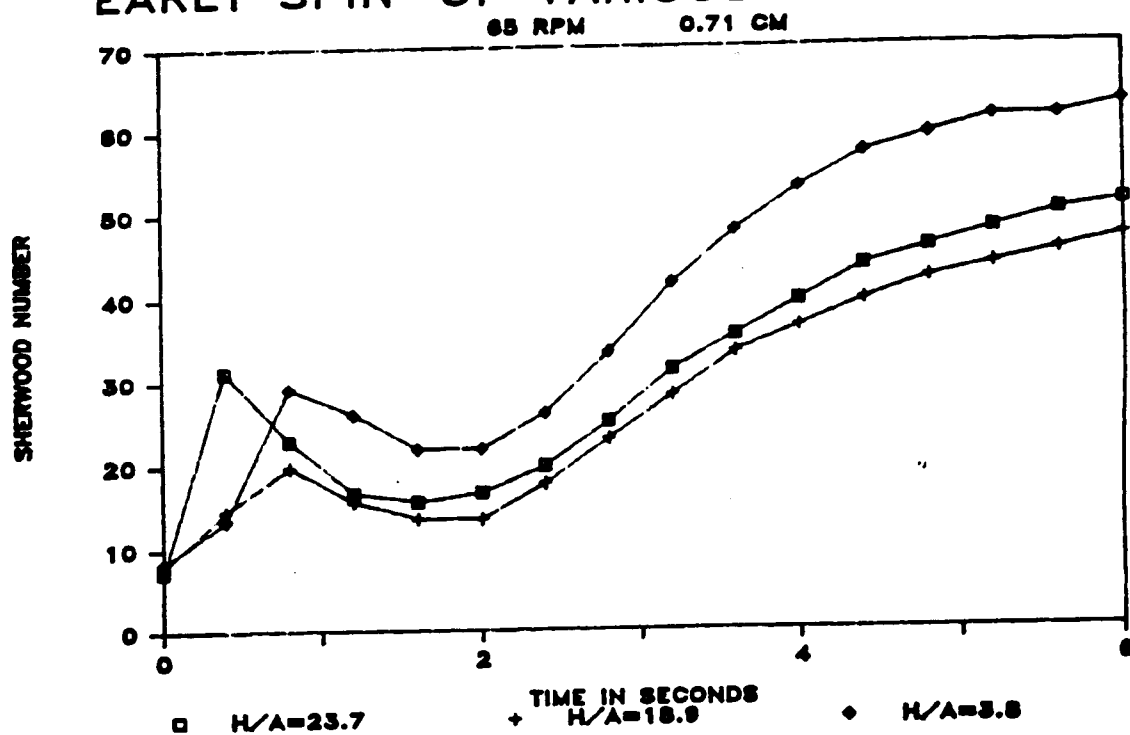


Figure 4.29: The Sherwood number vs. time during spin-up in various aspect ratio cylinders, 65 RPM.

ampoule is not perfectly round, so wobble may be an important mixing mechanism in real crystal growth systems. However, the wobble mechanism can be ruled out by the spin-down results discussed later.

The last explanation concerns the type II disturbance found by Tatro and Mollo-Christensen [64]. Here the flow through the Ekman layer is large enough to become unstable. Type II instabilities propagate out of the Ekman layer into the bulk fluid (i.e. outside the Ekman layer in the cylinder interior). Waves are not continuously generated because the Ekman layer decays, probably on the viscous time scale. This explanation is not without problems. Tatro and Mollo-Christensen [64] experimentally modelled steady Ekman layers which are found in hurricanes. They had a steady rotating cylinder with a steady suction at the central axis. This flow is most closely approximated in spin-down. Brice et al. [10] incorrectly labeled this as spin-up in their review and applied it to the transient fluid mechanics found in spin-up during ACRT. One cannot be certain that this type of instability occurs in transient spin-up from rest. In the experiments reported on here, the Ekman layer was steady only for a small fraction (the Ekman time) while the cylinder was rotating is much longer than the Ekman time. Since the second peak was not seen until after the Ekman time that would mean the type II disturbance occurred as the Ekman layer decayed. If a flow is going unstable, it seems that the instability should occur when the flow is strongest not when it is decaying.

Results for spin-down to rest is shown in figures 4.30 and 4.31 for 40 and 65 RPM, respectively. In both cases, the 0.71 cm electrode data show double peaks. Log-log plots of Sherwood number vs. time scaled with the Ekman time (figures 4.32 and 4.33) and log-log plots of the Sherwood number vs. time scaled with the viscous time (figures 4.34 and 4.35) show that the first peak is caused within the Ekman time scale and the second within the viscous time scale. At 12 RPM, the

data are singularly peaked (figure 4.36), occurring in the Ekman time scale (figure 4.37). If the mechanism causing the second peak is the same in spin-up and spin-down, wobble can be ruled out as the cause. In spin-down to rest, the ampoule is not rotating so there is no wobble.

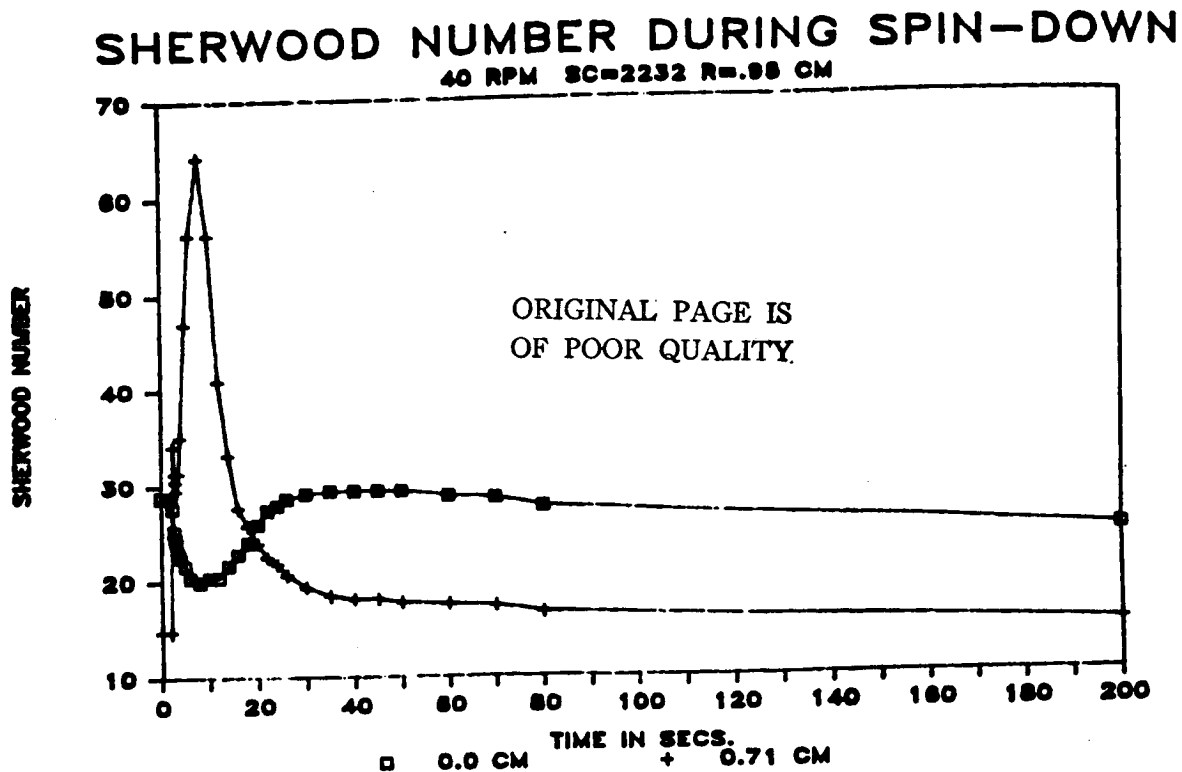


Figure 4.30: The Sherwood number vs. time during spin-down at 40 RPM.

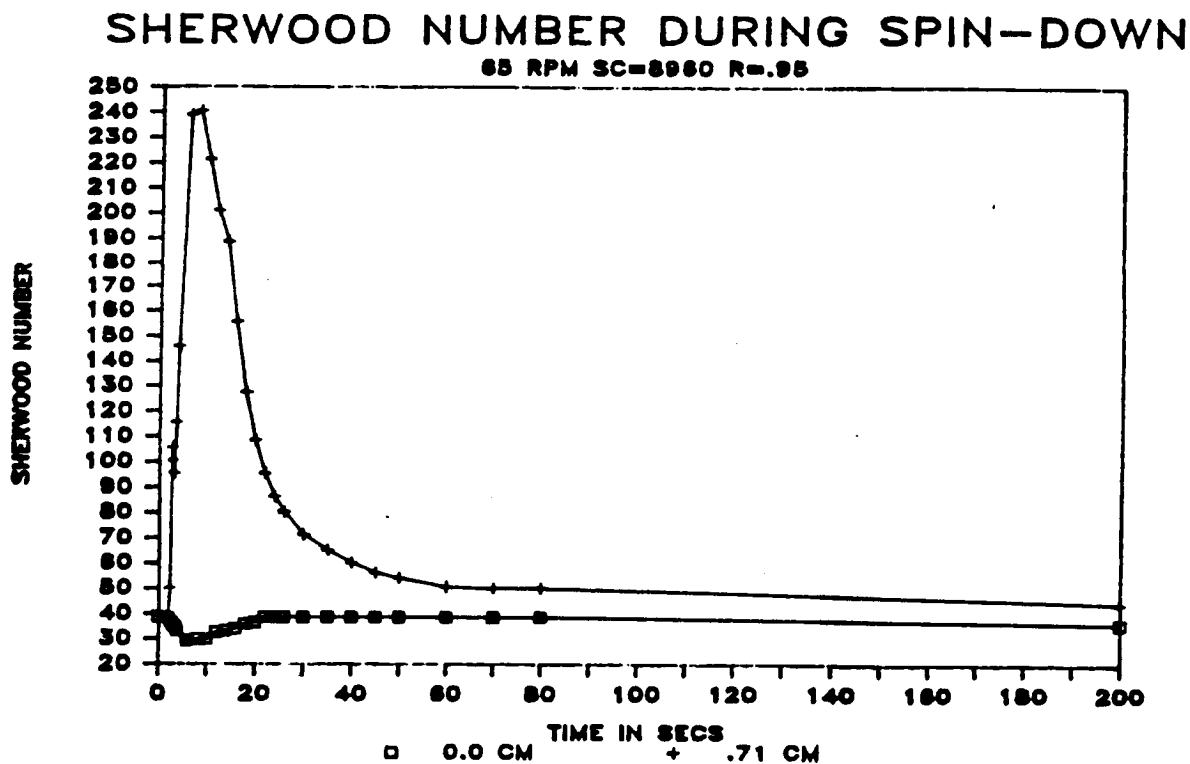


Figure 4.31: The Sherwood number vs. time during spin-down at 65 RPM.

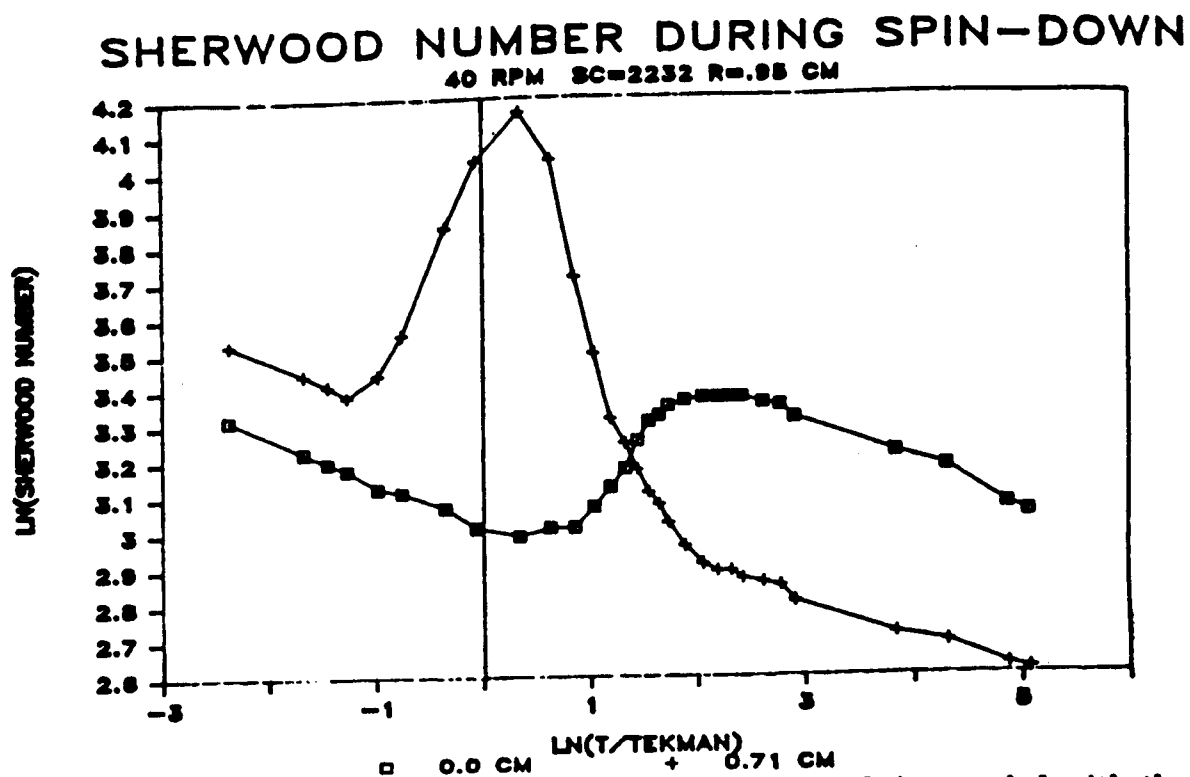


Figure 4.32: The log of the Sherwood number vs. the log of time scaled with the Ekman time during spin-down at 40 RPM.

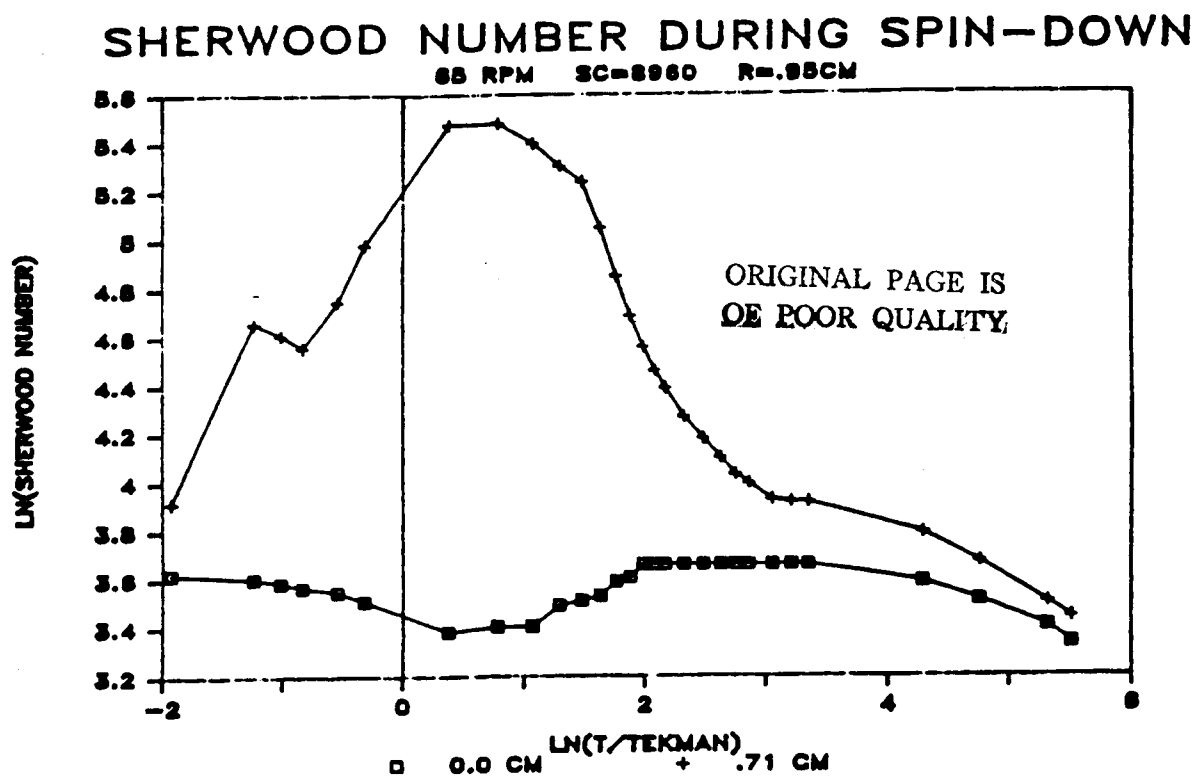


Figure 4.33: The log of the Sherwood number vs. the log of time scaled with the Ekman time during spin-down at 65 RPM.

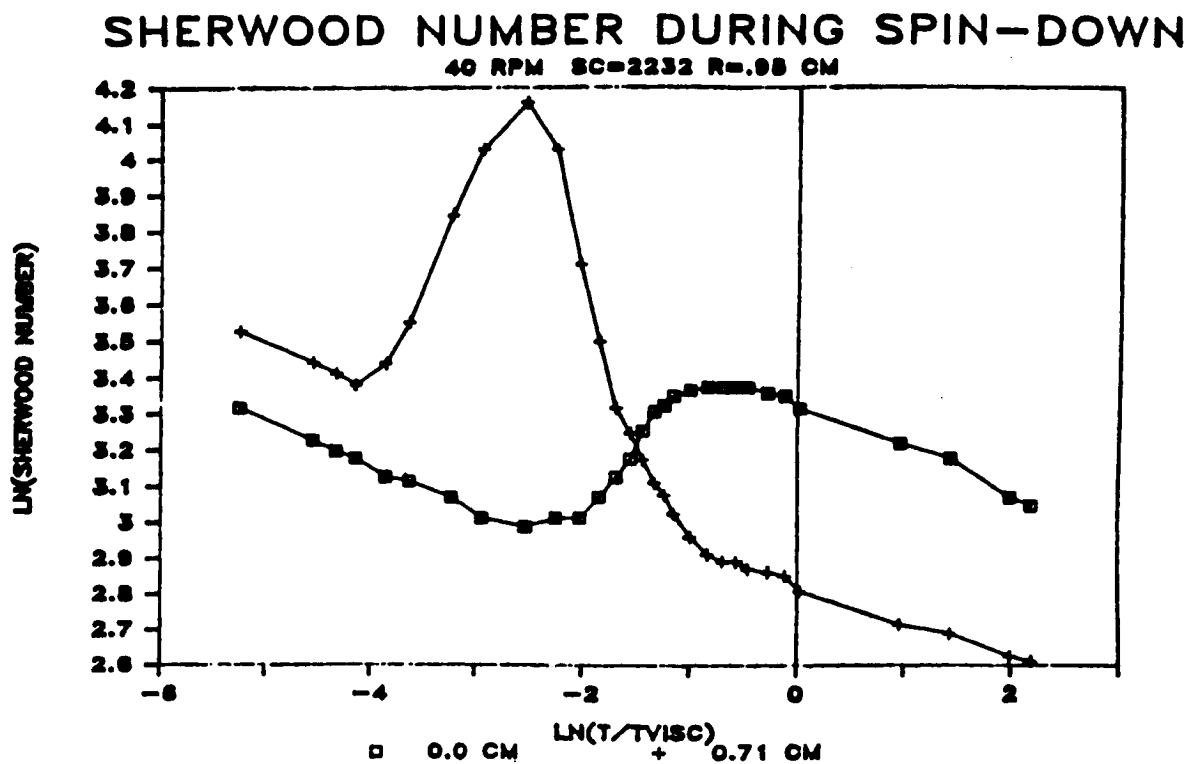


Figure 4.34: The log of the Sherwood number vs. the log of time scaled with the viscous time during spin-down at 40 RPM.

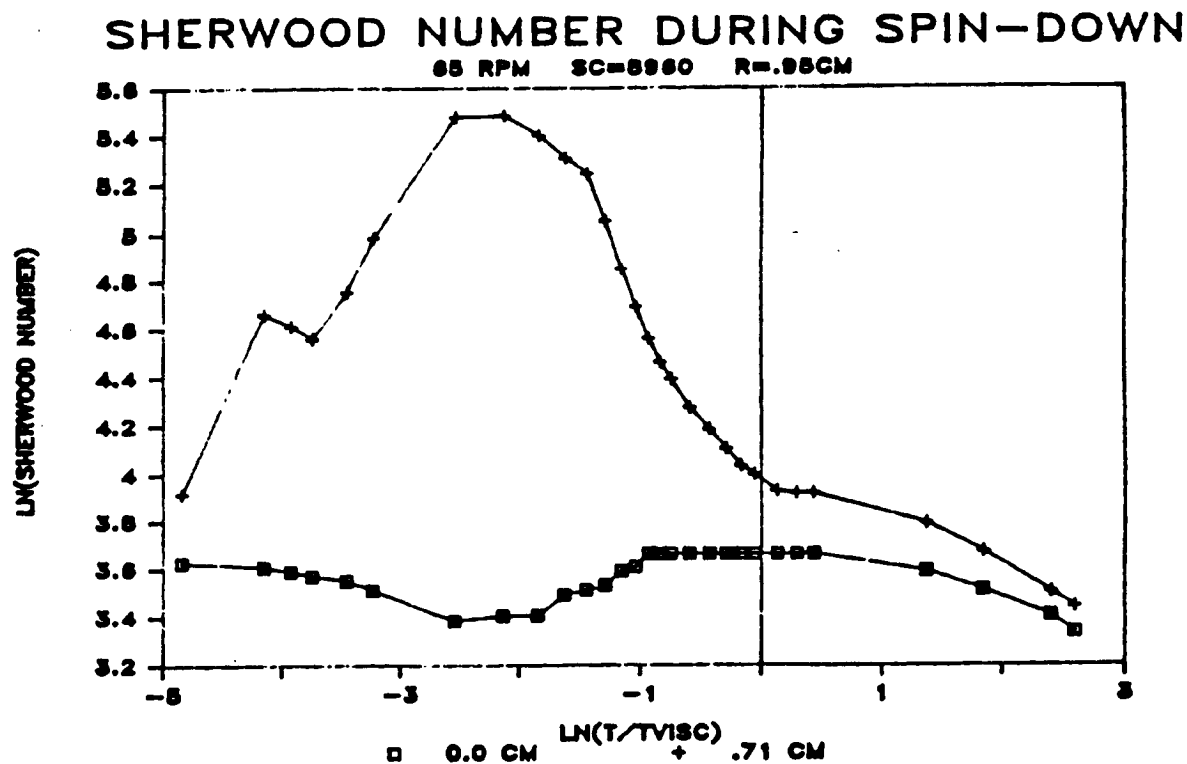


Figure 4.35: The log of the Sherwood number vs. the log of time scaled with the viscous time during spin-down at 65 RPM.

# SHERWOOD NUMBER DURING SPIN-DOWN 12 RPM TALL CYLINDER R=1.212 CM

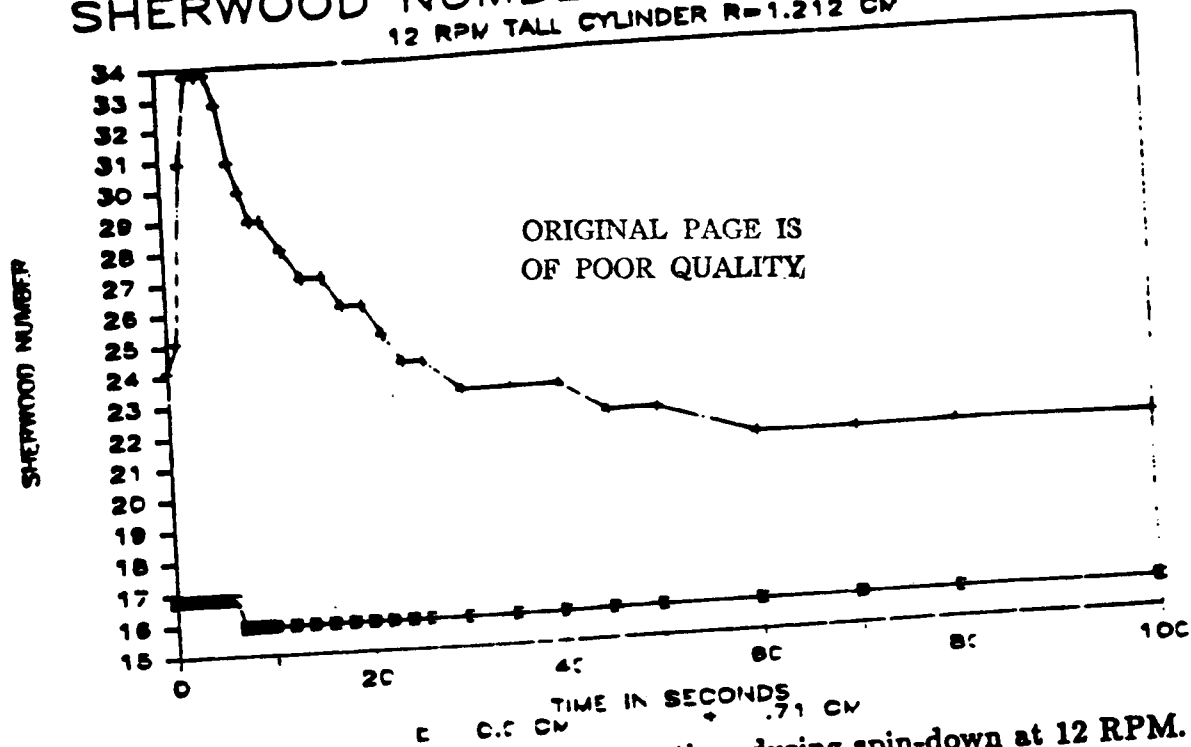


Figure 4.36: The Sherwood number vs. time during spin-down at 12 RPM.

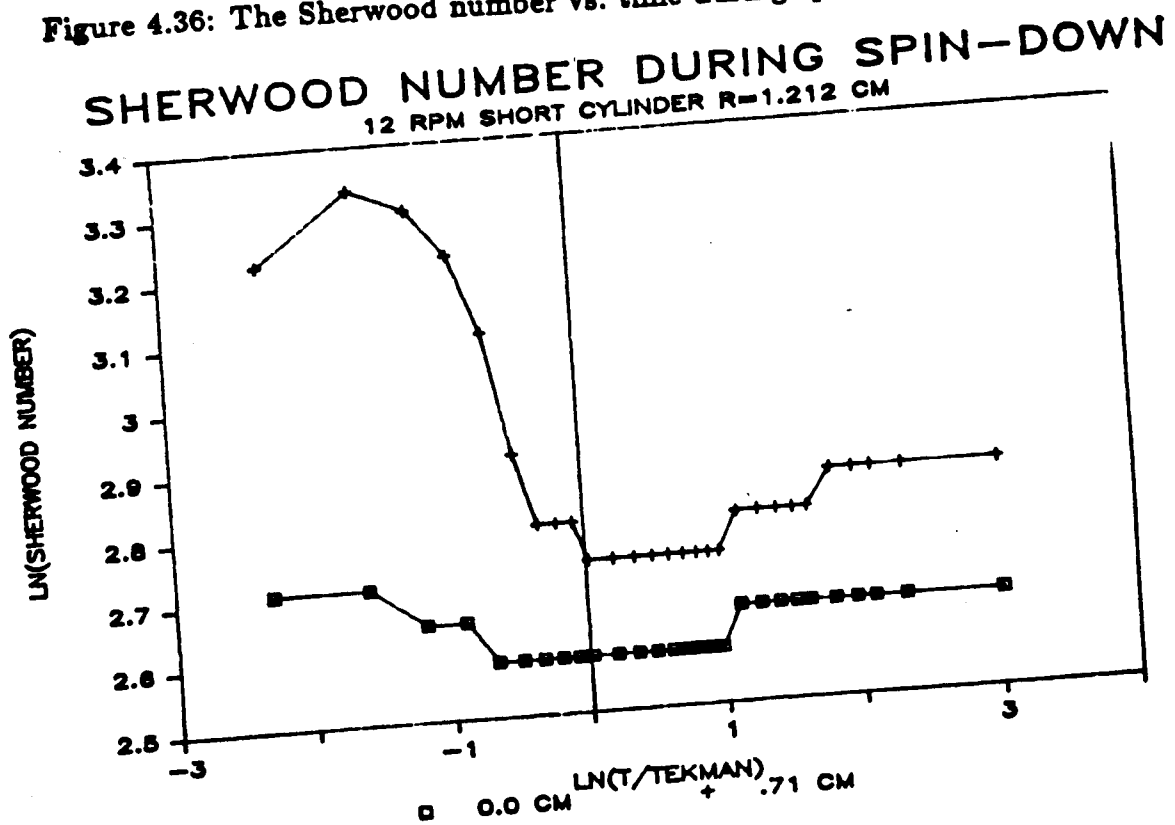


Figure 4.37: The log of the Sherwood number vs. the log of time scaled with the Ekman time during spin-down at 12 RPM.



### 4.2.3 Viscous Time Scale Mass Transfer

The term "viscous time scale mass transfer" refers to the condition where the second peak in the Sherwood number begins to dominate the interfacial mass transfer. The secondary peaks appear regardless of the Schmidt number and appear to be functions only of the Ekman number. The Schmidt number was varied from about 2000 to 9000 by altering the inert electrolyte concentration. Figures 4.38 and 4.39 show the Sherwood number vs. time during spin-up for three rotation rates (18, 16 and 13 RPM) in two 1.212 cm radius cylinders that were 4.64 cm and 22.9 cm tall. The two figures are qualitatively similar, while the results for each rotation rate are different. The 18 RPM curve is doubly peaked. The 16 RPM curve has a sharp peak and a weak knee, where the Sherwood number decreases at a fairly slow rate. The 13 RPM curve is singularly peaked.

Figures 4.40 through 4.45 show the data of figure 4.38 as log-log plots of Sherwood number vs. either time scaled with the Ekman time or time scaled with the viscous time. The first peaks are all caused by Ekman layer pumping (figures 4.40, 4.42 and 4.44). The second peak of the 18 RPM data comes from a viscous effect (figure 4.45). The knee of the 16 RPM data is probably the disturbance not accounted for in the theories of spin-up [5,6,7,8,52,53] (figure 4.44). It lasts four times longer than the Ekman time, but the disturbance generating the knee was not strong enough to produce the large peak found in the 18 RPM data. At 13 RPM, only the secondary flows caused within the Ekman time produce interfacial mass transfer (figures 4.40 and 4.43).

Figures 4.46 through 4.52 give the "viscous time scale mass transfer" analysis during spin-down. As in the spin-up investigations, the rotation rates were 13, 16 and 18 RPM. The first peak occurred on the Ekman time scale (figures 4.47, 4.48

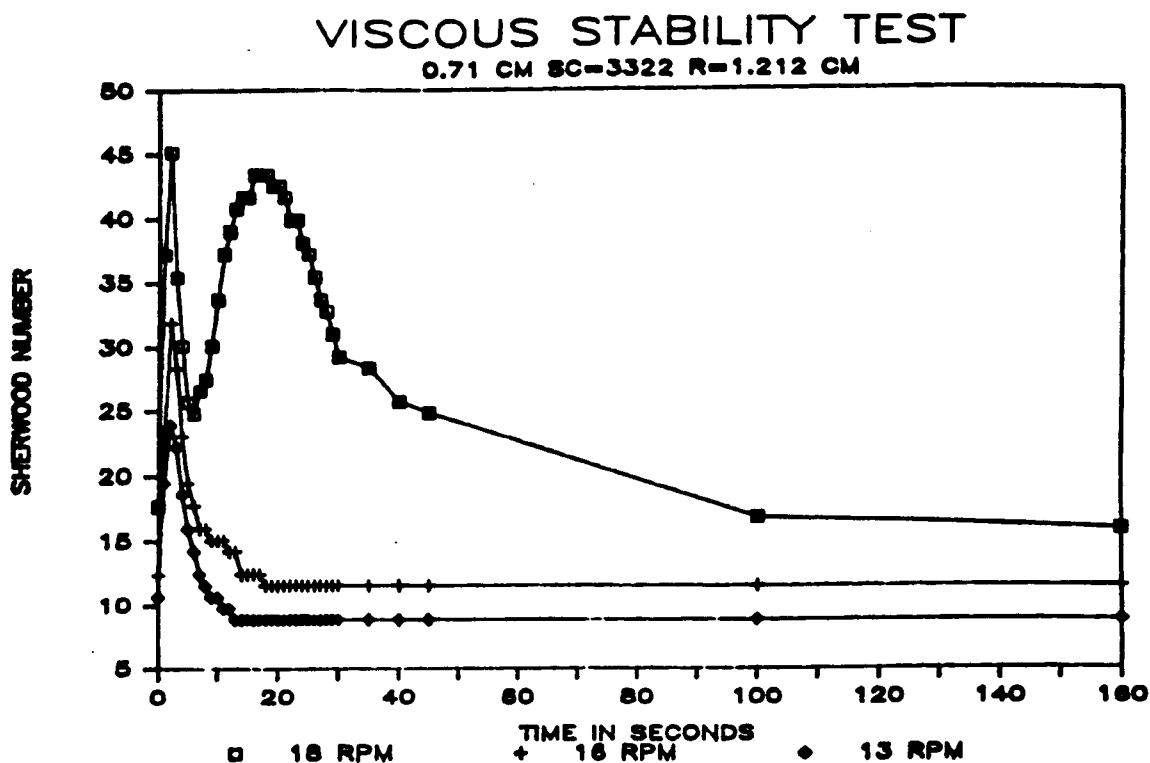


Figure 4.38: Sherwood number vs. time for spin-up in short cylinders for 13, 16, 18 RPM.

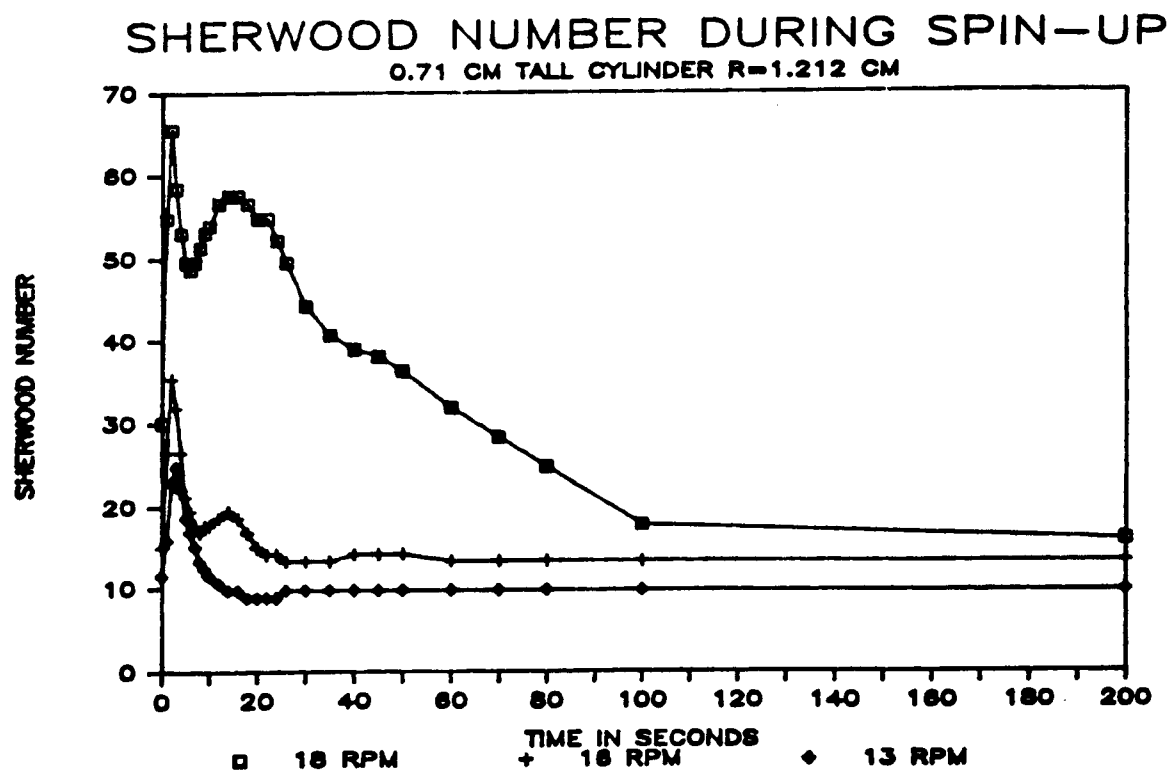


Figure 4.39: Sherwood number vs. time for spin-up in tall cylinders for 13, 16, 18 RPM.

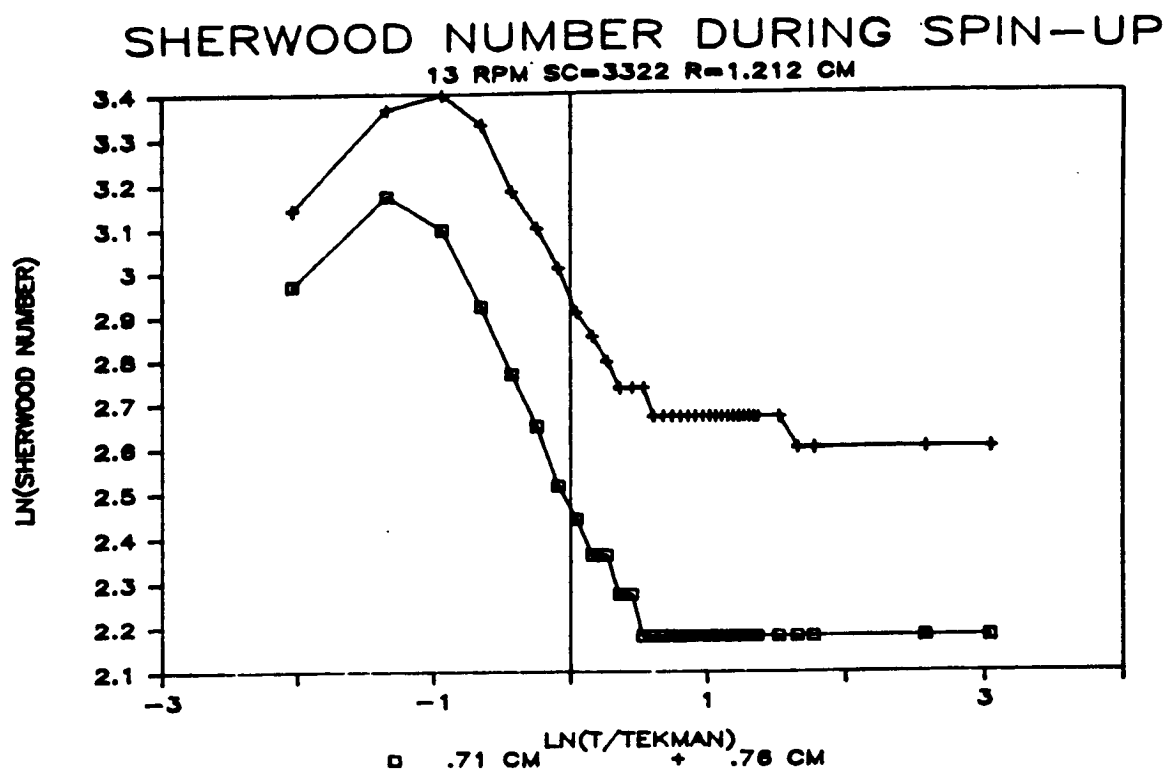


Figure 4.40: The log of the Sherwood number vs. the log of time scaled with the Ekman time during spin-up at 13 RPM.

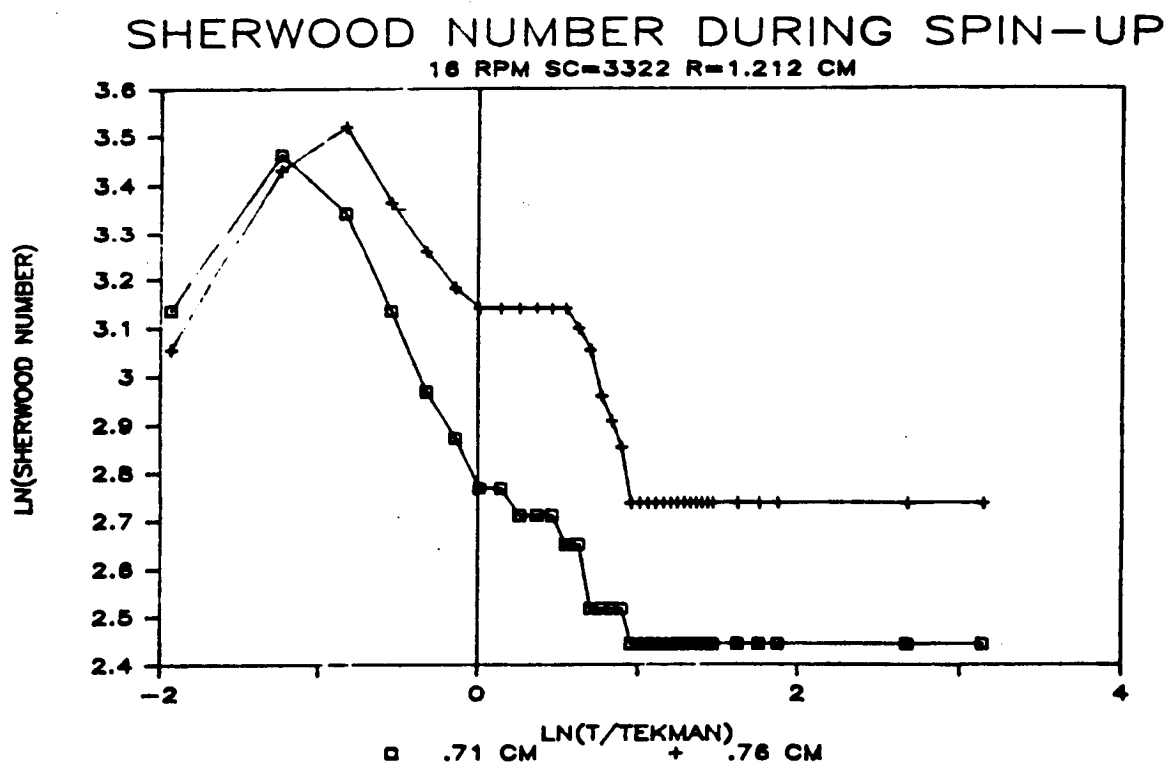


Figure 4.41: The log of the Sherwood number vs. the log of time scaled with the Ekman time during spin-up at 16 RPM.

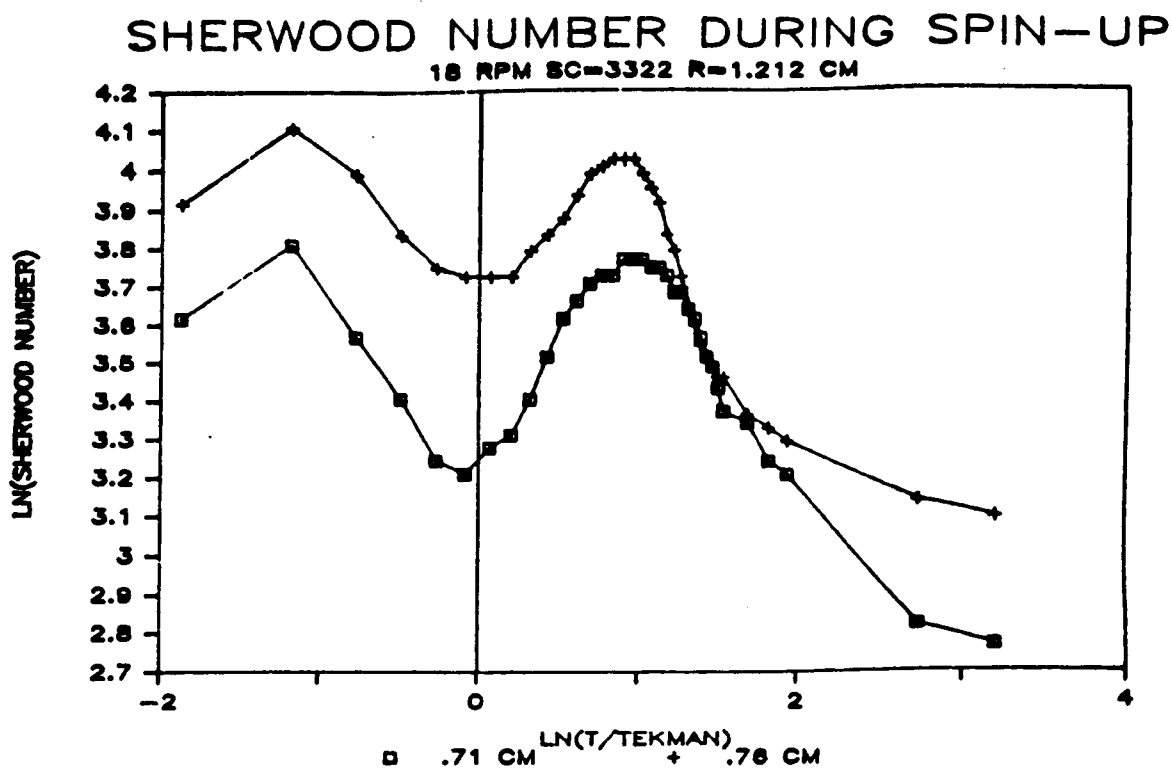


Figure 4.42: The log of the Sherwood number vs. the log of time scaled with the Ekman time during spin-up at 18 RPM.

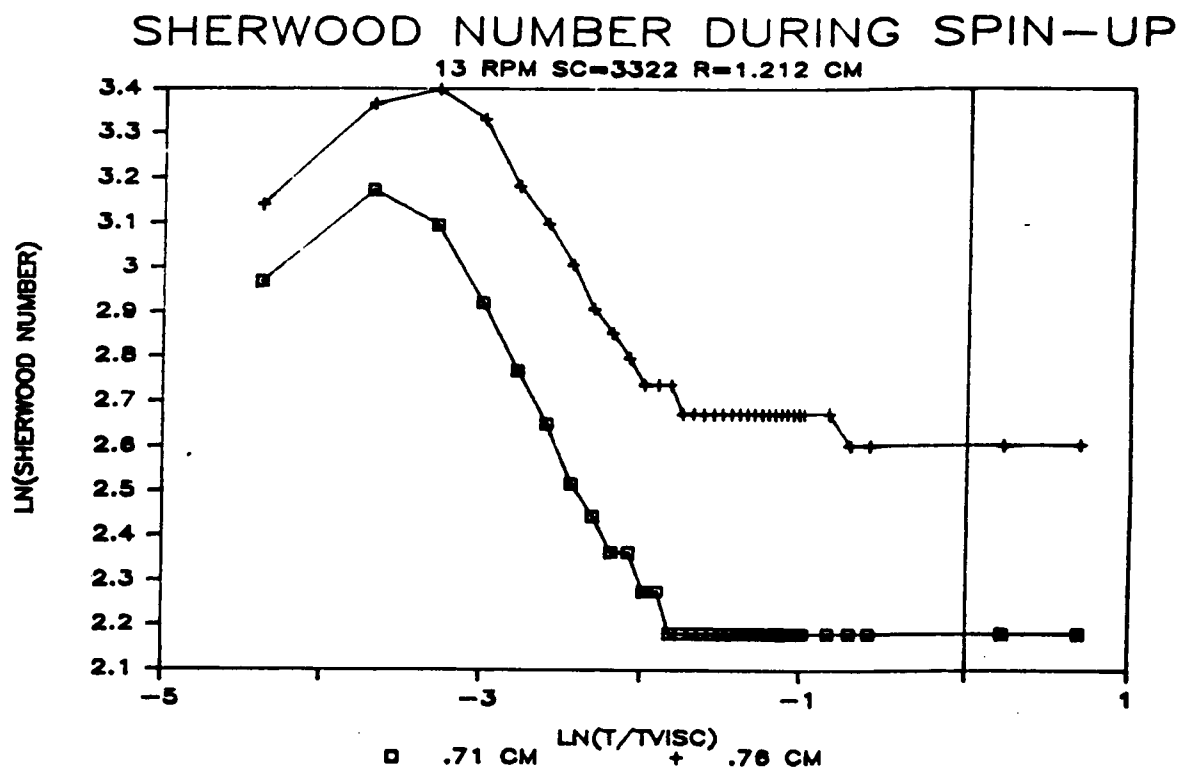


Figure 4.43: The log of the Sherwood number vs. the log of time scaled with the viscous time during spin-up at 13 RPM.

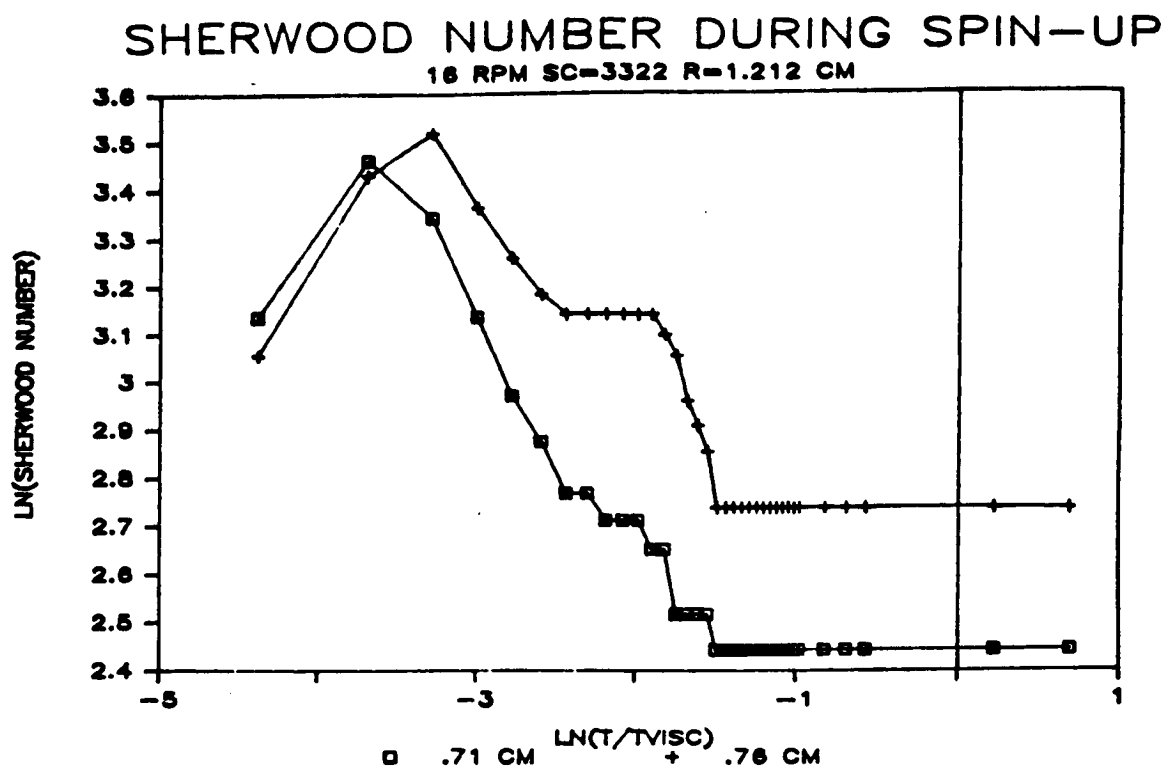


Figure 4.44: The log of the Sherwood number vs. the log of time scaled with the viscous time during spin-up at 16 RPM.

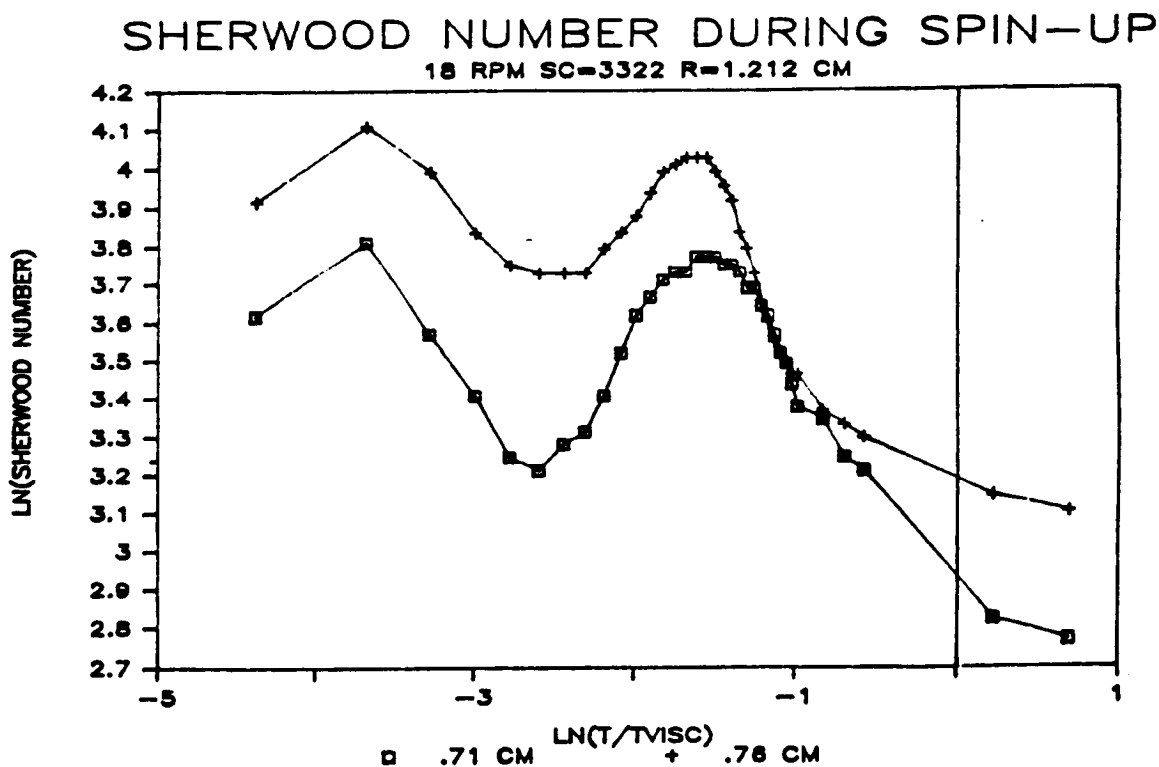


Figure 4.45: The log of the Sherwood number vs. the log of time scaled with the viscous time during spin-up at 18 RPM.

and 4.49). The lowest rotation rate does not produce a second peak (figure 4.50). At 16 RPM, the majority of the interfacial mass transfer occurred in the Ekman time frame. As in the 16 RPM spin-up data, there is a small knee in the data where the Sherwood number decreases slowly (figure 4.51). At 18 RPM, the second peak is not enhancing the interfacial mass transfer, but retarding it (figure 4.51). That is, the peak is concave upward. There may have been a roll cell circulation over the endwall, like those discussed in the flow visualization results, causing the fluid there to be depleted of reactant. At longer times, the roll cell must have weakened, because the Sherwood number approaches a final constant value.

The Sherwood numbers shown in figures 4.46 through 4.52 were measured at 0.76 and 0.71 cm from the central axis 180 degrees apart. The results reveal that the viscous instability is axisymmetric. Doping axisymmetry is important in some applications of BS grown crystals. Since the viscous time scale effects are axisymmetric and at large rotation rates provide more interfacial mass transfer than the secondary flows produced during the Ekman time scale, they can be exploited to generate strong interfacial mass transfer in the BS technique.

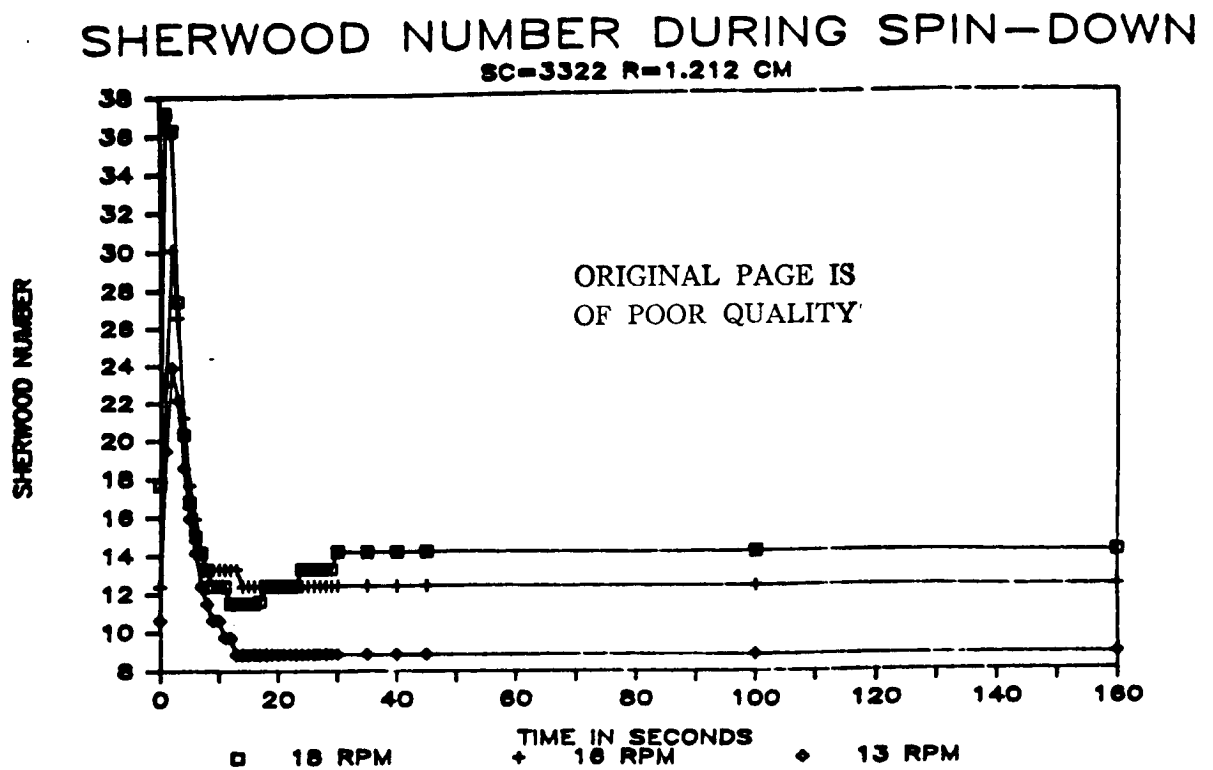


Figure 4.46: The Sherwood number vs. time during spin-down for 13, 16, 18 RPM.

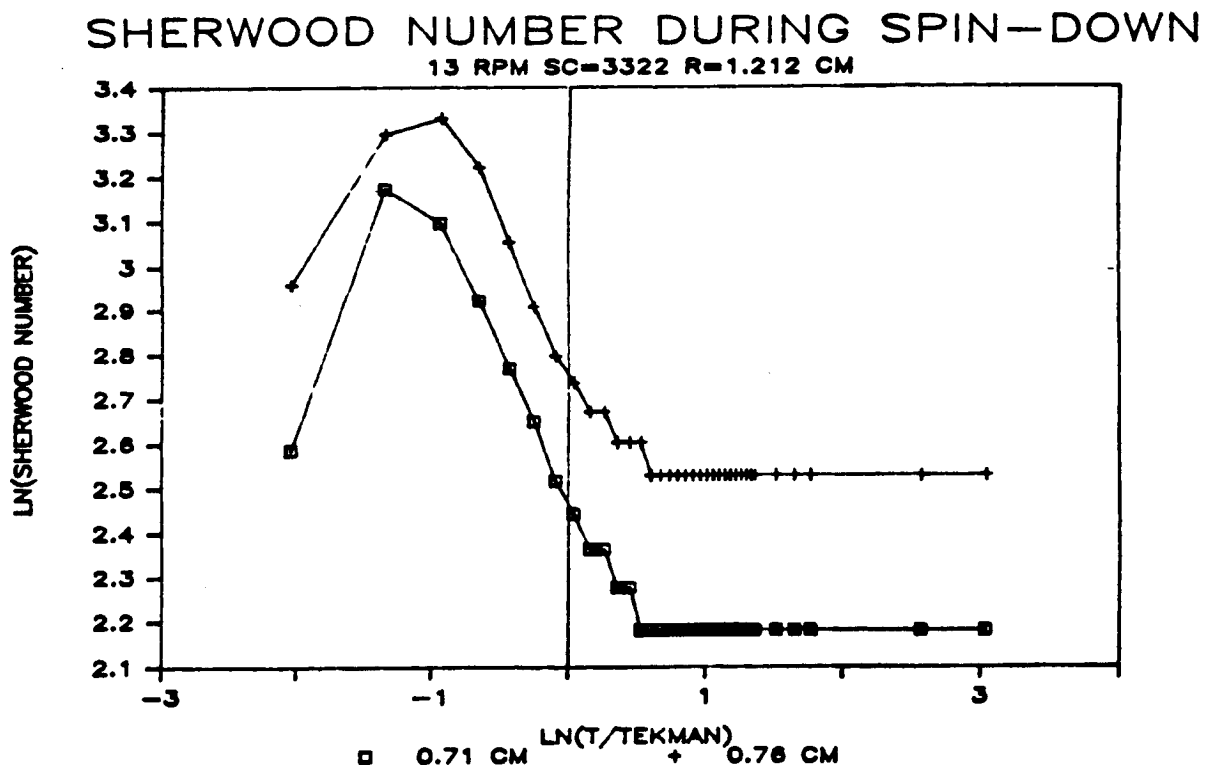


Figure 4.47: The log of the Sherwood number vs. the log of time scaled with the Ekman time during spin-down at 13 RPM.

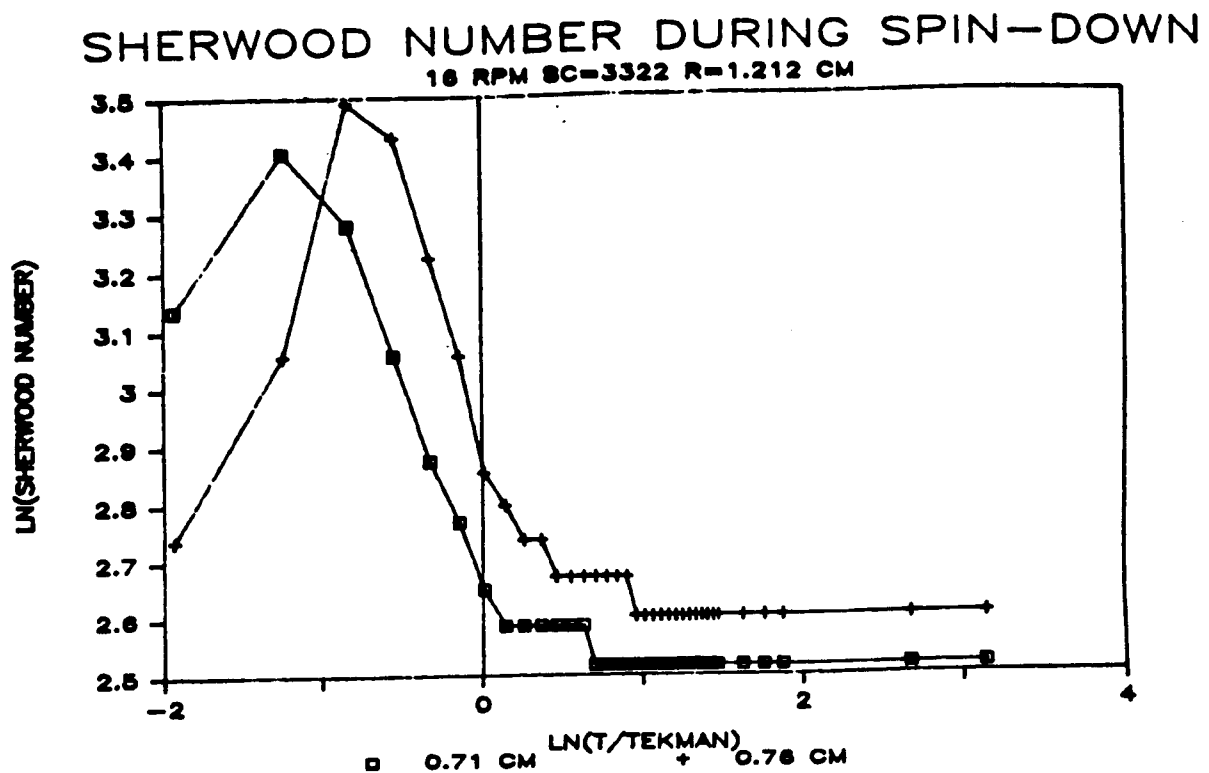


Figure 4.48: The log of the Sherwood number vs. the log of time scaled with the Ekman time during spin-down at 16 RPM.

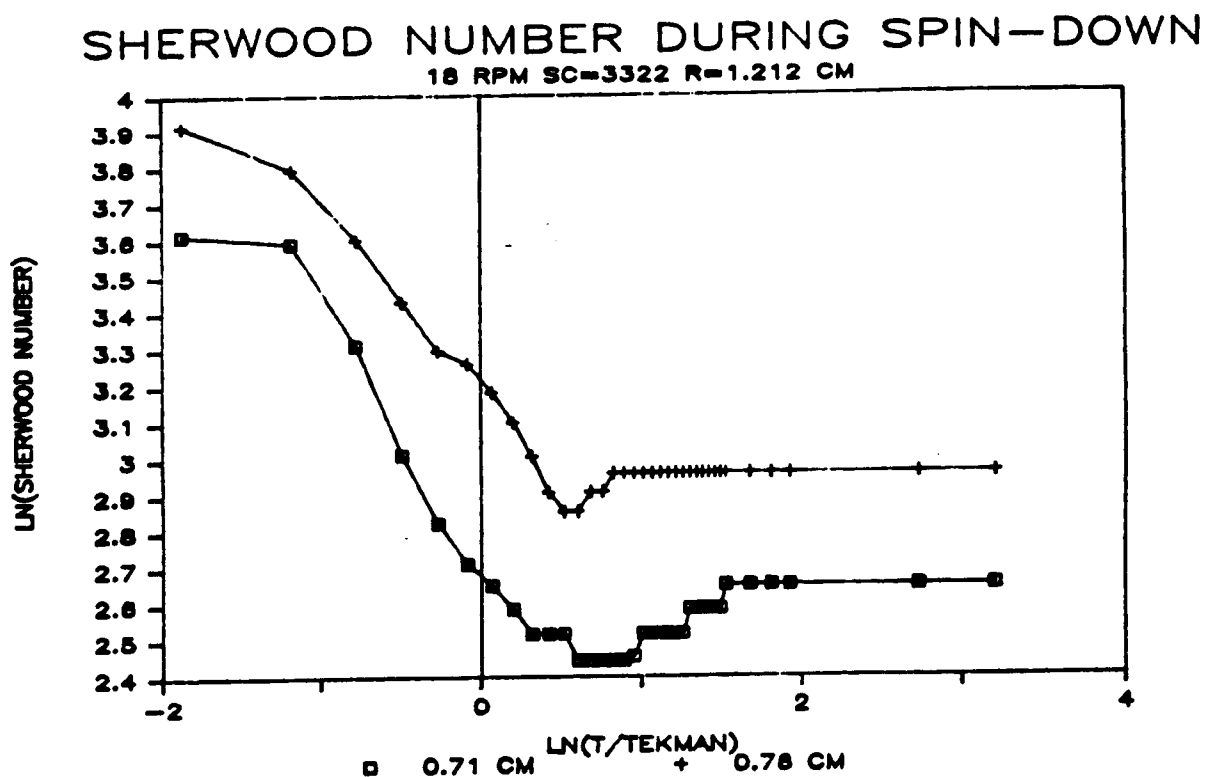


Figure 4.49: The log of the Sherwood number vs. the log of time scaled with the Ekman time during spin-down at 18 RPM.



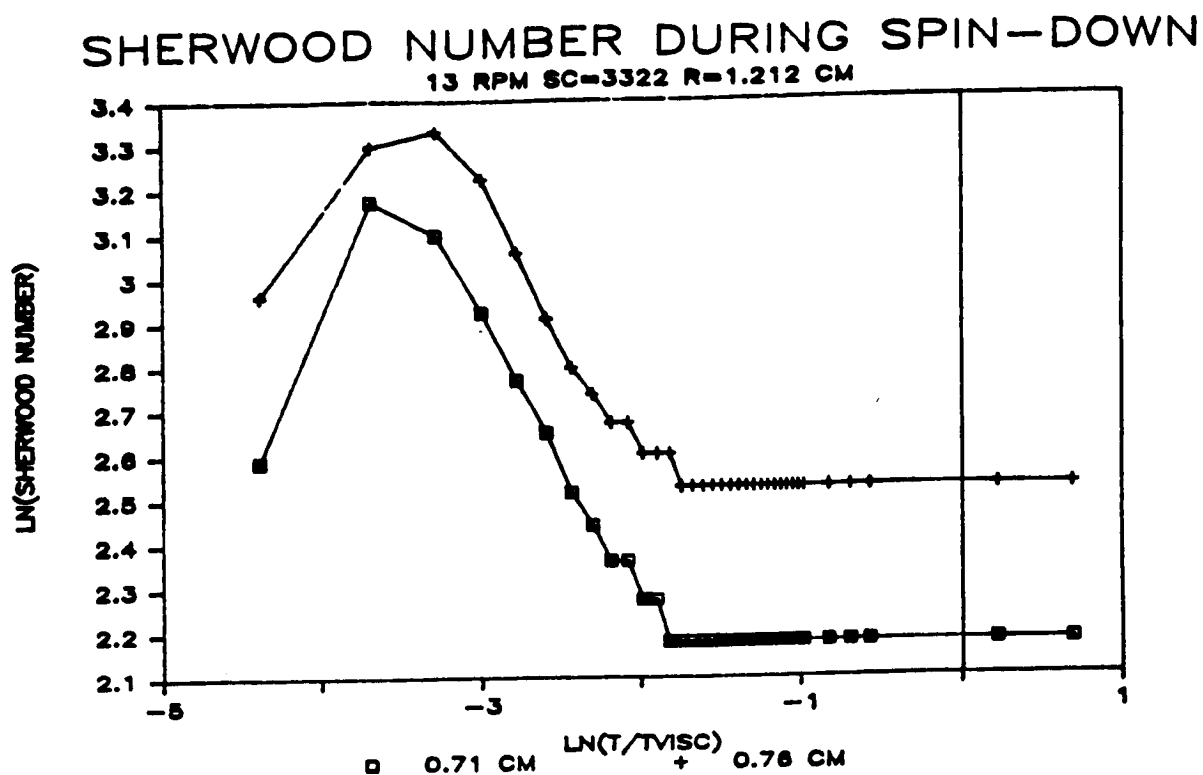


Figure 4.50: The log of the Sherwood number vs. the log of time scaled with the viscous time during spin-down at 13 RPM.

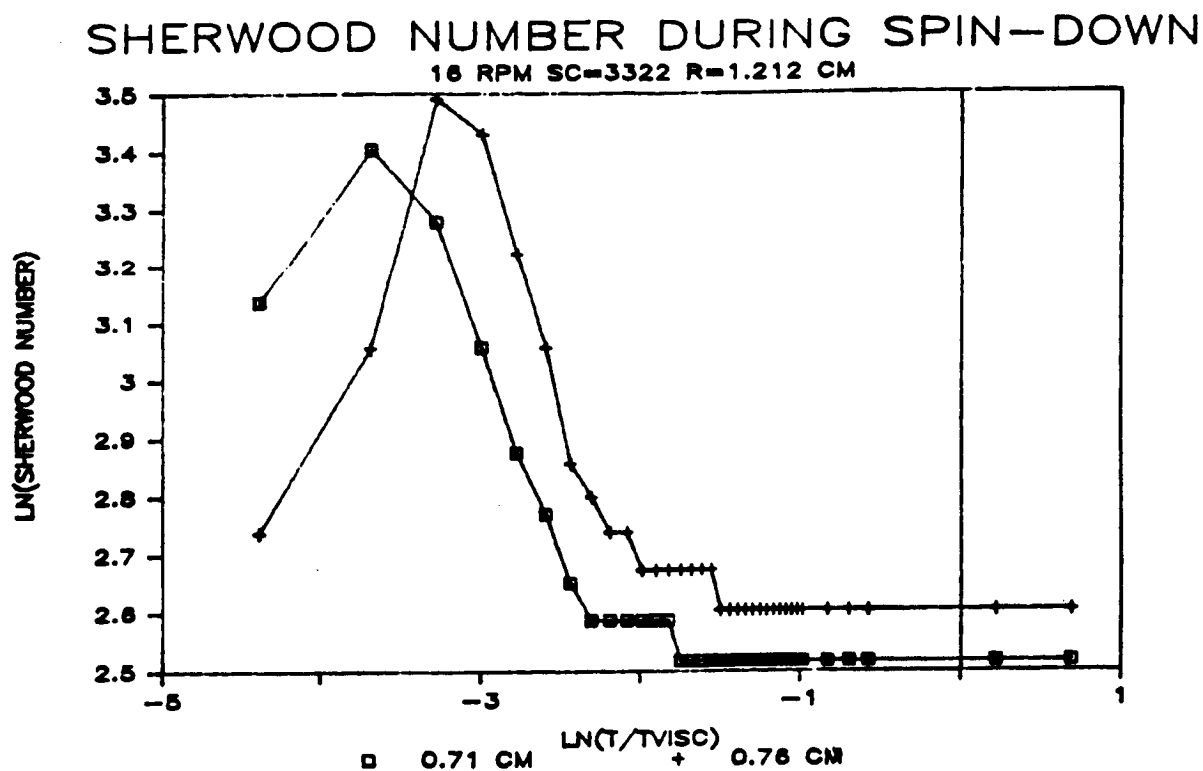


Figure 4.51: The log of the Sherwood number vs. the log of time scaled with the viscous time during spin-down at 16 RPM.

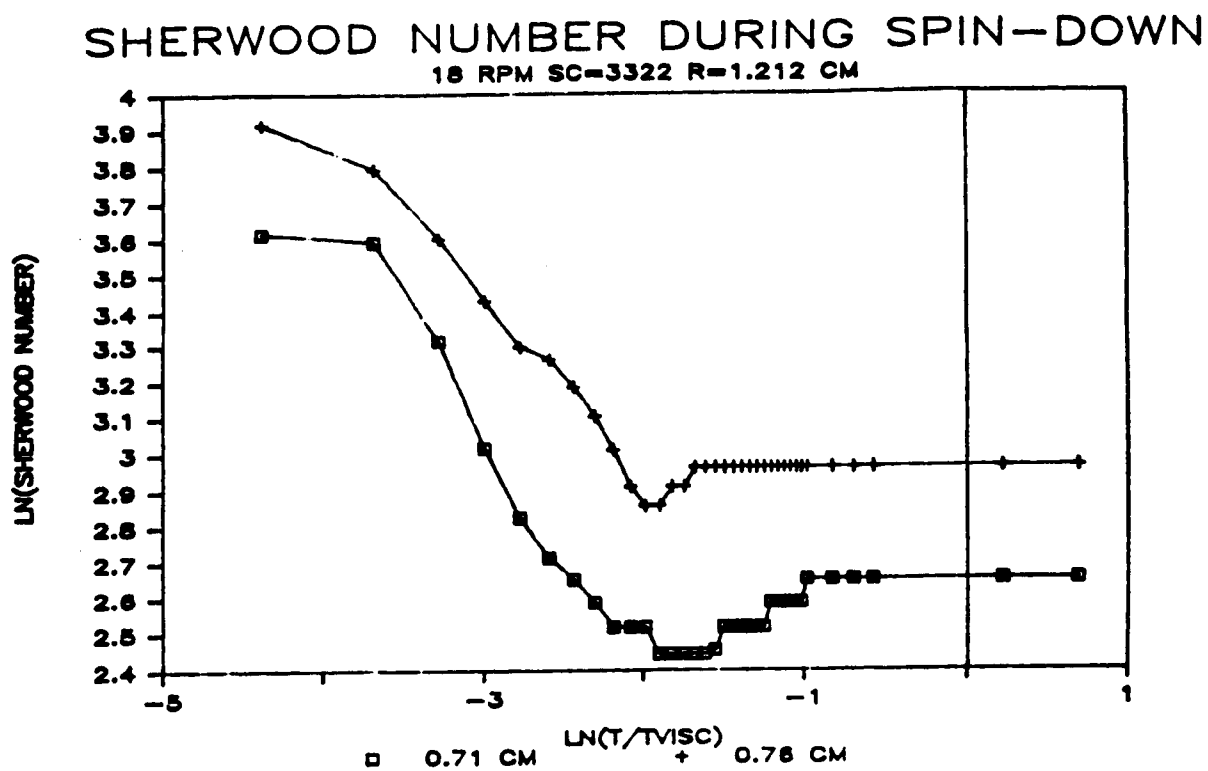


Figure 4.52: The log of the Sherwood number vs. the log of time scaled with the viscous time during spin-down at 18 RPM.

#### 4.2.4 Electrochemical Results for Short Period ACRT

In this part of the investigation, the cylinder was periodically spun-up and spun-down for periods of equal duration. Four rotation rates were used. For each rotation rate, 3 periods were used. The rotation rates were chosen in light of the Brice et al. [10] "optimum mixing parameters." These authors claim that below a critical Ekman number (0.00368), the bulk mixing is strongly non-axisymmetric on spin-down. However, the results of the last subsection showed that the interfacial mass transfer from the bulk liquid to the interface remains axisymmetric well below their critical Ekman number.

This difference between the results given in this thesis and the results of Brice et al. [10] can be easily reconciled. Flow visualization is useful when one wants to see the effects of ACRT on the bulk fluid. Brice et al. [10] base their conclusions on results for bulk flow visualization. Both the flow visualization results given here and those of Brice et al. show that non-axisymmetric bulk mixing may occur. The electrochemical results presented here are for interfacial mass transfer from the bulk fluid to the electrode interface. Crystal growth is a problem in interfacial transport. As long as the conditions along the interface are axisymmetric, the crystal composition will be axisymmetrically. This is true even if the bulk mixing above the interface is nonaxisymmetric. Therefore, bulk fluid flow observations may not give an accurate picture of the mixing occurring at the liquid solid interface.

Considering the above arguments, Brice et al.'s [10] results, and the present long time period results, the four rotation rates were chosen as follows: two above and two below Brice et al.'s [10] critical Ekman number. One of the two values below Brice et al.'s [10] critical numbers was chosen to be within the Ekman number range used in the long time period results. The third rate was chosen to be near

the maximum rotation rate limit at which it was felt the equipment could be safely operated. This last rotation rate was well below the critical limit given by Brice et al. [10]. It was chosen to see if the strong non-axisymmetric mixing predicted by Brice et al. [10] would produce strong non-axisymmetric interfacial transport.

The data in this section are shown two ways. They are presented as Sherwood number vs. time and as Sherwood number vs. time scaled with the ACRT period. In the second method of presentation, spin-up begins where the abscissa is equal to an even integer and spin-down begins where the abscissa is equal to an odd integer.

Figure 4.53 through 4.58 show the Sherwood number vs. time at 12 RPM for 14, 30 and 60 second ACRT periods. The Ekman number is 0.0161 and the Ekman time is about 6 seconds. The long rotation period investigations showed that the Sherwood number transients occurred within the Ekman time for  $Ek > 0.0074$ . The 14 second period produced spin-up and spin-down occurring on the order of the Ekman time. The 30 second data had a greater average Sherwood number, see Table 4.1. The 60 second period data shows long time periods where the Sherwood number is constant. The viscous time scale is on the order of 49 seconds in these experiments.

The average Sherwood numbers are based on the maximum number of complete ACRT cycles available in the data. Thus if the data was available for 45 seconds and the period was 7 seconds, the average was taken over the first six periods.

Figure 4.59 through 4.64 show the Sherwood number vs. time at 20 RPM for 14, 30 and 60 second ACRT periods. The Ekman number is 0.00967 and the Ekman time is 4.9 seconds. Again the Ekman number is over the critical value which produced a single peak in the Sherwood number during the long rotation period

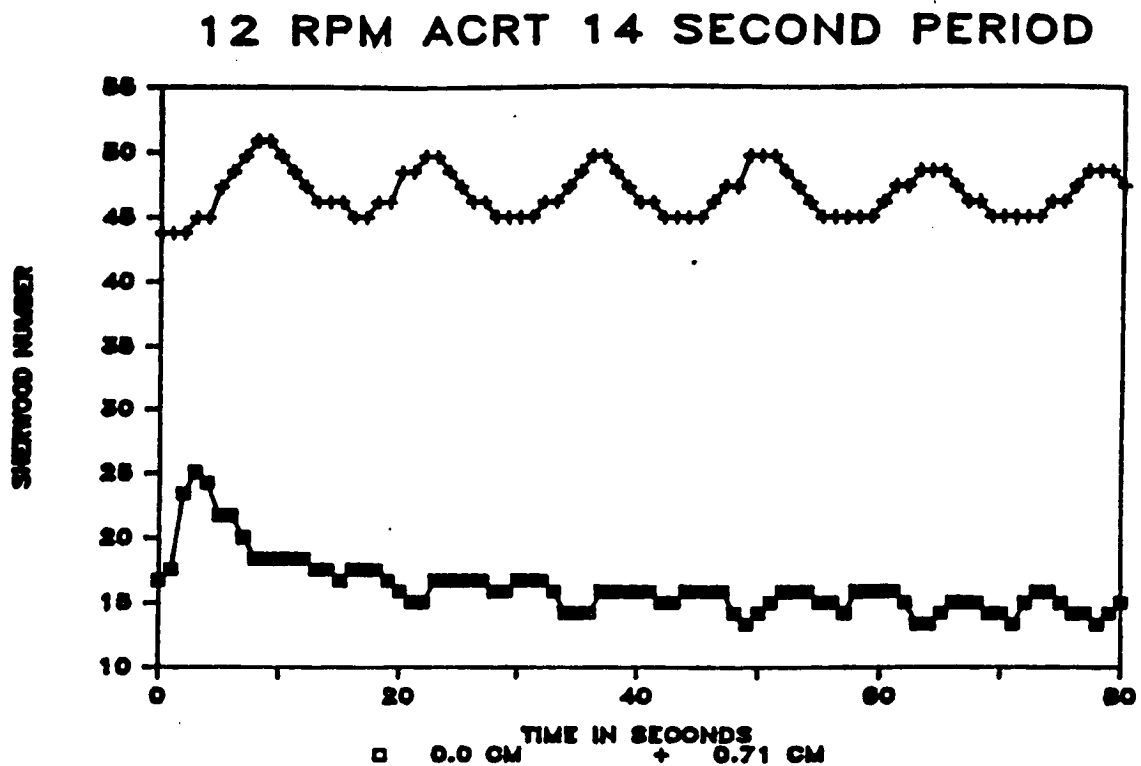


Figure 4.53: The Sherwood number vs. time for ACRT at 12 RPM and a 14 second period.

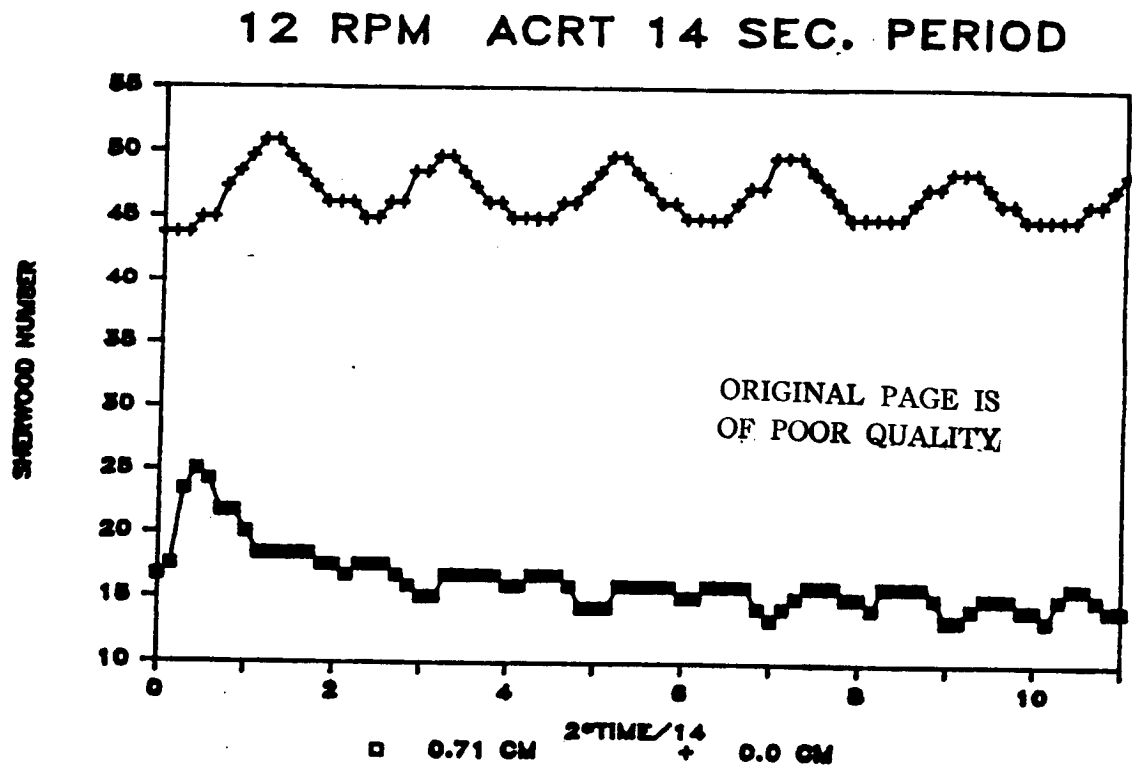


Figure 4.54: The Sherwood number vs.  $2 \cdot t$  scaled with the cycle period for ACRT at 12 RPM and a 14 second period.

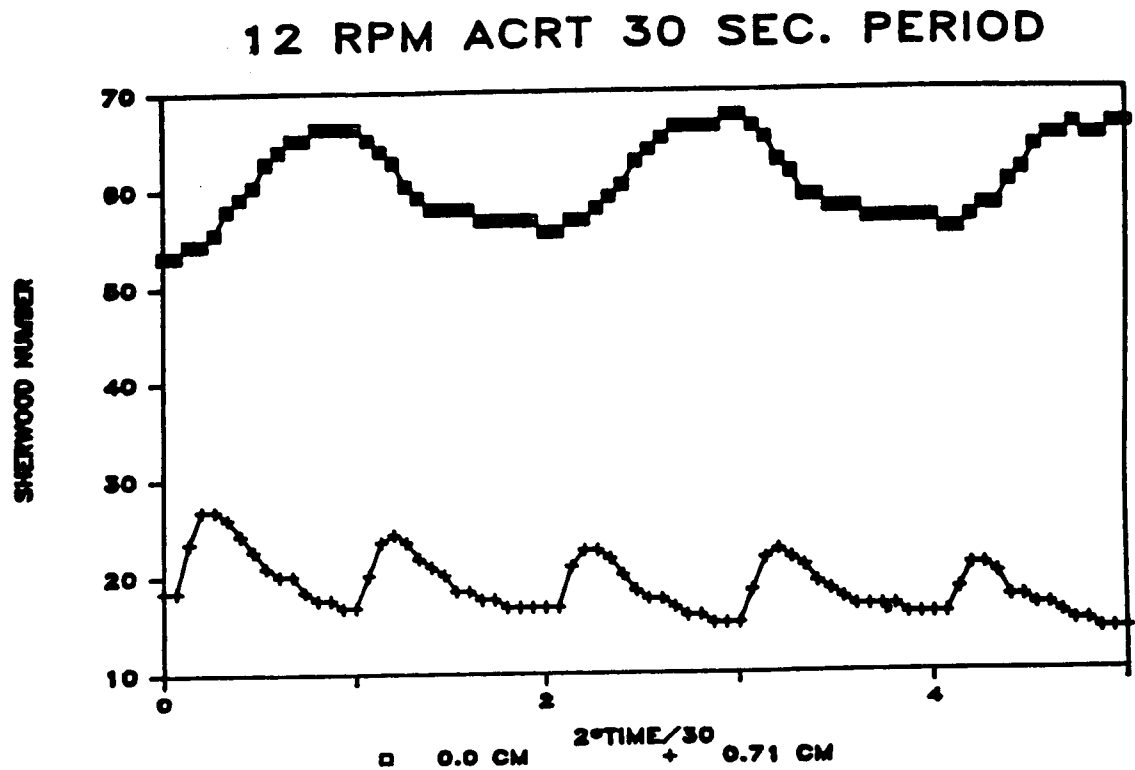


Figure 4.55: The Sherwood number vs. time for ACRT at 12 RPM and a 30 second period.

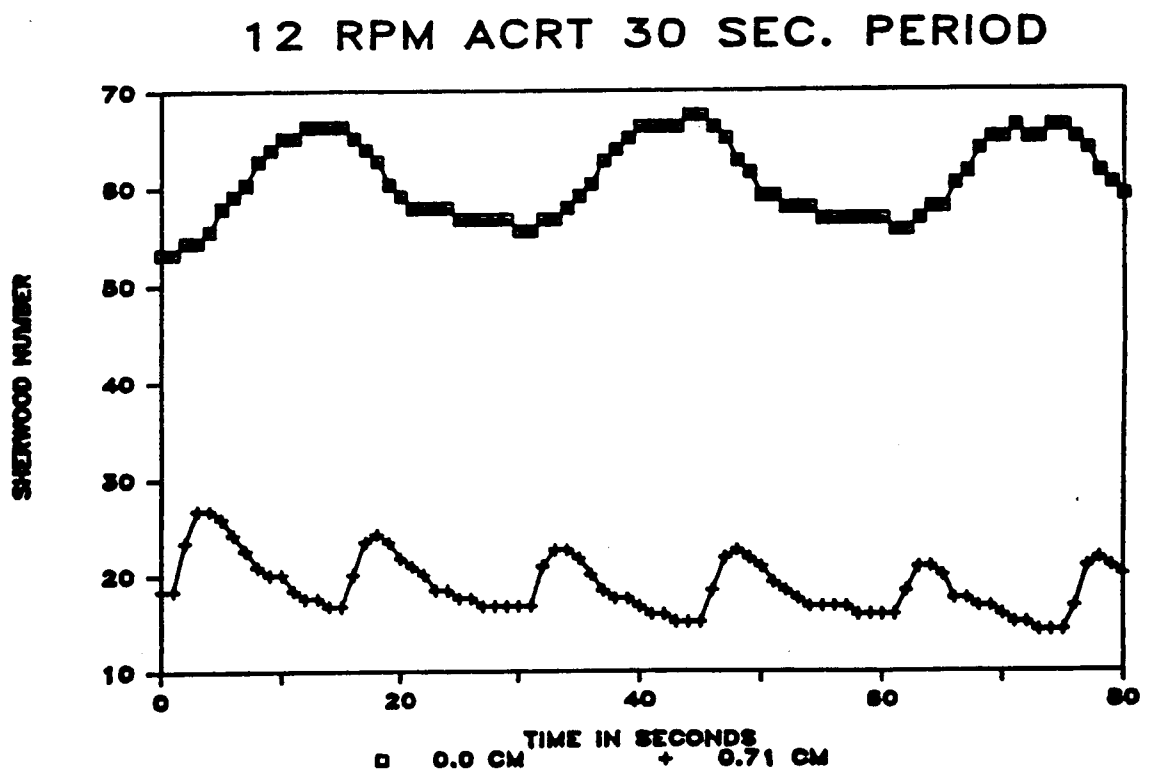


Figure 4.56: The Sherwood number vs.  $2 \cdot t$  scaled with the cycle period for ACRT at 12 RPM and a 30 second period.

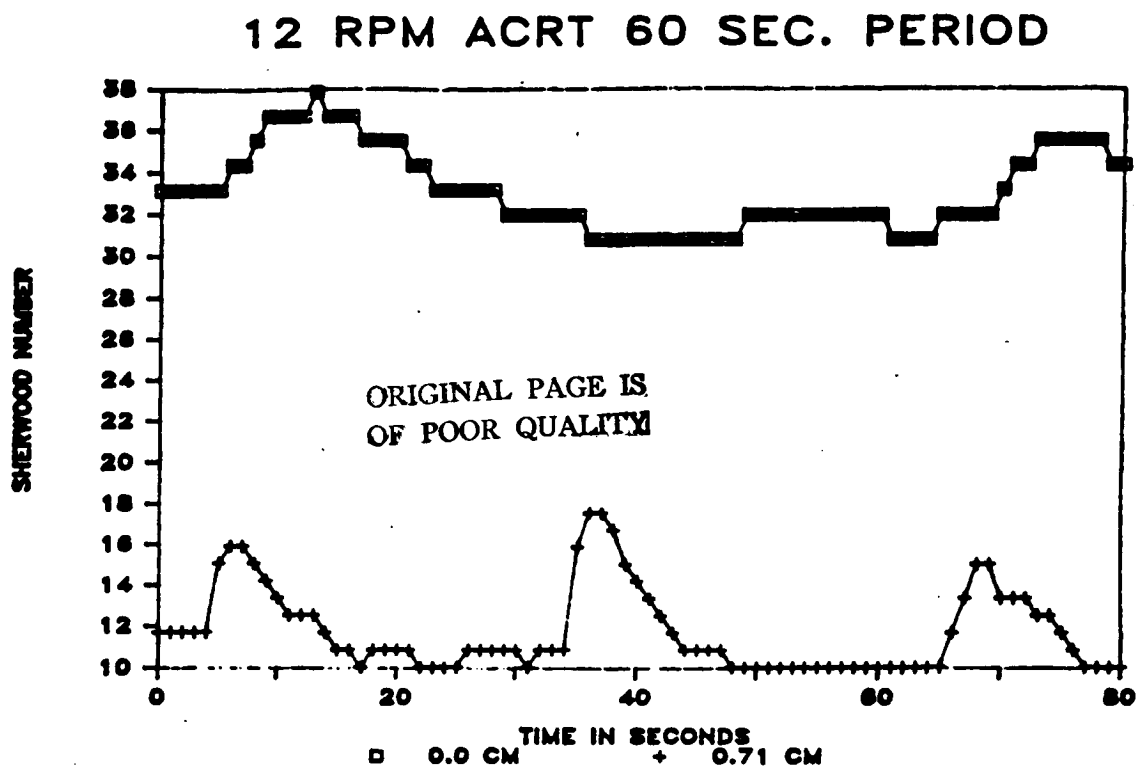


Figure 4.57: The Sherwood number vs. time for ACRT at 12 RPM and a 60 second period.

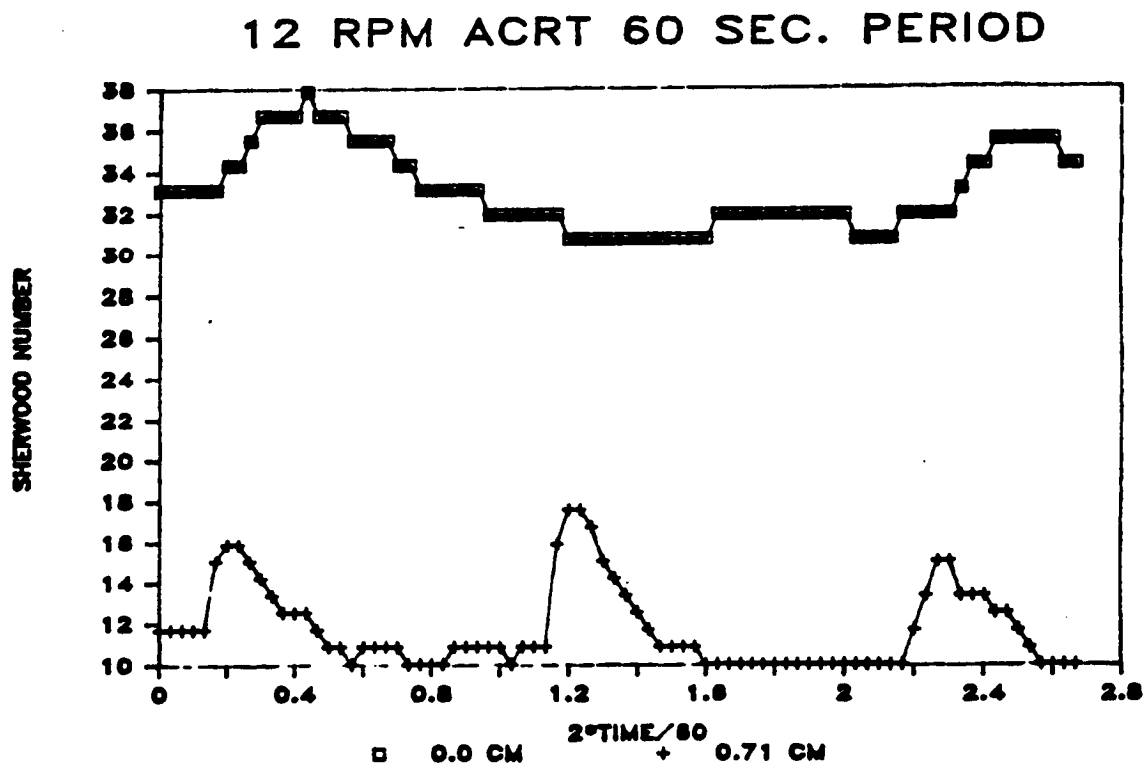


Figure 4.58: The Sherwood number vs.  $2 \cdot t$  scaled with the cycle period for ACRT at 12 RPM and a 60 second period.

Table 4.1: The average, maximum and minimum Sherwood number during ACRT for various periods.

RPM	Period seconds	Location CM number	Maximum Sherwood number	Minimum Sherwood number	Average Sherwood number
12	14	0.0	50.9	43.9	46.8
12	14	0.71	25.1	13.4	16.2
12	30	0.0	67.4	53.2	60.7
12	30	0.71	26.7	14.2	18.9
12	60	0.0	37.9	30.8	33.1
12	60	0.71	17.6	10.0	11.7
20	14	0.0	110	54.4	84.1
20	14	0.71	35.9	11.7	16.8
20	30	0.0	137	54.4	101
20	30	0.71	36.8	15.0	21.5
20	60	0.0	132	45.0	81.9
20	60	0.71	23.4	10.0	12.2
65	10	0.0	103	53.0	76.8
65	10	0.71	41.6	23.9	32.9
65	20	0.0	132	42.7	92.5
65	20	0.71	64.7	31.9	46.6
65	30	0.0	125	22.1	85.0
65	30	0.71	57.6	26.6	45.0
100	20	0.0	232.7	73.3	171.9
100	20	0.71	65.6	37.2	54.0
100	40	0.0	238	67.7	166
100	40	0.71	72.7	35.4	59.2
100	60	0.0	238	61.8	164
100	60	0.71	76.2	26.6	61.3



investigations. Table 4.1 shows that the average Sherwood number is greatest for the 30 second period. As in the 12 RPM 60 second period data, the 60 second period data shows long time periods where the Sherwood number is constant. The viscous time scale is on the order of 49 seconds.

At this point enough data have been presented to state some important observations. The maximum in the Sherwood number at the center always lagged the maximum in the Sherwood number at the edge. This same result was observed in the long rotation period studies. The transient in the Sherwood number at the edge occurred on the order of the Ekman time. In the results presented so far, spin-down caused the center Sherwood number to decrease sharply with time. This could have been caused by the stagnation vortex seen in the visualization work and follows the results of the long rotation period studies. During spin-down in the long rotation period work, the center Sherwood number always decreased with time. The decrease was ascribed to the formation of a stagnation vortex becoming depleted of reactant, causing the mass transfer to drop off. This may be occurring during short period ACRT.

The frequency of the Sherwood number oscillations during ARCT is interesting to note. One would expect the natural frequency to be equal to the ACRT frequency, since ACRT drives the hydrodynamics. The center data do have a frequency equal to the ACRT frequency and may be understood as follows. On spin-up, the interfacial mass transfer is enhanced because of the flow of fluid toward the interface induced by the radial flow outward along the interface in the Ekman layer. On spin-down the interfacial mass transfer is retarded, presumably by the formation of the stagnation vortex already described. Thus, spin-up enhances and spin-down retards the interfacial mass transfer and the frequency of the Sherwood number at the center is equal to the ACRT forcing frequency.

# 20 RPM ACRT 14 SEC. PERIOD

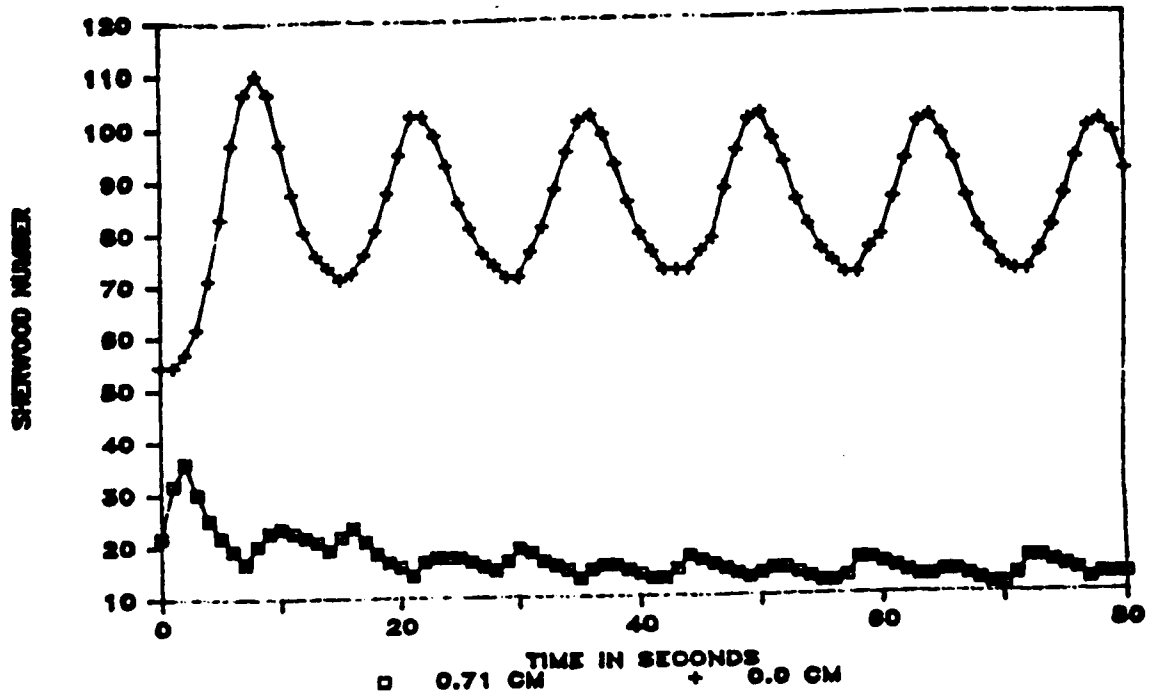


Figure 4.59: The Sherwood number vs. time for ACRT at 20 RPM and a 14 second period.

# 20 RPM ACRT 14 SEC. PERIOD

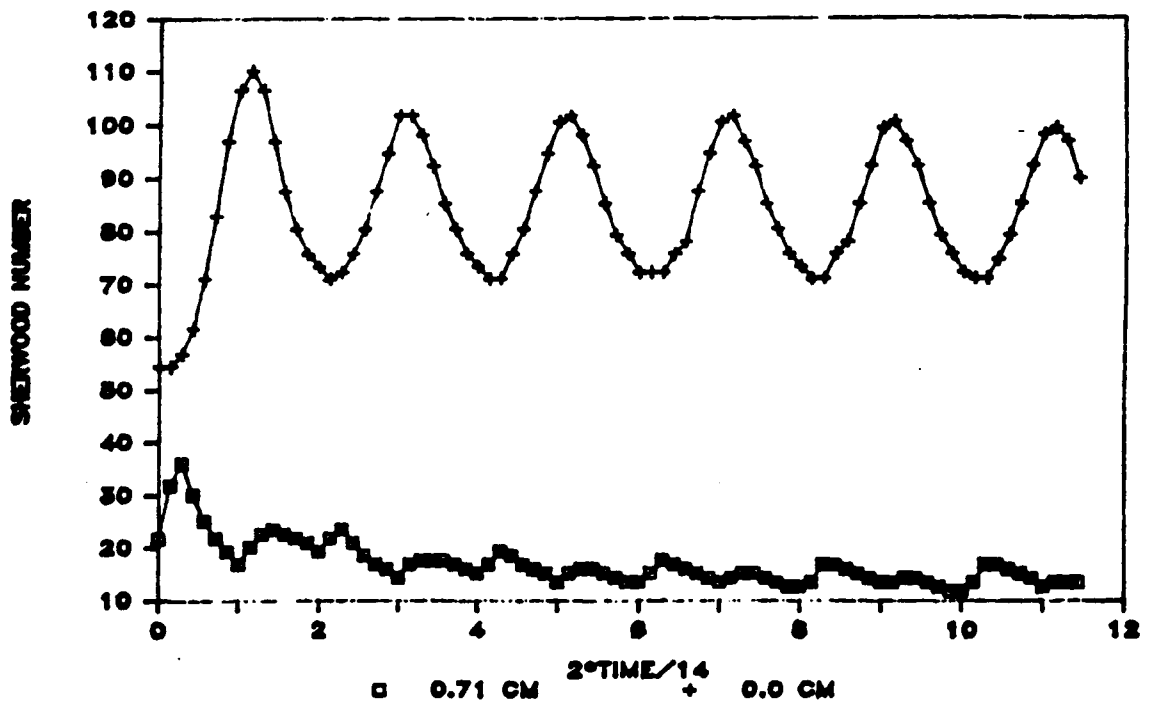


Figure 4.60: The Sherwood number vs.  $2 \cdot t$  scaled with the cycle period for ACRT at 20 RPM and a 14 second period.

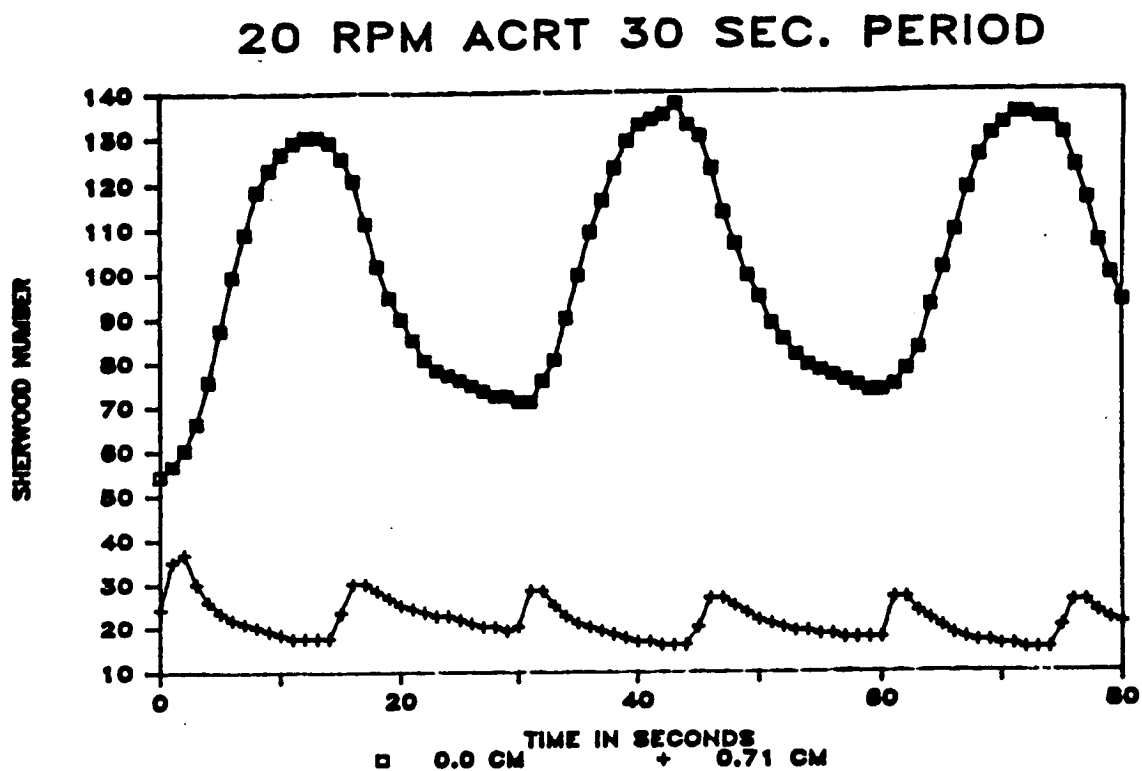


Figure 4.61: The Sherwood number vs. time for ACRT at 20 RPM and a 30 second period.

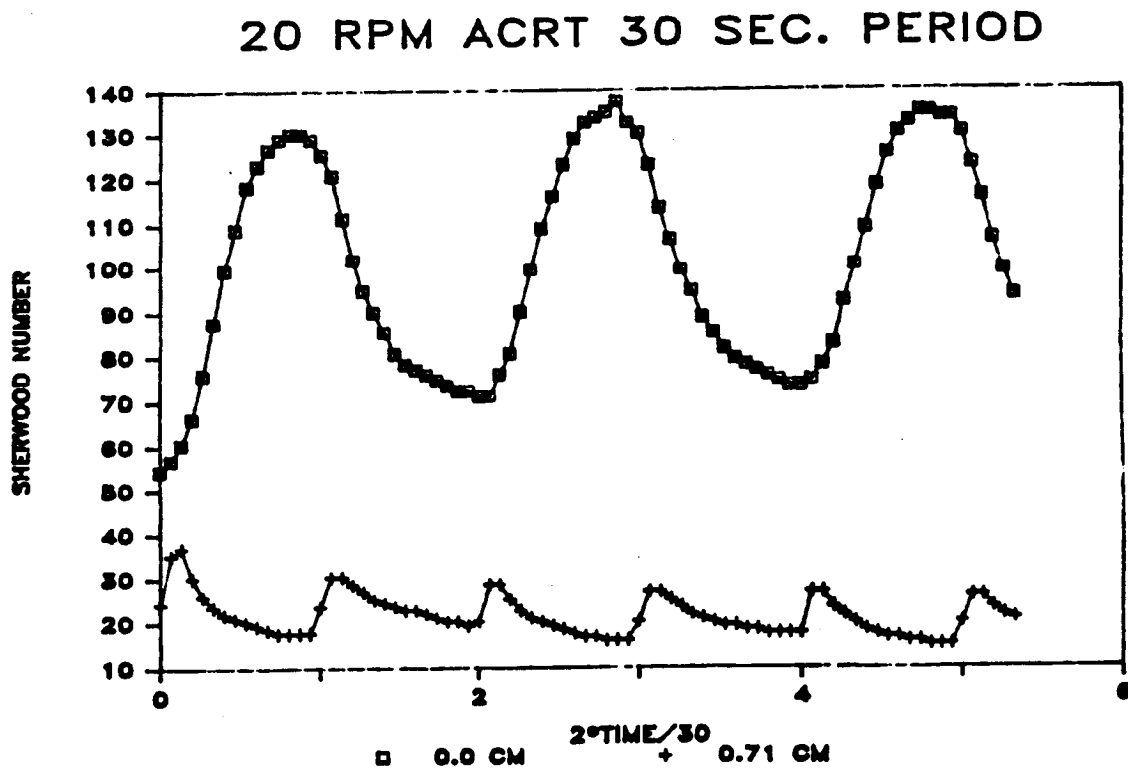


Figure 4.62: The Sherwood number vs.  $2 \cdot t$  scaled with the cycle period for ACRT at 20 RPM and a 30 second period.

### 20 RPM ACRT 60 SEC. PERIOD

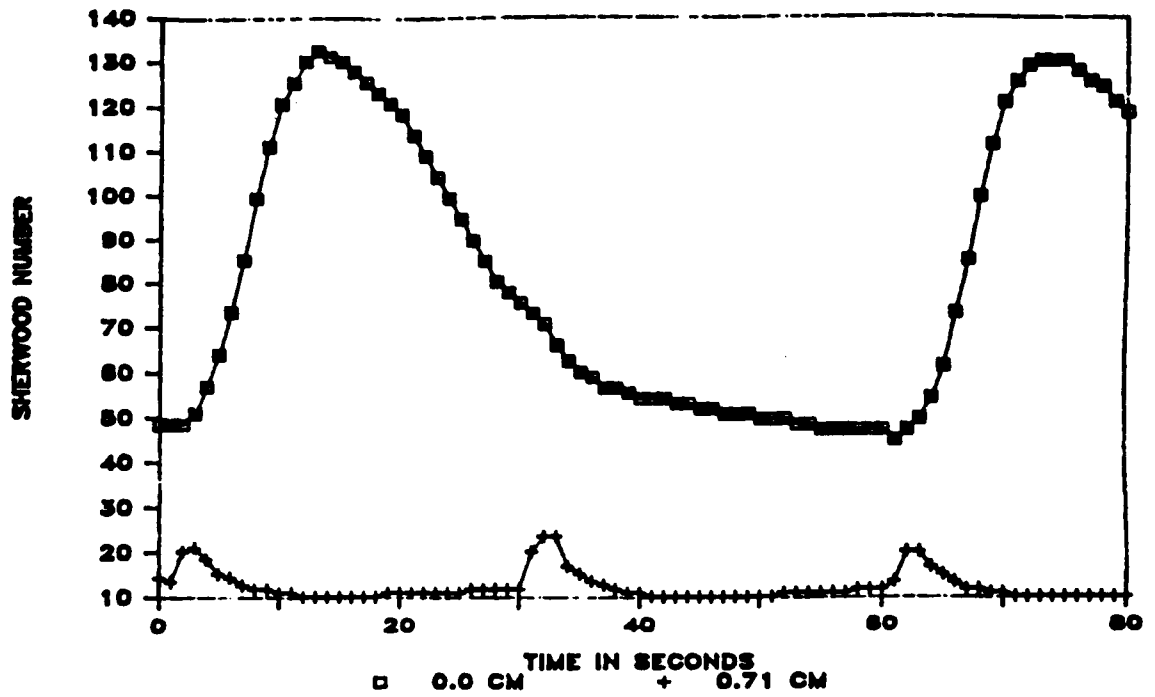


Figure 4.63: The Sherwood number vs. time for ACRT at 20 RPM and a 60 second period.

### 20 RPM ACRT 60 SEC. PERIOD

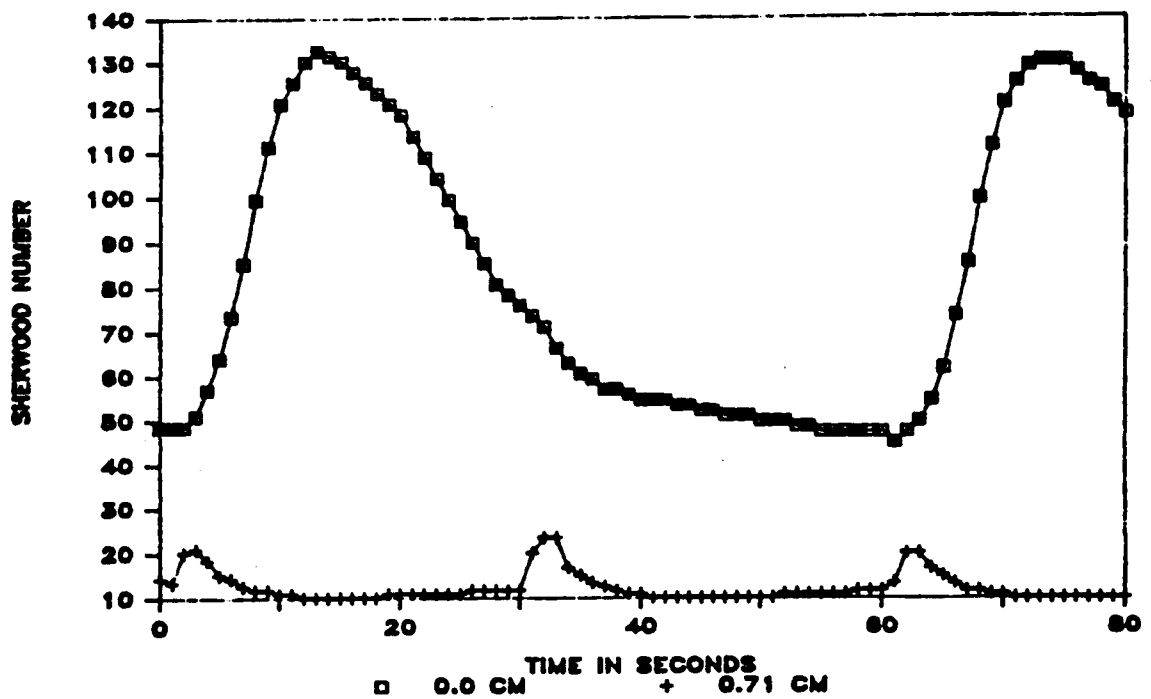


Figure 4.64: The Sherwood number vs.  $2\pi t$  scaled with the cycle period for ACRT at 20 RPM and a 60 second period.

The oscillations of mass transfer at the edge is another story. The frequency is twice the ACRT forcing frequency. Pumping inside the Ekman layer is the reason. On spin-up, the radial outflow of fluid in the Ekman layer enhances interfacial mass transfer. This same result was seen in the rigid body rotation studies. On spin-down, the radial inflow of fluid in the Ekman layer also enhances the interfacial mass transfer. Again this was seen in the rigid body rotation studies. In one ACRT cycle, there is an enhancement in the interfacial mass transfer during both spin-up and spin-down. Thus, the frequency of the oscillations in Sherwood number at the edge is twice the ACRT frequency.

Figures 4.65 through 4.70 show the Sherwood number vs. time at 65 RPM for 10, 20 and 30 second periods. The Ekman number is 0.00205 and the Ekman time is 3.2 seconds. The Ekman number is less than that needed to produce two peaks in the Sherwood number in the long rotation period studies. The graphs are very different than the two sets of graphs given for the 12 and 20 RPM short ACRT period data. During spin-up and spin-down the edge Sherwood number has two peaks, while the center Sherwood number has only one peak. The second peak on spin-up and spin-down for the 10 second period data are obscured by the first peaks of spin-down and spin-up. The second peaks do not have enough time to manifest themselves before the first peak of the next cycle takes over.

For the above rotations rates, the initial stages of spin-up actually retard the interfacial mass transfer at the center. This is most clearly demonstrated in figures 4.66, 4.68 and 4.70 where time is scaled with the ACRT period. This phenomenon was first seen in the 20 RPM, 14 second period run (figure 4.59). The most likely cause is flow reversal. The flow visualization experiments revealed a stagnation vortex at the central axis along the endwall during spin-down. The long rotation period data showed a decrease in the interfacial mass transfer at the center during

## 65 RPM ACRT 10 SEC. PERIOD

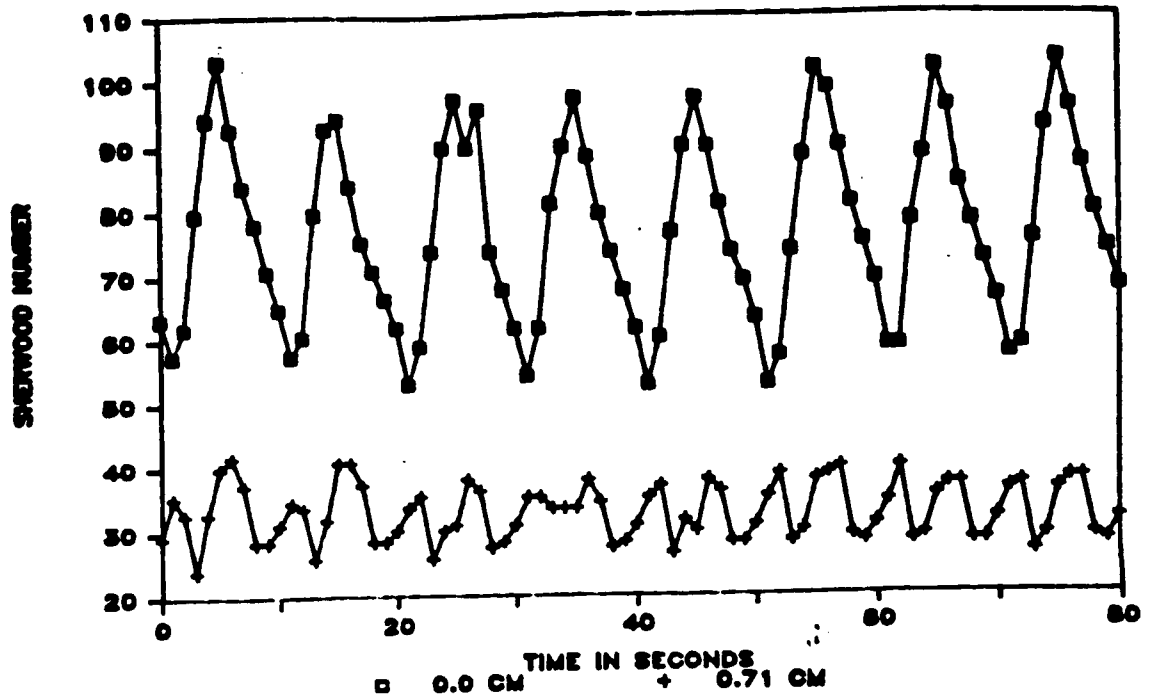


Figure 4.65: The Sherwood number vs. time for ACRT at 65 RPM and a 10 second period.

## 65 RPM ACRT 10 SEC. PERIOD

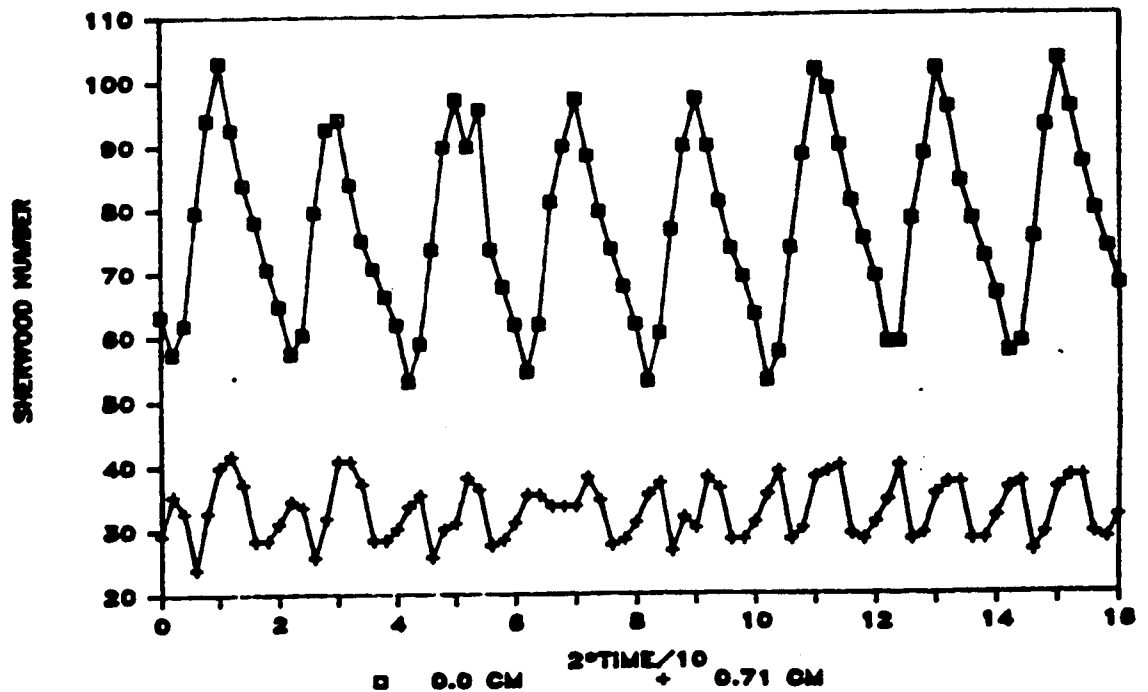


Figure 4.66: The Sherwood number vs.  $2\pi t$  scaled with the cycle period for ACRT at 65 RPM and a 10 second period.

# 65 RPM ACRT 20 SEC. PERIOD

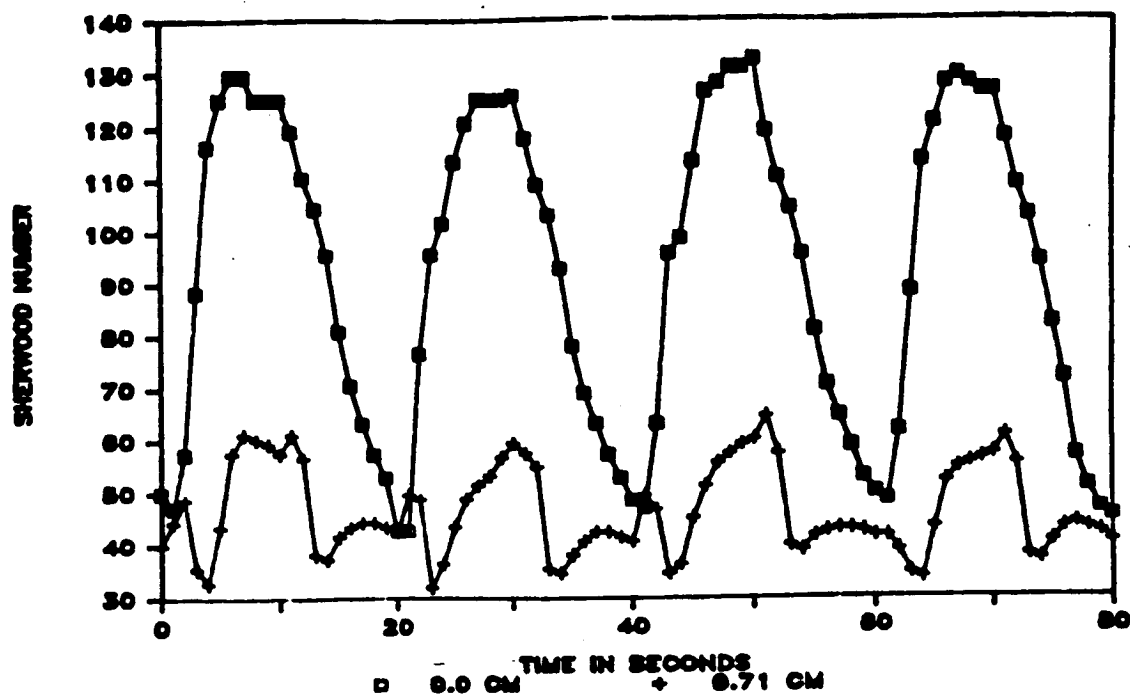


Figure 4.67: The Sherwood number vs. time for ACRT at 65 RPM and a 20 second period.

# 65 RPM ACRT 20 SEC. PERIOD

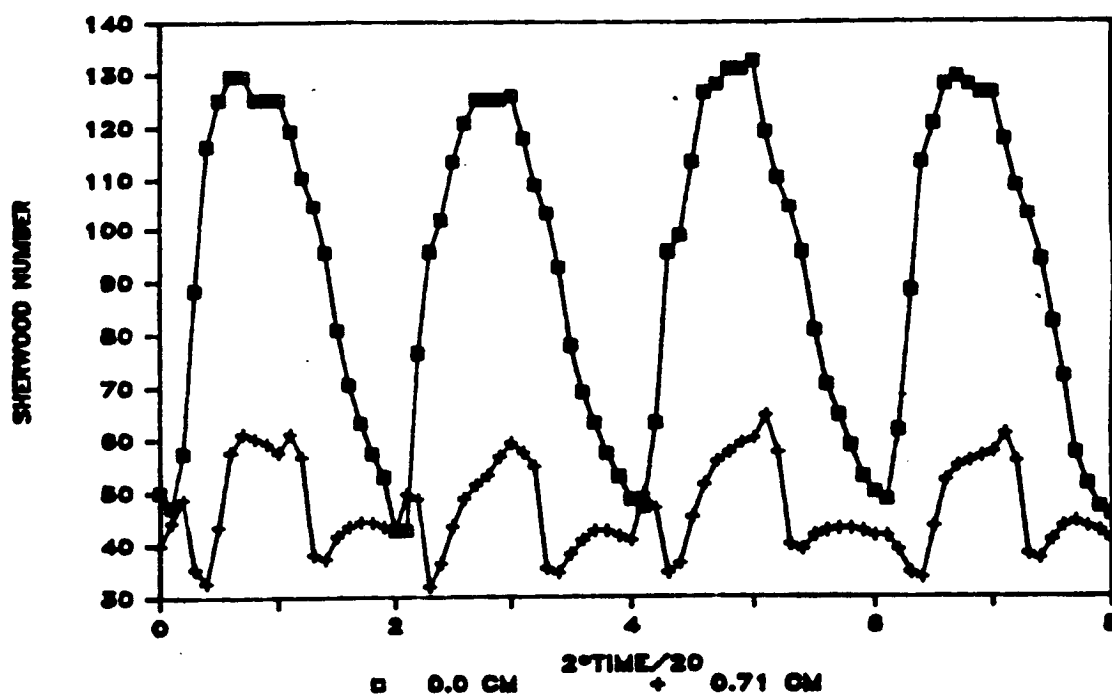


Figure 4.68: The Sherwood number vs.  $2 \cdot t$  scaled with the cycle period for ACRT at 65 RPM and a 20 second period.

# 65 RPM ACRT 30 SEC. PERIOD

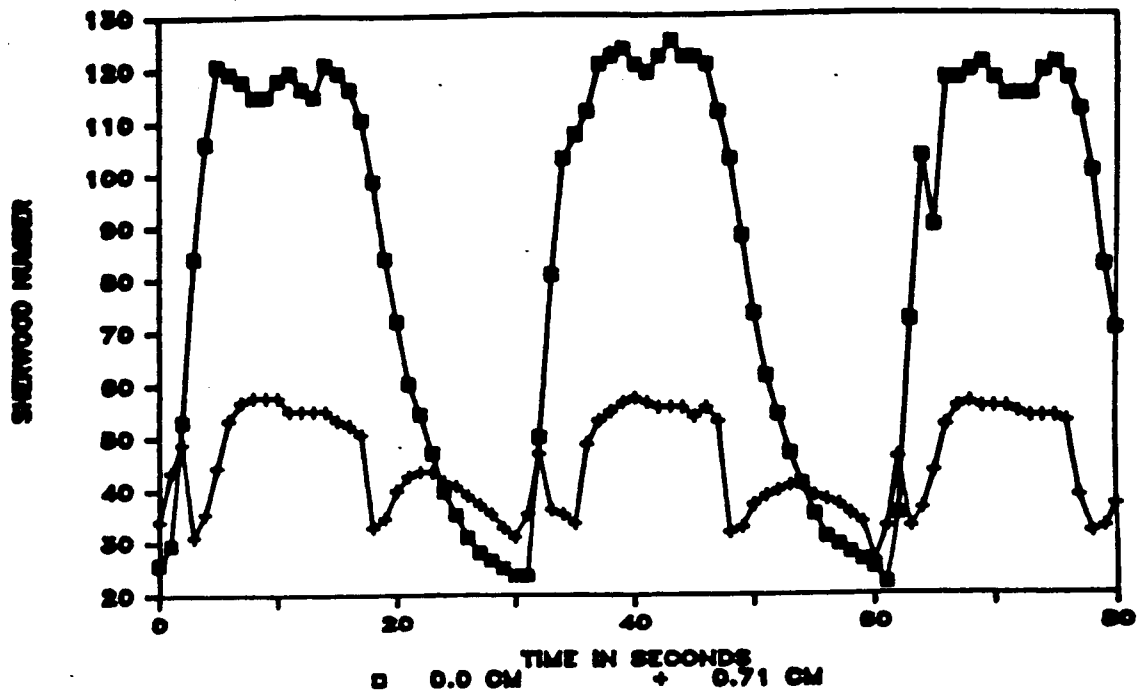


Figure 4.69: The Sherwood number vs. time for ACRT at 65 RPM and a 30 second period.

# 65 RPM ACRT 30 SEC. PERIOD

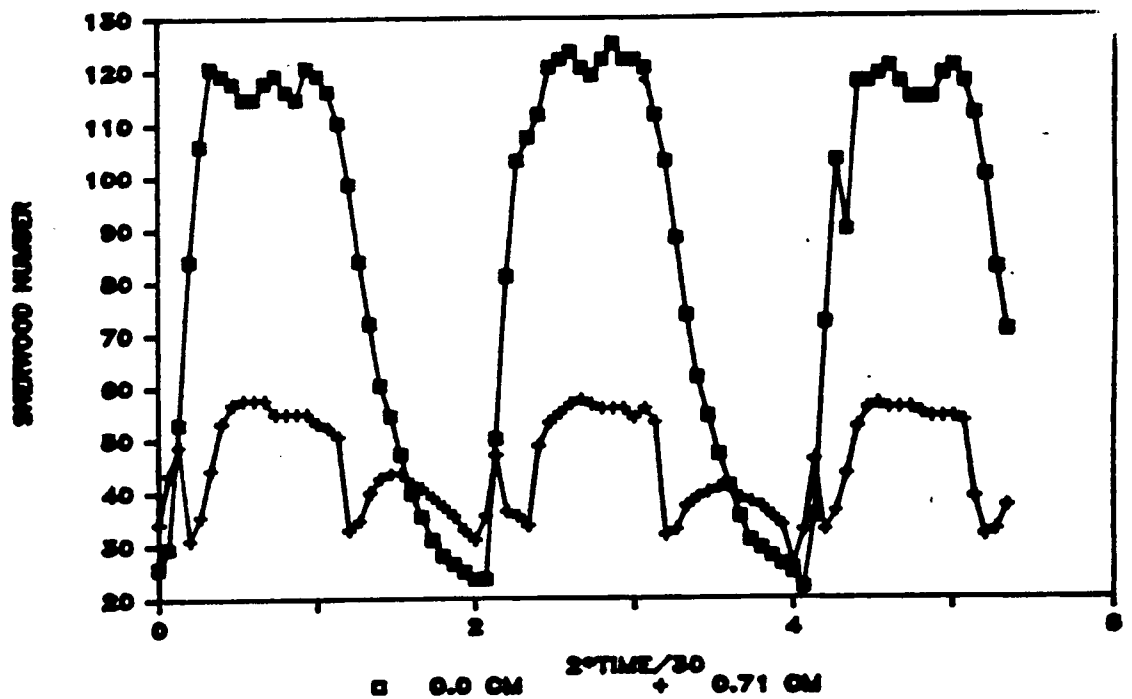


Figure 4.70: The Sherwood number vs.  $2 \cdot t$  scaled with the cycle period for ACRT at 65 RPM and a 30 second period.

ORIGINAL PAGE IS  
OF POOR QUALITY



spin-down. This has been ascribed to the stagnation vortex becoming depleted of reactant. It may well be that the flow induced by spin-up overcomes this vortex. The interfacial mass transfer at the edge does not show a decrease in the interfacial mass transfer in the initial stages of spin-up. The flow visualization experiments did not show any stagnation vortices over the regions away from the central axis along the endwall during spin-down. While computer simulations did reveal vortices along the endwall during spin-down, they did not stagnate [55]. They formed and moved inward towards the central axis. At the edge it does not appear that spin-up overcomes the flow induced by spin-down.

The fluid motion induced during spin-up is caused by centrifugal force throwing fluid outward along the cylinder endwall. Since the force is proportional to the distance away from the rotation axis, it is weakest at the central axis. This is where the flow visualization experiments show the stagnation vortex. The decrease in the interfacial mass transfer during the initial stages of spin-up at the center may be caused by spin-up having to overcome the stagnation vortex formed in spin-down. The vortex must be slowed, causing the mass transfer to decrease. Once the vortex is annihilated, the mass transfer begins to increase. At the outer edge, there is no decrease in the interfacial mass transfer during the initial stages of spin-up because the centrifugal force is great enough to overcome any inward fluid motion.

The reason the initial decrease in the Sherwood number at the center is not seen in the 12 RPM data is that the inertia of the fluid is small and spin-up can readily overcome the spin-down vortex. For the longer time periods at 20 RPM, the transients in the interfacial mass transfer are nearly over. The interfacial mass transfer during the initial stages of spin-up is not retarded because the stagnation vortex is weak enough to be overcome. Hence, the retarding of the interfacial mass transfer is not seen.

Figures 4.71 through 4.76 show the data for the 100 RPM short period ACRT. The results are not very different than those found in the 65 RPM trials. Even at these rotation rates, which Brice et al. [10] claim to be highly unstable, the interfacial mass transfer follows the same pattern as seen at 65 RPM.

The paper by Brice et al. [10] and the flow visualization experiments performed here show that the bulk mixing can be non-axisymmetric. A series of experiments were made at the same Ekman numbers as the previous two series (65 and 100 RPM). Instead of monitoring the center electrode, a second edge electrode was monitored. The center electrode was shorted to the nickel endplug. The two edge electrodes were placed as closely as possible to the same radial position, but they were 180 degrees opposed. If the theoretically predicted [10] non-axisymmetric bulk mixing should cause non-axisymmetric interfacial mass transfer, this placement of the electrodes would have detected it.

Figures 4.77 through 4.86 show the results of the axisymmetry tests. These figures show that the interfacial mass transfer remained nearly axisymmetric. The two point electrodes experienced changes in the mass transfer on the same time scale. When a paired comparison test is performed on the Sherwood numbers for the two electrodes, they are shown to be from different populations. Thus, the two electrodes are not the same [75]. Any differences in the data taken 180 degrees apart can be ascribed to the fact that the electrodes differ in position by an electrode radius (see Appendix B). Once again, these results show the limitations of flow visualization applied to crystal growth. While crystal growth is an interfacial phenomenon, flow visualization reveals only bulk mixing. Thus, interfacial mass transfer measurements should be used to set the criterion for optimal mixing conditions, rather than flow visualization.

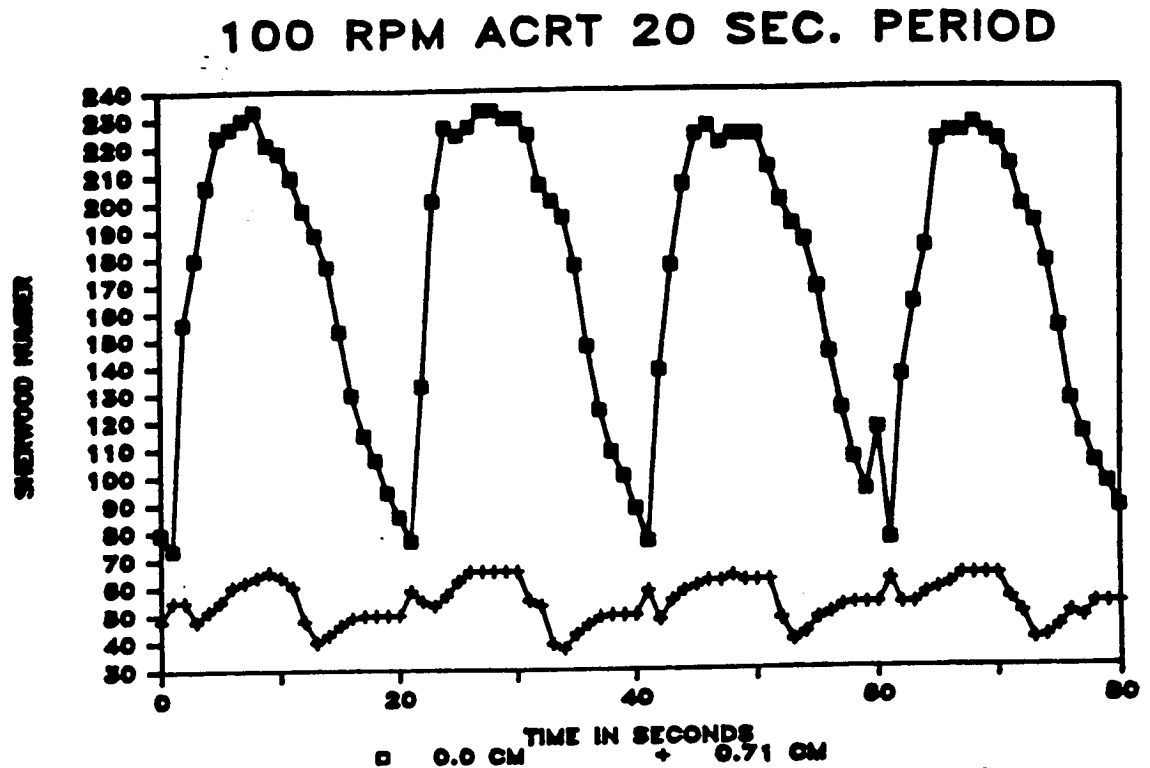


Figure 4.71: The Sherwood number vs. time for ACRT at 100 RPM and a 20 second period.

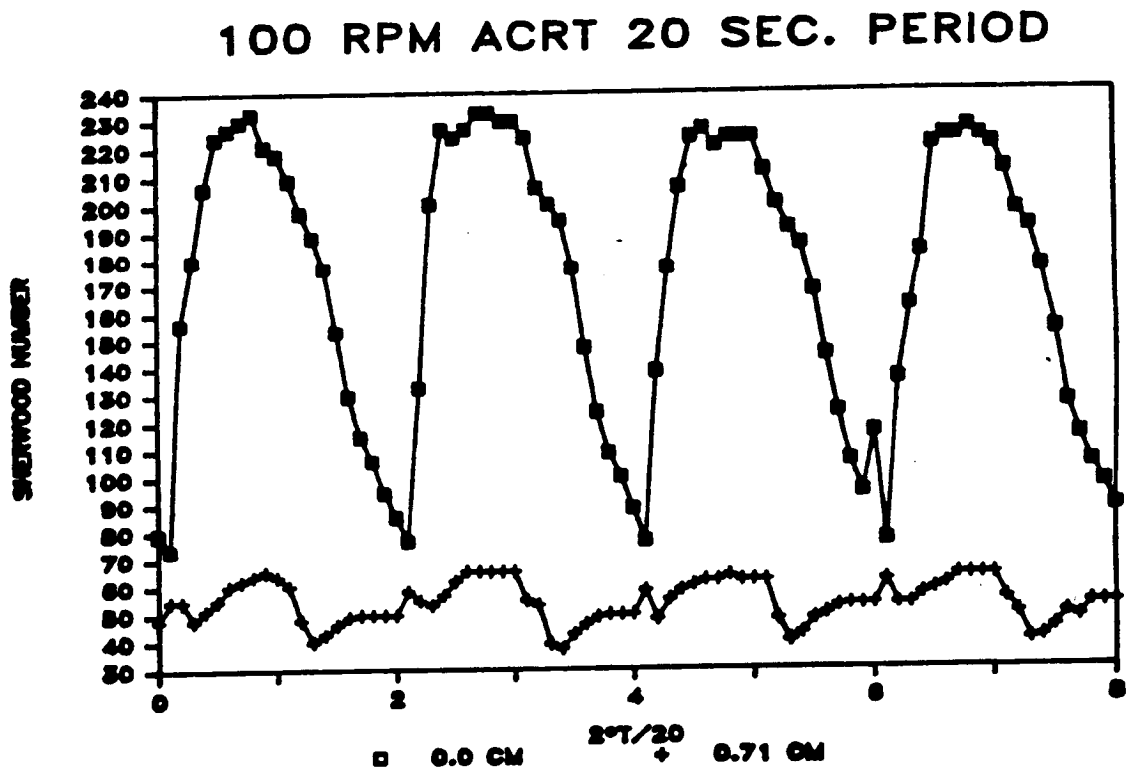


Figure 4.72: The Sherwood number vs.  $2\pi t$  scaled with the cycle period for ACRT at 100 RPM and a 20 second period.

# 100 RPM ACRT 40 SEC. PERIOD

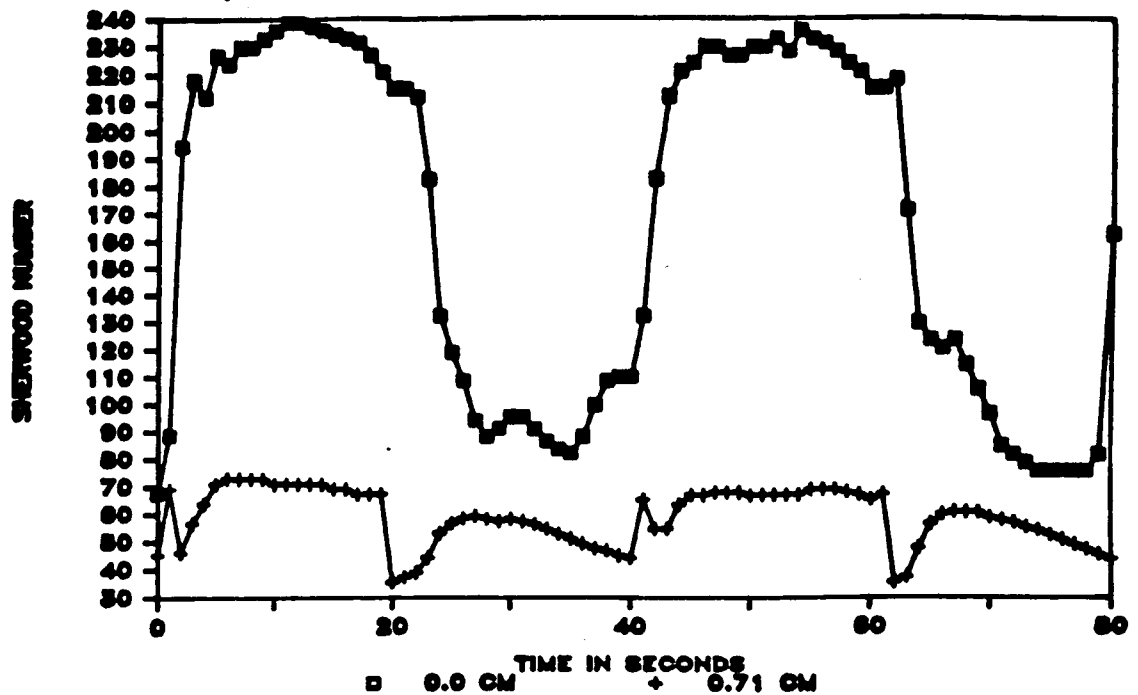


Figure 4.73: The Sherwood number vs. time for ACRT at 100 RPM and a 40 second period.

# 100 RPM ACRT 40 SEC. PERIOD

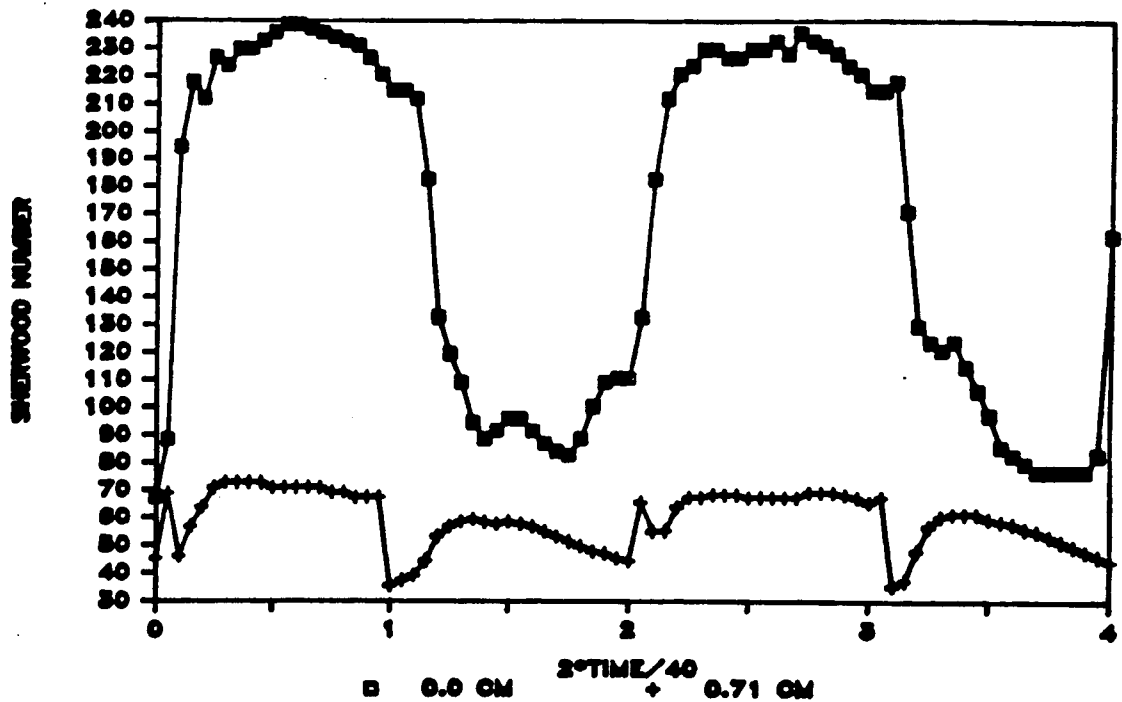


Figure 4.74: The Sherwood number vs.  $2 \cdot t$  scaled with the cycle period for ACRT at 100 RPM and a 40 second period.

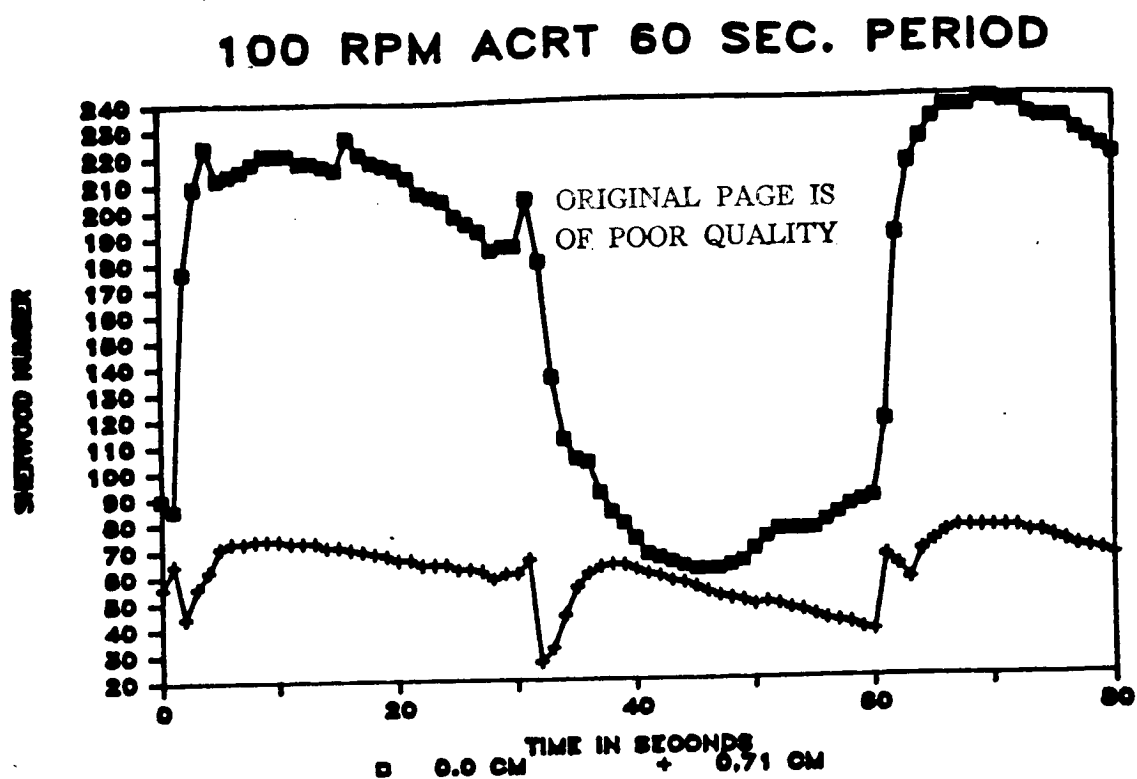


Figure 4.75: The Sherwood number vs. time for ACRT at 100 RPM and a 60 second period.

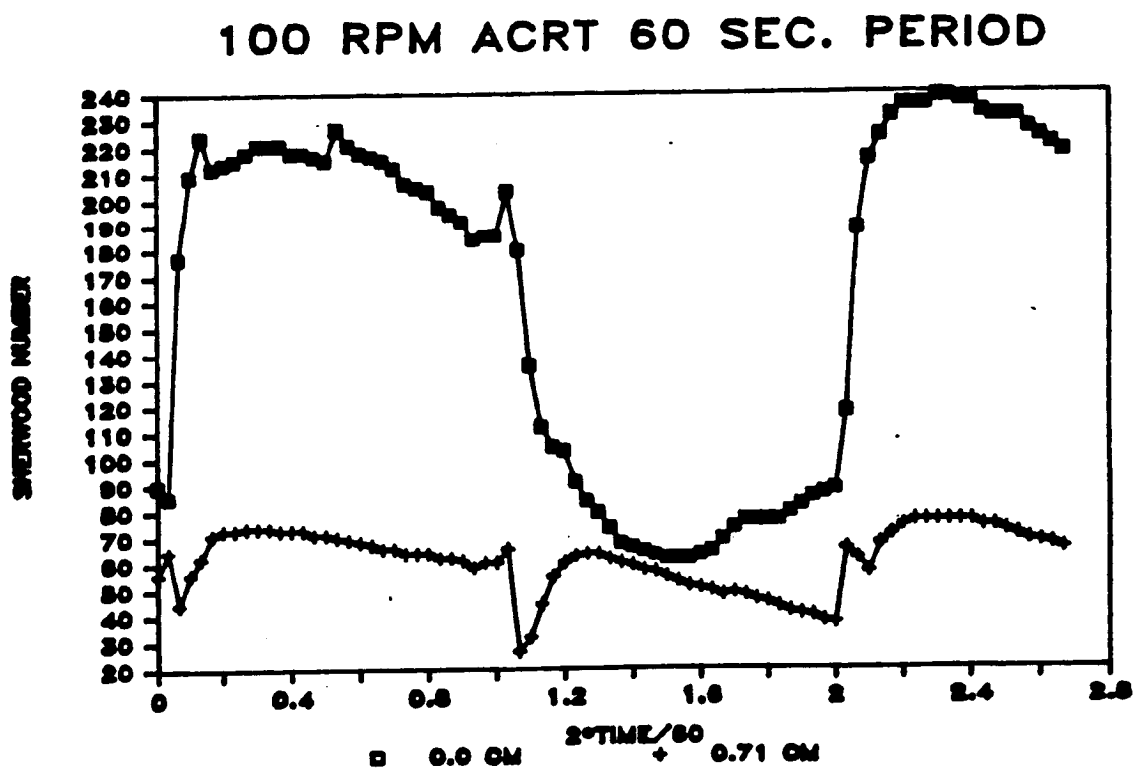


Figure 4.76: The Sherwood number vs.  $2 \cdot t$  scaled with the cycle period for ACRT at 100 RPM and a 60 second period.

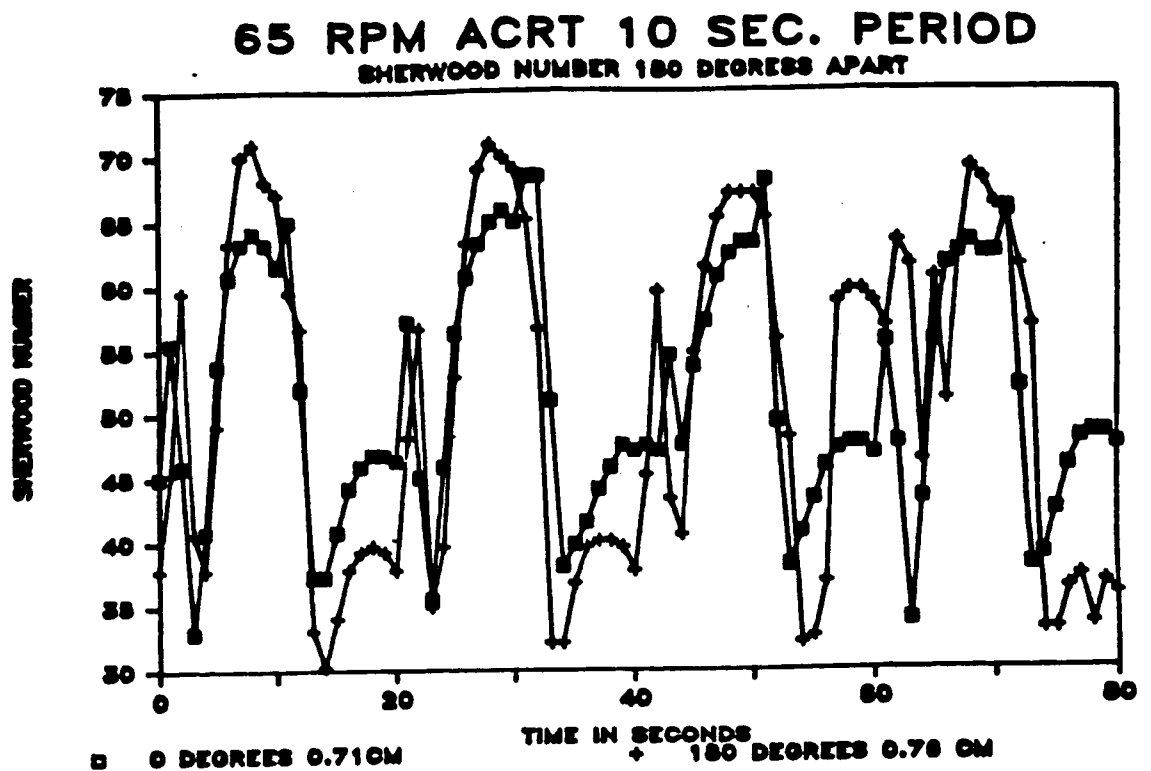


Figure 4.77: The Sherwood number vs. time for ACRT at 65 RPM and a 10 second period. The two electrodes are 180 degrees opposed.

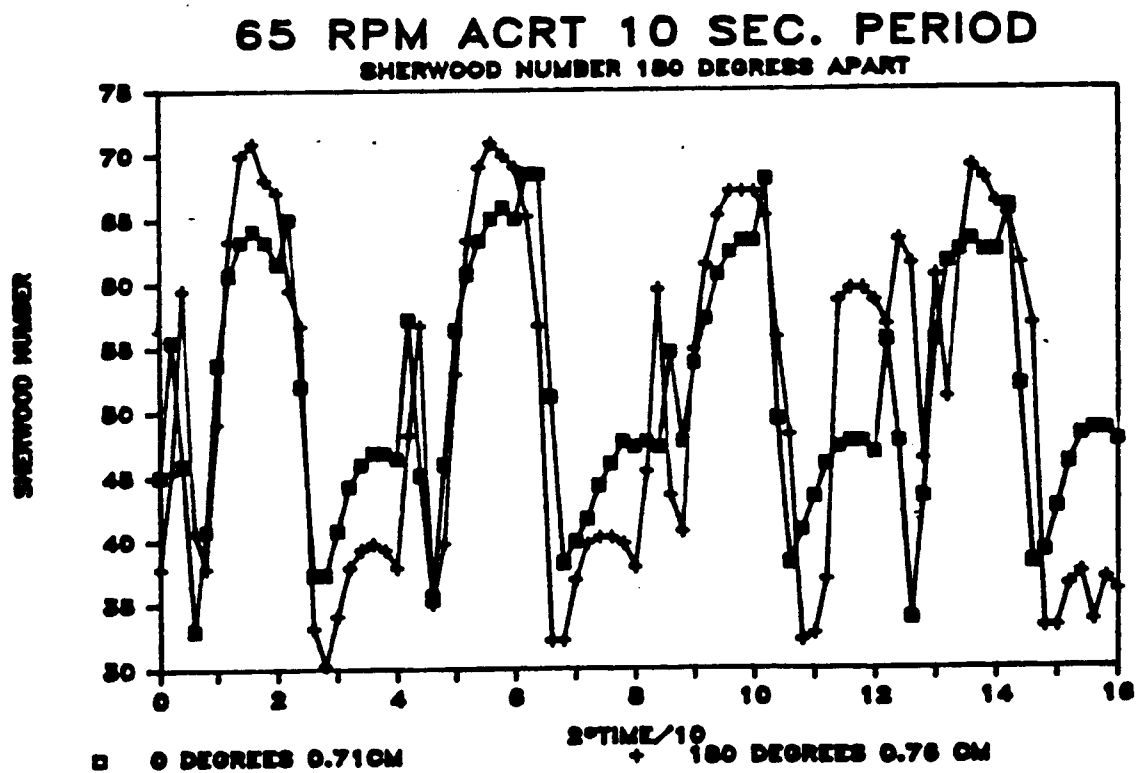


Figure 4.78: The Sherwood number vs.  $2 \cdot \text{time}$  scaled with the cycle time for ACRT at 65 RPM and a 10 second period. The two electrodes are 180 degrees opposed.

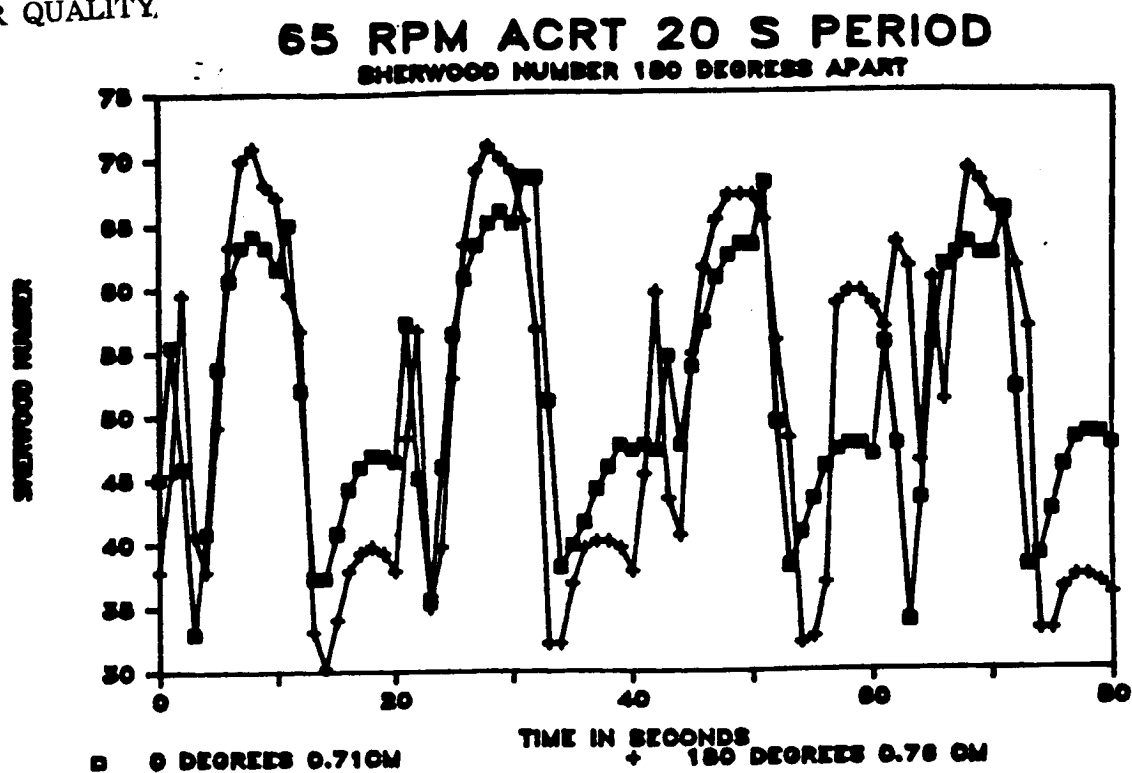


Figure 4.79: The Sherwood number vs. time for ACRT at 65 RPM and a 20 second period. The two electrodes are 180 degrees opposed.

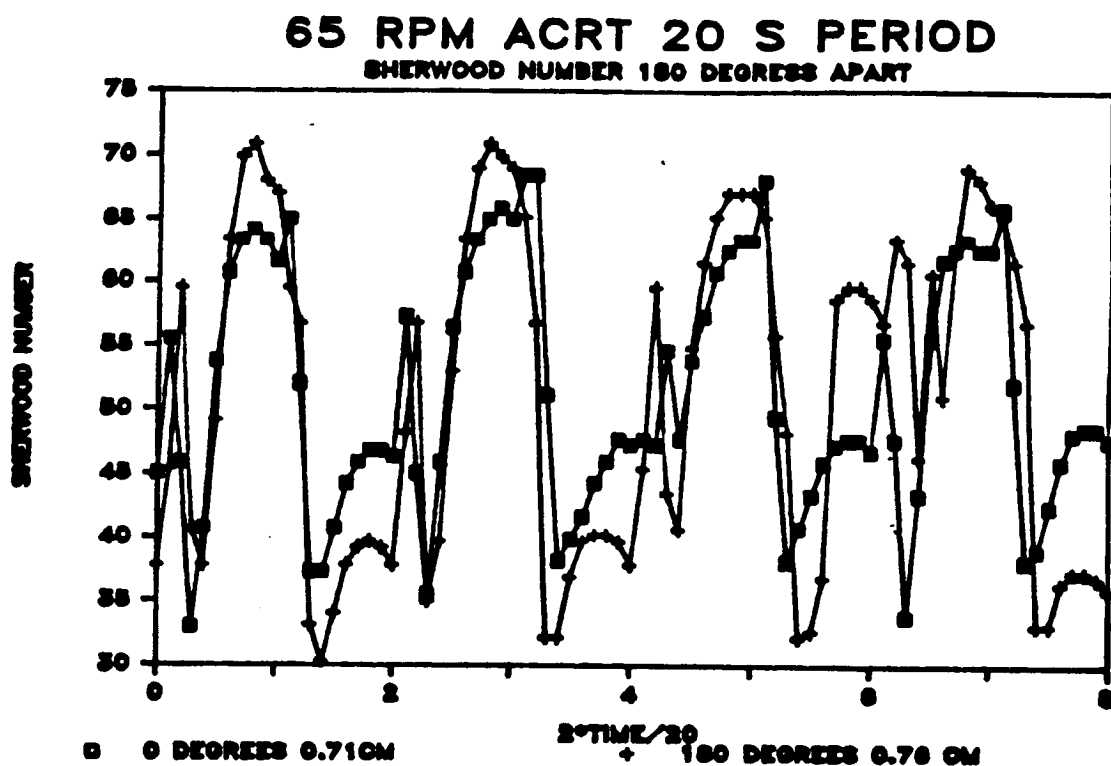


Figure 4.80: The Sherwood number vs.  $2 \cdot \text{time} / 20$  scaled with the cycle time for ACRT at 65 RPM and a 20 second period. The two electrodes are 180 degrees opposed.

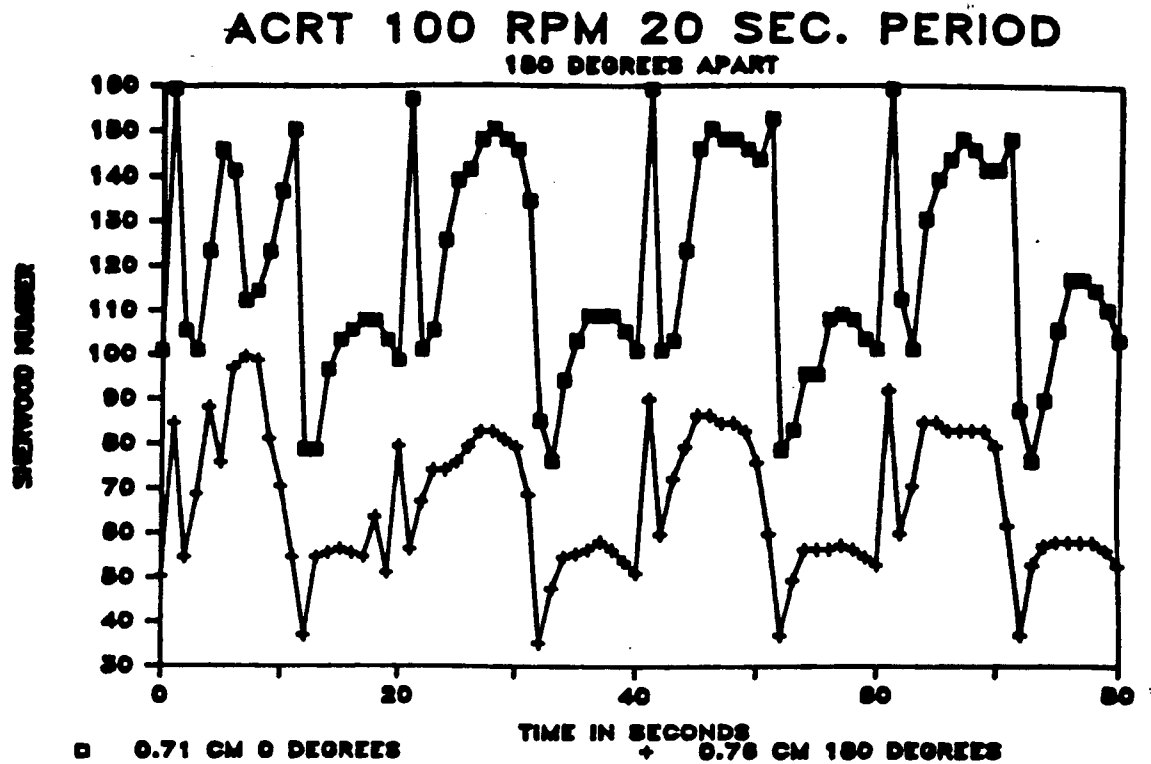


Figure 4.81: The Sherwood number vs. time for ACRT at 100 RPM and a 20 second period. The two electrodes are 180 degrees opposed.

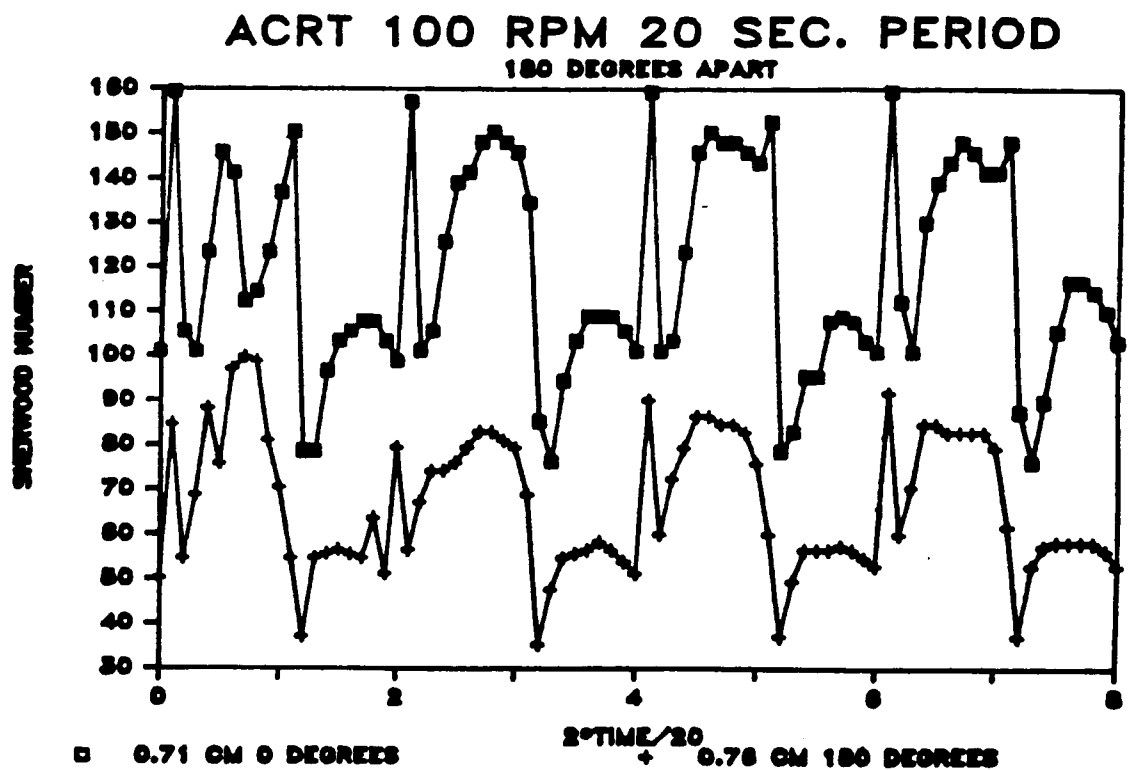


Figure 4.82: The Sherwood number vs. 2\*time scaled with the cycle time for ACRT at 100 RPM and a 20 second period. The two electrodes are 180 degrees opposed.



# 100 RPM ACRT 40 SEC. PERIOD 180 DEGREES APART

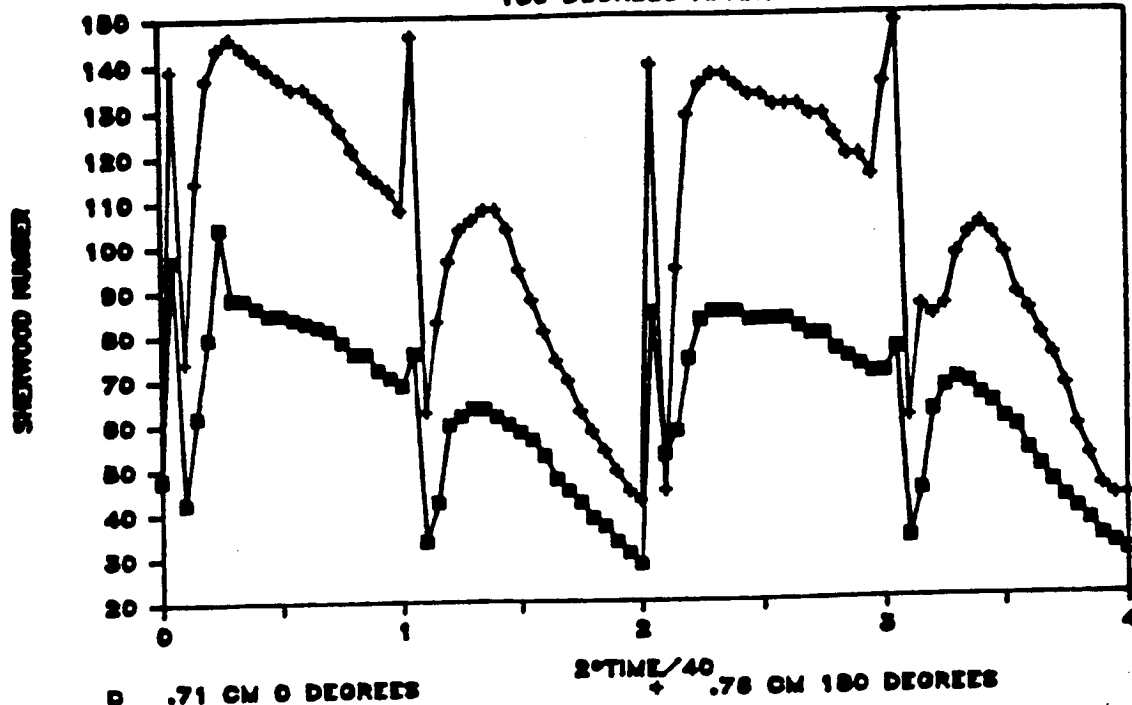


Figure 4.83: The Sherwood number vs. time for ACRT at 100 RPM and a 40 second period. The two electrodes are 180 degrees opposed.

# 100 RPM ACRT 40 SEC. PERIOD 180 DEGREES APART

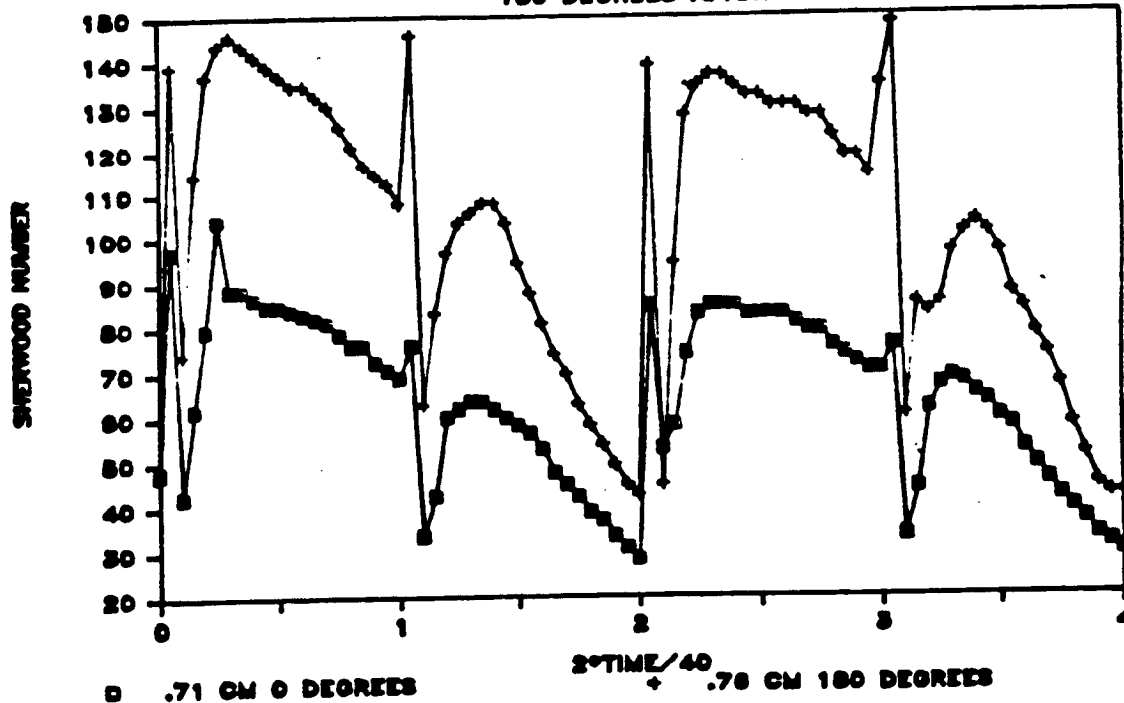


Figure 4.84: The Sherwood number vs. 2\*time scaled with the cycle time for ACRT at 100 RPM and a 40 second period. The two electrodes are 180 degrees opposed.

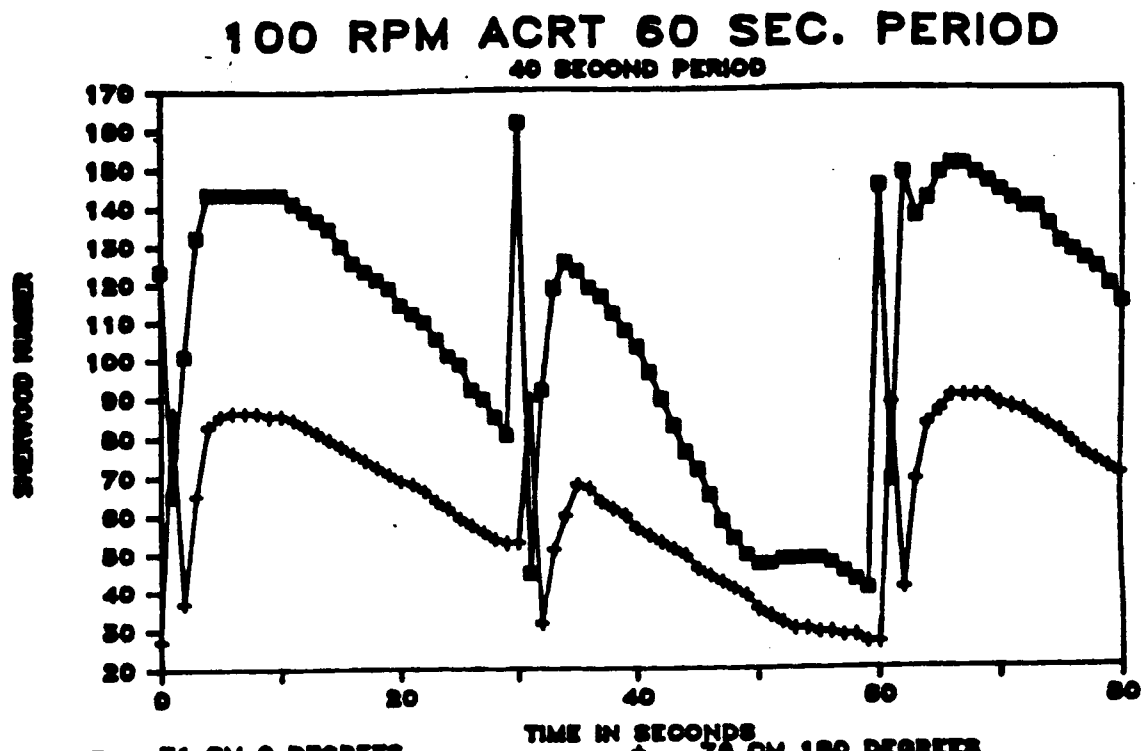


Figure 4.85: The Sherwood number vs. time for ACRT at 100 RPM and a 60 second period. The two electrodes are 180 degrees opposed.

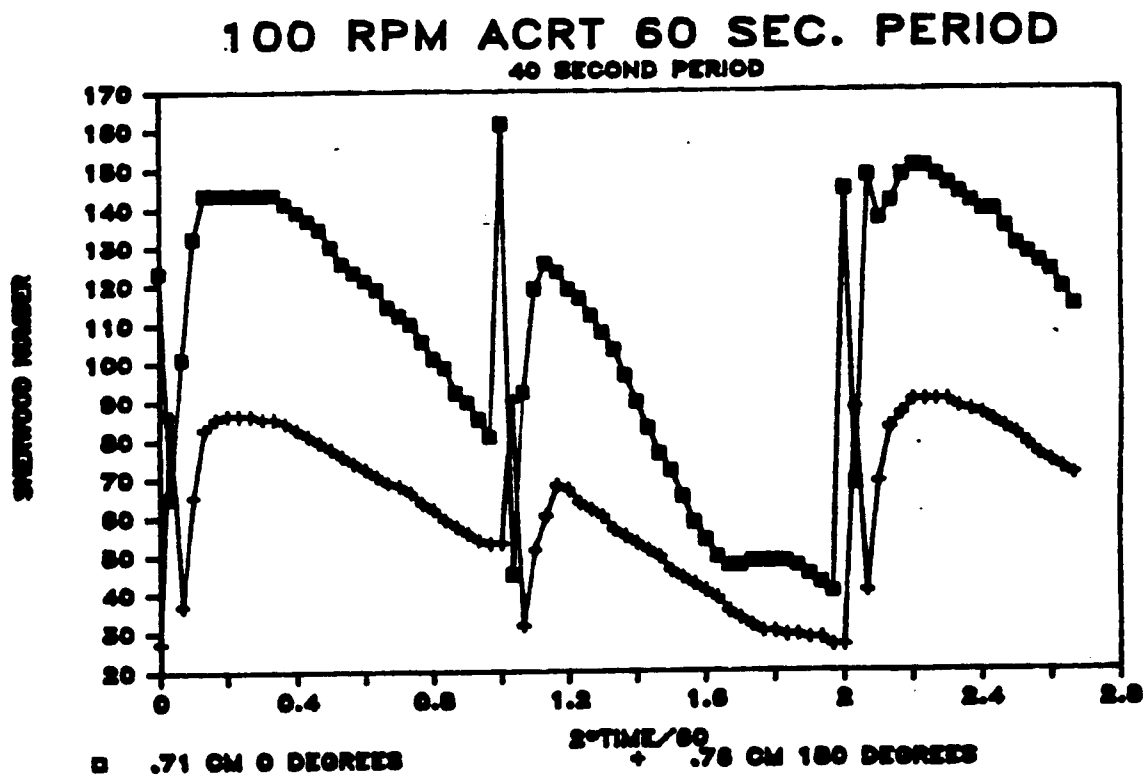


Figure 4.86: The Sherwood number vs.  $2 \cdot \text{time} / 60$  scaled with the cycle time for ACRT at 100 RPM and a 60 second period. The two electrodes are 180 degrees opposed.

#### 4.2.5 Mass Transfer Under Linear ACRT Conditions

A dimensionless group mentioned in the literature review was the Rossby number. It gives the ratio of the inertial to Coriolis forces. It is a gauge that determines the importance of the spatial change in angular velocity during ACRT. As the Rossby number approaches zero, the angular velocity of the fluid does not deviate very much from its original velocity, upon an impulsive change in the rotation rate. The Navier-Stokes equation [65] becomes a linear partial differential equation [52]. The resulting flows are referred to as linear ACRT. For Rossby numbers approaching unity, the Navier-Stokes equation becomes non-linear because the spatial angular velocity change is large [52]. Furthermore, in linear spin-up the Stewartson layer remains attached to the cylinder wall [52]. The available theory for mixing in ACRT does not take this into account [10].

Experiments were conducted with a Rossby number equal to 0.08. This was the smallest Rossby number that the experimental apparatus achieve. The rotation rate was controlled manually and, as previously mentioned, 150 RPM was the maximum rotation rate for safe operation. Figures 4.89 through 4.92 show the Sherwood number during linear ACRT for 20 and 60 second periods between 138 and 150 RPM. The motor control circuit was only capable of altering the rotation speed between rest and one preselected value, thus these experiments were conducted manually. As in the non-linear studies the edge mass transfer oscillated at twice the frequency of the center and the center mass transfer had a frequency equal to the ACRT forcing frequency.

For the 12 RPM runs shown in figures 4.89 through 4.92, the Ekman number was 0.0161 and the Ekman time was 6.3 seconds, the same values as those in the non-linear 12 RPM investigations. Spin-up has a single peak like those in the

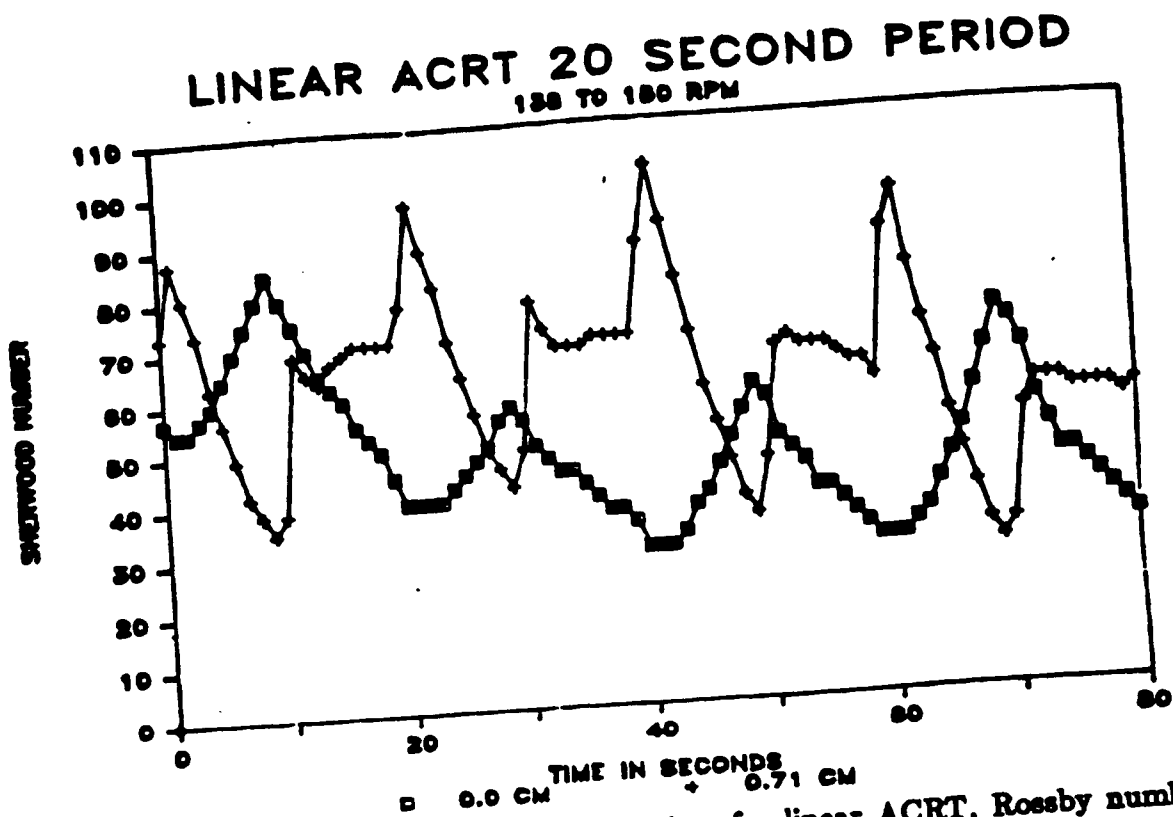


Figure 4.87: The Sherwood number vs. time for linear ACRT, Rossby number = 0.08, and a 20 second period.

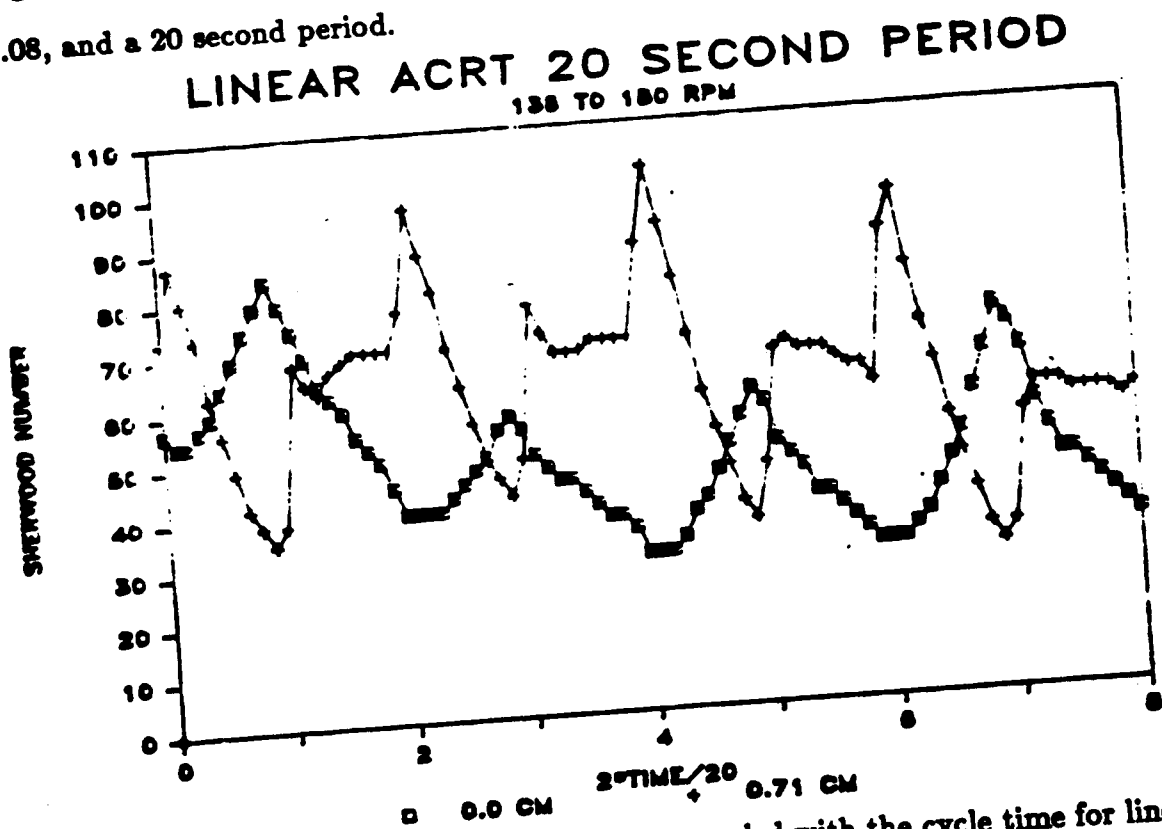


Figure 4.88: The Sherwood number vs. 2\*time scaled with the cycle time for linear ACRT, Rossby number = 0.08, and a 20 second period.

ORIGINAL PAGE IS  
OF POOR QUALITY

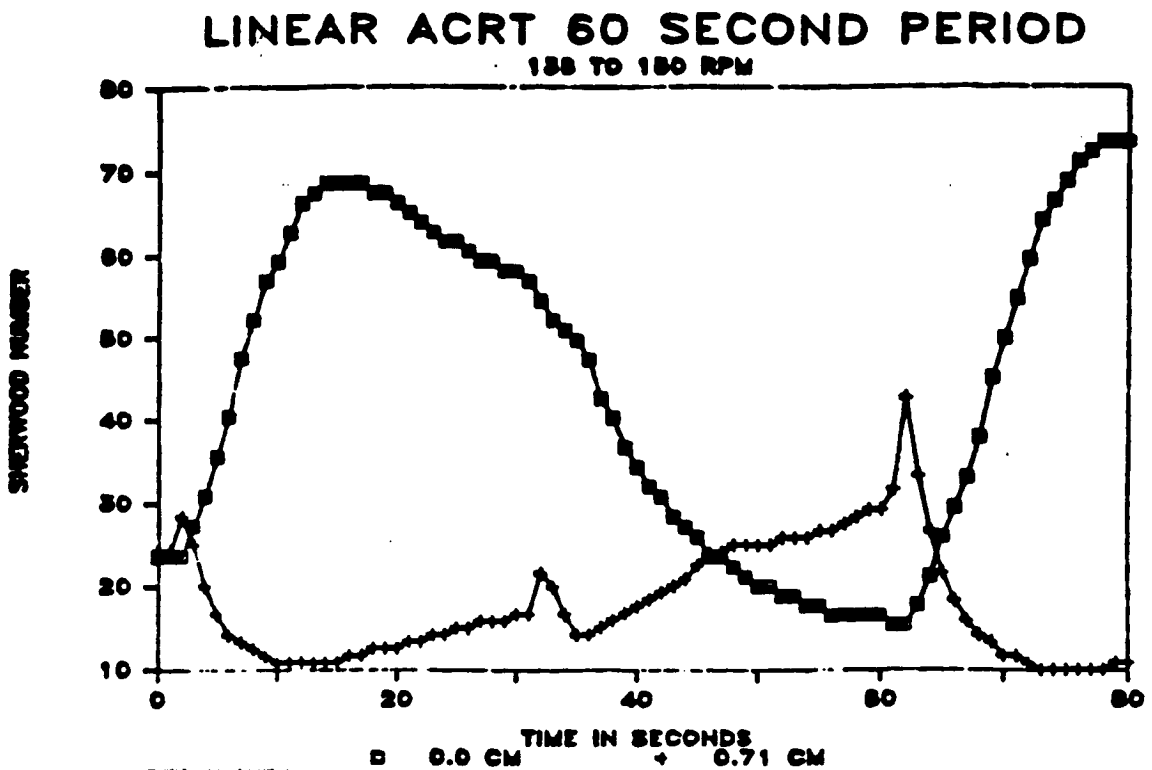


Figure 4.89: The Sherwood number vs. time for linear ACRT, Rossby number = 0.08, and a 60 second period.

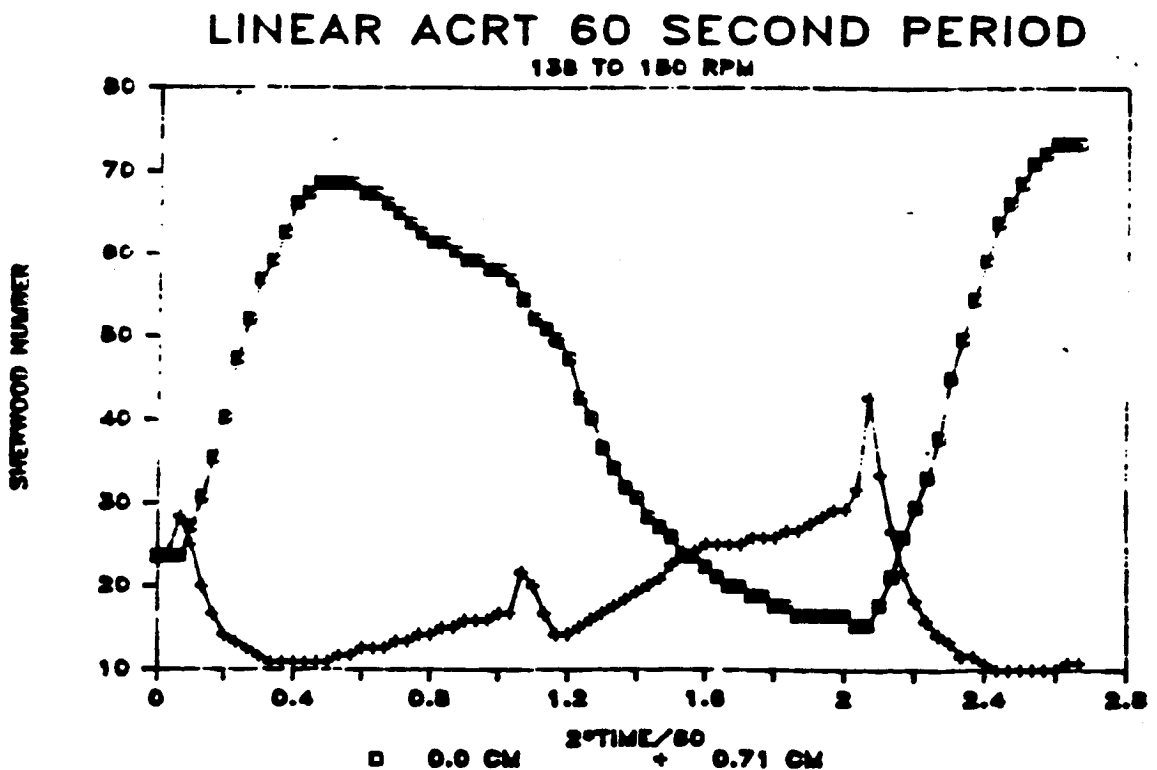


Figure 4.90: The Sherwood number vs.  $2 \cdot \text{time}$  scaled with the cycle time for linear ACRT, Rossby number = 0.08, and a 20 second period.

nonlinear studies. Spin-down has a sharp peak and then a broad increase, until the next spin-up cycle, which was not seen in the non-linear work.

## 5 DISCUSSION

### 5.1 Modelling Long Period ACRT

Statistical curve fits are used to predict Sherwood number during spin-up and spin-down. All the statistical fits were checked for transformable nonadditivity using the tests provided in Box et al. [66]. Existing theoretical models for mass transfer in a rotating fluid are confined to spin-up. The turbulence flow separation and vortices observed during spin-down makes finding an analytic solution too difficult.

Most of the mass transfer vs. time plots look like a log-normal distribution function. In general, the Sherwood number was fitted to an equation having the same form as the log-normal distribution function. Table 5.1 gives, in outline form, the curve fits for the Sherwood numbers. Table 5.2 gives the experimental conditions used to obtain the equations in Table 5.1.

### 5.2 Comparison of Long Period Spin-Up Results with Theoretical Models

Treating the interface as a rotating disk during ACRT is often used in theoretical models [52]. Many theoretical models for spin-up in cylinders begin by investigating the flow generated between two disks of infinite extent undergoing an impulsive increase in rotation rate [5]. Benton and Clark [52] point out that the theories need only slight modification to account for spin-up in closed cylinders. Once the velocity profiles are determined, they are placed in the convective-diffusion equation (Equation 2.30) to solve for the concentration profile [65]. Using this procedure, Levich [67] solved the convective-diffusion equation for a single, finite size, rotating disk at a steady state in an infinite fluid. There are no time dependent terms in

Table 5.1: Correlations for the spin-up data.

1. SPIN-UP FROM REST

(a) CENTER ELECTRODE

$$i. Ln(Sh) = 3.756 + 0.364\left(\frac{t}{t_{Ek}}\right) - 116.4Ek + 7.315(10^{-5})Sc$$

$$R^2 = 81.0\%$$

$$ii. Ln(Sh) = -7.312 - 1.012Ln(Ek) - 0.611Ln\left(\frac{t}{t_\nu}\right) - 0.107\left(Ln\left(\frac{t}{t_\nu}\right)\right)^2 \quad R^2 = 95.5\%$$

(b) EDGE ELECTRODES

$$i. Ln(Sh) = -370.63Ek + 0.0932Sc + 14.48Ln(Ek) - 436.13Ln(Sc) + 4.575Ln\left(\frac{r}{R}\right) - 0.325Ln\left(\frac{t}{t_{Ek}}\right) - 0.146\left(Ln\left(\frac{t}{t_{Ek}}\right)\right)^2 \quad R^2 = 91.0\%$$

$$ii. A = -5.23 - 2.22\frac{t}{t_{Ek}} + 0.781Ln\left(\frac{t}{t_{Ek}}\right) - 0.630Ln(Ek) + 0.852Ln(Sc) - 0.932Ln\left(\frac{r}{R}\right) \\ Sh = 6.313 + 4.688 * (10^{-3})EXP(A) \quad R^2 = 78.6\%$$

$$iii. \text{ Use Result from Equation IB1 with } \frac{t}{t_{Ek}} = 1.0$$

$$iv. Ln(Sh) = -5.49 + 5.18 * (10^{-5})Sc + 9.30\frac{t}{t_\nu} - 6.659Ln\left(\frac{t}{t_\nu}\right) - 1.10\left(Ln\left(\frac{t}{t_\nu}\right)\right)^2 \quad R^2 = 86.8\%$$

$$v. Ln(Sh) = -346 - 0.43 * (10^{-3})Sc + 44.0Ln(Sc) + 0.06716\left(Ln\left(\frac{t}{t_\nu}\right)\right)^2 + 0.878\left(Ln(Ek)\right)^2 + 2.655Ln\left(\frac{r}{R}\right) \quad R^2 = 84.7\%$$

2. SPIN-DOWN TO REST

(a) CENTER ELECTRODE

$$i. Sh = 25.806Ek^{0.912}Sc^{0.632} + 4.973\left(\frac{t}{t_\nu}\right) - 0.974\left(\frac{t}{t_\nu}\right)^2 \quad R^2 = 99.5\%$$

$$ii. \text{ Use the results of IA1 with } \frac{t}{t_{Ek}} = 1.0 \text{ for the Sherwood numbers.}$$

(b) EDGE ELECTRODES

$$i. Ln(Sh) = -21.9 - 1720Ek + 4.672Ln(Ek) - 1.43 * (10^{-3})Sc + 7.97Ln(Sc) - 0.150\left(Ln\left(\frac{t+2}{t_{Ek}}\right)\right)^2 \quad R^2 = 81.4\%$$

$$ii. Ln(Sh) = -34.9 - 0.773Ln(Ek) - 4.57Ln(Sc) + 0.372Ln\left(\frac{H}{R}\right) + 3.814Ln\left(\frac{r}{R}\right) - 1.65Ln\left(\frac{t}{t_{Ek}}\right) + 0.467\left(Ln\left(\frac{t}{t_{Ek}}\right)\right)^2 \quad R^2 = 76.1\%$$

where,  $Sh$  = Sherwood number,  $Ek$  = Ekman number,  $Sc$  = Schmidt number,  $t$  = time,  $r$  = Radial position,  $R$  = Radius,  $H$  = Length of cylinder and the subscripts  $\nu$  and  $Ek$  denote the characteristic viscous and Ekman times, respectively.



Table 5.2: VALIDITY REGIONS FOR EQUATIONS IN TABLE 5.1

(ALL LENGTHS ARE GIVEN IN CM)

Equation	Ekman		Schmidt		Position		Radius		Times
	min.	max.	min.	max.	min.	max.	min.	max.	
I.A.1	0.00176	0.00995	3320	8960	0.0	0.0	0.95	1.21	$0 < t < t_{EK}$
I.A.2	0.00176	0.00995	3320	8960	0.0	0.0	0.95	1.21	$t_{Ek} < t < t_\nu$
I.B.1	0.00919	0.0219	3320	6093	0.71	0.76	0.95	1.21	$0 < t < t_{Ek}$
I.B.2	0.00176	0.00746	2230	8960	0.71	0.76	0.95	1.21	$0 < t < t_{Ek}$
I.B.3	0.00919	0.0219	3320	6093	0.71	0.76	0.95	1.21	$t_{Ek} < t < t_\nu$
I.B.4	0.00176	0.00337	3320	8960	0.71	0.71	0.95	0.95	$t_{Ek} < t < t_\nu$
I.B.5	0.00337	0.00746	3320	8960	0.71	0.76	0.95	1.21	$t_{Ek} < t < t_\nu$
II.A.1	0.00176	0.00504	2230	8960	0.0	0.0	0.95	0.95	$0 < t < t_\nu$
II.A.2	0.00504	0.00919	3320	8960	0.0	0.0	0.95	1.21	$0 < t < t_\nu$
II.B.1	0.00176	0.00488	2230	8960	0.71	0.71	0.95	0.95	$0 < t < t_\nu$
II.B.2	0.00504	0.00995	2230	3320	0.71	0.76	0.95	1.21	$0 < t < t_{Ek}$

the equation, so it is of little value in modeling mass transfer to a cylinder endwall. Levich's equation was very useful for calculating the diffusion coefficient from experiments on a rotating disk of the type shown in figure 2.9. Levich's equation is:

$$i_{Lim} = 0.62nF\nu^{-\frac{1}{2}}C_{bulk}\omega^{\frac{1}{2}}D^{\frac{1}{2}} \quad (5.41)$$

where  $n$  is the number of moles of electrons transferred per mole of reactant,  $F$  is Faraday's constant,  $\nu$  is the kinematic viscosity,  $\omega$  is the rotation rate,  $C_{bulk}$  is the bulk concentration of reactant, and  $D$  is the diffusivity of the reactant in the solution. If the physical properties in equation 5.41 are known, one can measure the limiting current density on a rotating disk and calculate the diffusivity. This procedure was used to calculate the diffusivity using data like that shown in Figure 3.9 for each batch of electrolyte used in this investigation.

Bruckenstein et al. [73] solved the problem of mass transfer to a rotating disk after an impulsive increase in the rotation rate. Bruckenstein's equation includes a time dependency. The major conclusion to be drawn from this model is that the fluid mechanics are decoupled from the mass transfer. Solution of the convective-diffusive equation is simplified because the fluid flow is constant. Viewed differently, the transient involves only the time it takes for the fictitious film thickness to reach a new steady state. The graphs of Sherwood number vs. time given here often showed the mass transfer transients last much longer than the Ekman time. Bruckenstein et al.'s model, in Sherwood number notation is:

$$\omega t = \frac{0.4375[F(Y) - F(L)]}{Q} \quad (5.42)$$

where:

$$Q = 0.8058 * Sc^{-\frac{1}{3}} \quad (5.43)$$

$$Y = \frac{Sh_f}{Sh_t} \quad (5.44)$$

$$L = \frac{Sh_f}{Sh_o} \quad (5.45)$$

$$F(x) = 0.5 * Ln\left(\frac{1-x^3}{(1-x)^3}\right) - 3^{\frac{1}{2}} ATAN\left(\frac{2x+1}{3^{\frac{1}{2}}}\right) \quad (5.46)$$

where  $ATAN$  is the arctangent and the subscripts  $o$ ,  $f$ , and  $t$  signify the initial, final and time  $t$  values of the Sherwood number ( $Sh$ ), respectively. Here  $Sc$  is the Schmidt number,  $Ln$  is the log in base  $e$ , and  $\omega$  is the angular velocity. This equation may be rearranged to:

$$F(Y) = 2.286Qt\omega + F(L) \quad (5.47)$$

In a given experiment, the only variable is  $t$ . The value of  $Sh_f$  cannot be determined for a rotating cylinder endwall. Bruckenstein's equation is for a rotating disk and unlike a rotating disk, the walls of a rotating cylinder permit the fluid to reach rigid body rotation, preventing  $Sh_f$  from reaching Bruckenstein's prediction. The Sherwood number in a rotating cylinder increases and then decays back toward its original value. It may be of interest to use Bruckenstein's to curve fit the increasing segment of the Sherwood number vs. time curve obtained in the rotating cylinder experiments. In order to apply Bruckenstein's model applies to a rotating cylinder,  $Sh_f$  becomes an adjustable parameter.

The initial increases in Sherwood number were converted to the form required in the Bruckenstein model. A value of  $Sh_f$  was guessed and used to calculate  $Y$ , since  $Sh_t$  was known from experiment. The left hand side of equation 5.47 was regressed against the first term on the right hand side. The value of  $Sh_f$  giving the largest value of R-squared without transformable non-additivity was taken to be the value having the best fit to the data. The intercept obtained in the regression was placed in equation 5.45 to solve for  $L$ . Since  $Sh_f$  was guessed and  $Sh_o$  was known,  $L$

could be calculated. Comparison of the value of  $L$  obtained from the guessed value of  $Sh_f$  did not agree with the value calculated from the regression intercept. In fact, the calculated value always came out negative, which has no physical meaning. The results of the regression are presented in Table 5.3.

The regression results of the edge and center data differ. The first conclusion to be drawn is that the interface did not even act as a rotating disk after an impulsive increase in the rotation rate. If it had, the regression equations would have been the same for the center and edge positions. Bruckenstein's model is based on the same uniform access of fluid to the disk as in Levich's model. The available theories for spin-up [5,52] predict that the Stewartson layer crosses over the position of the edge electrode very early during spin-up, thereby affecting the access of reactant to the edge electrode. The most likely reason why the regression equations for the edge and center electrodes are different is because of the Stewartson layer blocking access to the edge electrode. The regression equations obtained from Bruckenstein's model for the center electrode show the equation may be used for times much greater than the Ekman time. Even though the Ekman layer flow is no longer steady, according to the available theories on spin-up [5,52], fluid is still pumped outward, causing suction over the center electrode, extending the range of the model past the Ekman time.

Futhermore, if the rotating cylinder endwall acted as a rotating, the slope and intercept would have certain values. If Bruckenstein's model held, the constant in front of the  $F(Y)$  terms in the equations given in Table 3 would be unity and the value of  $L$  obtained from the regression intercept would agree with that obtained from the guessed value of  $Sh_f$ .

The intermediate rotation rate data for the edge electrodes did not fit Bruck-

enstein's model at all. There is no apparent reason for this lack of fit; the data for rotation rates above and below this region do fit.

Bruckenstein's model for an impulsive increase in the rotation rate model does not apply to a cylinder undergoing impulsive spin-up. The functionality does describe the rate of increase during the early stages of spin-up. The model is certainly better than Levich's for spin-up in cylinders, which has been applied to a rotating cylinder endwall [10].

How does the mass transfer coefficient to a rotating cylinder endwall compare that of a rotating disk? The physical property data necessary to answer this question are incorporated into the Schmidt and Ekman numbers. The ratio mass transfer coefficient for a rotating disk to the average value of that obtained experimentally is given by:

$$\frac{K_{m,RD}}{K_{m,AVG}} = .62Ek^{-\frac{1}{2}}Sc^{\frac{1}{3}}Sh_{AVG}^{-1}\frac{L}{R} \quad (5.48)$$

where  $K_{m,RD}$  is the mass transfer coefficient for a disk rotating at the same angular velocity used in spin-up during the ACRT cycle,  $K_{m,AVG}$  is the average mass transfer coefficient for an ACRT cycle,  $Ek$  is the Ekman number for the ACRT cycle,  $Sc$  is the Schmidt number for the ACRT cycle,  $Sh_{AVG}$  is the average Sherwood number for the ACRT cycle,  $L$  is the characteristic length used in the Sherwood number and  $R$  is the cylinder radius used in the Ekman number. An order of magnitude estimate for the mass transfer coefficient ratio is about 20. (Typical experimental values for the dimensionless groups are  $Ek = 10^{-3}$ ,  $Sc = 10^3$ ,  $Sh_{AVG} = 10$ , and  $\frac{L}{R} = 1$ .) There is no similarity between the cylinder endwall undergoing ACRT and the rotating disk.

Table 5.3: RESULTS OF THE STATISTICAL FITS TO BRUCKENSTEIN'S MODEL

$A = 2.286\omega tQ$  CENTER ELECTRODE

Equation	R SQUARED	RPM	Sc	Ek	Time
$A = 1.253 * F(Y) + 2.501$	94.2 %	65	8960	0.0029	$0 < t < 6s$
$A = 2.234 * F(Y) + 1.874$	97.3%	40	2230	0.00315	$0 < t < 10s$
$A = 1.533 * F(Y) + 1.006$	93.5%	12	3320	0.00995	$0 < t < 26s$

EDGE ELECTRODE

Equation	R SQUARED	RPM	Sc	Ek	Time
$A = 2.923 * F(Y) + 2.147$	97.5%	12	3320	0.00995	$0 < t < 4s$
$A = 1.936 * F(Y) + 3.168$	87.3%	65	8960	0.0029	$0 < t < 5s$

COULD NOT OBTAIN A FIT WITH AN Ek == 0.00315 or 0.00663

### 5.3 Optimum Non-Linear ACRT Period

The objective in Bridgman crystal growth is to obtain homogeneous defect free crystals. This is an easy statement to make but a difficult objective to achieve. Many parameters can influence these desired results, the interface curvature, the amount of convection in the melt, the amount of impurity present and the growth rate. Given a zero growth rate for sufficient a amount of time and a planar interface the melt and solid will come to equilibrium and the solid at the interface will have a constant radial composition. However, a growth rate of zero is an impractical idealization, the growth rate must be finite to obtain crystals. Furthermore, a zero growth rate does not ensure a defect-free crystal, it only ensures a radial compositionally homogeneous crystal.

The maximum growth rate for a single crystal growth will be set by constitutional supercooling (see the literature review for more details). To obtain large single crystals, a slightly convex interface is desirable. Any spurious nucleation occurring at the solid-melt-ampoule intersection will be grown out when the interface is slightly convex. However, a curved interface implies radial temperature gradients, which produce convection and convection can produce compositional inhomogeneities (see the literature review). Thus the operating parameters favorable for obtaining a single crystal ingot are those which may produce compositional inhomogeneities in the Bridgman-Stockbarger apparatus.

There are many ways to overcome the free convection caused by radial temperature gradient. Convection may be suppressed by using a magnetic field, using reduced gravity by growing in space, or overwhelming it with forced convection. ACRT is used to do just that. The advantage of ACRT is that it produces mixing just where it is needed the most, at the melt-solid interface.

Chapter 4 presented mass transfer results from a large number of different conditions. Some conditions produces large average Sherwood numbers, others yielded larger spatial differences, while others gave large temporal variations. These variations in Sherwood number during solidification suggest that crystals should grow with compositional striations. It will be shown in Appendix 3 that solid state diffusion should play a key role is the elimination of these striations. A logical question to be asked is, what ACRT conditions produce crystals with the least compositional variations.

In order to obtain crystals without radial composition variations using ACRT, the interface mass transfer should have as small a radial variation as possible. Figures 5.1 through 5.5 show the average Sherwood number vs. ACRT period. They show that the average Sherwood number at the outer edge is fairly independent of the ACRT period, while the average Sherwood number at the center appears to be parabolic with the ACRT period. When the average Sherwood number at the edge is subtracted from the average Sherwood number at the center, one obtains a measure of the spatial variation in a ACRT cycle. This difference is also parabolic with the ACRT period because the edge is fairly independent of the ACRT period. Thus the difference can be fitted to an equation of the form:

$$\Delta SH_{AVG} = A_1 + A_2 T_P + A_3 T_P^2 \quad (5.49)$$

where  $\Delta Sh$  is the difference in the Sherwood number,  $A_1, A_2, A_3$ , are constants found during the curve fit and given in Table 5.4, and  $T_P$  is the length on the ACRT period in seconds. The first derivative of equation 5.49 with respect to the ACRT period gives the extremum condition and the second derivative tells whether it is a maximum or a minimum (since all the values of  $A_3$  are negative, the extrema are maximums). The values of the extrema are given in Table 5.5.



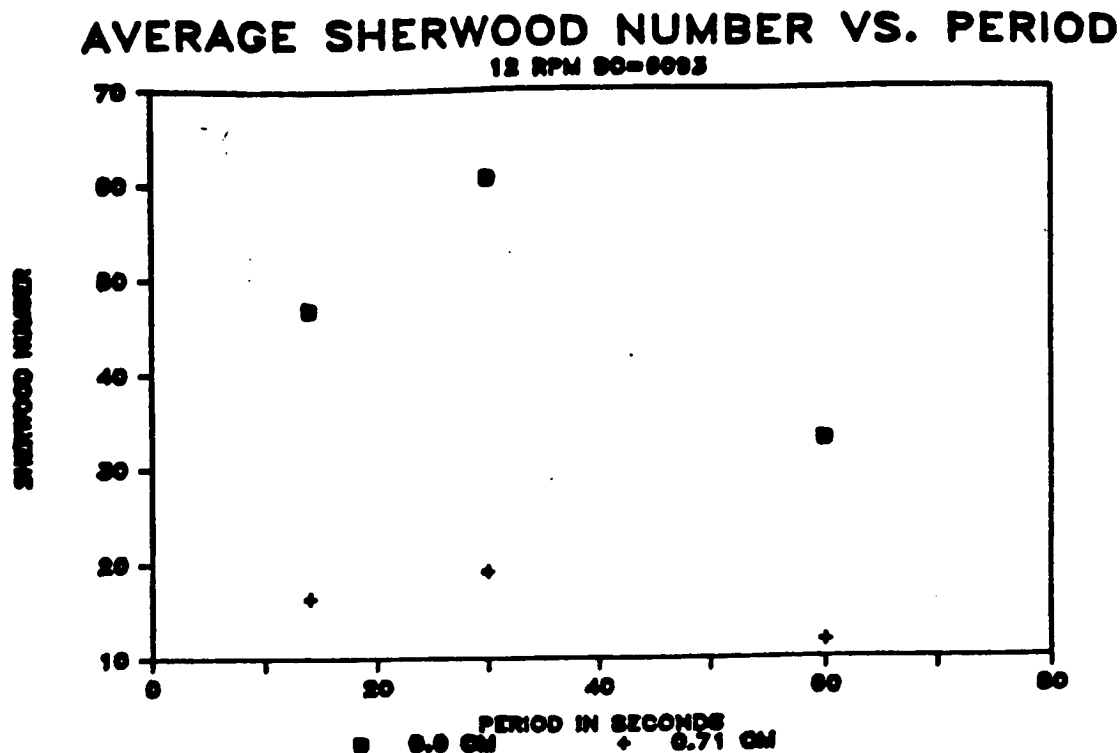


Figure 5.1: The average Sherwood number vs. the ACRT period length for 12 RPM and a Schmidt number equal to 6090.

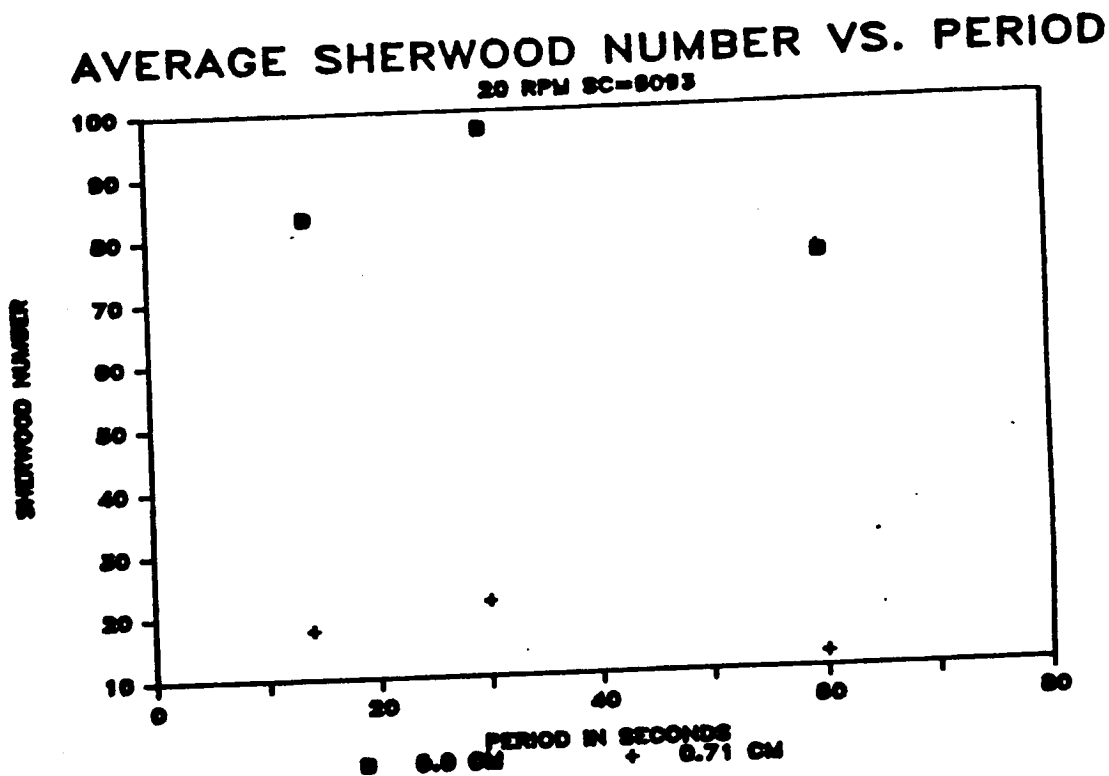


Figure 5.2: The average Sherwood number vs. the ACRT period length for 20 RPM and a Schmidt number equal to 6090.

ORIGINAL PAGE IS  
OF POOR QUALITY

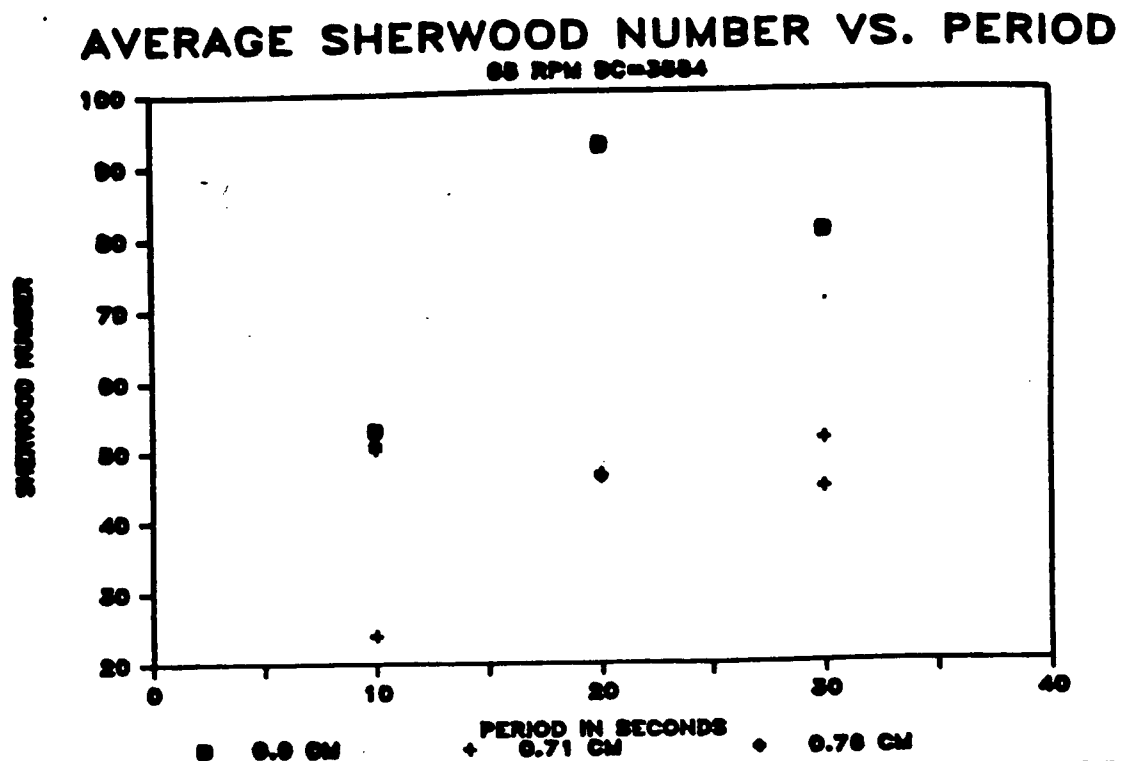


Figure 5.3: The average Sherwood number vs. the ACRT period length for 65 RPM and a Schmidt number equal to 3580.

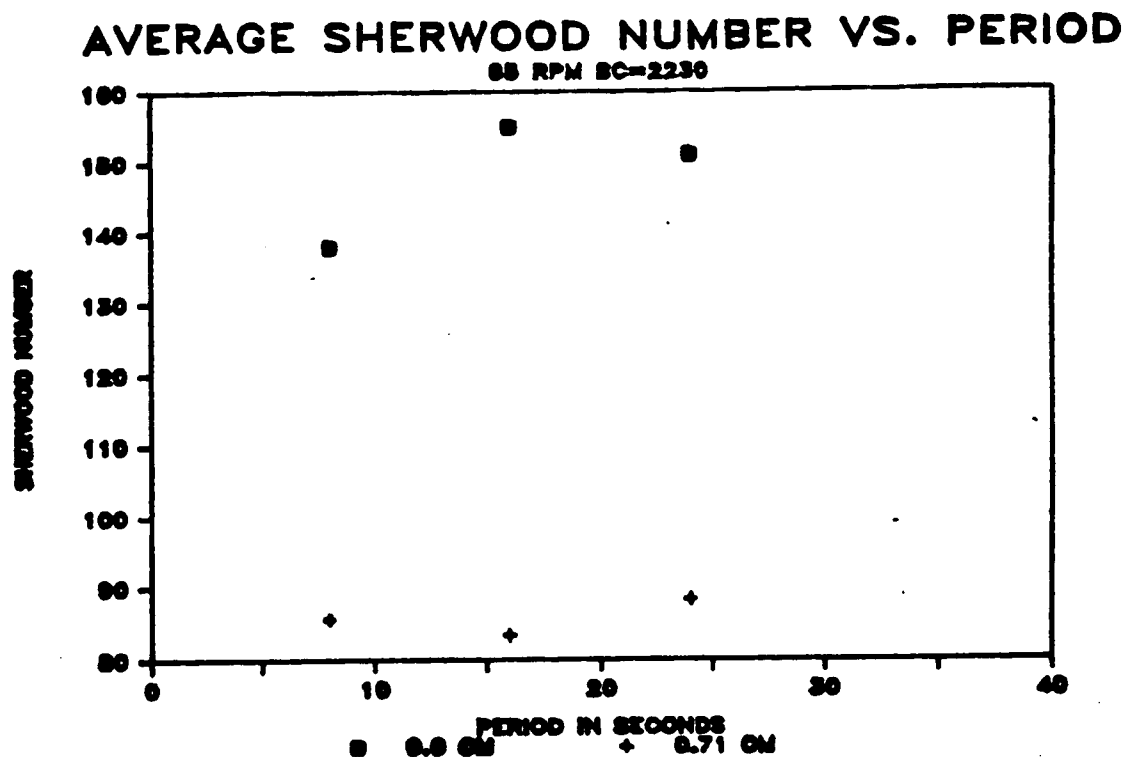


Figure 5.4: The average Sherwood number vs. the ACRT period length for 65 RPM and a Schmidt number equal to 2230.

ORIGINAL PAGE IS  
OF POOR QUALITY

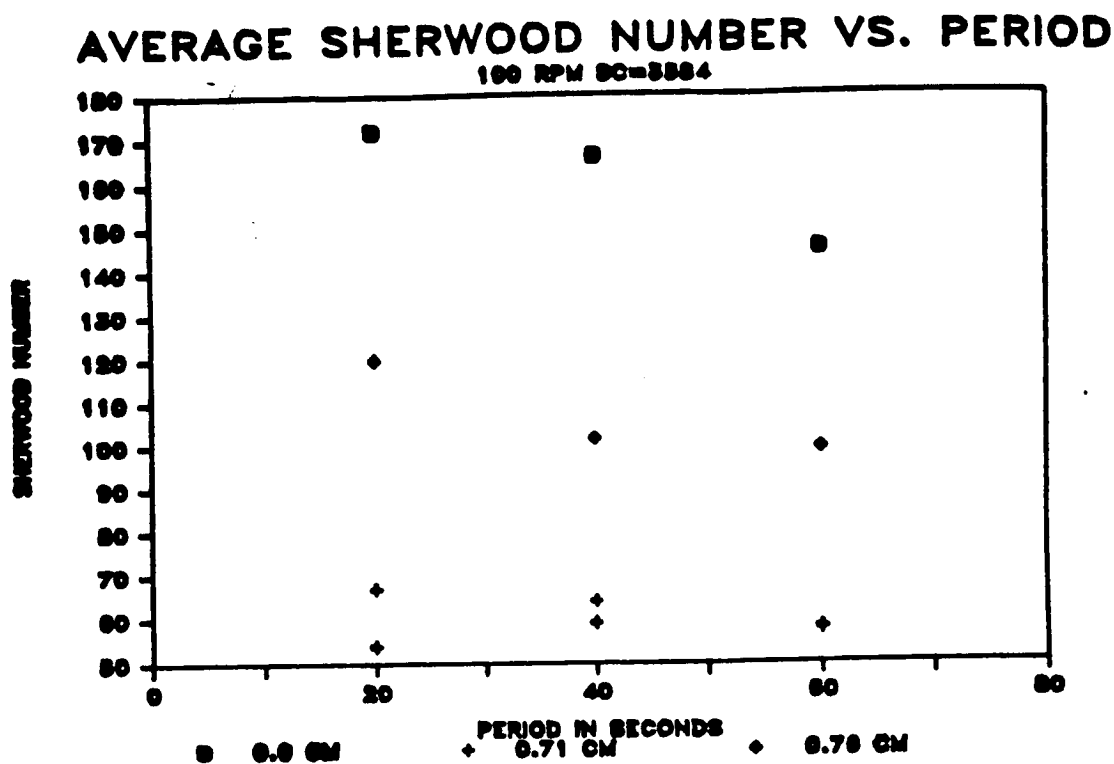


Figure 5.5: The average Sherwood number vs. the ACRT period length for 100 RPM and a Schmidt number equal to 3580.

Table 5.4: The values of the constants in equation 5.1.

RPM	Ekman Number	Schmidt Number	$A_1$	$A_2$	$A_3$
12	0.0161	6090	8.11	2.00	-0.0297
20	0.00967	6090	47.9	1.55	-0.0215
65	0.00205	3580	-10.9	5.22	-0.122
65	0.00194	2230	4.7	7.72	-0.221
100	0.00133	3580	99.5	1.004	-0.0202

The ACRT period giving the most interfacial mixing can be predicted by knowing the Ekman and Schmidt numbers. The correlation obtained to predict this value is:

$$\frac{T_{P1}}{t_{Ek}} = -59.5 - 2.65 \ln(Ek) + 6.213 \ln(Sc) \quad (5.50)$$

where  $T_{P1}$  is the ACRT period in seconds giving the most mixing,  $t_{Ek}$  is the Ekman time,  $Ek$  is the Ekman number,  $Sc$  is the Schmidt number, and  $\ln$  is the log in base  $e$ . The equation has an R-squared value of 83 percent.

In order to obtain homogeneous crystals, the spatial difference in the average Sherwood number at the edge and at the center should be a minimum. This would minimize radial composition variations in a Bridgman crystal. However, equation 5.49 is for maximum mixing and using the ACRT period predicted by it given may give the worst crystals.

Perhaps there is another measure which may be used to pick the best ACRT conditions. The previous criterion was based on trying to minimize the spatial differences during an ACRT cycle. However, looking at the temporal differences during an ACRT cycle may aid in predicting the best ACRT cycle.

Figures 5.6 through 5.10 show the ratio of the difference between the maximum Sherwood number and the minimum Sherwood number to the average Sherwood number vs. the ACRT period for a number of experimental conditions. This ratio is a quantitative indication of the fluctuation in the interfacial mass transfer during an ACRT period. Ideally, the ordinate would have a value of zero. That is, the interfacial mass transfer would be constant throughout the ACRT cycle. Figures 5.6 through 5.10 shows that the interfacial mass transfer during an ACRT cycle do not approach the ideal results. The graphs do show that as the ACRT period decreases,

the temporal variation decreases. Hence the temporal and spatial criteria agree; as the ACRT period is shortened, the smaller the magnitude of the compositional striations.

One question remains, what rotation rate should be used? Figure 5.11 gives the answer. This figure shows the ratio of average Sherwood number at the center to that at the edge vs. the Ekman number. It indicates that the larger the rotation rate the smaller the radial difference in the average Sherwood number along the interface. These larger rotation rates have Ekman numbers less than that needed to produce two peaks in the edge mass transfer for the long period ACRT experiments. In order for the edge Sherwood number to approach the center Sherwood number, the second disturbance is needed to raise the average Sherwood number at the edge.

#### 5.4 Linear ACRT

The theories for linear spin-up differ from those for non-linear spin-up in that the Stewartson layer remains attached to the cylinder wall during linear spin-up [52]. Behind the Stewartson layer in non-linear ACRT the fluid is nearly spun-up. Thus, much of the fluid motion at a given location near, but above, the endwall has ceased after the Stewartson layer crosses that location. Therefore the results for interfacial mass transfer at the edge during non-linear spin-up should be different from those of linear spin-up.

Figure 5.12 is a plot of the average Sherwood number in linear ACRT vs. the ACRT period. For small periods, the edge has a greater average Sherwood number than the center. For longer periods, the average Sherwood number at the center is greater than at the edge. In the non-linear studies, the center always had a larger average Sherwood number than the edge. Figures 5.13 and 5.14 show the

Table 5.5: The ACRT period giving the largest interfacial mixing from equation 5.48.

RPM	Ekman Number	Schmidt Number	Period (Seconds)
12	0.0161	6090	33.6
20	0.00967	6090	36.1
65	0.00205	3580	21.4
65	0.00194	2230	17.5
100	0.00133	3580	24.9

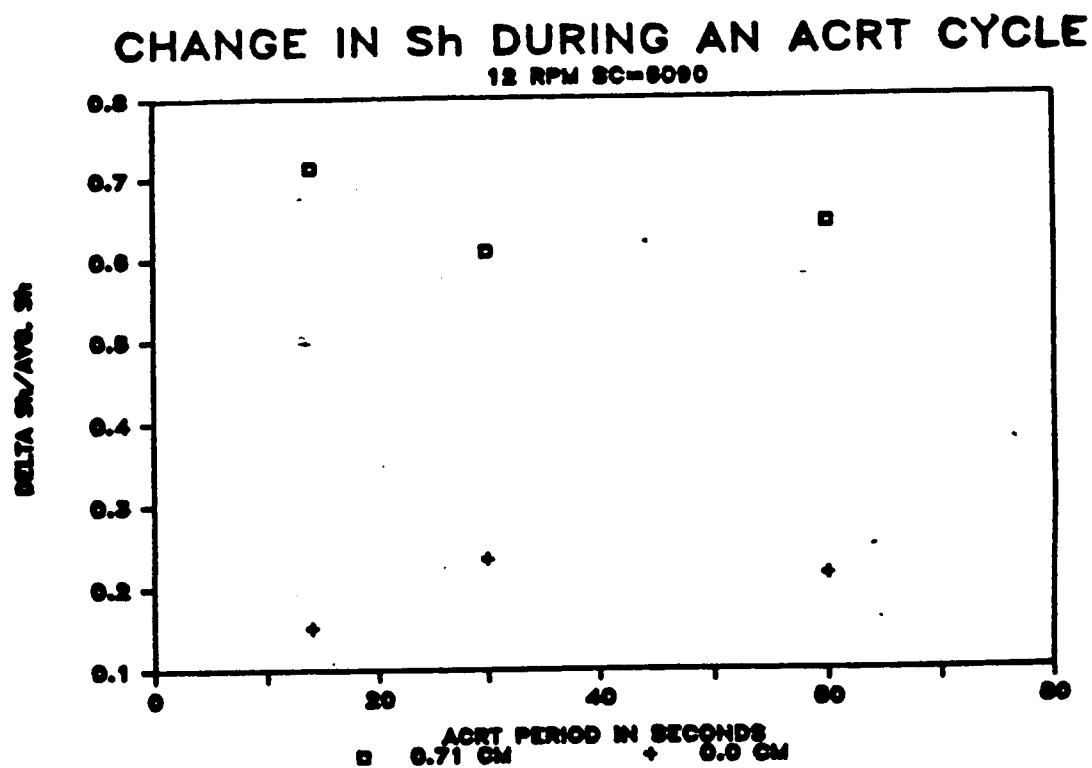


Figure 5.6: The temporal variation of the Sherwood number with ACRT period for 12 RPM and Schmidt number equal to 6090. Delta  $Sh$  equal  $Sh_{max}$  minus  $Sh_{min}$ .

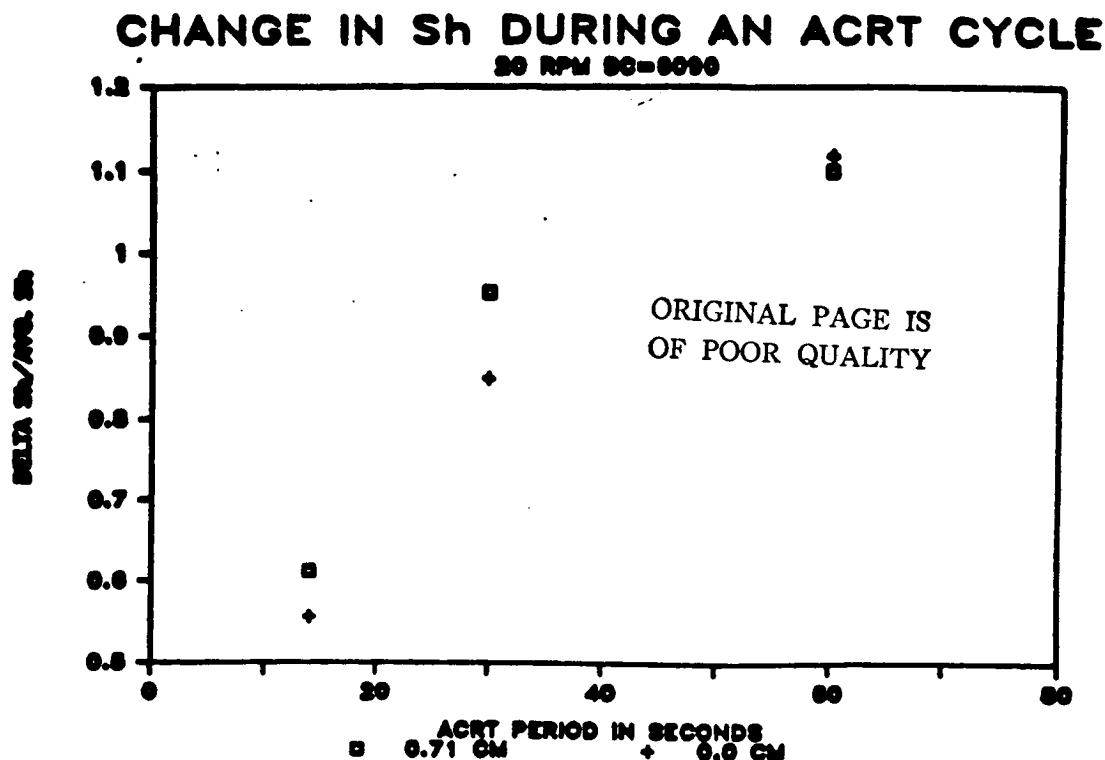


Figure 5.7: The temporal variation of the Sherwood number with ACRT period for 20 RPM and Schmidt number equal to 6090. Delta  $Sh$  equal  $Sh_{\max}$  minus  $Sh_{\min}$ .

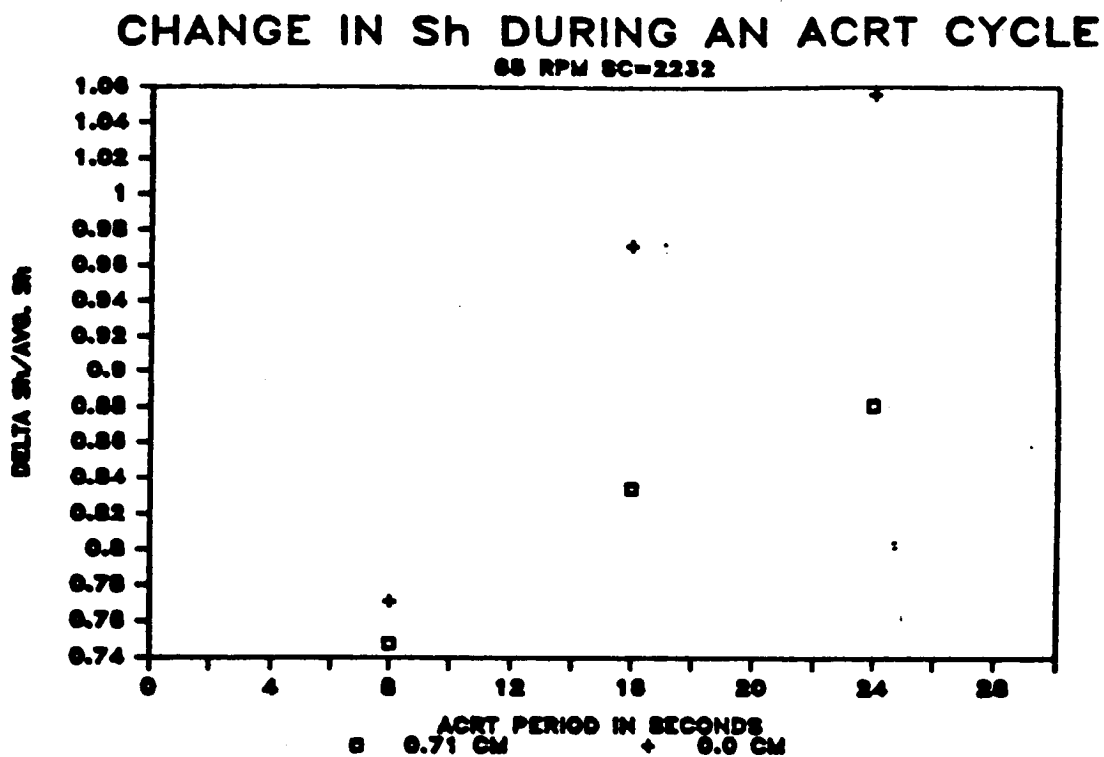


Figure 5.8: The temporal variation of the Sherwood number with ACRT period for 65 RPM and Schmidt number equal to 2230. Delta  $Sh$  equal  $Sh_{\max}$  minus  $Sh_{\min}$ .

## CHANGE IN $Sh$ DURING AN ACRT CYCLE

65 RPM SC=3580

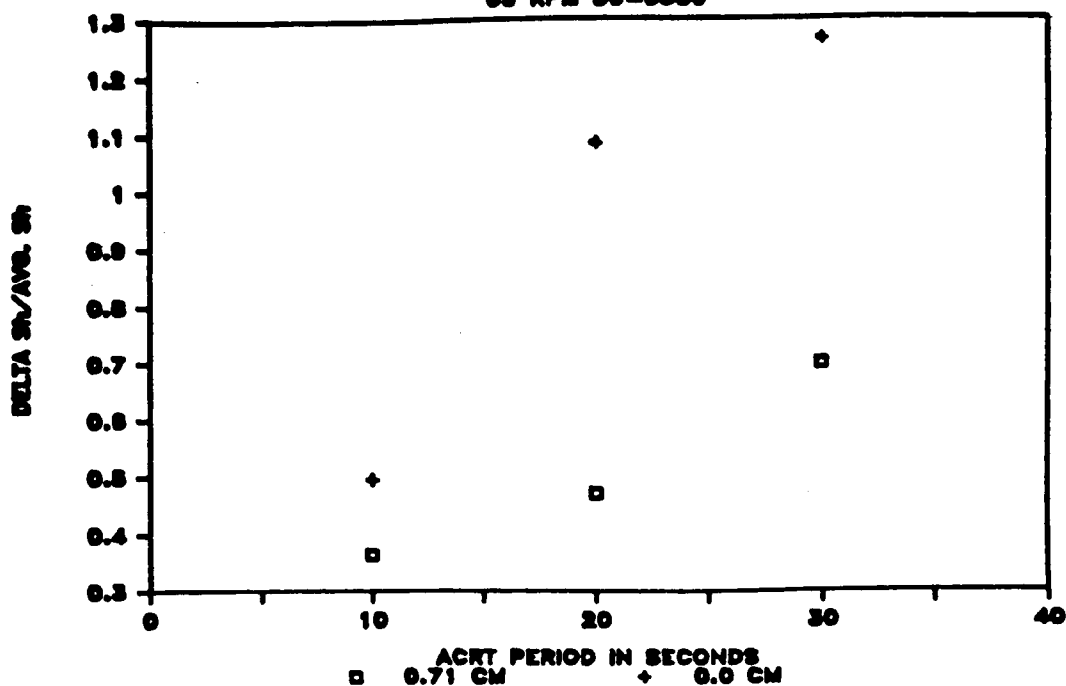


Figure 5.9: The temporal variation of the Sherwood number with ACRT period for 65 RPM and Schmidt number equal to 3580. Delta  $Sh$  equal  $Sh_{max}$  minus  $Sh_{min}$ .

## CHANGE IN $Sh$ DURING AN ACRT CYCLE

100 RPM SC=3580

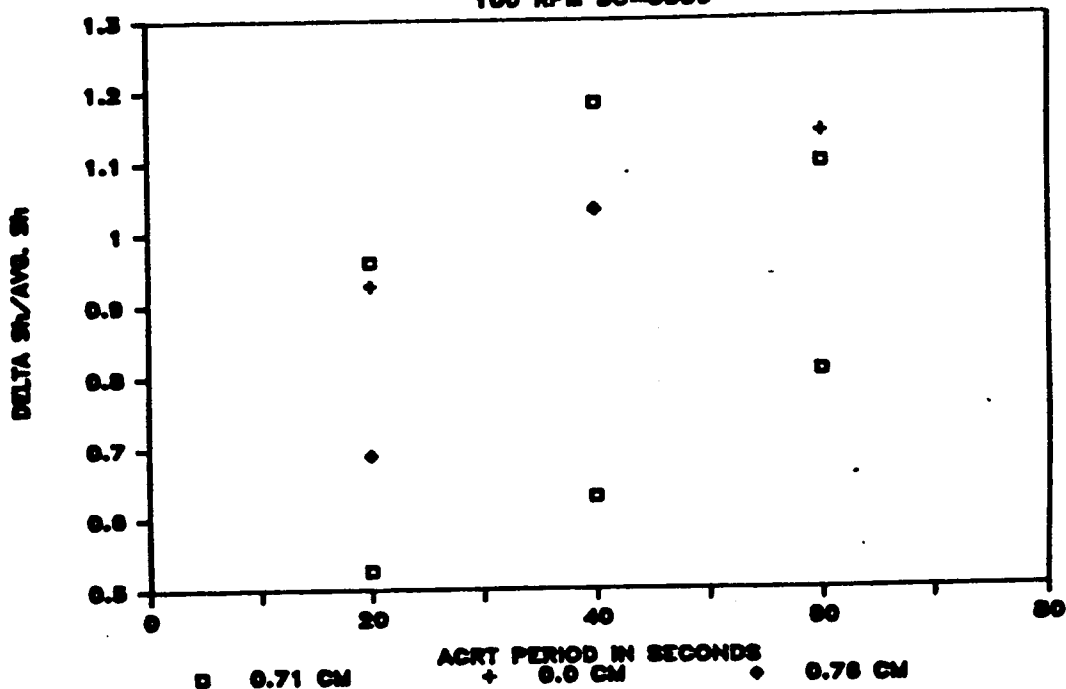


Figure 5.10: The temporal variation of the Sherwood number with ACRT period for 100 RPM and Schmidt number equal to 3580. Delta  $Sh$  equal  $Sh_{max}$  minus  $Sh_{min}$ .



ORIGINAL PAGE IS  
OF POOR QUALITY

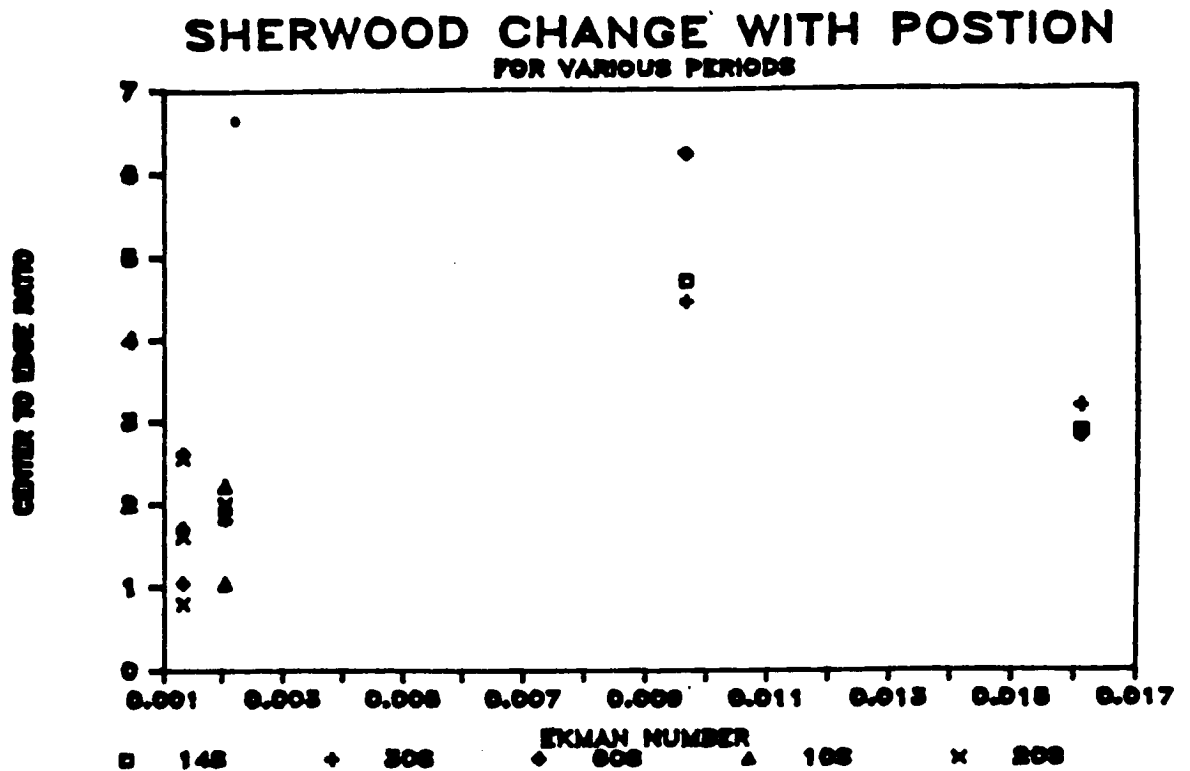


Figure 5.11: The ratio of the average Sherwood number at the center to that at the edge vs. the Ekman number. The closer the ratio is to unity, the smaller the variation with position along the interface.

difference in the maximum and minimum values of the Sherwood number at the center and edge, respectively, for linear and non-linear ACRT. In non-linear ACRT the difference between the maximum and minimum values is always less than in linear ACRT. In linear spin-up, the average Sherwood number at the center is fairly independent of the ACRT period, while in non-linear ACRT the average Sherwood number depends on the period.

The differences between linear and non-linear spin-up are caused by the difference in the behavior of the Stewartson layer. In linear spin-up, the Stewartson layer remains attached to the wall, while in non-linear spin-up it moves radially inward. Since the Stewartson layer remains attached to the cylinder wall during linear ACRT, the edge electrode is not blocked off as it is in non-linear ACRT. This permits the reactant direct access to electrode throughout the entire spin-up process.

The differences between linear and non-linear spin-down are caused by the differences in the centrifugal force in the two cases. In linear spin-down, the final state for the fluid is an angular velocity very close to the original angular velocity. Thus, as the fluid spins-down the centrifugal force resists fluid motion and may keep the flow from becoming turbulent.

ORIGINAL PAGE IS  
OF POOR QUALITY

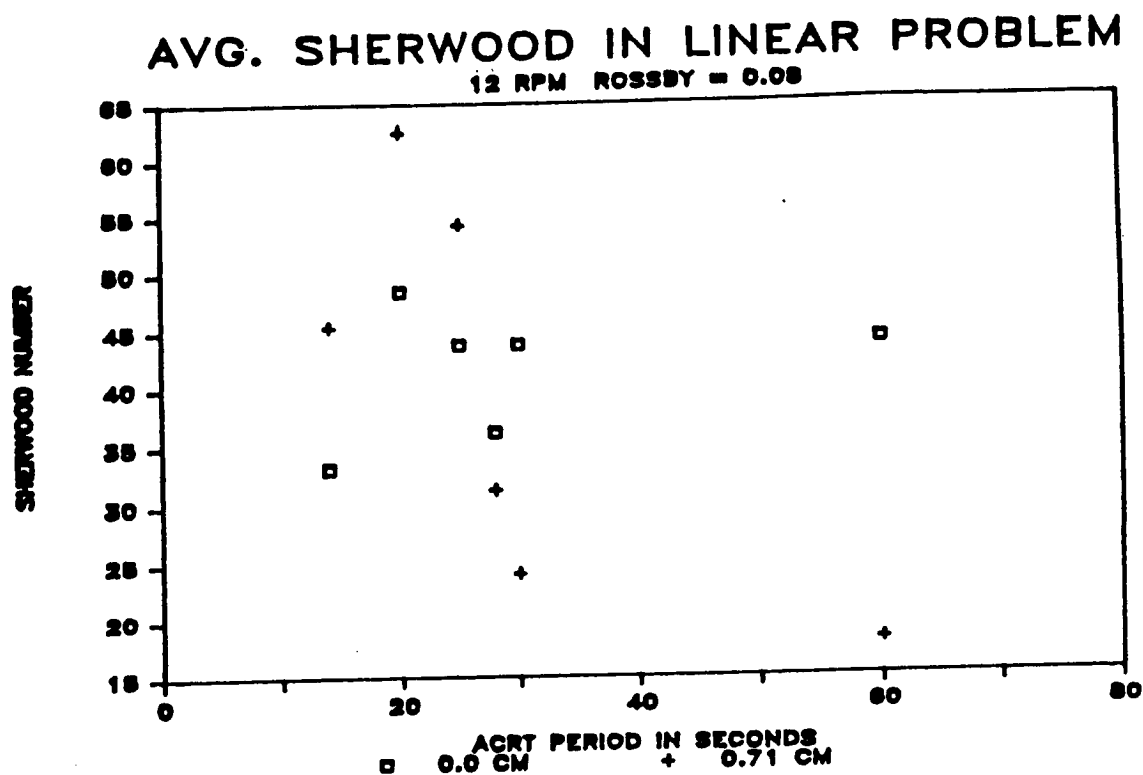


Figure 5.12: The average Sherwood number vs. the ACRT period for Rossby number = 0.08.

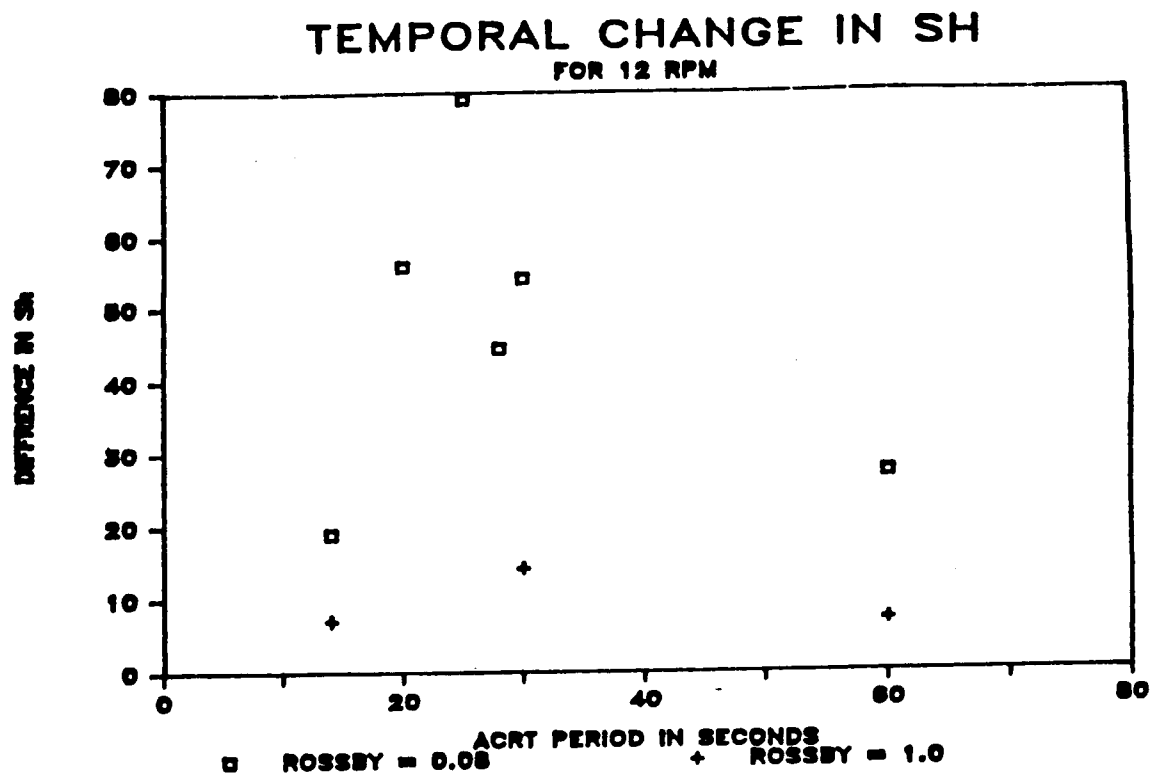


Figure 5.13: The difference in the maximum and minimum Sherwood number during linear and non-linear ACRT at the center.

ORIGINAL PAGE IS  
OF POOR QUALITY

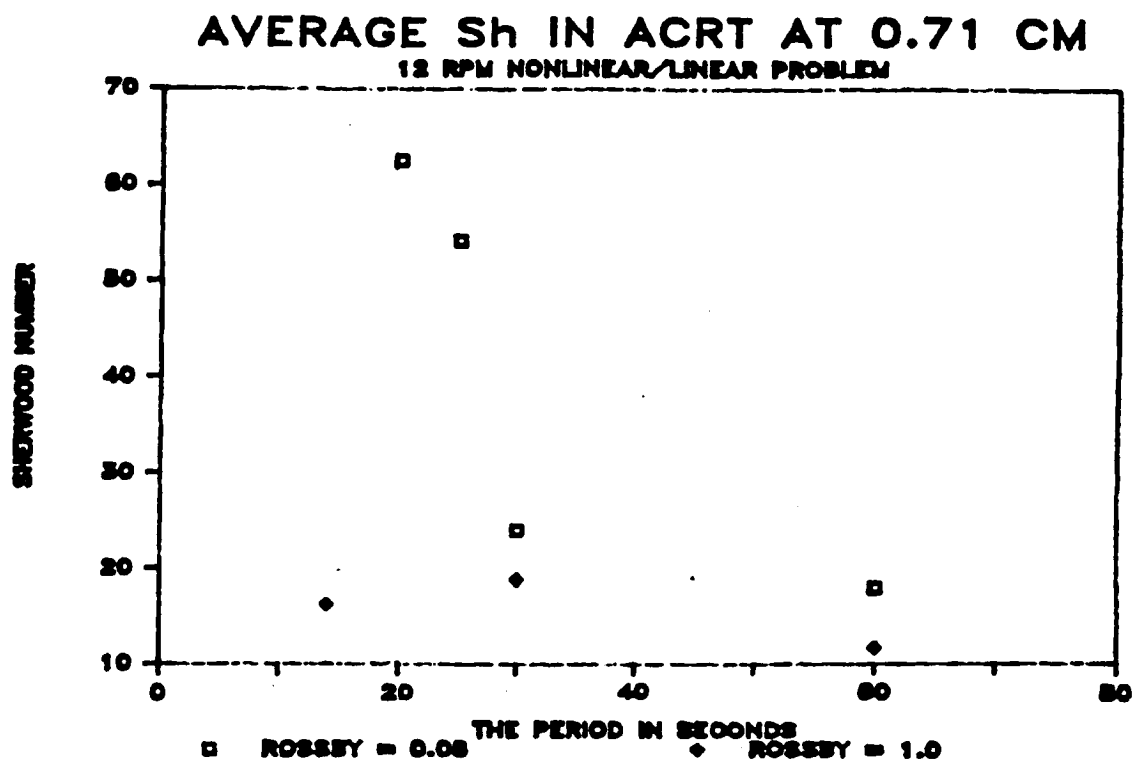


Figure 5.14: The difference in the maximum and the minimum Sherwood number during linear and non-linear ACRT at the edge.